COMPUTATIONAL AND EXPERIMENTAL STUDY OF SOLAR AIR HEATER WITH VARIOUS DUCT CROSS-SECTIONS AND ARTIFICIAL ROUGHNESS

Thesis

Submitted in partial fulfillment of the requirements for the degree of

DOCTOR OF PHILOSOPHY

by

NIDHUL K.
(177085ME029)

DEPARTMENT OF MECHANICAL ENGINEERING

NATIONAL INSTITUTE OF TECHNOLOGY KARNATAKA,

SURATHKAL, MANGALORE-575025

MAY, 2022

COMPUTATIONAL AND EXPERIMENTAL STUDY OF SOLAR AIR HEATER WITH VARIOUS DUCT CROSS-SECTIONS AND ARTIFICIAL ROUGHNESS

Thesis

Submitted in partial fulfillment of the requirements for the degree of

DOCTOR OF PHILOSOPHY

by

NIDHUL K.
(177085ME029)

Under the guidance of

Dr. AJAY KUMAR YADAV   **Dr. ANISH S.**

DEPARTMENT OF MECHANICAL ENGINEERING

NATIONAL INSTITUTE OF TECHNOLOGY KARNATAKA,

SURATHKAL, MANGALORE-575025

MAY, 2022

DECLARATION

I hereby *declare* that the Research Thesis entitled **"COMPUTATIONAL AND EXPERIMENTAL STUDY OF SOLAR AIR HEATER WITH VARIOUS DUCT CROSS-SECTIONS AND ARTIFICIAL ROUGHNESS"** which is being submitted to the **National Institute of Technology Karnataka, Surathkal** in partial fulfillment of the requirements for the award of the degree of **Doctor of Philosophy** in **Department of Mechanical Engineering** is a *bonafide report of the research work carried out by me*. The material contained in this Research Thesis has not been submitted to any other Universities or Institutes for the award of any degree.

Register Number: **177085ME029**

Name of the Research Scholar: **NIDHUL K.**

Signature of the Research Scholar:

Department of Mechanical Engineering

Place: NITK, Surathkal

Date: 13/05/2022

CERTIFICATE

This is to *certify* that the Research Thesis entitled **"COMPUTATIONAL AND EXPERIMENTAL STUDY OF SOLAR AIR HEATER WITH VARIOUS DUCT CROSS-SECTIONS AND ARTIFICIAL ROUGHNESS"** submitted by **NIDHUL K. (Register Number: 177085ME029)** as the record of the research work carried out by him, *is accepted as the Research Thesis submission* in partial fulfillment of the requirements for the award of the degree of **Doctor of Philosophy.**

Dr. AJAY KUMAR YADAV
Research guide
Date: 13/05/2022

Dr. ANISH S.
Research guide
Date: 13/05/2022

Chairman -DRPC
Date: 13/05/2022

Dedicated
to
my
Beloved Parents

&

Teachers

Whose Love and Support
Sustained Me Throughout

ACKNOWLEDGMENT

thank Dr. Venkatesh Lamani, Dr. Thippeswamy, Madagonda Biradar, Dr. Shankar, Dr. Tabish, Anteneh W., Addisu, Sangappa, Rudramurthy, Jagadeesh, Vysakh, Aravind, and the list seems to be endless.

I would like to take this opportunity to express my gratitude and respect to my parents, Sri Narayanan V. K. and Smt. Leela K., for their blessings and love. Their perseverance and willingness to shield me from any social and financial responsibilities facilitated my higher studies and brought me at the doorstep of a doctoral degree. Last but not least, I honestly acknowledge the unconditional support of my dear wife, Nijina, who joined as a life partner with me in the final stages of my research work. In addition, I express gratitude to my parents-in-law, Sri Jayaraj V. K. and Smt. Nishi for their blessings and love. I am thankful to be a part of such a wonderful family.

NIDHUL K.

MAY, 2022

NITK, SURATHKAL

ABSTRACT

Thermo-hydraulic performance and exergetic efficiency of solar air heater (SAH) with various duct cross-sections and artificial roughness have been investigated using numerical and experimental methodology. The RNG k-ε model with enhanced wall treatment is employed to study the turbulent flow behavior. Validation of the CFD results for smooth and artificially roughened SAH (triangular duct and duct with semi-cylindrical sidewalls) with theoretical correlations and experimental data indicates reasonable accuracy.

In triangular duct SAH, the performance of inclined ribs and V-ribs have been studied at inclinations ($30° \leq \beta \leq 90°$) to the primary flow for fixed relative rib height (e/D) and pitch (P/e). It is observed that V-ribs in triangular duct provides a maximum thermo-hydraulic performance parameter (THPP) of 2.01 with a 23% enhancement in exergetic efficiency compared to smooth SAH. Further, the performance of triangular duct SAH with inclined ribs in an indirect type solar dryer is studied. Dryer with ribbed triangular duct SAH exhibits a 60.4% and 55% reduction in moisture ratio for food samples robusta and nendran, respectively, for the same drying time compared to a dryer with a ribbed rectangular duct SAH. In addition, the design enhances the drying characteristics with 93.3% increase in average diffusivity coefficient for banana food samples.

CFD analysis of SAH design with semi-cylindrical sidewalls and continuous W-baffles provides THPP in the range of 1.70 to 2.27. Maximum enhancement in thermal and exergetic efficiency is obtained as 40.7% and 95.4%, respectively, relative to conventional SAH at $Re = 5000$. Based on the optimum results obtained from CFD, an experimental setup for SAH with semi-cylindrical sidewalls and multiple discrete inclined baffles is fabricated. The experimental results indicate that THPP is further enhanced for discrete inclined baffles with the gap at the trailing apex, with a peak value of 2.69. This design has higher collector efficiency (55 to 70%) compared to ribbed rectangular SAH design exhibiting 30 to 55%. Further, the design exhibits higher exergetic efficiency owing to lower exergy losses and higher collector efficiency. Maximum exergetic efficiency of 2.2% is obtained at lower Re, higher than that obtained for rectangular duct SAH with a similar kind of artificial roughness. In addition, at low Re, this SAH design has a higher coefficient of performance (COP)

than conventional SAH designs. Hence, a SAH design having lower number of sharp corners and artificial roughness capable of generating multiple secondary flow can enhance the heat transfer rate with higher thermo-hydraulic performance.

Keywords: Solar air heater, Artificial roughness, Triangular duct, Thermo-hydraulic performance parameter, Collector efficiency, Exergetic efficiency.

CONTENTS

LIST OF FIGURES

LIST OF TABLES

NOMENCLATURE

A	Area, m^2
V	Average velocity of air, m/s
U_b	Bottom loss coefficient, W/m^2K
R^2	Coefficient of determination
COP	Coefficient of performance
F_R	Collector heat removal factor
CFD	Computational fluid dynamics
h_w	Convective heat transfer coefficient due to wind, $W/m^2\,K$
d	Distance of gap from the sidewalls, m
t_e	Edge thickness, m
L_{env}	Exergy loss due to convective and radiation heat transfer to the environment, W
L_f	Exergy loss due to fluid friction, W
L_{ht}	Exergy loss due to heat transfer from absorber plate to the air, W
L_{abs}	Exergy loss during absorption of solar radiation by the absorber plate, W
f	Friction factor
g	Gap width, m
GCI	Grid convergence index
q	Heat flux, W/m^2
h	Heat transfer coefficient, W/m^2K
H	Height of the duct, m
D	Hydraulic diameter, m
ITSD	Indirect type solar dryer
t_i	Insulation thickness, m
IPCC	Intergovernmental Panel on Climate Change
IEA	International Energy Agency
L	Length, m
$\dot{m}$	Mass flow rate of air, kg/s
MR	Moisture Ratio

U_L	Net heat loss coefficient, W/m^2K
Nu	Nusselt number
L_{opt}	Optical exergy loss, W
F'	Plate efficiency factor
ΔP	Pressure drop, Pa
p	Pumping power, W
Ra	Rayleigh number
χ^2	Reduced Chi-square
R_H	Relative baffle height, m
R_P	Relative baffle pitch, m
Re	Reynolds number
e	Rib height, m
P	Rib pitch, m
U_b	Side loss coefficient, W/m^2K
w	Single V shaped rib width, m
SAH	Solar air heater
I	Solar insolation; W/m^2
C_p	Specific heat of air, $J/kg.\ K$
T_g	Temperature of glass, K
T_s	Temperature of sun, K
THPP	Thermo-hydraulic performance parameter
B	Thickness of the food samples, m
t	Time. min
U_t	Top loss coefficient, W/m^2K
Q_u	Useful energy output, W
W	Width of the duct, m

Greek letters

α	absorptivity
η_c	Carnot efficiency
η_{cc}	Collector efficiency

ρ	Density of air, kg/m^3
μ	Dynamic viscosity of air, $N.s/m^2$
ε	emissivity
η_{ex}	Exergetic efficiency
β	Inclination of artificial roughness to the primary flow, °
$\tau\alpha$	Product of transmissity and absorptivity
γ	Solar air heater inclination w.r.t. ground level, °
σ	Stefan-Boltzmann constant, W/m^2K^4
$\bar{\bar{\tau}}$	Stress tensor
ΔT	Temperature difference, K
λ	Thermal conductivity of air, $W/m. K$
λ_i	Thermal conductivity of insulation, $W/m.K$
η_{th}	Thermal efficiency

Subscripts

p	absorber plate
a	air
b	bulk
g	glass
i	inlet
o	outlet
r	roughened

CHAPTER 1

INTRODUCTION

Energy in numerous forms has been vital in global economic advancement and industrialization. As the world's population has grown and expanded material needs, the pace of energy consumption has increased to a rate that the conventional energy sources tend to exhaust. As per the International Energy Agency (IEA), global energy demand in 2021 is expected to rise by 4.6 %, offsetting the 4% decline in 2020 and boosting demand above 2019 levels (IEA Annual report 2020). This demand recovery would cause a 5% increase in CO_2 emissions. As a result, scientists and engineers are working towards a paradigm shift from conventional fossil fuels towards renewable energy sources. For achieving economic development, the importance of energy is universally acknowledged, with historical data confirming the strength of economic activity and energy availability. Accelerating global energy consumption for economic growth has significantly strained fossil fuel resources and increased concern over global warming effects and climate changes. As a result, it is anticipated that global ambient temperature will rise 2 °C by 2050 (Bastida et al. 2019; Al-Shetwi et al. 2020). The implications of the decreasing reserves and accelerating demand will be an escalation in prices, perhaps even higher than the inflation rate. Furthermore, there is concern about the pollution created by the combustion of fossil fuels in the environment.

This scenario has been prioritized at the world level, and harnessing renewable energy resources is sustainable. Sustainable development is commonly defined as "economic development meeting the requirements of the present without compromising future generation's ability to meet their needs." In the current scenario, energy is one of the vital aspects to achieve sustainable development. Supply of energy for the long-term at a reasonable cost combined with effective utilization is required for sustainable development within society. This calls for the deployment of renewable energy resources, indicating the close connection between sustainable development and renewable energy sources.

In this context, during the last two decades, there has been a worldwide research and development effort in renewable energy resources and systems. Renewable energy

sources such as solar energy, wind energy, and geothermal energy are abundant and sustainable for the future without creating any adverse impact on the environment, unlike conventional fossil fuel sources. According to IEA renewable energy market update 2021, renewable capacity additions surged by 45% annually to 280 GW, the highest since 1999, with renewables contributing 90% globally to new power capacity expansion. Among the renewable sources of energy, solar energy has been employed for drying and preserving food since prehistoric times. Subsequently, there has been significant development in utilizing solar energy for various applications since the 1970s oil crisis.

1.1 Solar Energy

Since prehistoric times, man has recognized that solar energy is beneficial and employed in drying and preserving food. The sun, the source of life on earth, provides a "free energy" source and can power a process. With a diameter of 1.39×10^9 m, the sun has an intense hot gaseous matter with an effective temperature of 5762K. The total energy output of 3.8×10^{20} MW from the sun is radiated outwards in all directions. However, when this energy arrives at the earth's surface, it reduces due to the upper atmosphere and clouds (Fig. 1.1). Hence, only a small fraction equal to 1.7×10^{14} kW is intercepted by the Earth (Kreith and Kreider 1978).

Nevertheless, even with this small fraction, 30 min of solar radiation is sufficient to meet energy demand for one year worldwide. The amount of solar radiation received also varies with latitude, elevation, season, and time variation during a particular day. Most developing countries receive high solar energy density within the tropical belt. Consequently, solar energy as an alternate source of energy can be utilized beneficially.

In this context, solar energy could be the future source of energy due to the following reasons:

- Global energy demand can be achieved as it is the most abundant energy source and freely available with no cost among the available renewable energy resources (Lewis 2007).

- It is non-exhaustible and can give higher output efficiencies than other renewable energy resources (Nozik 1978).

2

- Direct solar energy with the highest potential can be harnessed for varying applications in different forms.
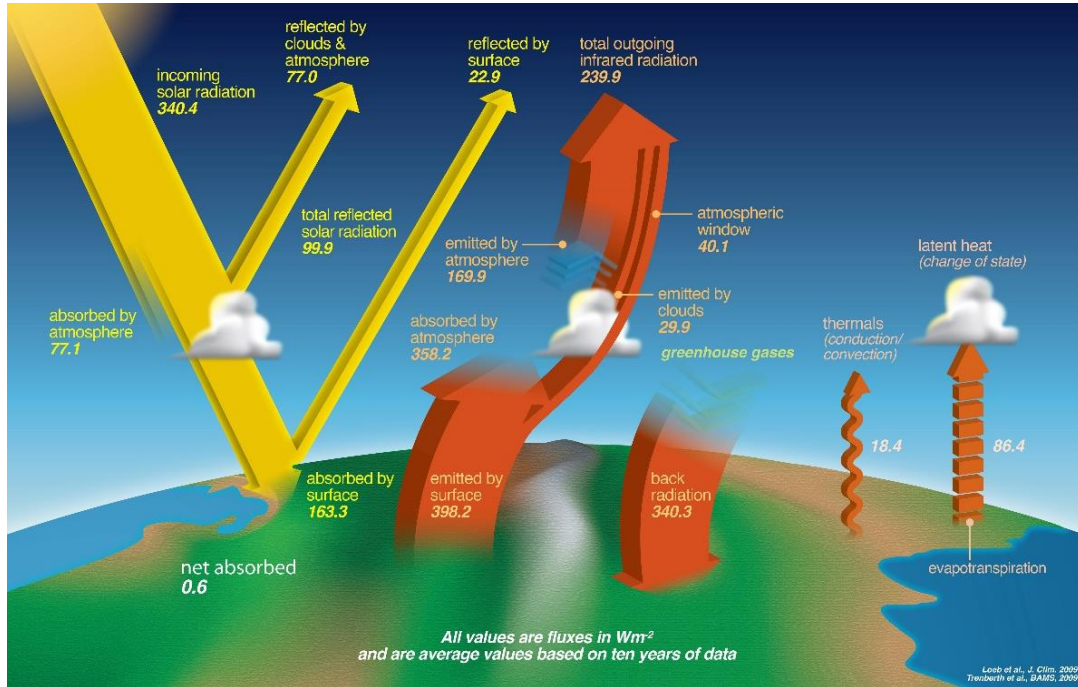
Fig. 1.1 Solar energy available on the earth's surface.

(https://www.nasa.gov/sites/default/files/thumbnails/image/ceres-poster-011-v2.jpg).

Table 1.1: The global potential for all renewable energy sources
(Source: IPCC 2012).

Renewable Energy Sources	Global Technical Potential (EJ)	
	Minimum	Maximum
Direct Solar Energy	1575	49837
Geothermal Energy (Electricity)	118	1109
Wind Energy	85	580
Biomass	50	500
Ocean Energy	7	331
Geothermal Energy (Heat)	10	312
Hydropower	50	52

The global potential (in exajoule) for all renewable energy sources assessed by Intergovernmental Panel on Climate Change (IPCC) is listed in Table 1.1. Solar energy can be used in two fundamental aspects (Duffie and Beckman 1994). The first category includes various local applications characterized by on-site solar energy collection, conversion, and consumption. Passive solar energy in buildings, solar radiation collectors for heat production, and photovoltaic arrays for electricity generation are a few which fall within this category. In contrast, solar power plants such as photovoltaic, solar thermal power plants, ocean thermal energy conversion (OTEC), etc., require high direct radiation and are categorized in the offsite facet of solar usage.

1.2 Various Methods of Solar Energy Utilization

Solar energy utilization is broadly classified into direct and indirect methods (Fig. 1.2). Solar thermal and photovoltaic conversion techniques are considered direct means of solar energy utilization, and indirect methods comprise hydro, wind, biomass, wave energy, and OTEC.
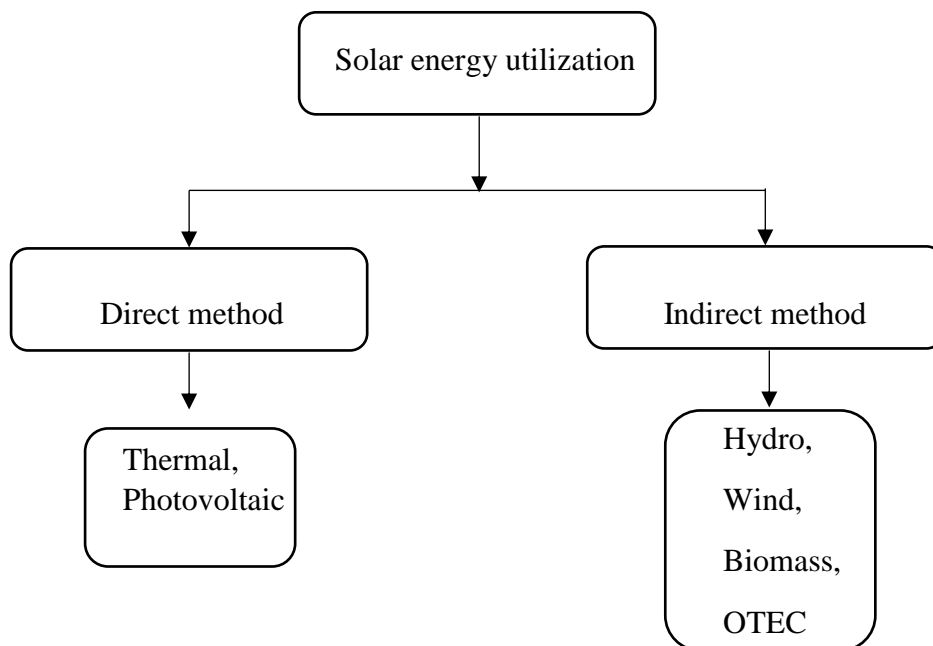
Fig. 1.2 Classification of solar energy utilization methods.

In a solar photovoltaic system, solar radiation is converted into direct current through the electrical process and can be used in various domestic and industrial applications. Whereas in solar thermal, heliothermal process is used to generate thermal energy from

solar radiation and is widely employed in solar air heating, water heating, space heating, and drying. Solar to thermal conversion systems have a substantially better conversion efficiency than solar to electrical conversion systems. This is primarily due to the limitations of reduced photon absorption and low photon to electricity conversion efficiency. When it comes to fulfilling the energy needs of diverse applications in the process industries, heat energy is favored above electrical energy. As a result, one of the most appealing alternatives for producing thermal energy for process heat applications is a solar thermal energy system. Hence, solar thermal energy has a vast potential to replace traditional energy sources.

Industry-related process heat accounts for more than a third of total global energy consumption. Steam produced from fossil fuels constitutes 10% of energy in the metal sector, 23% in petroleum refining, 80% in pulp and paper, and 60% in the food processing industries as industrial process heat (Einstein et al. 2001). In India, industrial process heating applications account for 32% of total energy consumption (Berkel 2018). Solar thermal systems are utilized as a heat source for domestic and large-scale applications such as water heating, space heating, power generation, and process industries.

1.3 Solar thermal energy systems

Solar energy is most commonly harnessed and utilized using a collection device exposed directly to the radiation from the sun. The collection device is mainly of two types, non-concentrating and concentrating. In the former, metal (usually aluminum or copper) coated with black paint is exposed to the sun directly. The absorbed energy in heat is transferred to the working fluid. In the latter, solar radiation is concentrated to a focal point using a curved reflecting surface. Further, solar thermal energy systems are classified based on operating temperature, the axis of tracking, concentration nature, and optical device.

Solar thermal systems can be grouped into three categories based on their operating temperatures: (a) low temperature (30 to 150 °C), (b) medium temperature (150 to 400 °C), and (c) high temperature (>400 °C) (Kalogirou 2003). Solar thermal systems are classified into Single-axis tracking (LFR and PTC) and two-axis tracking (PDC) systems based on the tracking axis. Based on the method of concentration of solar

radiation, they are classified as stationary collectors or non-concentrating (FPC, ETC) and concentrating collectors (LFR, PTC, CR, and PDC).

1.3.1 Non-concentrating collectors

In non-concentrating collectors, solar radiation is incident on the absorber plate through one or more transparent covers. These collectors are fixed permanently in a position or orientation and hence termed as stationary collectors. Thermal energy in the form of heat is transferred from the absorber plate to the working fluid, which flows through the device. When working fluid is water, the device is termed "solar water heater," and for air, it is termed "solar air heater." In this type of collector, apart from direct radiation, diffuse solar radiation also contributes to the total heat flux incident on the absorber plate. Commonly employed non-concentrating solar thermal collectors are flat plate and evacuated tube collectors.

Among the non-concentrating collectors, flat plate collectors are the most commonly employed type of collector. In this type, a significant portion of the solar radiation is transmitted through a transparent cover onto an absorber plate coated in black to increase the absorptivity. Due to high absorptivity, a large portion of incident solar radiation is absorbed and then transferred as thermal (heat) energy to the working fluid. Flat plate collectors generally do not require sun tracking and are permanently fixed in a position oriented towards the equator, facing north in the southern hemisphere and south in the northern. The collectors are placed at an inclination equal to the location's latitude with 10 to 15° variation depending upon the application and working fluid. Evacuated tube collector (ETC) features a heat pipe (the absorbing surface), a sealed copper pipe carrying the working fluid that undergoes evaporation and condensation. The heat pipe is placed inside a vacuum-sealed tube to reduce the heat loss to the environment inherent in FPC.

1.3.2 Concentrating collectors

Concentrating collectors, equipped with a sun-tracking technique, comprise a reflective concentrator and possess a much higher concentration ratio (aperture area to absorber area). A higher concentration ratio is achieved by employing suitable reflecting surfaces resulting in increased heat flux density on the absorber surface. Hence, they are

potentially used for high-temperature thermal applications. Parabolic trough collectors (PTC), Parabolic dish collectors (PDC), and Linear Fresnel collectors (LFR) are various types of concentrating collectors. A parabolic reflector concentrates the solar rays onto a receiver positioned along the reflector's focal line in a PTC. The heat is absorbed by the working fluid flowing through the receiver. In a PDC, the parabolic reflector concentrates light on the receiver positioned at the reflector's focal point. As the receiver's size is smaller than PTC, PDC is suitable for small-scale power generation applications. Fresnel reflectors concentrate solar rays using thin flat mirror strips onto tubes where the working fluid flows. Due to the application of flat mirrors, a more reflective surface is employed in the same amount of space compared to parabolic reflectors.

1.4 Flat plate solar air heater

A flat plate solar air heater is a heat exchanger in which radiant energy of the incident sun rays is transferred as heat energy to air (working fluid). For low to medium temperature range applications, flat plate collectors (FPCs) form the heart of the solar energy collection systems and are the most commonly employed type of collector. The following are the advantages of FPCs over other types of solar collectors:

(i) They are fixed in a position and do not require sun tracking,

(ii) Components of solar radiation such as direct, diffuse, and reflected components are absorbed,

(ii) Simple in construction with no moving components and requires lower maintenance.

1.4.1 Components of flat plate solar air heater

Conventional flat plate solar air heater consists of a transparent (glass) cover at the top, absorber plate, and insulation at the bottom and sidewalls, as shown in Fig. 1.3. The absorber plate is made of a high thermal conductivity material, such as aluminum or copper. Solar radiation is transmitted through a transparent cover usually made of glass onto the absorber plate. It is desirable that the absorber plate absorbs the maximum amount of incident solar radiation and emits a minimum. A significant portion of the solar radiation falling on the absorber plate is within 0.2 to 2.5 μm wavelength, and that

emitted by the hot absorber plate is more than 2.5 μm. Hence, a selective coating is applied to maximize the absorptivity (α) and minimize emissivity (ε) to obtain a higher α/ε ratio. The transparent cover reduces convection heat losses from the heated absorber plate to the ambient air. Insulation is provided on the bottom and sidewalls of the SAH using Rockwool or glass wool to prevent heat loss from the absorber plate. Sun tracking arrangement is generally not required as they are permanently fixed in a position.
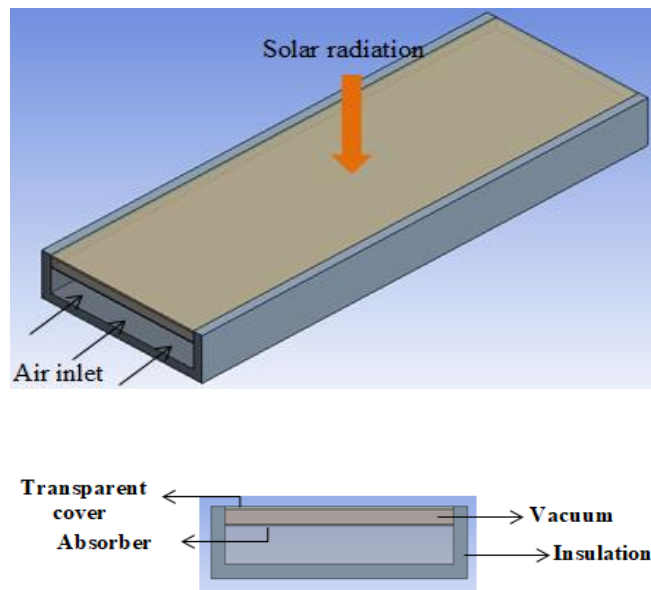
Fig. 1.3 Pictorial representation of a flat plate solar air heater.

1.4.2 Classification of flat plate solar air heater

Flat plate solar air heaters can be classified into many possible designs based on the materials and configurations. Close (1963) classified flat plate SAH into three basic types: type I, type II, and type III according to the air duct location. The simplest form is type I, wherein the transparent cover and the absorber plate form the top and bottom of the SAH, respectively, and the space between them is the air duct (Fig. 1.4). The air duct is split into two portions in type II by the absorber plate, unlike type I, with a single air stream above the absorber plate. As the air flows through the top and bottom of the absorber plate, the convective heat transfer rate is enhanced, and conduction heat loss through the bottom of the plate is reduced, reducing the insulation quantity at the bottom of the SAH as compared to type I (Fig. 1.5). In type III, a vacuum between the transparent cover and the absorber plate reduces the convective heat transfer. It leads

to higher radiation heat exchange as the temperature of the transparent cover decreases (Fig. 1.6).
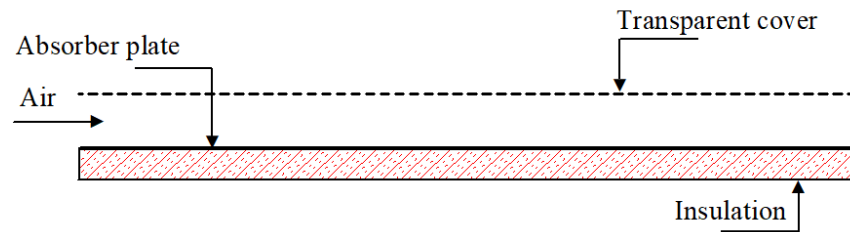
Fig. 1.4 Schematic representation of type I flat plate solar air heater.
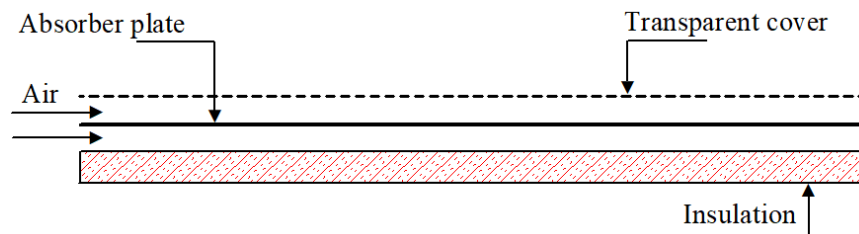
Fig. 1.5 Schematic representation of type II flat plate solar air heater.
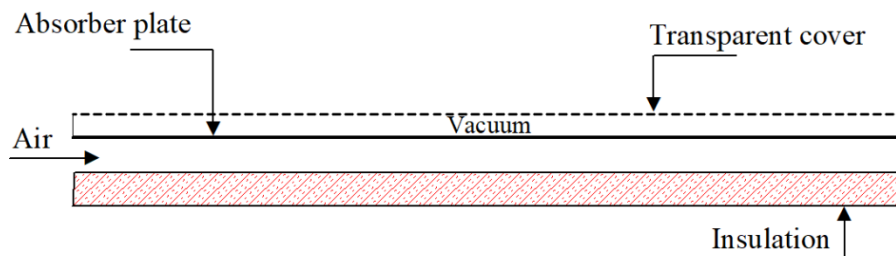
Fig. 1.6 Schematic representation of type III flat plate solar air heater.

Later, according to the type of absorbing surface employed, Garg (2000) classified flat plate SAH under six categories. They are: (i) Simple flat plate, (ii) finned plate, (iii) corrugated plate, (iv) matrix type absorber plate, (v) overlapped transparent type, and (vi) transpiration type. Among them, simple flat plate SAH is the most widely employed type of SAH. As discussed above, it is composed of a transparent cover and an absorber plate with insulation to reduce the bottom heat loss. The air duct location may be either above, below, or both above and below the plate. In simple flat plate SAH, the convective heat transfer coefficient value is low and is enhanced by employing fins on the absorber plate in the airflow passage. This modified simple flat plate SAH version is termed the finned-plate SAH (Fig. 1.7). Another classification of flat plate SAH is

the corrugated plate SAH, in which the absorber plate is designed with corrugations of rounded or V-troughs (Fig. 1.8). A corrugated absorber plate facilitates a higher heat transfer area and enhances the convective rate.
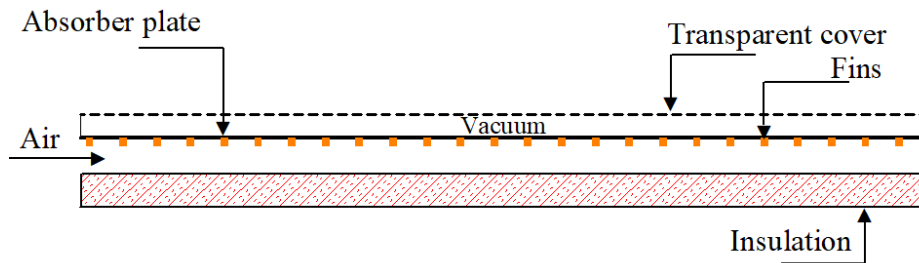
Fig. 1.7 Schematic representation of finned-plate solar air heater.
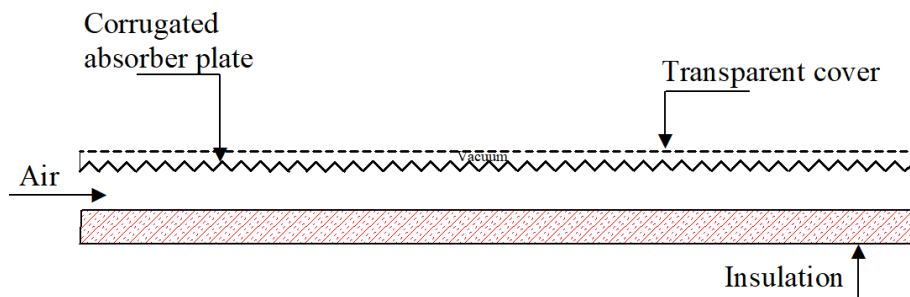
Fig. 1.8 Schematic representation of corrugated-plate solar air heater.

In matrix type SAH design, an absorbing matrix such as wire screen meshes, cotton gauge, or any other loosely packed porous material is placed in the airflow passage between the transparent cover and the absorber plate to increase the heat transfer area to volume ratio. The matrix material behaves as a large set of black bodies, increasing the absorptivity significantly compared to a regular solid absorber plate. Based on airflow direction, Lansing et al. (1979) studied upward (Fig. 1.9) and downward flow (Fig. 1.10) configurations of matrix type SAH. Overlapped transparent type SAH consists of a series of parallel glass plates overlapping with the lowermost portion blackened, as shown in Fig. 1.11 (Selçuk 1971). Inlet air stream with uniform velocity flows through and in between the glass plates with lower pressure drop and higher heat transfer area. The transpiration type SAH is a variation of matrix type SAH with matrix material as a honeycomb-like structure placed between the glass and absorber plate (Fig. 1.12). Air enters through the top, gets heated by the incident solar radiation, and then passes through the honeycomb structure (Hexagonal shape), wherein it attains

maximum temperature. In this design, the convective and radiation heat losses through the glass are minimized (Lalude and Buchberg 1971).
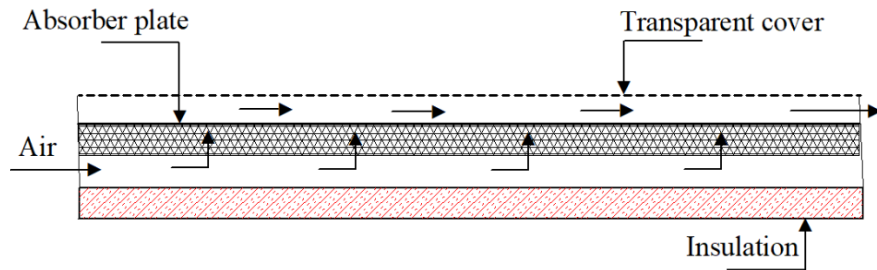
Fig. 1.9 Schematic representation of upward flow matrix type solar air heater.
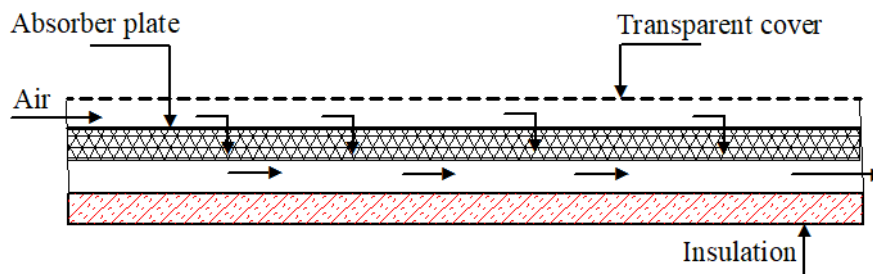
Fig. 1.10 Schematic representation of downward flow matrix type solar air heater.
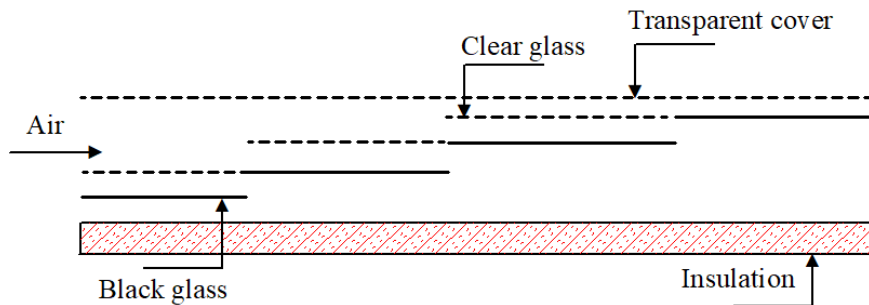
Fig. 1.11 Schematic representation of overlapped transparent type solar air heater.
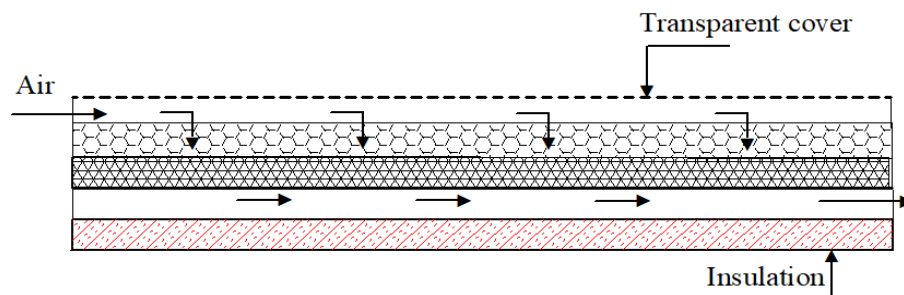
Fig. 1.12 Schematic representation of transpiration type solar air heater.

In all of the above-discussed designs, the number of air passes from inlet to outlet of the SAH is single. Even though the pumping power is lower in single-pass SAH, the

thermal losses are higher due to higher plate temperature and lower thermal efficiency. It is observed that when the number of passes increases, net thermal losses are lower (Satcunanathan and Deonarine 1973). Hence, flat plate SAHs are also classified based on the number of air passes through the SAH duct as single-pass, double-pass (Fig. 1.13), and multiple-pass SAH.
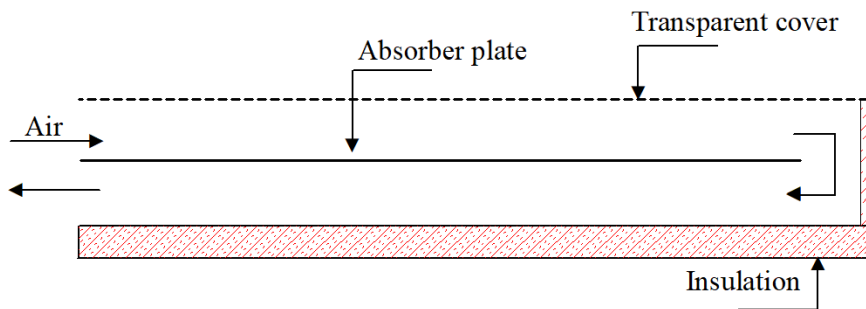
Fig. 1.13 Schematic representation of double pass solar air heater.

1.5 Artificial roughness in the solar air heater

Owing to simplicity in construction, lower maintenance, and low-pressure drop, single-pass flat plate SAHs have been widely used for medium to low-temperature applications. However, flat plate SAHs have an inherent disadvantage of lower thermal efficiency attributed to the low thermal conductivity of air and lower convective heat transfer rate between absorber plate and air. Lower convective heat transfer rate is attributed to the development of the boundary layer and increasing thickness of the laminar sublayer over the hot absorber plate leading to higher thermal resistance and heat losses. In concern to this, active and passive methods have been employed by researchers to improve the thermal performance, of which the passive approach has gained interest. In this regard, researchers have used extended surfaces in various configurations underneath the heated absorber plate, turbulators/fins, termed as artificial roughness, which will be discussed comprehensively in the subsequent chapter.

Ribs/turbulators in flat plate SAH create additional turbulence and interrupt the growing sub-layer. However, as the ribs resist the flow due to the blockage effect, they create additional pressure drop, demanding higher pumping power input. Hence, while designing artificial roughness for SAH, the functional objective is to enhance the heat

transfer rate with a minimum possible increase in pressure drop. In this regard, energy and exergy performance analysis are conducted, and the same is compared with the conventional smooth plate solar air heater.

1.6 Applications of flat plate solar air heater

Hot air from flat plate SAH can be used for various low to medium-temperature applications. The thermal conversion mode is a simple technology that can be readily adapted to any application site. The most common applications include drying agricultural products. People have been employing energy from the sun to dry and preserve their harvest, space heating and cooling of buildings, and process heating in industrial applications.

1.6.1   Drying of Agricultural products

For a developing nation where agriculture forms the economy's backbone, drying and preserving farm harvest is of prime importance. From ancient times, people relied on the Sun to dry and preserve the agricultural harvest (Ekechukwu 1999). However, open sun drying (direct drying) had inherent demerits, such as loss of quality and longer drying time (Saini et al. 2017). In this regard, indirect drying with the help of a flat plate SAH, termed as indirect type solar dryer (ITSD), has the flexibility of natural and forced convection modes of operation, thereby enabling better control over drying temperature and improving the quality of dried products. ITSD comprises a drying chamber and a solar air heater to supply hot air to remove the moisture content of the samples kept in the drying chamber. ITSDs are classified as active and passive dryers based on the mode of operation.

1.6.2   Space heating and cooling of buildings

Flat plate SAH can effectively harness solar thermal energy for need-based applications in residential and commercial space and reduce excessive use of fossil fuels, thereby reducing greenhouse emissions. There are two types of space heating systems – active and passive air-based systems. The passive systems, often part of a building design, depend upon building features like orientation w.r.t. sun, structure, shape, or materials. In contrast, active systems can be installed with few modifications to facilitate air movement in a duct, irrespective of the building design.

1.6.3 Industrial applications

As the industrial heat requirement constitutes a significant portion of the total energy requirements, SAHs can be readily employed in process heat requirements, solar cooling and air conditioning, seawater distillation, and solar drying. Considering the price escalation and limited fossil reserves, SAHs for industrial applications are gaining momentum. For example, hot air is employed in the plastic and timber industries to cure plastics and season timber. Further, hot air can regenerate dehumidifying materials such as silica gel.

1.7 Structure of the thesis

Chapter 1 presents the importance of renewable energy systems, particularly solar energy systems, for a sustainable future. A brief introduction of various solar thermal energy systems, and their applications are discussed. In addition, a brief outline of the thesis is included.

Chapter 2 presents a comprehensive and critical review of artificial roughness in SAH. It contains the study on the impact of various artificial roughness parameters and configurations on the fluid flow structure and thermo-hydraulic performance categorized into subsections based on the duct geometry. Furthermore, the conclusive summary, motivation, and objectives of the present study are detailed.

Chapter 3 presents a numerical and experimental methodology involved in achieving the objectives. A detailed description has been given on computational domain, boundary conditions, and flow physics set up. Computational simulations are validated with the experimental results and theoretical correlations. Further, the SAH design with artificial roughness delivering the maximum thermo-hydraulic performance is fabricated and studied experimentally.

Chapter 4 presents a 3D computational study of the thermo-hydraulic performance of V-ribbed triangular duct SAH. Additionally, exergy analysis is carried out to quantify the various exergy losses and hence the exergetic efficiency.

Chapter 5 presents a 3D computational study of energy-efficient SAH design with a triangular cross-section and inclined ribs for an indirect type solar dryer. The thermo-hydraulic performance of the same is then compared with conventional rectangular

ducts with similar artificial roughness for the same heat input. Furthermore, the drying characteristics of various food samples are experimentally tested to confirm the superior performance of the indirect type solar dryer.

Chapter 6 presents a 3D computational study of a SAH duct with semi-cylindrical sidewalls to enhance the strength of the secondary flow. With W-baffles as artificial roughness, the thermo-hydraulic and exergetic performance of the design is compared to the conventional rectangular duct SAH with similar kind of artificial roughness.

Chapter 7 presents a computational and experimental study of the impact of secondary flow strength in various configurations of discrete W-baffled SAH duct with semi-cylindrical sidewalls on the energy and exergetic performance and comparison of the same with conventional rectangular duct SAH with similar kind of artificial roughness.

Major conclusions and recommendations for future work are presented in **Chapter 8**.

CHAPTER 2

LITERATURE REVIEW

To improve the performance of a flat plate solar air heater (SAH), several active and passive techniques have been developed by various researchers, of which the latter has gained a lot of attention. Researchers have used various flow turbulators/fins, called artificial roughness, placed underneath the heated absorber plate. Artificial roughness in the form of ribs was employed in the flat plate SAH to disrupt the growing sub-layer and create additional turbulence. However, artificial roughness causes resistance to the airflow and generates further pressure drop, demanding more pumping power. Hence, the functional objective of designing an appropriate artificial roughness is to minimize the pressure drop while enhancing the heat transfer rate.

Further, improvement in the overall performance of the SAH was achieved by selecting the optimum flow and geometric parameters. Various rib types and configurations were studied to optimize geometric and operating parameters. Hence, the impact of rib profile and configuration on the flow structure, various kinds of ribs employed in rectangular and triangular duct SAH, exergy analysis, and application of ribbed SAH in indirect type solar dryer are discussed to identify substantial research gaps.

2.1 Impact of rib parameters on flow characteristics

The presence of rib alters the flow pattern causing a change in the heat transfer and friction factor characteristics of the SAH duct. The changes induced in the flow patterns depend upon various rib parameters such as rib height (e), rib pitch (P), rib inclination (β), and rib gap width (g). Height and pitch of the rib were expressed as relative roughness height (e/D) and relative roughness pitch (P/e), respectively. This section discusses the variation in flow pattern caused by the ribs and the optimum value of various rib parameters obtained by studies established in the literature. The subsequent section will cover the detailed review of various types of ribs categorized according to their configuration and the resulting enhancement in Nusselt number (Nu) and friction factor (f).

2.1.1 Impact of roughness height

While designing an artificial roughness for SAH, the objective is to keep the roughness height of the order of laminar-sublayer thickness. This ensures that the roughness height is large enough to disrupt the laminar sublayer of the turbulent boundary layer profile while keeping the pressure drop to a minimum. The roughness height influences flow separation near the roughness walls, and the reattachment occurs in the wake region of the roughness (Prasad and Saini 1988).
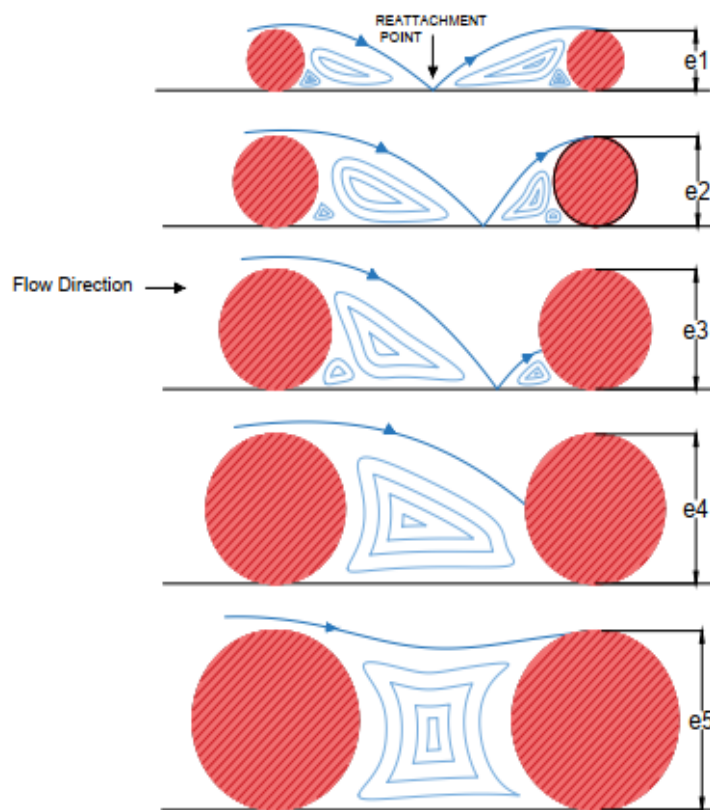
Fig. 2.1 Impact of rib height on the flow pattern.

It was also reported that the peak heat transfer rate occurs at the reattachment point. For larger rib (artificial roughness) height, additional turbulence in the bulk flow increases pressure drop, and heat transfer rate drops owing to the absence of flow reattachment (Fig. 2.1). Optimum rib height for a given configuration varies with the rib pitch (Alam and Kim 2017a; Singh and Singh 2018a). Optimum values of P/e reported by various studies are given in Table 2.1.

Table 2.1: Relative rib height values corresponding to maximum heat transfer for different ribs in the solar air heater.

Rib geometry	e/D
Transverse continuous (Prasad and Saini 1991)	0.033
Wedge shape (Bhagoria et al. 2002)	0.033
V-shape (Momin et al. 2002)	0.034
Discrete transverse (Sahu and Bhagoria 2005)	0.033
Metal grit rib (Karmare and Tikekar 2007)	0.044
Arc (Saini and Saini 2008)	0.042
Discrete inclined (Aharwal et al. 2009)	0.037
U-shape (Bopche and Tandale 2009)	0.039
Multiple V-shape (Hans et al. 2010)	0.043

2.1.2 Impact of rib pitch

Peak heat transfer was attained at the point of reattachment due to the presence of the rib. For $P/e < 8$, flow reattachment does not occur as the ribs were closely placed, and for $P/e \geq 8$, flow reattachment occurs in the inter-rib region, as shown in Fig. 2.2.
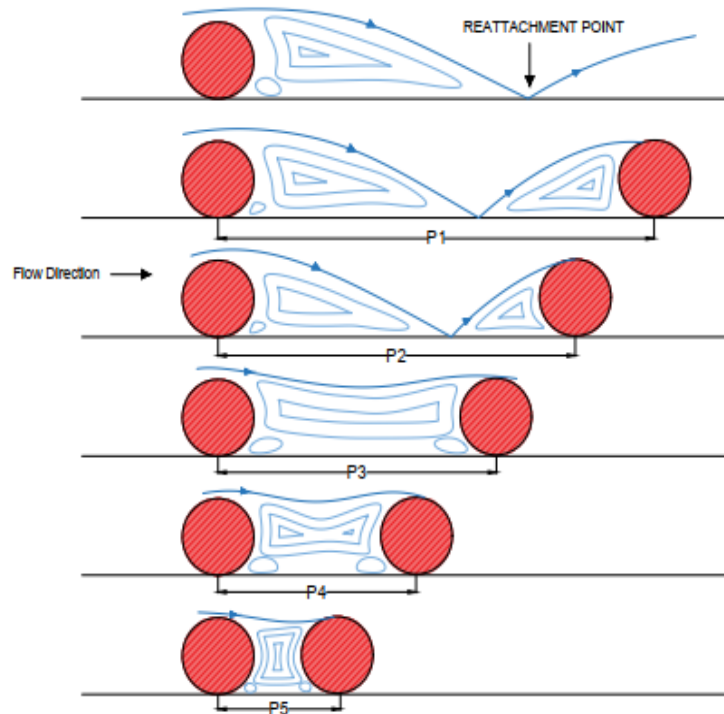
Fig. 2.2 Impact of rib pitch on the flow pattern.

19

However, for *P/e* > 10, the number of reattachment points decreases, owing to a decrease in the ribs (Prasad and Saini 1988). Hence, a lower pressure drop was obtained for higher *P/e* values. For maximum thermo-hydraulic performance, *P/e* = 10 is recommended (Hans et al. 2009; Alam and Kim 2017a; Singh and Singh 2018a) as it has the highest reattachment points along the length of the absorber plate. Optimum values of *P/e* reported by various studies are given in Table 2.2.

Table 2.2: Relative rib pitch values corresponding to maximum heat transfer for different ribs in the solar air heater.

Rib geometry	*P/e*
Transverse continuous (Prasad and Saini 1991)	10
Wedge shape (Bhagoria et al. 2002)	7.6
V-shape (Momin et al. 2002)	10
Discrete transverse (Sahu and Bhagoria 2005)	13.3
Rib-groove (Jaurker et al. 2006)	6
Metal grit (Karmare and Tikekar 2007)	17.5
Discrete inclined (Aharwal et al. 2009)	10
U-shape (Bopche and Tandale 2009)	10
Discrete W-shape (Kumar et al. 2009)	10

2.1.3 Impact of rib inclination

For a rib placed orthogonal to the main flow stream, the vortices formed behind the rib were stagnant and resulted in high-temperature regions, subsequently lowering the heat transfer rate. Placing the rib at an angle to the duct's longitudinal axis creates a secondary flow that moves from the leading end to the rib's trailing end. Due to air movement along the rib surface, it gets heated up, and it merges with the primary flow at the trailing edge of the rib (Fig. 2.3). This creates a spanwise variation in the heat transfer rate within the duct. Inclined ribs beneath the absorber plate increased the overall performance of the SAH compared to transverse ribs (Hans et al. 2009; Alam and Kim 2017a; Singh and Singh 2018). Further studies were conducted employing 'V' and 'W' shape ribs to take advantage of the secondary flow, discussed later. The

optimum values of rib inclination angle (*β*) reported by various studies are given in Table 2.3.
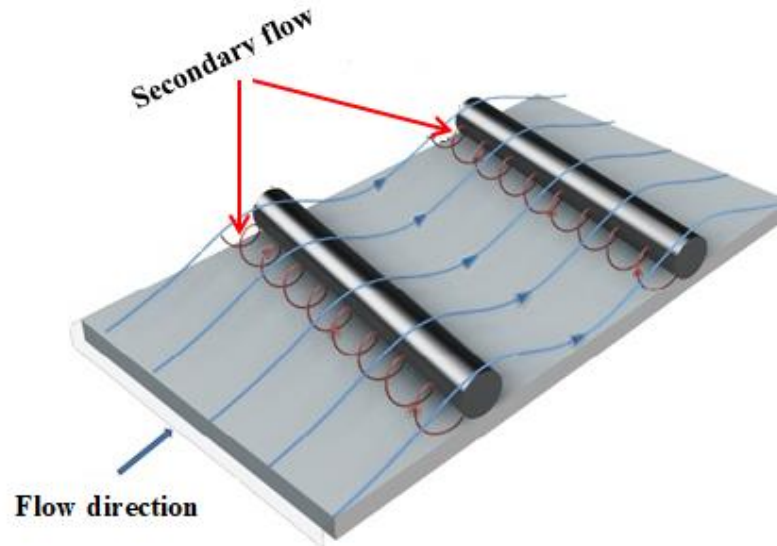
Fig. 2.3 Secondary flow generated due to an inclined rib.

Table 2.3: Rib inclination values corresponding to maximum heat transfer for different ribs in the solar air heater.

Rib geometry	Rib inclination (*β*)
Inclined (Gupta et al. 1997)	60°
Expanded metal mesh (Saini and Saini 1997)	62°
V-shape (Momin et al. 2002)	60°
Discrete transverse (Sahu and Bhagoria 2005)	90°
Arc shape (Saini and Saini 2008)	60°
Discrete W-shape (Kumar et al. 2009)	60°
Discrete Inclined (Aharwal et al. 2009)	60°
Multiple V-shape (Hans et al. 2010)	60°
W-shape (Lanjewar et al. 2011)	60°

2.1.4 Impact of the gap in a continuous rib

In specific designs, gaps have been provided in the ribs to create an additional zone of high turbulence and mixing, which will magnify the heat transfer. The passage of primary and secondary flow streams through the gaps accelerates the retarded boundary

layer formed downstream of the rib, producing a higher heat transfer rate relative to continuous ribs (Aharwal et al. 2008). The gap width and position optimized the heat transfer rate; gaps of smaller width do not allow sufficient flow, whereas those with larger width retard the flow (Aharwal et al. 2009; Singh et al. 2011). The flow pattern for an inclined rib with gaps is shown in Fig. 2.4. Concerning the gap location, the gap near the leading edge of the rib reduces the strength of the cross-flow and fails to energize the primary flow stream. A gap near the trailing edge increases the strength of the cross-flow and, subsequently, the heat transfer rate (Singh et al. 2011).
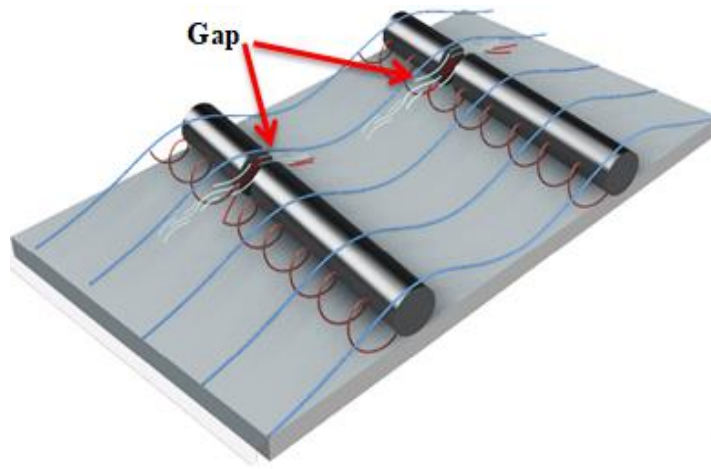
Fig. 2.4 Impact of the gap on flow pattern generated by inclined rib.

2.1.5 Impact of rib cross-section

As flow separation and flow reattachment play a vital role in the overall performance of a SAH, the cross-section of the rib is of prime importance while designing artificial roughness. Ribs with sharp corners such as square cross-sections caused the early flow separation when compared to a smooth cross-section, namely circular. With low turbulence and gradual flow separation, circular cross-sections yield lower augmentation in Nusselt number (Nu) than square or triangular cross-sections (Fig. 2.5). However, circular rib cross-sections have a lower friction factor (f) than other rib cross-sections (Singh et al. 2015; Ahn 2001).
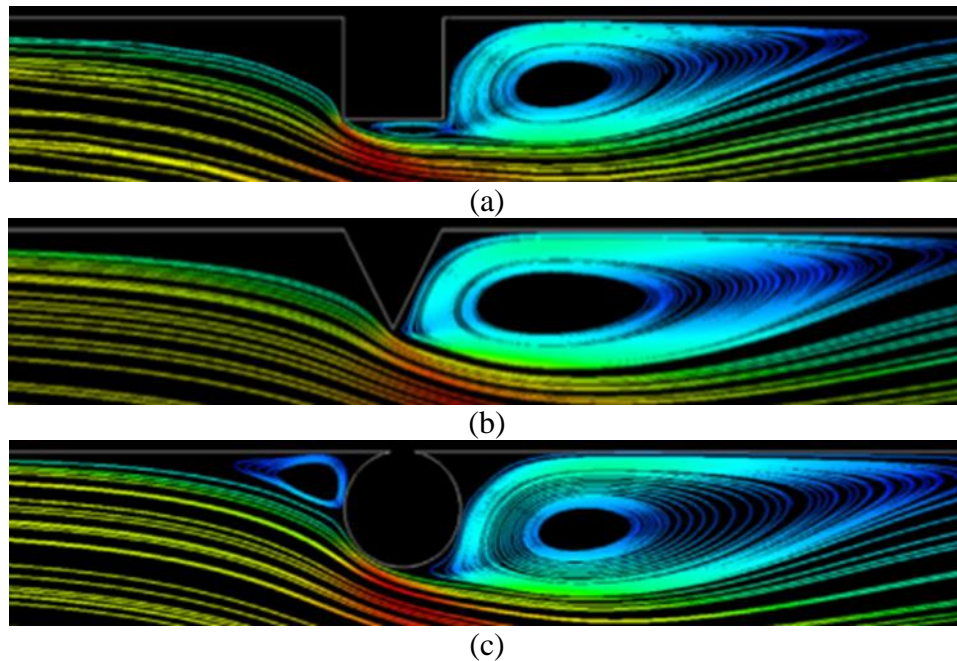
Fig. 2.5 Flow pattern with varying rib profiles (a) Square, b) Triangular, and (c) Circular cross-section (Singh and Singh 2018a).

2.2 Various configurations of artificial roughness employed in rectangular duct SAH

Artificial roughness in the form of ribs/baffles was employed to enhance the convective heat transfer coefficient in turbulent flow through SAH. Prasad and Mullick (1983) carried out experimental studies on circular wires (Fig. 2.6 (a)), having a diameter less than the thickness of the laminar sub-layer. For relative rib height (*e/D*) equal to 0.019 and relative rib pitch (*P/e*) of 12.7, circular wires delivered a 14% improvement in efficiency at *Re* = 5000. Further, Prasad and Saini (1988) varied *e/D* (0.020 - 0.033) and *P/e* (10 - 20) to study the impact on the overall performance of SAH. With an increase in *e/D*, the rate of increase of Nusselt number (*Nu*) decreased in context to increase in the rate of friction factor (*f*). Whereas, with an increase in *P/e*, both *Nu* and *f* decreased. They extended the study, including the flow and geometric properties, to obtain optimal overall performance enhancement (Prasad and Saini 1991). Upon applying ribs (Fig.2.6 (a)), *Nu* doubled with a four-fold increase in *f*. For a fixed *P/e* of 10, Gupta et al. (1993) studied the effect of *e/D* (0.018 - 0.052) and duct aspect ratio (6.8 ≤ *W/H* ≤ 11.5) on the thermo-hydraulic performance of SAH operating in the turbulent flow regime (3000 ≤ *Re* ≤ 18000). They found that the heat transfer rate

decreased with an increase in *W/H* and *e/D*. The decrease in heat transfer rate with *W/H* may be attributed to the increase in the duct's span wise length. Experimental data was then used to correlate *Nu* and *f* with *e/D*, *W/H*, and *Re*. With similarly shaped ribs having *e/D* (0.01 - 0.03) and *P/e* (10 - 40), Verma and Prasad (2000) reported an optimal overall performance of 71%.

2.2.1 Transverse ribs

With wires employed as transverse ribs, the pressure drop was too high to undermine the significant gain in the heat transfer rate. In search of a solution for this, Karwa et al. (1999) analyzed the impact of rib chamfer on the duct's pressure drop characteristics (Fig. 2.6 (b)). Heat transfer rate was doubled, corresponding to three times increment in friction factor for a chamfer angle of 15°. They further studied the impact of mass flow rate on the ribbed SAH's overall performance by varying the airflow passage height. The study reported a 10 to 40% enhancement in thermal efficiency relative to smooth SAH. For higher temperature applications, higher *e/D* was desired, whereas, for applications requiring higher mass flow rates, lower *e/D* gave higher performance enhancement. These results were in conformance with previous studies, wherein the efficiency of SAH increased with a decrease in depth until an optimal aspect ratio (Bhargava and Rizzi 1990; Hegazy 1996). In addition, Sharma and Kalamkar (2015) reported better heat transfer efficiency for high aspect ratio ducts.

Optimization of many parameters to obtain maximum overall performance in SAH urged the need for CFD simulations. Early CFD analysis on SAH includes the study of twelve different configurations of ribs with equilateral triangular (Fig. 2.6 (c)) cross-section using a 2-D model with Renormalization-group (RNG) *k*-ε turbulence model for *P/e* and *e/D* in the range of 7.14 - 35.71 and 0.021 - 0.042, respectively (Yadav and Bhagoria 2014). Similar studies were conducted on rib cross-sections, namely circular (Yadav and Bhagoria 2013a) and chamfered ribs. The maximum thermo-hydraulic performance parameter (THPP) of 2.11 was reported for *e/D* = 0.042 and *P/e* = 7.14, owing to a 3.07 times increase in *Nu* for a corresponding increase of 3.37 in the friction factor (*f*).
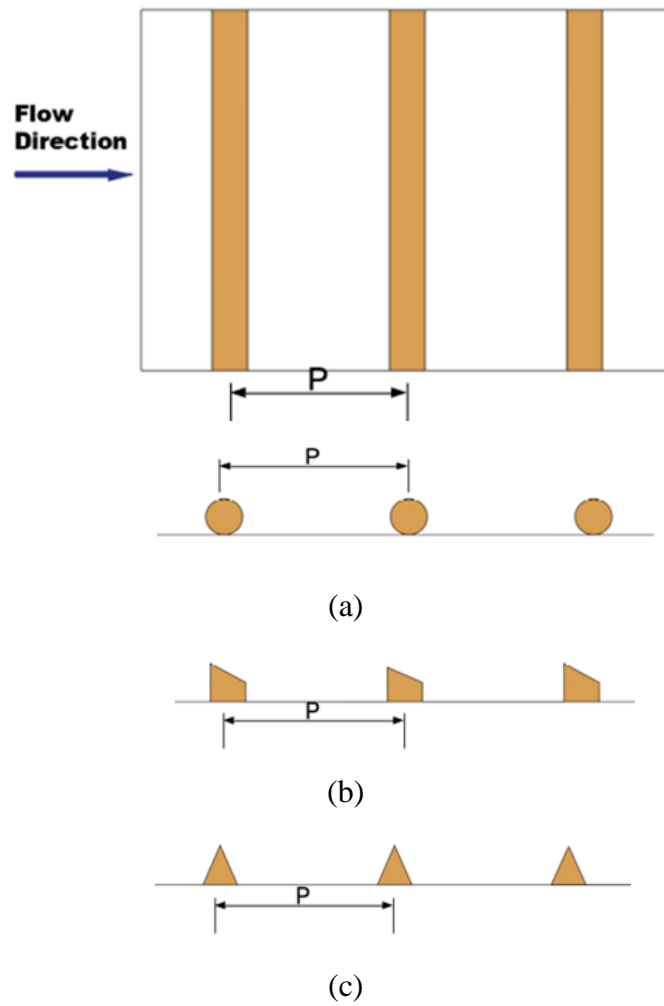
Fig. 2.6 Various cross-sections of continuous transverse ribs (a) circular, (b) chamfered rib, and (c) triangular.

Sahu and Bhagoria (2005) put forward the idea of "gaps" in the transverse ribs employed in SAH (Fig. 2.7). The gaps were provided by arranging the ribs in a staggered manner. With a maximum increment of 1.4 in Nu, 83% thermal efficiency was obtained compared to smooth SAH. Higher thermal efficiency was attributed to the additional flow separation at the side edges of the discrete rib, creating a cross-flow that hinders the thermal boundary layer's development after reattachment. Table 2.4 highlights various studies on transverse ribs with parametric range and significant results.
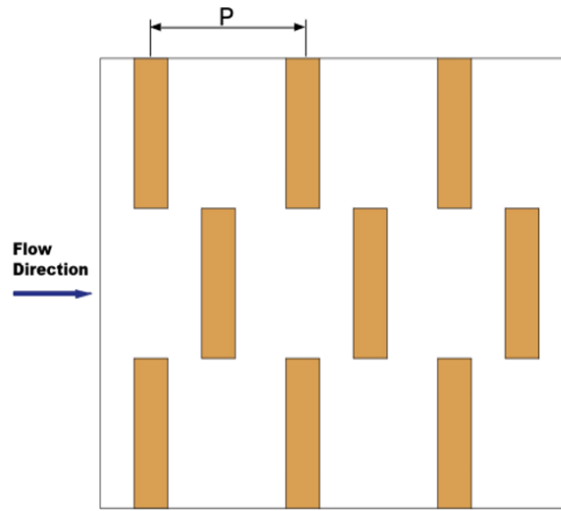
Fig. 2.7 Discrete transverse ribs.

Table 2.4: Study of transverse ribs with parametric range and significant outcomes.

Roughness shape	Parameters	Significant observations
Circular transverse	$e/D = 0.019$	$\eta_{th} = 14\%$
(Prasad and Mullick 1983)	$P/e = 12.7$	
Circular transverse	$e/D = 0.02 - 0.033$	$(Nu_r/Nu_s)_{max} = 2.38,$
(Prasad and Saini 1988)	$P/e = 10 - 20$	$(f_r/f_s)_{max} = 4.25,$
Circular transverse	$e/D = 0.01 - 0.03$	$(Nu_r/Nu_s)_{max} = 2.08,$
(Verma and Prasad 2000)	$P/e = 10 - 40$	$(f_r/f_s)_{max} = 1.80$
Triangular transverse	$P/e = 7.14 - 35.71$	$(Nu_r/Nu_s)_{max} = 3.07,$
(Yadav and Bhagoria 2014)	$e/D = 0.021 - 0.042$	$(f_r/f_s)_{max} = 3.35$

2.2.2 Inclined ribs

With transverse ribs, heat transfer enhancement was reported with a higher increment in pressure drop that affected the improvement in the overall performance of SAH. As the span-wise airflow in discrete ribs resulted in the higher overall performance of SAH, studies were conducted on ribs inclined to flow stream (Fig. 2.8) to impart higher velocity to the cross-flow. A maximum enhancement of 25% was reported in thermal efficiency with 60° inclined ribs relative to the smooth plate SAH (Gupta et al. 1997). Later, Aharwal et al. (2008) reported that additional turbulence could be generated by providing ribs with a gap capable of releasing secondary flow and primary flow through

26

it. For fixed rib height, pitch, inclination ($\beta = 60°$), the width of the gap (g/e), and position of the gap (d/W) were varied, resulting in an enhancement of 2.59 times in Nu for a maximum increment of 2.87 times in f. A higher thermo-hydraulic performance parameter (THPP) in the range of 1.4 to 1.8 was obtained relative to transverse ribs.
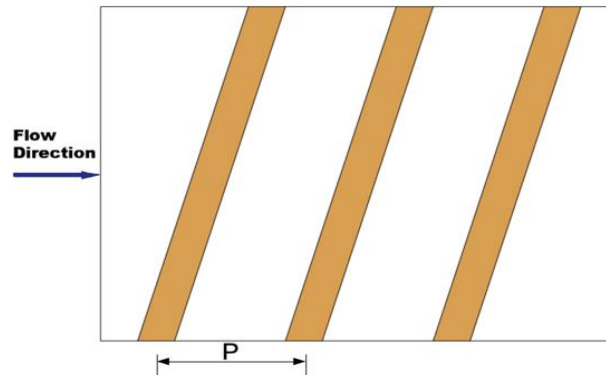
Fig. 2.8 Continuous inclined ribs.

Table 2.5: Study of inclined ribs with parametric range and significant outcomes.

Roughness shape	Parameters	Significant observations
Inclined	$e/D = 0.023 - 0.050$;	$(\eta/\eta_s) = 1.16 - 1.25$
(Gupta et al. 1997)	$W/H = 6.8 - 11.5$; $\beta = 60°$	
Inclined	$d/W = 0.16 - 0.66$,	$(Nu_r/Nu_s)_{max} = 2.59$
(Aharwal et al. 2008)	$g/e = 0.5 - 2$,	$(f_r/f_s)_{max} = 2.87$
Discrete inclined	$e/D = 0.018 - 0.037$;	$(Nu_r/Nu_s)_{max} = 2.83$
(Aharwal et al. 2009)	$P/e = 4 - 10$;	$(f_r/f_s)_{max} = 3.60$
	$d/W = 0.16 - 0.5$;	
	$g/e = 0.5 - 2$	
	$\beta = 30°- 90°$	

Further, Aharwal et al. (2009) studied the effect of P/e, e/D, and β on the overall performance of SAH by varying them in the range of 4 - 10, 0.018 - 0.037, and 30° - 90°, respectively. A higher rate of enhancement in Nu and f were obtained as 2.83 and 3.60 times, respectively. The rib's gap allows the primary and secondary flow to escape through it, energizing the flow within the reattached boundary layer. This increases the

turbulence and convective heat transfer rate in the zone behind the rib. Table 5 highlights various studies on inclined ribs with parametric range and significant results.

2.2.3 V-shape rib

As the research articles concluded that the cross-flow generated by inclined ribs had a significant contribution in enhancing the overall performance of SAH compared to transverse ribs, subsequent research focused on developing more cross-flow by modifying the shape of the rib. In this quest, studies came up with a "V" design of the rib (Fig. 2.9) capable of generating two cross-flows. Momin et al. (2002) implemented V-rib with $\beta = 60°$ and reported an enhancement in Nu by a factor of 1.14 times relative to inclined ribbed SAH. An increase in the number of secondary flow vortices contributed to the higher heat transfer rate when compared to inclined rib with a single secondary flow. By varying P/e, a similar study reported maximum augmentation in Nu and f of 2.34 and 2.45 times, respectively, for $\beta = 60°$ (Istanto et al. 2016).

To further increase the span-wise flow, Hans et al. (2010) introduced the concept of multiple cross-flows using multiple V-rib (Fig. 2.10) in a flat plate SAH. For Re in the range of 2000 to 20000, multiple V-ribs were studied for varying P/e, e/D, and β. For $W/w = 6$, Nu was enhanced six times for a corresponding increase of five times in f at $\beta = 60°$. Jin et al. (2015) performed a CFD analysis to optimize the V-rib configuration. For W/w ranging from 3 to 10, the maximum THPP of 1.93 was reported for $W/w = 5$ at $\beta = 45°$. Further, Patil (2015) reported that multiple V-rib provides an optimal gain in solar energy at $Re < 20000$. Karwa et al. (2005) employed the concept of gaps in V-rib (Fig. 2.11), intending to create turbulence at multiple locations along the spanwise direction of the SAH. They also compared the same to the discontinuous configuration of V-rib for both V-up and V-down cases. The study revealed the superiority of discrete V-down ribs over continuous V-rib in up and down configuration with optimum $\beta = 60°$. Singh et al. (2011) further investigated the performance of SAH by varying the gap width and gap location. The optimum gap width obtained was equal to the rib height. More importantly, the gap in the proximity of the rib's trailing tip improved the heat transfer rate significantly than the gap near the leading tip. It was also found that the optimum gap location was independent of P/e and β. For $g/e = 1$, $d/W = 0.65$ and $\beta = 60°$, maximum increment in Nu and f were recorded as 3.04 and 3.11 times,

respectively. Kumar et al. (2012) experimentally studied the impact of gaps in the same configuration as multiple V-ribs provided a significant enhancement in *Nu* compared to a single V-rib (Fig. 2.12). Maximum enhancement in *Nu* was obtained 6.32 times than smooth SAH for *g/e* = 1 and *d/W* = 0.69.
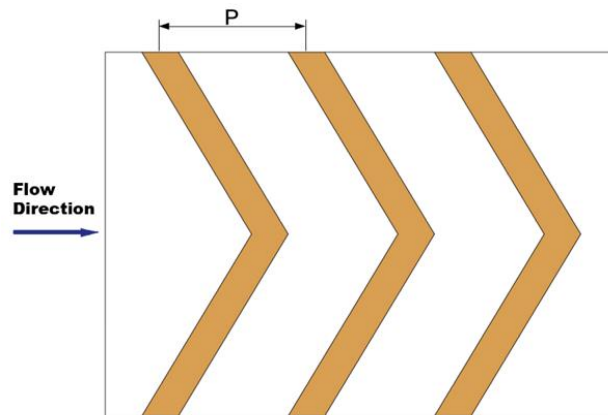
Fig. 2.9 V-shape ribs with the apex at the downstream.
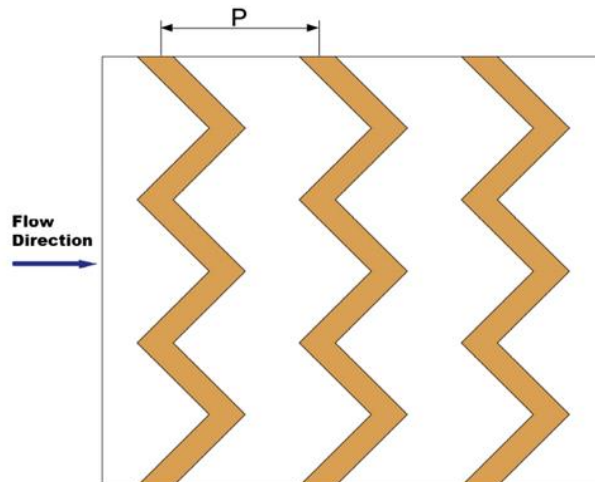
Fig. 2.10 Multiple V-shape ribs.

Staggered ribs were combined with discrete V-ribs to create additional turbulence in the inter-rib regions (Patil et al. 2011). For a fixed *β* = 60°, *P/e* =10 and *e/D* = 0.043, maximum enhancement in *Nu* was obtained as 2.85 times smooth plate SAH. Further, maximum *Nu* enhancement increased to 3.18 times upon varying the staggered rib dimensions.
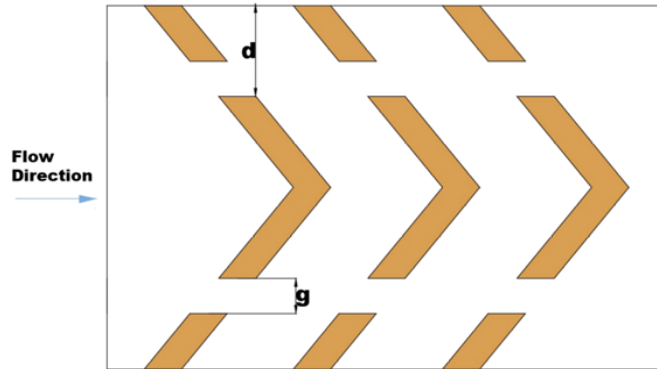
Fig. 2.11 Discrete V-shape ribs.
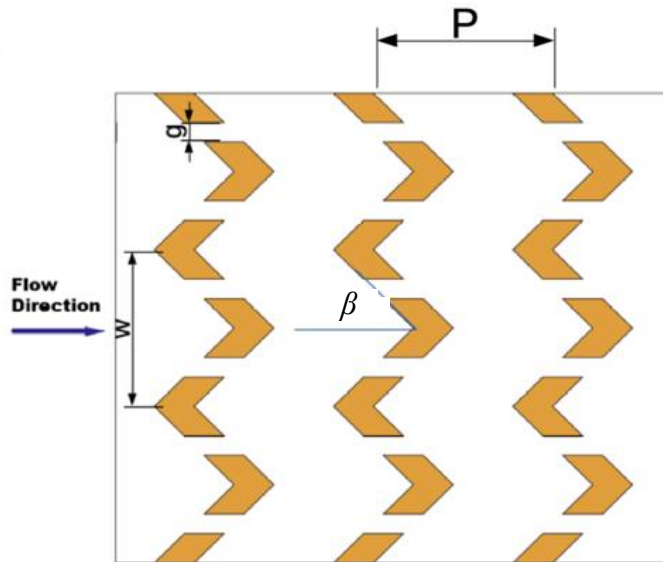
Fig. 2.12 Multiple V-shape ribs with the gap.
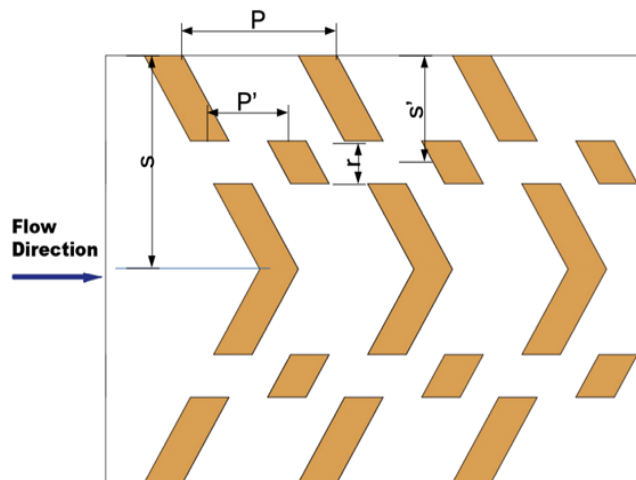
Fig. 2.13 V-shape with staggered rib pieces.

The concept of the staggered rib (Fig. 2.14) was further evaluated in conjunction with multi V-rib by keeping a fixed dimension and position of the rib. For P/e (4 - 14), e/D (0.026 - 0.057) and β (40° - 80°), peak augmentation in Nu was recorded as 2.45 times for an increase of 3.34 times in f, for $\beta = 80°$, $P/e = 12$ and $e/D = 0.044$ (Deo et al. 2016). Table 2.6 highlights studies on various V-ribs and significant results.

Table 2.6: Study of V-shape ribs with parametric range and significant outcomes.

Roughness shape	Parameters	Significant observations
Discrete V-shape (Singh et al. 2011)	$g/e = 0.5 - 2.0$, $d/w = 0.20 - 0.80$, $P/e = 4 - 12$, $\beta = 30° - 75°$, $e/D = 0.015 - 0.043$	$(Nu_r/Nu_s)_{max} = 3.04$ $(f_r/f_s)_{max} = 3.11$
V-shape (Momin et al. 2002)	$e/D = 0.02 - 0.034$, $P/e = 4 - 10$, $\beta = 30° - 90°$	$(Nu_r/Nu_s)_{max} = 2.30$ $(f_r/f_s)_{max} = 2.83$
V-shape (Istanto et al. 2016)	$W/H = 12$, $P/e = 10$, $e/D = 0.033$, $\beta = 30° - 80°$	$(Nu_r/Nu_s)_{max} = 2.34$ $(f_r/f_s)_{max} = 2.45$
Multiple V-shape (Hans et al. 2010)	$e/D = 0.019 - 0.043$, $P/e = 6 - 12$, $W/w = 1 - 10$, $\beta = 30° - 75°$	$(Nu_r/Nu_s)_{max} = 6$ $(f/f_s)_{max} = 5$
Multiple V-shape (Jin et al. 2015)	$P/e = 3 - 20$, $e/D = 0.03 - 0.11$, $\beta = 30° - 75°$	$THPP_{max} = 1.93$
Discrete multiple V-shape (Kumar et al. 2012)	$e/D = 0.043$, $P/e = 10$, $W/w = 6$, $g/e = 0.5 - 1.5$, $\beta = 60°$	$(Nu_r/Nu_s)_{max} = 6.32$ $(f_r/f_s)_{max} = 6.12$
multiple discrete V-shape and staggered rib (Deo et al. 2016)	$P/e = 4 - 14$, $e/D = 0.026 - 0.057$, $\beta = 40° - 80°$, $g/e = 1$	$(Nu_r/Nu_s)_{max} = 3.34$ $(f_r/f_s)_{max} = 3.38$

2.2.4 W-shape rib

Lanjewar et al. (2011a) investigated the effect of multiple secondary flow vortices employing W-ribs for a fixed *P/e*. For varying *e/D* (0.018 - 0.033) and *β* (30° - 75°), maximum increment in *Nu* and *f* was reported as 2.36 and 2.01 times, respectively for *β* = 60°. Further, they investigated W-up rib and compared with W-down rib for fixed *P/e* = 10, *e/D* = 0.033 and *β* = 45° (Lanjewar et al. 2011b). W-down ribs demonstrated higher overall performance in the range of 1.46 to 1.95 than W-up ribs, where performance ranged from 1.21 to 1.73. In the down rib configuration, only one of the apex of W-rib was incident to the flow stream, wherein the limbs directed the flow near the sidewalls of the duct to the center portion, enhancing the heat transfer rate. In up rib configuration, two apices were incident to flow stream, and the flow was redirected towards the sidewalls by the limbs, causing a reduction in heat transfer enhancement.

Further, W-rib with a gap (Fig. 2.14) near the apex, forming a staggered rib pattern, was experimentally analyzed by varying *e/D* and *β* for a fixed *P/e* = 10 (Kumar et al. 2009). Maximum enhancement in *Nu* was lower than that obtained for continuous W-rib with higher enhancement in *f*. This may be due to the reduction in cross-flow strength due to the gap's location. Table 2.7 highlights the various studies on W-ribs with parametric range and significant results.
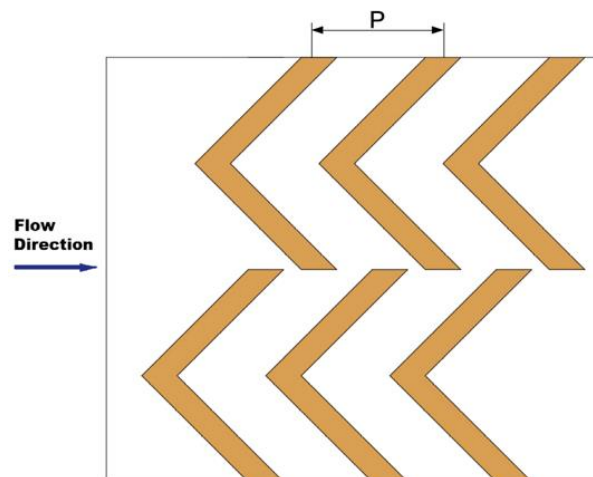
Fig. 2.14 Discrete staggered W-ribs.

Table 2.7: Study of W-shape ribs with parametric range and significant outcomes.

Roughness shape	Parameters	Significant observations
Discrete W-shape Kumar et al. (2009)	e/D = 0.016 - 0.033, P/e = 10, β = 30° - 75°	$(Nu_r/Nu_s)_{max}$ = 2.16, $(f_r/f_s)_{max}$ = 2.75
Continuous W-shape Lanjewar et al. (2011b)	e/D = 0.033, P/e = 10, W/H = 8, β =30° - 75°	$(Nu_r/Nu_s)_{max}$ = 2.36, $(f_r/f_s)_{max}$ = 2.01

2.2.5 Arc rib

Transverse wires bent in the shape of an arc were employed as ribs to facilitate cross-flow of air within the SAH (Fig. 2.15). Arc ribs (P/e = 10) were analyzed by varying e/D and β in the range of 0.021 to 0.042 and 30° to 60°, respectively (Saini and Saini 2008). This design enhanced Nu by 3.80 times at the expense of pressure drop, accounting for an increase in f by 1.75 times.
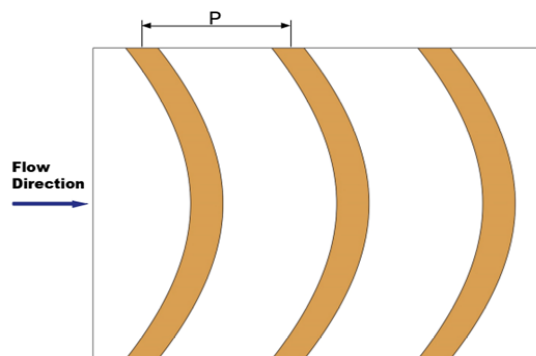
Fig. 2.15 Arc shape ribs.
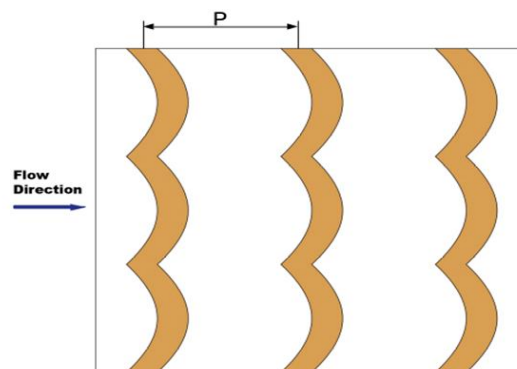
Fig. 2.16 Multiple arc shape ribs.
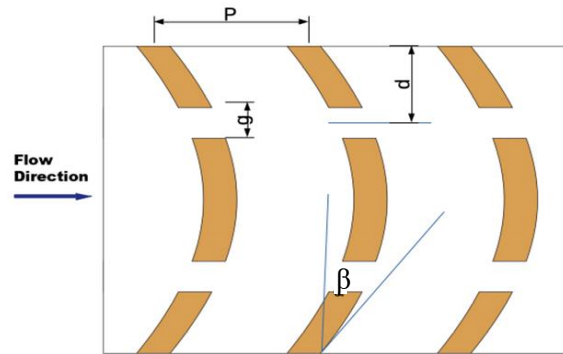
Fig. 2.17 Discrete arc shape ribs.

As the enhancement in *Nu* was not as profound as that obtained for multiple V-ribs, Singh et al. (2014) explored the secondary flow vortices and corresponding enhancement in the performance of SAH using multiple arc ribs (Fig. 2.16). For varying *e/D* (0.018 - 0.045), *P/e* (4 - 6), β (30° - 75°), and *W/w* (1 - 7), increment in *Nu* was reported to be 5.07 times with an accompanied enhancement in *f* of 3.71 times. Maximum THPP of 3.4 was reported for β = 60°, *W/w* = 5, *P/e* = 8 and *e/D* = 0.045. Lanjewar et al. (2015) reviewed various ribs employed in SAH and put forward the idea of double arc rib configuration. Double arc rib was tested experimentally in both up and down configurations reporting that down-rib performed better than all other configurations studied for the *Re* range of 3600 to 18000. In addition, the double arc up-rib demonstrated poor performance relative to a single arc rib. Further, Pandey et al. (2016) studied the impact of gaps in arc-shaped ribs (Fig. 2.18) to create additional turbulence in the inter-rib region. Keeping other parameters fixed, they varied the width and location of the gap and reported a peak augmentation of 4.96 and 5.86 times in *Nu* and *f*, respectively, for *g/e* = 1 and *d/W* = 0.65.
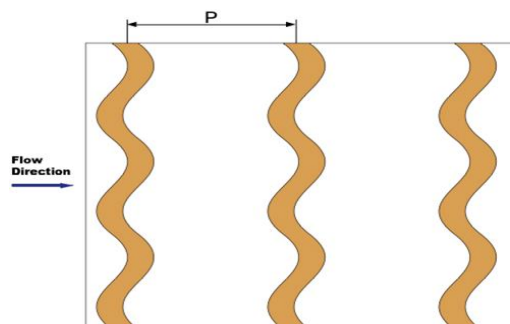
Fig. 2.18 S-shape ribs.
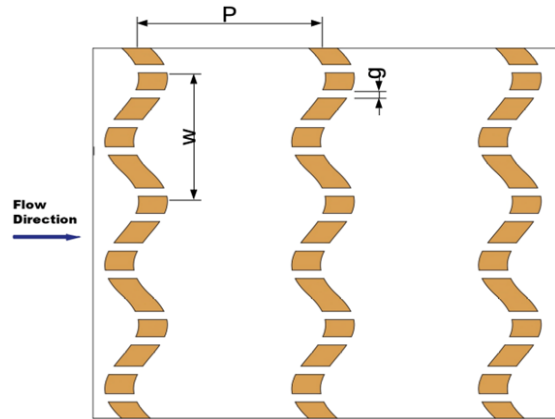
Fig. 2.19 Discrete S-shape ribs.

Discrete arc ribs were explored for $g/e = 0.5$ - 2.5, $d/W = 0.2$ - 0.8 and $\beta = 15°$ - $75°$ for performance improvement in SAH. The results showed an enhancement of 2.63 and 2.44 times in Nu and f, respectively for $g/e = 1$, $d/W = 0.65$, and $\beta = 30°$ (Hans et al. 2017).

Table 2.8: Study of arc shape ribs with parametric range and significant outcomes.

Roughness shape	Parameters	Significant observations
Arc shape (Saini and Saini 2008)	$e/D = 0.021$ - 0.042, $P/e = 10$, $\beta/90 = 0.33$ - 0.66	$(Nu_r/Nu_s)_{max} = 3.8$ $(f_r/f_s)_{max} = 1.75$
Multiple arc shape (Singh et al. 2014)	$e/D = 0.018$ - 0.045, $P/e = 4$ - 16, $W/w = 1$ - 7, $\beta = 30°$ - $75°$	$(Nu_r/Nu_s)_{max} = 5.07$, $(f_r/f_s)_{max} = 3.71$
Multiple arc shape with gap (Pandey et al. 2016)	$e/D = 0.016$ - 0.044, $P/e = 4$ - 16, $W/w = 1$ - 7, $g/e = 0.5$ - 2, $\beta = 30°$ - $75°$	$(Nu_r/Nu_s)_{max} = 5.85$, $(f_r/f_s)_{max} = 4.96$
S-shape (Kumar et al. 2017)	$e/D = 0.022$ - 0.054, $P/e = 4$ - 16, $W/w = 1$ - 4, $\beta = 30°$ - $75°$	$(Nu_r/Nu_s)_{max} = 4.64$, $(f_r/f_s)_{max} = 2.71$
Discrete S-shape (Wang et al. 2020)	$e/D = 0.023$ - 0.036, $P/e = 20$ - 30, $g/e = 1$ - 2, $W/w = 3$ - 5	$(Nu_r/Nu_s)_{max} = 5.42$, $(f_r/f_s)_{max} = 5.87$

To further enhance *Nu*, Kumar et al. (2017) experimentally investigated circular wires arranged in 'S' shape (Fig. 2.19) as ribs. For *W/w* = 3, peak augmentation of 4.64 and 2.71 times was recorded for *Nu* and *f*, respectively. Wang et al. (2020) employed the S-shaped ribs (Fig. 2.20) with gaps to reduce the flow resistance and compared the performance with smooth plate SAH. For a fixed *e/D*, the effect of duct height, solar insolation, *P/e*, and *g/e* were evaluated. They reported that the solar insolation has no significant impact on thermal efficiency, whereas a substantial effect was measured when duct height was varied. A maximum enhancement of 5.42 and 5.87 times in *Nu* and *f*, respectively, with a 48% rise in thermal efficiency, were reported. Table 8 highlights the various studies on arc-ribs with parametric range and significant results.

2.2.6 Other types of ribs employed in rectangular duct SAH

Other geometrical configurations have been explored for flat plate SAH performance enhancement, apart from circular and square cross-section ribs of continuous and discrete nature in various forms such as transverse, inclined, and arc shapes. Some of the earlier rib designs include metal mesh (Saini and Saini 1997), wedge shape (Bhagoria et al. 2002), combined rib-groove (Jaurker et al. 2006), metal grits (Karmare and Tikekar 2007), chamfered rib-groove (Layek et al. 2007), combined transverse-inclined (Saini and Singal 2008) and U-shape ribs (Bopche and Tandale 2009). Saini and Saini (1997) employed metal mesh (Fig. 2.20) and reported augmentation of 4 and 5 times in *Nu* and *f*, respectively, compared to smooth plate SAH. Bhagoria et al. (2002) proposed ribs in the form of wedge shape arranged transverse to the flow (Fig. 2.21), which gave an increment of 2.4 and 5.3 in *Nu* and *f*, respectively, for a wedge inclination of 10° and *P/e* = 7.6. Compared to chamfered ribs, the smaller eddy size created behind the ribs caused a significant heat transfer rate improvement. Grooves were used in conjunction with transverse ribs to disrupt the recirculation zone (zone of low heat transfer) behind the ribs (Fig. 2.22) and to enhance SAH performance (Jaurker et al. 2006). Peak augmentation of 2.7 times was observed in the heat transfer rate at *P/e* = 6. The higher heat transfer rate was reported owing to the higher turbulence created by fluid vortices in the vicinity of the grooves. Employing the same concept additional turbulence was created with the chamfered rib-groove combination (Fig. 2.23) for *P/e* in the range of 4.5 - 10, chamfer angle of 5° - 30°, *e/D* = 0.022 to 0.04 and relative

groove location of 0.3 to 0.6. Maximum augmentation in *Nu* and *f* were reported as 3.24 and 3.78 times, respectively, for a relative groove position of 0.4 (Layek et al. 2007a).
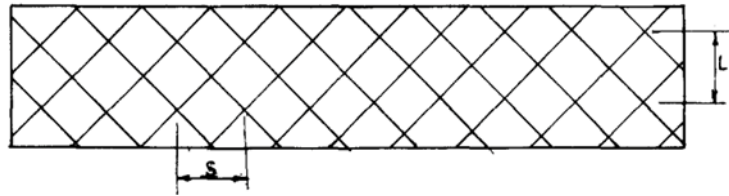
Fig. 2.20 Metal mesh type ribs (Saini and Saini 1997).
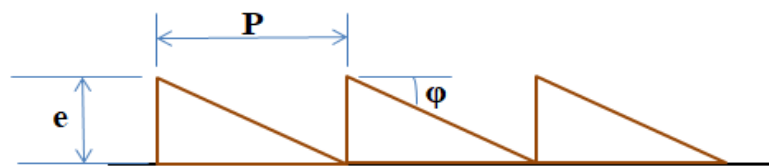
Fig. 2.21 Wedge shape ribs (Bhagoria and Solanki 2002).
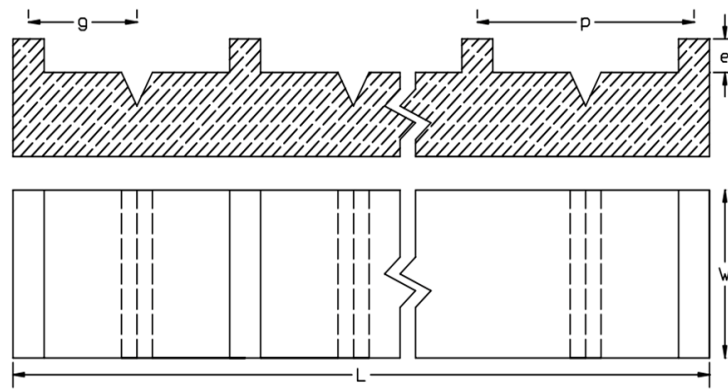
Fig. 2.22 Rib- groove combination (Jaurker et al. 2006).
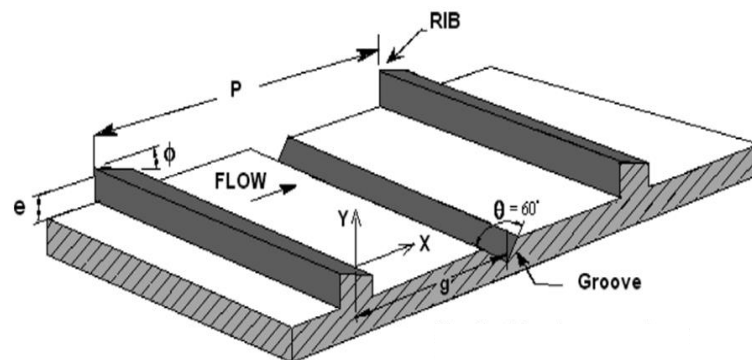
Fig. 2.23 Chamfered rib- groove combination (Layek at al. 2007).

Karmare and Tikekar (2007) investigated the performance of discretized metal grits (Fig. 2.24) for e/D (0.035 - 0.044) and P/e (12.5 - 36). The maximum enhancement in heat transfer obtained was two times higher than that obtained with continuous metal mesh for $e/D = 0.044$ and $P/e = 17.5$. For fixed $e/D = 0.030$, inclined ribs in pieces were explored in combination with continuous transverse ribs (Fig. 2.25), yielding maximum thermal efficiency in the range of 70 to 80% at $P/e = 8$ for lower Re (Varun et al. 2008). U-shaped turbulators (Fig. 2.26) enhanced Nu and f by 2.82 and 3.72 times, respectively, for a rib height of 1.5 mm and a rib pitch of 10 mm in the Re range of 3800 to 18000 (Bopche and Tandale 2009). This kind of rib allows air passage through it, reducing the recirculation zones' size compared to normal square ribs. Besides, the two horizontal edges of the ribs facilitate higher turbulence and mixing. Later, designs such as reverse L-shaped ribs (Gawande et al. 2016), semi ellipsoid shape (Alam and Kim 2016), hyperbolic ribs (Thakur et al. 2017), conical protrusions (Alam and Kim 2017b), etc. were employed as artificial roughness in SAH. Ribs of the shape of reverse 'L' (Fig. 2.27) created higher turbulence near the tip of the rib, facilitating an augmentation of 3.4 and 2.8 times in Nu and f, respectively, for $P/e = 7.14$ and $e/D = 0.042$ with a THPP in the range of 1.62 to 1.90 (Gawande et al. 2016).
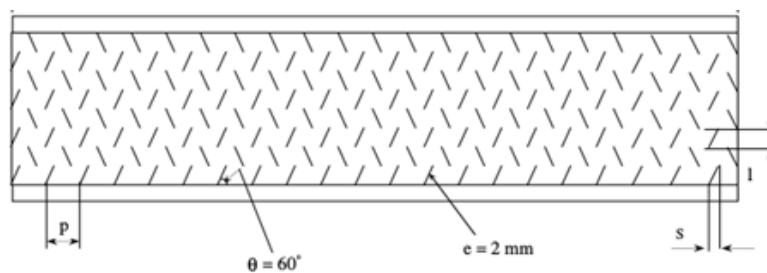
Fig. 2.24 Metal grit type ribs (Karmare and Tikekar 2007).
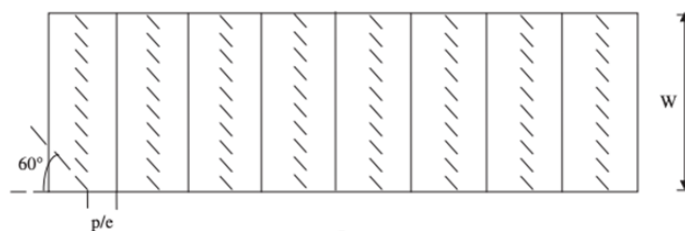
Fig. 2.25 combination of transverse and inclined ribs (Varun et al. 2008).
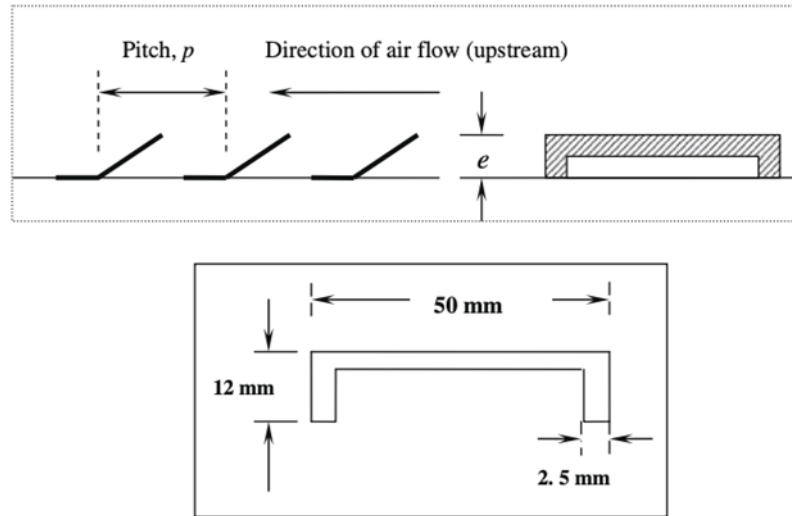
Fig. 2.26 Inverted U- shape ribs (Bopche and Tandale 2009).
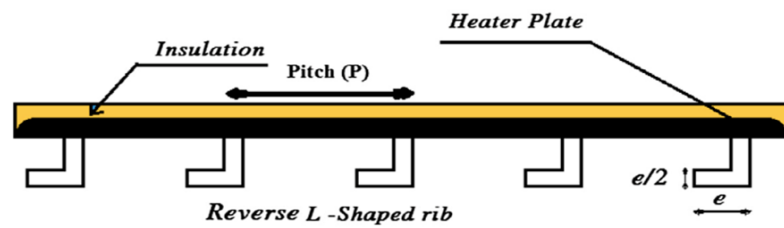
Fig. 2.27 Reverse L-shape ribs (Gawande et al. 2016).
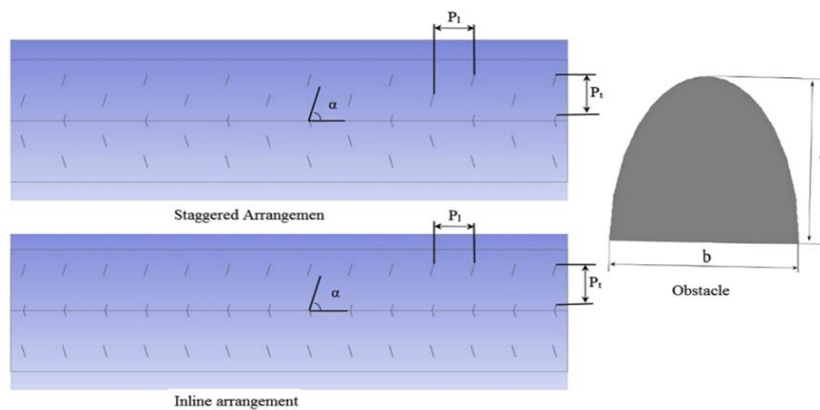
Fig. 2.28 Semi-elliptical ribs (Alam and Kim 2016).

A 3-D numerical study was conducted on SAH with semi-elliptical shape ribs (Fig. 2.28) in staggered and inline configurations beneath the absorber plate with apex downwards at different inclinations (30° - 90°). The staggered arrangement was found superior to the inline arrangement with a maximum enhancement of 2.05 and 6.93 times

for *Nu* and *f*, respectively, at β = 75° (Alam and Kim 2016). The hyperbolic ribs performance (Fig. 2.29) was analyzed using 2-D CFD analysis for *e/D* and *P/e* in the range of 0.015 - 0.06 and 5 - 40, respectively. Maximum THPP of 2.16 was obtained for *e/D* = 0.03 and *P/e* = 10 (Thakur et al. 2017). With lower pressure drop and higher heat transfer rate, hyperbolic ribs were superior to the rectangular, triangular, and semi-circular rib for the *Re* range 4000 to 6000. Protrusions in the shape of the cone were analyzed for *P/e* (6 - 12) and *e/D* (0.02 - 0.044) in the turbulent flow conditions (4000 $\leq$ Re $\leq$ 16000) (Alam and Kim 2017b). With the optimum rib configuration, maximum thermal efficiency and THPP were 69.8% and 1.34, respectively.
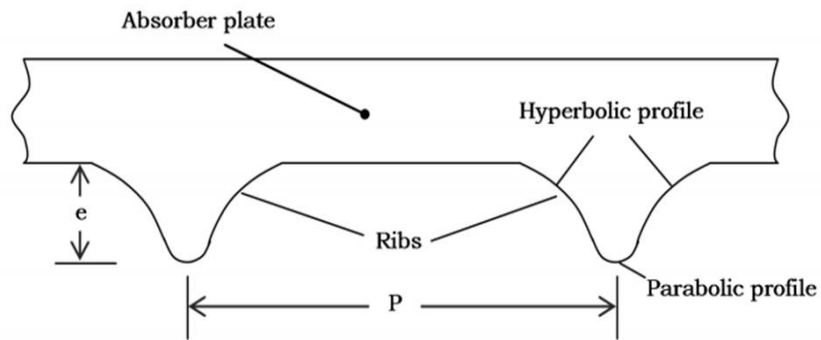
Fig. 2.29 Hyperbolic ribs (Thakur et al. 2017).

Apart from uniform rib designs, studies were also carried out on non-uniform rib structures such as sawtooth rib (Singh and Singh 2017), square wave (Singh and Singh 2018b), and multiple broken ribs (Singh et al. 2019). A rib profile, resembling a triangular wave, termed as sawtooth ribs (Fig. 2.30), was explored by placing it at an inclination to flow (45°) and by varying *P/e* (4 - 30) for a fixed *e/D* = 0.043. For *P/e* = 16, maximum enhancement in *Nu* and *f* were obtained as 2.18 and 3.34 times, respectively, at *Re* = 15000 (Singh and Singh 2017). Similar designs of non-uniform rib in the shape of a square wave profile (Fig. 2.31) were analyzed using a 3-D CFD model for *e/D* = 0.043 and *P/e* in the range of 4 to 30. Maximum increments in *Nu* and *f* were reported to be 2.14 and 3.55 times, respectively, with a higher THPP relative to uniform rib (Singh and Singh 2018b). Later, Singh et al. (2019) compared the performances of multiple broken ribs and square wave type ribs (Fig. 2.32) in a SAH using numerical and experimental analysis. For fixed *e/D* = 0.043 and *P/e* = 10, highest increments in *Nu* were recorded as 3.24 and 2.50 times, respectively. The enhancement in *f* with multiple transverse ribs was observed to be lower than the square wave type

rib. Multiple transverse ribs and square wave type ribs provided maximum THPP of 2.10 and 1.62 at *Re* of 15000, respectively, compared to smooth SAH.

Fig. 2.30 Saw tooth ribs (perpendicular to flow) (Singh and Singh 2017).
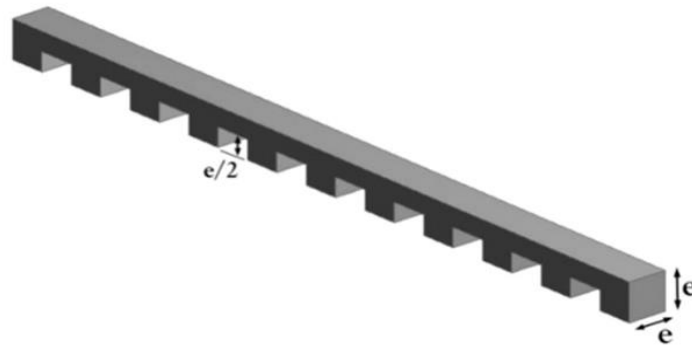
Fig. 2.31 Square wave ribs (Singh and Singh 2018b).
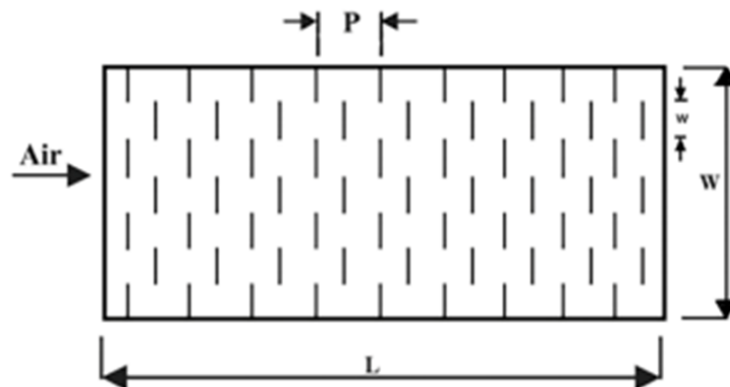
Fig. 2.32 Multiple broken ribs (Singh et al. 2019).

In recent times, miscellaneous type of rib designs such as twisted ribs (Kumar and Layek 2019b), pin fins (Manjunath et al. 2019), wavy triangular rib (Promthaisong and Eiamsa-ard 2019), helicoid fins (Purohit et al. 2019), reverse NACA profile ribs (Patel 2020), etc. were employed to enhance the SAHs overall performance. Twisted ribs (Fig.

33) placed at an angle to flow stream were experimentally analyzed for P/e (6 - 10), β (30° to 90°), twist ratio of 3 to 7 in the Re range of 3500 to 21000 (Kumar and Layek 2019b). Maximum THPP of 2.13 was obtained with 2.58 and 1.78 times enhancement in Nu and f, respectively, for P/e = 8, β = 60°, and the twist ratio of 3. A 3-D CFD analysis was carried out on pin fins for varying pitch (30 to 50 mm) and diameter (1 to 2.2 mm) placed beneath the absorber plate of a SAH for turbulent flow (4000 $\leq$ Re $\leq$ 24000). The study revealed that pin fins enhance turbulence and heat transfer rate resulting in a 14.2% increase in thermal efficiency relative to smooth SAH (Manjunath et al. 2019). Wavy triangular ribs (Fig. 34) were numerically studied by varying rib height (0.4 to 2 mm) and rib pitch (8 to 30 mm) for Re of 3000 - 20,000 (Promthaisong and Eiamsa-ard 2019). Maximum enhancement in Nu and f were 1.71 and 3.04, respectively. The highest THPP (= 2.62) was obtained at Re of 6000 for a rib height of 1.4 mm and pitch of 10 mm.

Helicoidal-shaped ribs were investigated in a SAH for varying pitch ratio (0.16 - 0.3) and fin diameter ratio (1.75 - 2) for Re in the range of (4800 - 25000). Nu was enhanced by 2.21 times relative to smooth SAH for a pitch ratio of 0.166 (Purohit et al. 2019). NACA profile ribs in reverse position were employed as artificial roughness in SAH to avoid sudden growth in turbulence along the rib and reduce the magnitude of pressure drop. The impact of P/e and e/D were numerically and experimentally explored for turbulent flow. For P/e = 5 and e/D = 0.065, THPP was obtained as 2.53 at Re = 6000 (Patel et al. 2020). The normal position of the NACA profile would facilitate smooth, streamlined flow along the rib surface and prevent the mixing in the laminar sub-layer of the thermal boundary layer. However, higher turbulence and eddy formation ensured better mixing of fluid layers with the reverse position, thereby enhancing the heat transfer rate. Nu and f were correlated with P/e, e/D, and Re to obtain expressions for the same, which could predict the values within $\pm$ 3% deviation from the experimental data. Table 2.9 highlights studies on various other types of ribs employed in rectangular duct SAH with parametric range and significant results.

Table 2.9: Study of various other ribs with parametric range and significant outcomes.

Roughness shape	Parameters	Significant observations
Wedge shape (Bhagoria et al. 2002)	e/D = 0.015 - 0.033, φ = 8°,10°,12°,15°	$(Nu_r/Nu_s)_{max}$ = 2.4 $(f_r/f_s)_{max}$ = 5.3
Rib-groove combination (Jaurker et al. 2006)	e/D = 0.018 - 0.036, P/e = 4.5 - 10	$(Nu_r/Nu_s)_{max}$ = 2.7 $(f_r/f_s)_{max}$ = 3.6
Chamfered rib - groove (Layek et al. 2007)	e/D = 0.022 - 0.04, P/e = 4.5 - 10	$(Nu_r/Nu_s)_{max}$ = 3.24 $(f_r/f_s)_{max}$ = 3.74
Metal grit (Karmare and Tikekar 2007)	e/D = 0.035 - 0.044, P/e = 12.5 - 36,	$(Nu_r/Nu_s)_{max}$ = 1.87 $(f_r/f_s)_{max}$ = 2.13
U-shape (Bopche and Tandale 2009)	e/D = 0.018 - 0.039, P/e = 6.67 - 57.14	$(Nu_r/Nu_s)_{max}$ = 2.82 $(f_r/f_s)_{max}$ = 3.72
Reverse L-shape (Gawande et al. 2016)	e/D = 0.042, P/e = 7.14 - 17.86,	$(Nu_r/Nu_s)_{max}$ = 2.82 $(f_r/f_s)_{max}$ = 2.43
Conical protrusions (Alam and Kim, 2017b)	P/e = 6 - 12, e/D = 0.020 - 0.044,	η_{max} = 69.8%, THPP = 1.346
Saw tooth (Singh and Singh 2017)	P/e = 4 - 30, e/D = 0.043	$(Nu_r/Nu_s)_{max}$ = 2.18 $(f_r/f_s)_{max}$ = 3.34
Square wave (Singh and Singh 2018b)	P/e = 4 - 30, e/D = 0.043	$(Nu_r/Nu_s)_{max}$ = 2.14, $(f_r/f_s)_{max}$ = 3.55, $(THPP)_{max}$ = 1.43
Twisted ribs (Kumar and Layek 2018)	P/e = 6 - 10, β = 30° - 90°,	$(Nu_r/Nu_s)_{max}$ = 2.46, $(f_r/f_s)_{max}$ = 1.78
Reverse NACA profile (Patel et al. 2020)	P/e = 5, 13.33, e/D = 0.043 - 0.13	$(Nu_r/Nu_s)_{max}$ = 1.97, $(f_r/f_s)_{max}$ = 2.93

2.3 Artificial roughness in triangular duct solar air heater

Even though triangular cross-section ducts were employed in the early 1990s to enhance the heat transfer rate with minimal pressure drop, the application in SAH was not explored in detail. Braga and Saboya (1996) reported that the inclusion of rib in a triangular duct enhances its overall heat transfer performance. Later, Guyer (1999) revealed that the triangular cross-sectional duct has a minimum pressure drop compared to circular, rectangular, and elliptical ducts. Luo et al. (2004) explored the effect of ribs (square cross-section) uniformly spaced on all three sides of the equilateral triangular duct on the thermal and hydraulic performance. They reported that convective heat transfer enhancement occurs at the expense of high axial pressure drop along the duct. Kumar et al. (2016) carried out a comprehensive review on the performance of triangular duct under laminar and turbulent flow conditions. The advantage of triangular duct relative to other duct cross-sections, impact of apex angle and passive heat transfer enhancement in triangular duct were discussed.

In recent times, there has been a growing interest in assessing the impact of duct cross-section on the performance of a SAH. Kumar et al. (2017) studied rectangular rib in triangular duct SAH for varying rib aspect ratio, relative rib height, and relative rib pitch in the range of 0.25 to 4, 0.02 to 0.04, and 5 to 15, respectively. A maximum thermohydraulic performance parameter (THPP) of 1.89 was obtained for the turbulent flow regime ($4000 \leq Re \leq 18000$). Further, they studied the impact of rib chamfering by varying the relative rib height and chamfer ratio in the range of 0.018 to 0.043 and 0 to 1, respectively. They reported a maximum enhancement of 2.88 in *Nu* at the expense of 3.52 times increase in *f*, respectively (Kumar et al. 2018). Singh (2018) numerically compared the performance of semi-circular and triangular ducts with V-down ribs and external recycle mode. It was reported that the external recycle mode of operation improves the thermal performance of both SAH models relative to operation without recycling. Further, they stated that the maximum pressure drop in triangular duct SAH was 73% lower than semi-circular duct SAH. Jain et al. (2019) numerically explored the effect of gap width and gap position in a discrete inclined rib at a fixed rib inclination and reported a maximum THPP of 1.98.

2.4 Exergy analysis of ribbed solar air heater

The above sections show that energy analysis determines the magnitude of improvement in the heat transfer rate and thermo-hydraulic performance of the SAH. However, various types of energy losses occurring in SAH have to be studied in detail to minimize the areas of irreversibility and losses. In this regard, exergy analysis helps to determine the losses and subsequently maximizes the exergy gain. Also, the encouraging exergy quality of solar rays has urged the relevant studies to enhance its absorption and distribution to the air flowing within the SAH. This section presents a review of available literature on exergy analysis for different rib configurations. Layek et al. (2007) studied the impact of rib height on the exergy performance of chamfered rib-groove, and demonstrated that entropy generated due to irreversibility increases with an increase in rib height. Gupta and Kaushik (2009) analyzed the impact of Re on exergetic performance of various rib cross-sections. For higher $Re \sim 20000$, V-ribs and circular ribs provided the highest exergetic efficiency (η_{ex}), whereas, for lower $Re \sim$ 4000, the combination of chamfered rib-groove resulted in higher exergy performance. With a similar analysis, pin-fin's optimum size was obtained, which would increase the absorption of solar insolation, subsequently reducing the exergy destructions (Nwosu 2010). Akpinar and Kocyigit (2010) reported that smooth plate SAH has larger irreversibility, which could be decreased with artificial roughness. They employed three different turbulators, namely triangular, leaf, and rectangular shaped, and obtained the highest exergetic efficiency for leaf-type turbulators. Singh et al. (2012) analyzed V-ribbed SAH and reported that ribs improve the exergetic efficiency by reducing irreversibility, having a maximum $\eta_{ex} \sim 1.9\%$ for lower Re. Four different corrugated absorber plates, namely normal, reverse, trapeze, and reverse trapeze corrugated plates, were analyzed based on the exergy destruction for similar input conditions. The normal corrugated plate reported the least exergy destruction compared to other corrugated plates (Benli 2013).

Exergy analysis of various types of ribs employed in SAH was conducted in the review article highlighting the importance of exergetic efficiency (Bisht et al. 2018). In the study, circular protrusions arranged in angular fashion provided the relatively highest exergetic efficiency for lower Re, and at higher Re, multi V-shaped ribs with gap

performed the best. With arc-shaped ribs, an improvement of 56% in exergetic efficiency was recorded over the smooth plate SAH for $e/D = 0.042$ (Sahu and Prasad 2016). Artificial roughness in the form of a conical surface lowers the irreversibility and improves the exergetic efficiency of the SAH compared to smooth plate SAH (Abuşka 2018). Xiao et al. (2019) reported a reduction of 65% in exergy destruction due to heat transfer to air with inclined vortex plates. This is attributed to a decrease in absorber plate temperature by 30 K, reducing the heat transfer's irreversibility. Kumar and Layek (2019a) carried out energy and exergy analysis of twisted tape turbulators fixed within rectangular duct SAH and reported the highest η_{ex} of 0.8%.

2.5 Application of ribbed SAH in indirect type solar dryer

Farmers have been using open sun drying from ancient times to preserve agricultural products (Ekechukwu 1999). However, the commonly employed open sun drying reduced only 16% of moisture content in paddy (Imoudu and Olufayo 2000). Besides, the loss of quality and ample drying time was one of the inherent drawbacks of open drying (Saini et al. 2017). Under these circumstances, indirect type solar dryers (ITSDs) emerged with the flexibility of forced and natural convection mode of operation with better control over drying temperature and better quality dried products. As the temperature of the air was reported to have a greater effect on the drying process, drying time was significantly reduced in an ITSD compared to relative humidity and velocity of air (Al-Juamily et al. 2007, Boughali et al. 2009, Putra and Ajiwiguna 2017). This may be attributed to the larger moisture-holding capacity of air at higher temperatures. Hence, researchers have focused on improving an integral part of ITSD (i.e., the flat plate solar air heater) that delivers hot air to the drying cabinet.

The concept of artificial roughness employed in flat plate SAH in isolation was taken as a lead by a few researchers to improve the drying performance of an ITSD. Karsli (2007) studied four different configurations of flat plate SAH and reported that the finned SAH had the highest energy and exergetic efficiency compared to the smooth SAH resulting in efficient drying. With the study of drying characteristics of red chili, Fudholi et al. (2014) reported that the air temperature at the dryer's inlet has a significant impact on the exergy efficiency of the drying chamber. Efficient drying of Henna with a reduction of 20% in drying time was reported in double pass SAH with trapezoidal

turbulators (Labed et al. 2016). A 2D numerical analysis of square rib roughened SAH reported a maximum temperature rise of 4°C in the drying cabinet with THPP in the range of 0.95 to 1.5 (Abhay et al. 2018). Drying characteristics of okra and chilli were studied using an ITSD having a trapezoidal duct SAH with V-corrugations (Goud et al. 2019). Recently, a reduction of 30% in drying time was reported by the application of tube-type SAH in the drying of apricot in a greenhouse dryer (Khanlari et al. 2020).

2.6 Summary of the literature review

Based on the above literature survey, a synopsis of the research carried out in the flat plate solar air heater domain has been comprehensively laid out. To narrow down further, specific areas such as the impact of ribs on flow pattern, various kinds of ribs employed in rectangular and triangular duct SAH are critically analyzed, and the following observations are made:

- Experimental studies on the performance of SAH with artificial roughness have been extensively carried out.

- In comparison to experimental studies, only meager studies are carried out using CFD. To arrive at optimal design and flow conditions for artificial roughened SAH, various parameters in different combinations have to be studied and analyzed.

- Even though extensive research has been carried out on generating secondary flow using ribs in rectangular duct SAH, the secondary flow strength in various other duct cross-sections and the thermo-hydraulic performance have not been explored in detail.

- Although the air temperature significantly impacts the drying process, studies focusing on flat plate SAH design modifications in indirect type solar dryers are meager.

2.7 Motivation

Amidst excessive use and alarming price rise of non-renewable energy sources, flat plate solar air heaters can be a reliable option for applications requiring a moderate rise in air temperature and mitigating environmental degradation. Further, in agricultural countries such as India, to preserve the harvest by maintaining the quality and in

reducing the extensive drying time, flat plate SAH, an integral part of indirect type solar dryer, has a vital role. In this regard, the energy losses from the SAH have to be reduced to enhance the heat gain without being offset by the additional pumping power. Studies should focus on improving the transverse heat transfer by creating multiple secondary flows via continuous and discrete inclined rib configurations; and duct cross-section modification. Hence, in-depth analysis is required to design ribs for SAH with an optimum configuration to mitigate the energy losses and increase the heat gain from the sun.

2.8 Objectives

The following objectives have been framed for the present thesis based on the research gaps mentioned.

1. Design a triangular duct solar air heater (SAH) with V-ribs as artificial roughness to maximize the thermo-hydraulic performance using computational fluid dynamics (CFD) simulations. Also, carry out exergy analysis to determine the various exergy losses occurring in ribbed triangular duct SAH and improve exergetic performance.

2. To compare the performance of inclined ribs in rectangular and triangular duct SAH using CFD and to incorporate ribbed triangular duct SAH in the indirect type solar dryer to study the drying characteristics experimentally.

3. Identify the design modifications required for the rectangular SAH to enhance the strength of the secondary flow and energy efficiency using CFD. To carry out energy and exergy analysis of W-baffle in solar air heater with semi-cylindrical sidewalls.

4. To design and fabricate SAH with semi-cylindrical sidewalls and discrete inclined baffles. Study the impact of gaps in discrete inclined baffles in a SAH with semi-cylindrical sidewalls experimentally and numerically.

CHAPTER 3

RESEARCH METHODOLOGY

This chapter describes the numerical and experimental methodology involved in achieving the objectives. A detailed description of the computational domain, boundary conditions, and flow physics setup has been given. Computational simulations are validated with the experimental results and theoretical correlations.

3.1 Computational domain

Solar air heater duct cross-section is modified in conjunction with artificial roughness to induce secondary flow and enhance thermo-hydraulic performance. In this regard, four different configurations of SAH are studied: a) triangular cross-section duct with V-ribs, b) triangular cross-section duct with inclined ribs, c) duct having semi-cylindrical sidewalls with W-baffles and d) duct having semi-cylindrical sidewalls with discrete multiple inclined baffles. The selection of the geometrical parameters conforms with the ASHRAE Standard (2003) and the experimental studies listed in the literature. Test section length of 800 mm is chosen so that flow becomes thermally developed before it exits the test section. Inlet and exit section lengths are more than $5\sqrt{(W \times H)}$ and $2.5\sqrt{(W \times H)}$, respectively, where W and H are the width and depth of the duct (ASHRAE Standard 2003). All the four 3-D CFD models are created using the Design Modeler of Ansys 2020 R1. Triangular duct SAH is designed with an equilateral triangular duct having a side length of 0.076 m, similar to the experimental study (Luo et al., 2004). Square cross-section ribs are placed beneath the absorber plate in the form of repeated inclined ribs (Fig. 3.1) and V-ribs (Fig. 3.2). For triangular duct, the performance of both inclined and V-ribs are studied by varying the rib inclination ($30° \leq \beta \leq 75°$) for a fixed relative roughness height (e/D) and relative roughness pitch (P/e) of 0.05 and 10, respectively (where 'e', 'P' and 'D' are the rib height, rib pitch, and hydraulic diameter).

(a)

(b)

(c)
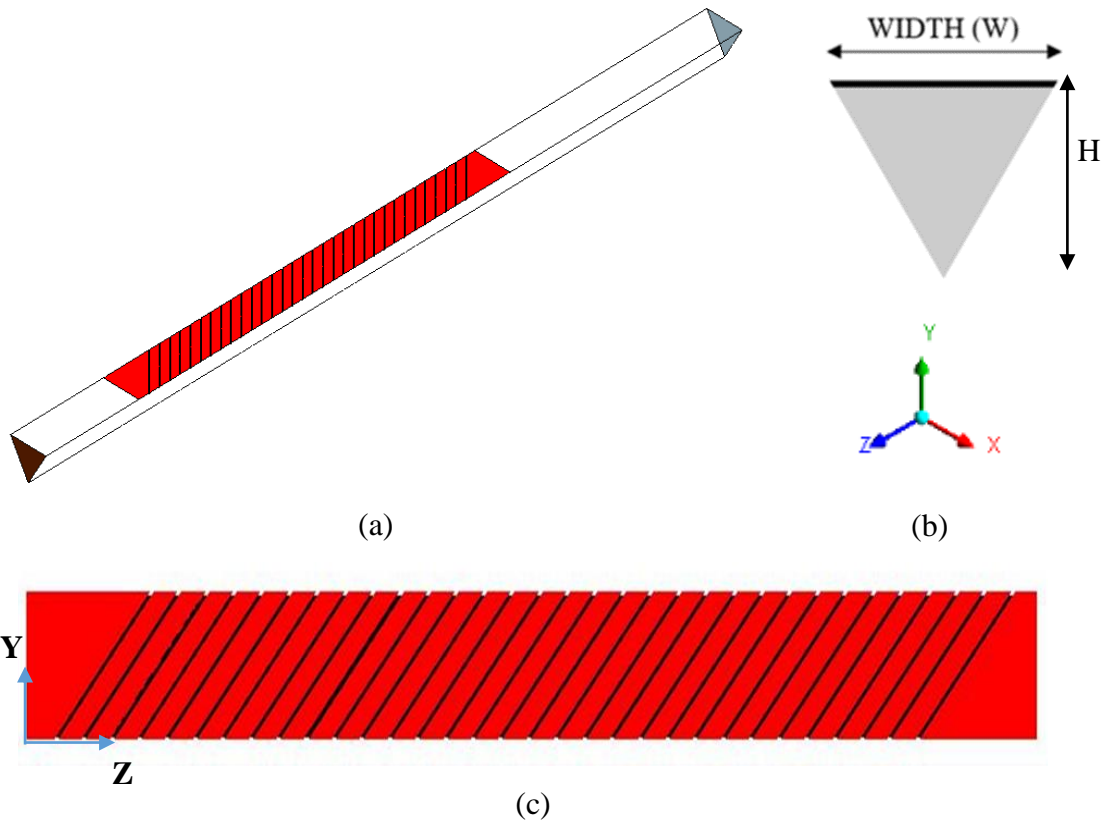
Fig. 3.1 Schematic representation of triangular duct SAH with inclined ribs (a) 3-D view, (b) duct cross-section, and (c) ribbed absorber plate (top view).

(a)

(b)   (c)
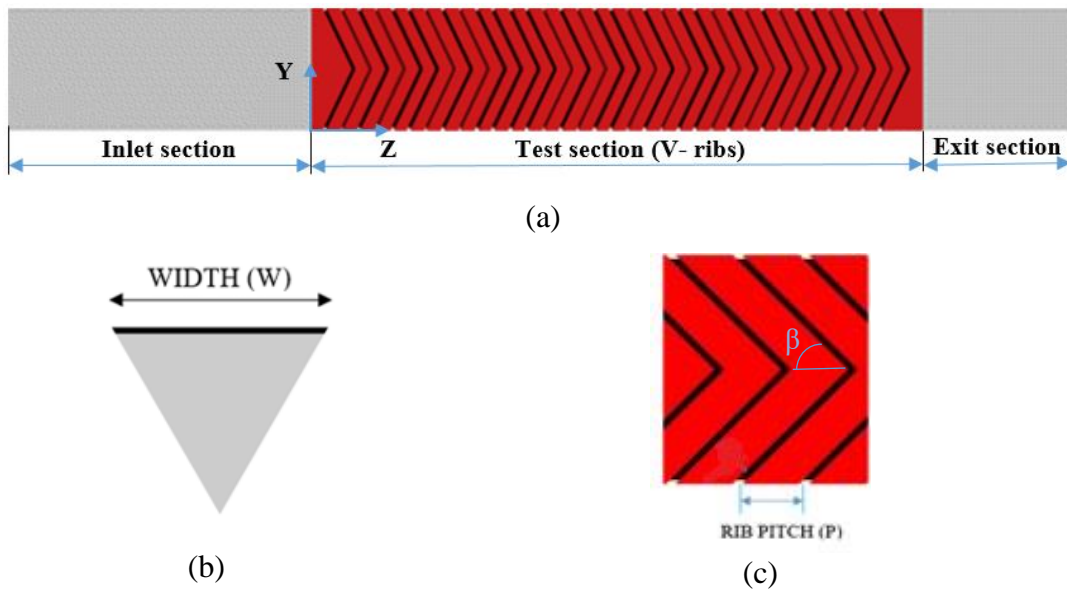
Fig. 3.2 Schematic representation of triangular duct SAH with V- ribs (a) top view, (b) duct cross-section, and (c) Magnified view of absorber plate with V-rib.

For SAH configuration with height (H), width (W), and semi-cylindrical sidewall diameter of 40 mm, 160 mm, and 40 mm, respectively, are chosen. W-baffles and discrete multiple inclined baffles are arranged underneath the absorber plate, as shown in Figs. 3.3 and 3.4, respectively. The effect of W-baffles is analyzed employing eight different geometric arrangements by varying R_H ($= e/D$) and R_P ($= P/D$) in the range of 0.046 to 0.115 and 0.46 to 1.15, respectively for a fixed baffle inclination (β) equal to 45˚. The performance of discrete multiple inclined baffles is studied by varying baffle pitch ($0.6 \leq R_P \leq 1$) for a fixed relative baffle height ($R_H = 0.1$) and inclination ($\beta = 45°$). Besides, for the optimum baffle pitch, the impact of the gap is studied w.r.t. three locations, i.e., at leading, trailing, and both leading and trailing apices.
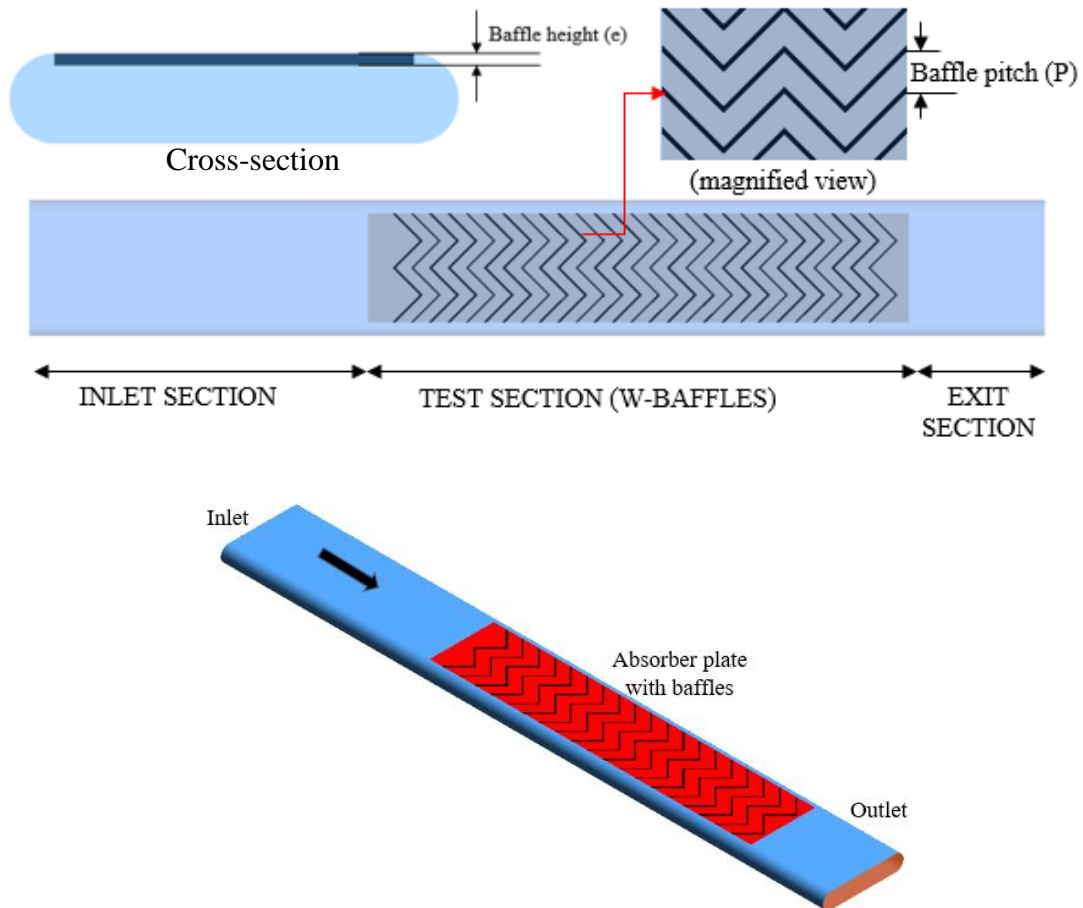
A 3-D view of the CFD model

Fig. 3.3 Schematic representation of SAH with semi-cylindrical sidewalls and W-baffles.

Cross-section view

Magnified view

(a)

Gap at the leading apex   Gap at the trailing apex   Gap at the leading and trailing apices

(b)
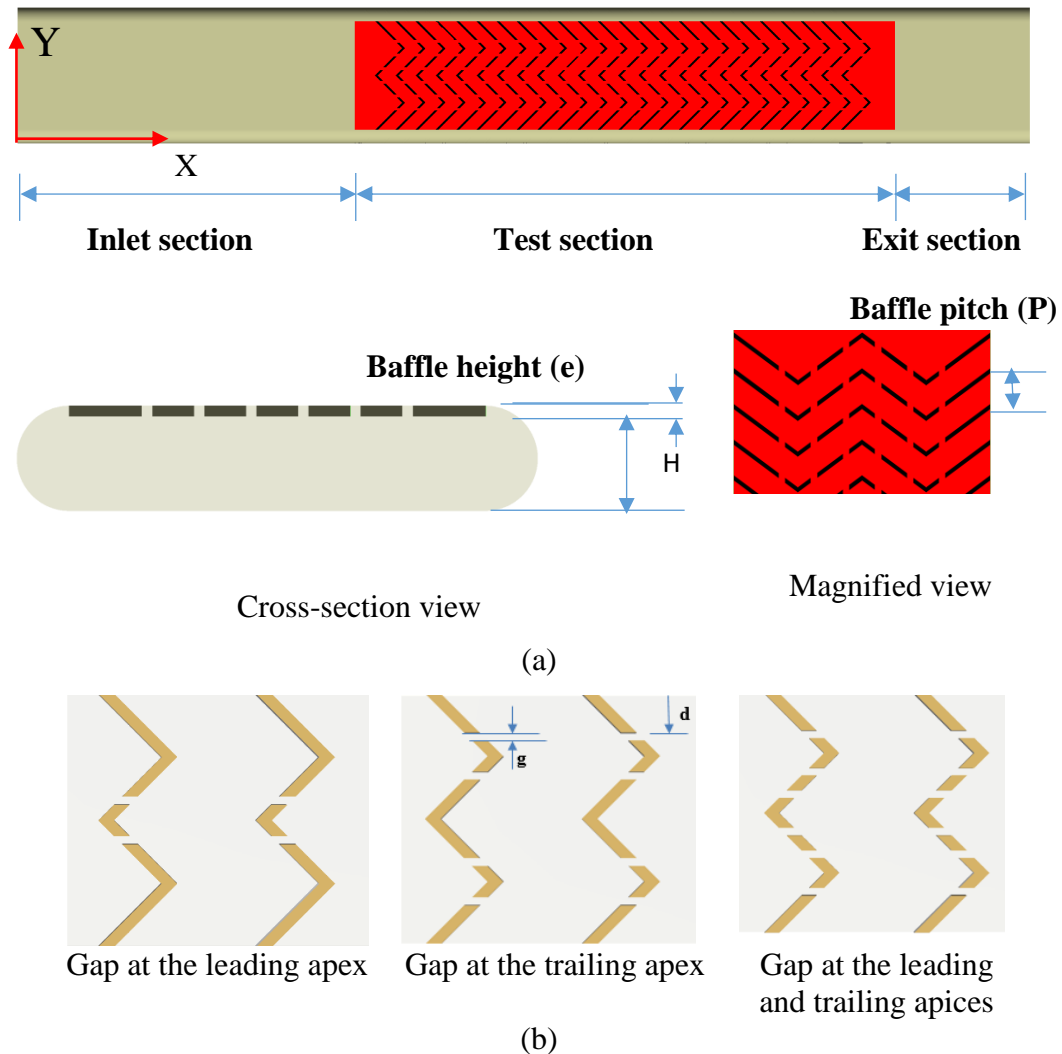
Fig. 3.4 (a) Schematic representation of SAH with semi-cylindrical sidewalls and discrete multiple inclined baffles, and (b) Three different configurations of discrete inclined multiple baffles

3.2 Meshing and grid sensitivity

The computational domain is discretized employing the structured non-uniform grids with a higher grid density ($y^+ \sim 1$) near the walls. The structured mesh is generated by dividing the domain into multi-blocks and employing edge sizing. With an appropriate biasing option, fine mesh is created near the walls to capture the flow details within the viscous laminar sublayer of the boundary layer profile. The Ansys Meshing module is employed to develop non-uniform hexahedral grids, shown in Figs. 3.5 and 3.6.

52
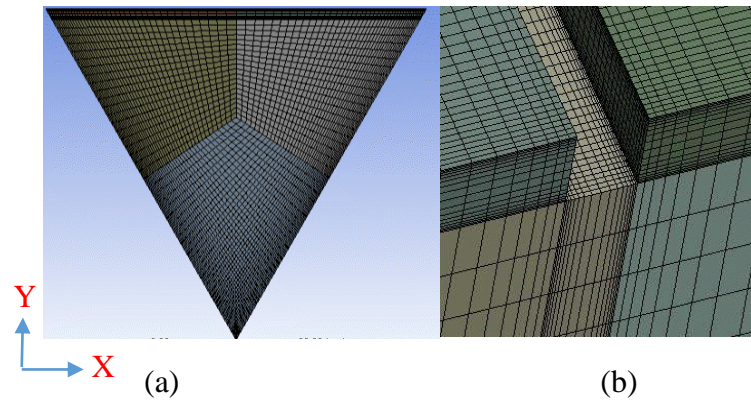
Fig. 3.5 Meshing of triangular duct (a) Structured hexahedral cells with non-uniform distribution, (b) Enlarged view of the mesh near the rib
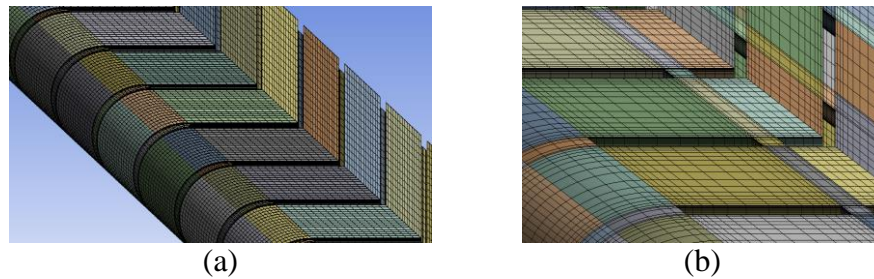
Fig. 3.6 Meshing of SAH duct with semi-cylindrical sidewalls (a) Structured mesh consisting of non-uniform hexahedral cells and (b) Enlarged view of the grid near discrete multiple inclined baffles.

Simulation results are then analyzed for varying grid elements in terms of Nusselt number (Nu) and friction factor (f) to ascertain that the results obtained are independent of the grid employed. For triangular duct SAH, with a less than 1% variation in the above variables (Fig. 3.7), the grid with 2.4 million elements is selected for further CFD simulations. In addition, the results of the grid-independent study are compared with the Grid convergence index (GCI) method proposed by Roache et al. (1986). This method is based on the application of Richardson's extrapolation. As the grid is refined, the spatial and temporal discretization errors approach zero asymptotically. With quadratic curve fitting for Nu and f, the value of R^2 (coefficient of determination) is 0.99. The error estimated for Nu and f with the GCI method (Roache et al. 1986 and Boache 1994) is 0.7% and 1.2%, respectively, with the mesh generated using 2.4 million elements.
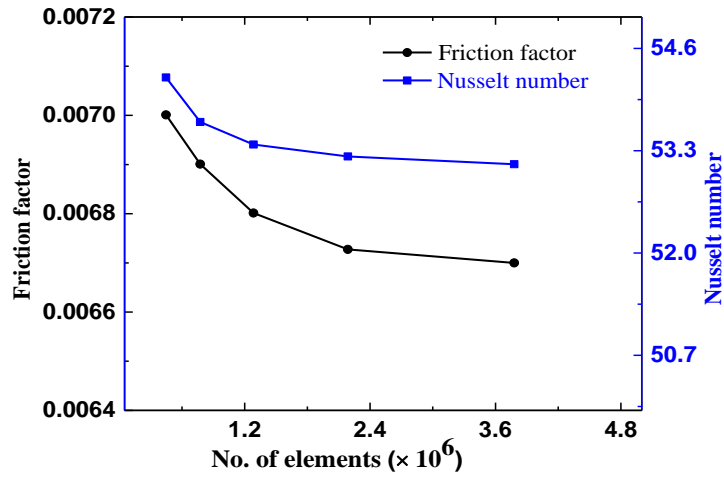
Fig. 3.7 Results of grid independence study for triangular duct SAH.

For SAH with semi-cylindrical sidewalls, the number of elements is varied from 0.8 to 2.1 million to conduct a grid independence study at $Re = 14000$. Upon varying the number of grid elements beyond 1.5 million, the variation in Nu and f is less than 1%, confirming that results are independent of the number of grid elements (Fig. 3.8).
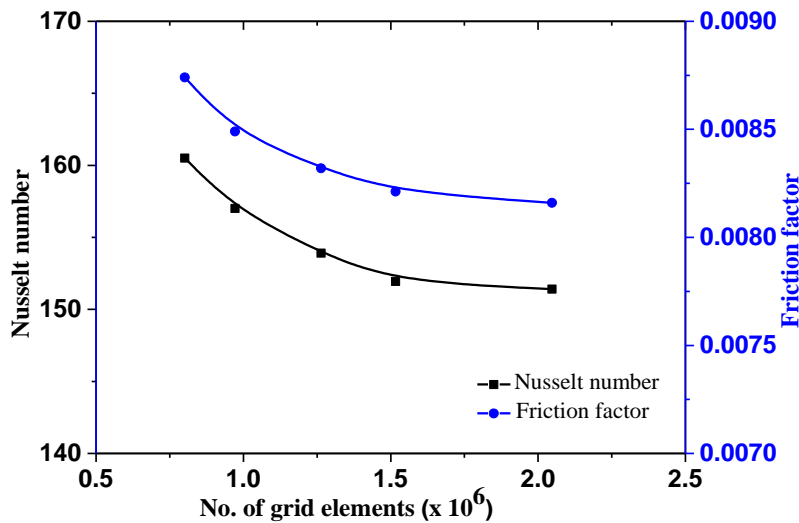
Fig. 3.8 Results of grid independence study for SAH with semi-cylindrical sidewalls.

3.3 CFD analysis

Three-dimensional simulations are performed to solve the steady-state continuity, momentum, and energy equations governing the flow, employing the finite volume implicit scheme to analyze the turbulent heat transfer features and secondary flow vortices.

Conservation of mass is given by:

$$\nabla \cdot (\rho \vec{V}) = 0 \qquad (3.1)$$

Conservation of momentum (Navier-Stokes equation) is expressed as:

$$\nabla \cdot (\rho \vec{V} \vec{V}) = -\nabla p + \nabla \cdot \left(\overline{\overline{\tau}} \right) + \rho \vec{g} \qquad (3.2)$$

Where τ is stress tensor and is given by:

$$\overline{\overline{\tau}} = \mu \left[\left(\nabla \vec{V} + \nabla \vec{V}^{\mathrm{T}} \right) - \frac{2}{3} \nabla \cdot \vec{V} I \right]$$

Where μ is molecular viscosity, and I is a unit tensor.

Conservation of energy with viscous dissipation is expressed as:

$$\nabla \cdot (\vec{V}(\rho E + p)) = \nabla \cdot \left(\lambda_{eff} \nabla T + \overline{\overline{\tau}} \cdot \vec{V} \right) \qquad (3.3)$$

Where,

$$E = \int_{T_{ref}}^{T} c_p dT + \frac{V^2}{2}$$

The governing equations are discretized using the SIMPLE algorithm and second-order upwind scheme. For better precision of the results, the suitability of various turbulence models are evaluated. Variation of Nusselt number and friction factor with Reynolds number reported by different turbulence models are shown in Figs. 3.9 (a) and (b), respectively. The comparison shows that the RNG k-ε turbulence model with enhanced wall treatment delivers the most precise results with an average deviation of 2.5% and 8.4%, respectively, for Nu and f. The same model has also been used and stated as most appropriate in earlier CFD studies available in the literature (Kumar et al. 2019; Jain et al. 2019).

The transport equations for the RNG k-ε model are written as:

$$\frac{\partial}{\partial x_i} (\rho k u_i) = \frac{\partial}{\partial x_j} \left(\alpha_k \mu_{eff} \frac{\partial k}{\partial x_j} \right) + G_k - \rho \varepsilon \qquad (3.4)$$

$$\frac{\partial}{\partial x_i}(\rho \varepsilon u_i) = \frac{\partial}{\partial x_j}\left(\alpha_\varepsilon \mu_{eff} \frac{\partial \varepsilon}{\partial x_j}\right) + C_{1\varepsilon}\frac{\varepsilon}{k}(G_k) - C_{2\varepsilon}\rho\frac{\varepsilon^2}{k} - R_\varepsilon \qquad (3.5)$$

Where G_k is the generation of turbulence kinetic energy due to the mean velocity gradient.
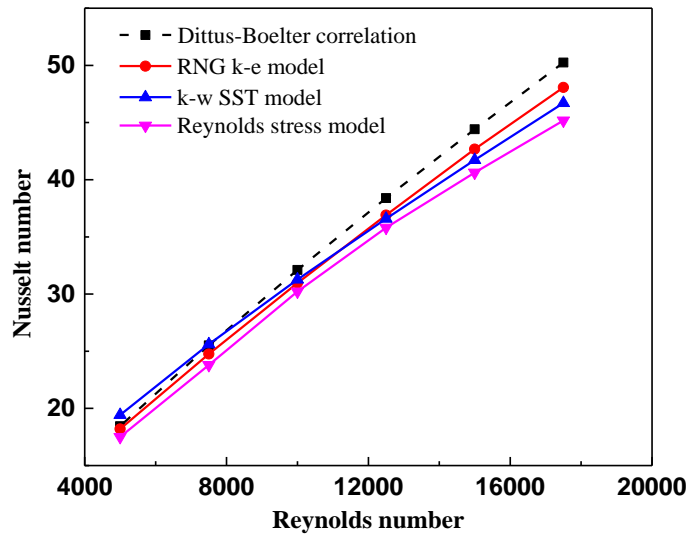
(a)
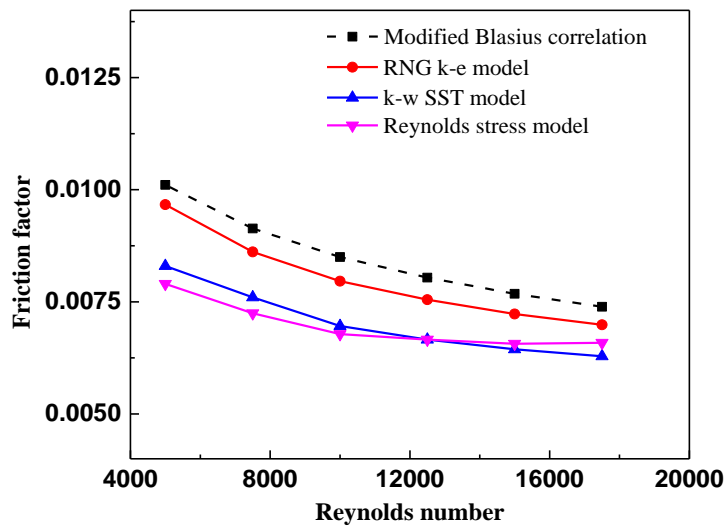
(b)

Fig.3.9 Turbulence model selection based on (a) Nusselt number and (b) friction factor.

To ascertain that the results obey continuity and energy conservation, residuals are set to 10^{-6} and 10^{-10}, respectively. In addition, mean plate temperature and pressure drop

across the length of the plate are monitored to confirm the steady-state attainment, and iterations are executed until any significant variations are noted in their values.

For the turbulent flow regime, the air temperature rise is small, and the variation in properties is less than 3.6%. Besides, this assumption is supported by the experimental study (Wang and Sundén 2007). Hence, the properties of air considered at the bulk mean temperature (Table 3.1) is assumed to be constant along the duct length (Bhushan and Singh 2010; Yadav and Bhagoria 2013b). In addition, the following assumptions are considered:

i.   The flow is in the turbulent regime under steady-state conditions.
ii.   The walls obey "no-slip" and "no-temperature jump" conditions.
iii.   The entry, test, and exit parts are separated thermally from each other.
iv.   The duct walls are insulated from their ambient conditions.

The air velocity at the inlet and the heat flux upon the absorber plate serve as the computational domain's input. The average air velocity at the inlet is computed using the Reynolds number based on the hydraulic diameter of the duct. Boundary conditions employed are given in Table 3.2.

Table 3.1: Thermo-physical properties of air.

Properties	Value	
Thermal conductivity (λ)	0.02588	*W/m.K*
Density (ρ)	1.164	*kg/m³*
Specific heat capacity (C_p)	1007	*J/kg.K*
Dynamic viscosity (μ)	1.87×10^{-5}	*kg/m.s*

Table 3.2: Assigned conditions at the boundaries of the domain

Name of the boundary	Boundary conditions/ values
Duct inlet	Air velocity
Absorber plate	Heat flux (1000 *W/m²*)
Duct outlet	Pressure (101.325 *kPa*)
Duct walls	Adiabatic wall

3.4 Energy analysis

The thermal and hydraulic performance of SAH with artificial roughness is quantified using dimensionless numbers, e.g., Nusselt number (Nu), friction factor (f), and thermo-hydraulic performance parameter (THPP).

At the inlet, Reynolds number (Re), based on the hydraulic diameter (D) of the duct, is specified as,

$$Re = \frac{\rho V D}{\mu} \tag{3.6}$$

Where 'V' is the average velocity.

The average convective heat transfer coefficient between the heated absorber plate and the flowing air is computed using Eq. (3.7). The average plate temperature (T_p) is the area-weighted average temperature of the absorber plate. The bulk mean fluid temperature is obtained as the volume-weighted temperature within the test section.

$$h = \frac{q}{(T_p - T_b)} \tag{3.7}$$

The convective heat transfer rate is obtained using the average Nusselt number (Nu) and is computed as follows,

$$Nu = \frac{hD}{\lambda} \tag{3.8}$$

With the pressure drop *(ΔP)* obtained from the study, friction factor (f) is computed as follows,

$$f = \frac{\Delta P D}{2\rho L V^2} \tag{3.9}$$

With artificial roughness, the convective heat transfer rate gets enhanced with an accompanying pressure drop. In this regard, it is desirable to design a configuration that yields the maximum augmentation in heat transfer at a minimum pressure drop. Hence, the thermo-hydraulic performance parameter (THPP) of SAH is defined by Eq. (3.9) (Webb and Eckert 1972), and the inclusion of ribs is justified only when the value is more than one.

$$THPP = \frac{(Nu_r/Nu)}{(f_r/f)^{1/3}} \tag{3.10}$$

Where, Nu_r and f_r denote Nusselt number and friction factor of artificially roughened SAH duct, respectively. Nu and f represents Nusselt number and friction factor of smooth SAH duct, respectively.

The coefficient of performance (COP) of the SAH is calculated as the ratio of heat gained by air to the pumping power (p), given by:

$$COP = \frac{\dot{m} C_p (T_o - T_i)}{p} \qquad (3.11)$$

The inlet (T_i) and outlet (T_o) air temperatures are obtained as the area-weighted average temperature at the inlet and outlet cross-section of the duct, respectively.

3.5 Exergy analysis

Even though energy analysis performed using the first law of thermodynamics is widely employed in engineering devices, it has an inherent weakness of disregarding the degradation of the energy quality during an energy conversion or exchange process. In such a scenario, exergy analysis identifies the areas of irreversibility in a process and improves exergetic efficiency. In addition, for applications such as SAHs, exergy analysis aids in comparison and in arriving at significant conclusions on the advantages and disadvantages of specific design modifications. In this study, exergy analysis of flat plate SAH is numerically carried out using a top-down iterative procedure (Tanda 2011; Singh et al. 2012) using MATLAB and is described below.

Step 1: For a given range of parameters and inlet air temperature equal to ambient temperature, an initial value of the air temperature difference (ΔT) is assumed to obtain the air outlet temperature as follows.

$$T_o = T_i + \Delta T \qquad (3.12)$$

The average temperature of the absorber plate is initialized as

$$T_p = \frac{T_o + T_i}{2} + 10 \qquad (3.13)$$

Step 2: To account for the heat losses, the net heat loss coefficient (U_L) is taken as the arithmetic sum of heat loss coefficient for the top (U_t), bottom (U_b) and sides (U_s) of the SAH. The top loss coefficient (U_t) is a function of several parameters such as absorber plate temperature, glazing temperature, etc. (Akhtar and Mullick 1999).

59

$$U_t^{-1} = \left[\frac{\sigma\left(T_p^2+T_g^2\right)\left(T_p+T_g\right)}{\frac{1}{\varepsilon_p}+\frac{1}{\varepsilon_g}-1} + \frac{\lambda_a Nu_g}{L_g}\right]^{-1} + \left[\sigma\varepsilon_g\left(T_p^2+T_g^2\right)\left(T_p+T_g\right)+h_w\right]^{-1} + \frac{t_g}{k_g} \quad (3.14)$$

Where

$$T_g = \frac{F_1 T_p + cT_a}{1+F_1}$$

$$F_1 = \frac{\left[12\times10^{-8}\left(T_a+0.2T_p\right)^3+h_w\right]^{-1}+0.3t_g}{\left[6\times10^{-8}\left(\varepsilon_p+0.028\right)\left(T_p+0.5T_a\right)^3+0.6L_g^{-0.2}\left(\left(T_p-T_a\right)\cos\gamma\right)^{0.25}\right]^{-1}}$$

$$c = \frac{\frac{T_S}{T_a}+\frac{h_w}{3.5}}{1+\frac{h_w}{3.5}}$$

$$T_s = 0.0522(T_a)^{1.5}$$

$$Nu_g = 1 + 1.44\left[1-\frac{1708}{Ra\cos\gamma}\right]^+ \left(1-\frac{1708(\sin 1.8\gamma)^{1.6}}{Ra\cos\gamma}\right) + \left[\left(\frac{Ra\cos\gamma}{5830}\right)^{0.33}-1\right]^+$$

Where [ ]*is defined by:

$X^* = \left(\frac{|X|+X}{2}\right)$; wherein 'X' is any quantity.

U_b and U_s vary with the design of the SAH and are calculated using equations (3.15) and (3.16).

$$U_b = \frac{\lambda_i}{t_i} \quad (3.15)$$

$$U_s = \frac{(L_p+W)t_e\lambda_i}{WL_p t_i} \quad (3.16)$$

Step 3: Using the energy balance, useful energy output (Q_{u1}) from the SAH under steady state is obtained as follows.

$$Q_{u1} = A_p\left[I(\tau\alpha) - U_L(T_p - T_a)\right] \quad (3.17)$$

Step 4: Airflow rate ($\dot{m}$) and *Re* through the SAH are calculated using equations (3.18) and (3.19), respectively.

$$\dot{m} = \frac{Q_{u1}}{c_p\Delta T} \quad (3.18)$$

$$Re = \frac{\dot{m}D}{\mu WH} \quad (3.19)$$

Step 5: Convective heat transfer coefficient (h) is obtained as follows

$$h = \frac{Nu\lambda}{D} \tag{3.20}$$

As the plate temperature is non-uniform along the collector length, useful gain is estimated by introducing heat removal factor (F_R) and the plate efficiency factor (F'). The heat removal factor is a function of the flow rate of the heat transfer fluid and is expressed as the ratio of heat delivered to that if the collector plate temperature equals that of the temperature of the air entering into the SAH. The plate efficiency factor represents the ratio of the actual useful energy gain that the absorbing plate had been at the local air temperature.

Step 6: Plate efficiency factor and heat removal factor are calculated using the following equations:

$$F' = \frac{h}{h+U_L} \tag{3.21}$$

$$F_R = \frac{\dot{m}C_p}{A_p U_L}\left\{1 - exp\left(-\frac{F'U_L A_p}{\dot{m}C_p}\right)\right\} \tag{3.22}$$

Step 7: The actual useful energy gain (Q_{u2}) found by using collector heat removal factor (F_R) is obtained as:

$$Q_{u2} = F_R A_p[I(\tau\alpha) - U_L(T_o - T_i)] \tag{3.23}$$

Step 8: From the above equation, a new value of T_p is obtained, and iterations are performed until $Q_{u1} \approx Q_{u2}$ and various parameters such as thermal efficiency (η_{th}), collector efficiency (η_{cc}), exergy losses and exergetic efficiency (η_{ex}) are obtained as follows.

Step 9: Thermal efficiency (η_{th}) of SAH is defined as the ratio of the useful heat absorbed to the total energy input.

$$\eta_{th} = \frac{Q_u}{IA_p} \tag{3.24}$$

Step 10: In a forced convection SAH, heat gain to the working fluid occurs at the expense of pumping power. Hence, collector efficiency is defined as the net heat gain ($Q_u - p/c$) to the total heat input.

$$\eta_{cc} = \frac{Q_u - \frac{p}{C}}{IA_p} \tag{3.25}$$

Where p is the pumping power, and C is an energy conversion factor for converting high-grade energy to low-grade energy, with a value of 0.2 (Tanda 2011).

Exergetic efficiency is defined as the ratio of net exergy flow to the exergy inflow due to solar irradiation falling on the absorber plate. The net exergy flow (E_n) is defined as the increase of the exergy flow of the air while passing through the SAH.

$$E_n = IA_p \eta_{th} \eta_c - p(1 - \eta_c) \tag{3.26}$$

Where $\eta_c = 1 - \frac{T_a}{T_s}$

The exergy inflow associated with solar irradiation on the absorber plate is given by

$$E_s = IA_p(1 - \frac{T_a}{T_{sun}}) \tag{3.27}$$

Step 11: The exergetic efficiency is computed as follows:

$$\eta_{ex} = \frac{E_n}{E_s} \tag{3.28}$$

A flow chart that summarizes the steps mentioned above is presented in Fig. 3.10.

For a fixed E_s, exergetic efficiency can be maximized by enhancing E_n. Net exergy flow is maximized when the exergy losses are minimized. Exergy loss during absorption of solar radiation by the absorber plate (L_{abs}), convective and radiation heat transfer to the environment (L_{env}), heat transfer from the surface of the absorber plate to the air (L_{ht}), flow friction (L_f) and Optical exergy loss (L_{opt}), are the various components of exergy losses in a SAH, and are calculated as follows.

$$L_{opt} = IA_p(1 - \tau\alpha) \tag{3.29}$$

$$L_{abs} = IA_p \tau\alpha(\eta_{ex} - (1 - \frac{T_a}{T_p})) \tag{3.30}$$

$$L_{env} = U_L A_p(T_p - T_a)(1 - \frac{T_a}{T_p}) \tag{3.31}$$

$$L_{ht} = IA_p \eta_{th}(\frac{T_a}{T_b} - \frac{T_a}{T_p}) \tag{3.32}$$

$$L_f = \dot{m}\Delta p \frac{T_a}{\rho T_m} \tag{3.33}$$
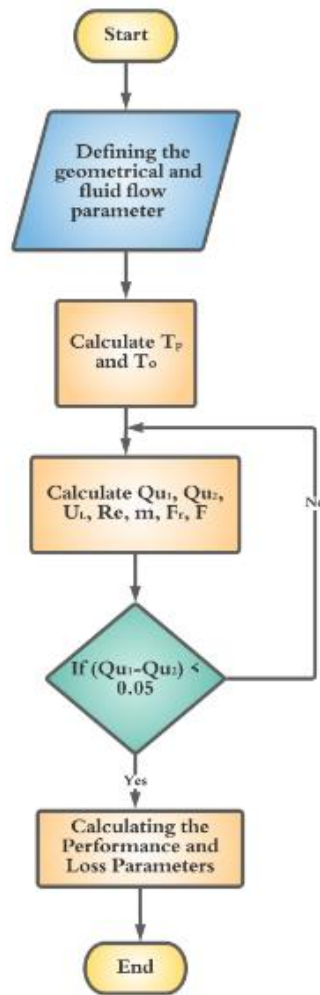
Fig. 3.10 Flow chart depicting the iterative procedure for exergy analysis.
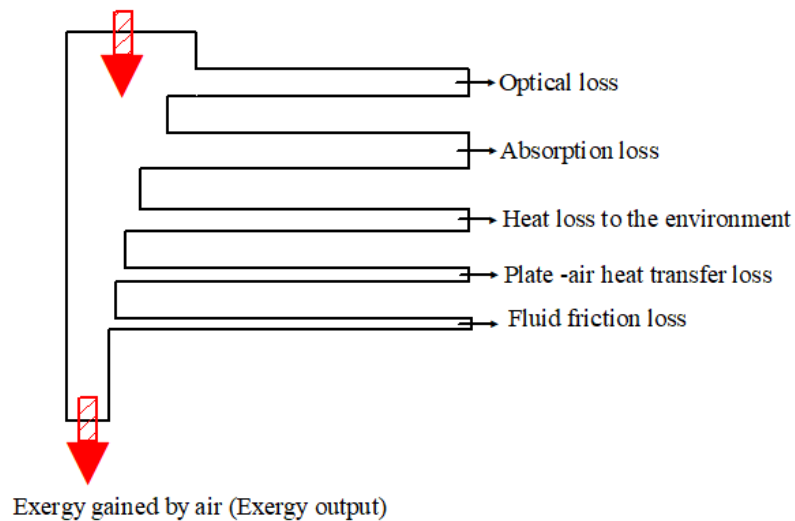
Fig. 3.11 Exergy flow in a flat plate solar air heater.

3.6 Experimental setup of solar air heater with semi-cylindrical sidewalls and discrete multiple inclined baffles

Indoor experimental setup of open-loop SAH with semi-cylindrical sidewalls is designed and fabricated following ASHRAE Standard (2003), as shown in Fig. 3.12 (a). SAH duct is divided into three sections, thermally separated from each other, and the optimum baffle configuration obtained from the CFD study is fabricated (Fig. 3.12 (b)). All the walls other than the top part of the absorber plate are insulated using ceramic wool to minimize heat loss to the environment. The schematic of the experimental setup is given in Fig. 3.12 (b). A differential pressure transducer (Yokogawa-EJA110E) and Vortex flowmeter (LUGB-Vortex Flow Meter) is employed to measure the drop in pressure along the test section length and flow rate of air, respectively. A halogen lamp-based solar simulator provides the absorber plate with a heat flux (1000 W/m^2). K-type thermocouples are fixed at 11 positions in a staggered manner to obtain the average absorber plate temperature, as shown in Fig. 3.12 (c).

In the present investigation, the essential parameters for uncertainty analysis are the Nusselt number (Nu), friction factor (f), and Reynolds number (Re). Uncertainty of the independent variables considered in this study are given in Table 3.3.

The uncertainty in Nu, f, and Re obtained from the below equations are 3.6%, 5.3%, and 3%, respectively (Kline 1953).

$$\frac{\delta Nu}{Nu} = \left[\left(\frac{\delta h}{h} \right)^2 + \left(\frac{\delta k}{k} \right)^2 + \left(\frac{\delta D}{D} \right)^2 \right]^{0.5} \tag{3.34}$$

Where,

$$\frac{\delta h}{h} = \left[\left(\frac{\delta Q}{Q} \right)^2 + \left(\frac{\delta A_p}{A_p} \right)^2 + \left(\frac{\delta (T_{pm} - T_{fm})}{(T_{pm} - T_{fm})} \right)^2 \right]^{0.5};$$

$$\frac{\delta Q}{Q} = \left[\left(\frac{\delta \dot{m}}{\dot{m}} \right)^2 + \left(\frac{\delta C_P}{C_P} \right)^2 + \left(\frac{\delta \Delta T}{\Delta T} \right)^2 \right]^{0.5}$$

$$\frac{\delta Re}{Re} = \left[\left(\frac{\delta V}{V} \right)^2 + \left(\frac{\delta \mu}{\mu} \right)^2 + \left(\frac{\delta \rho_{air}}{\rho_{air}} \right)^2 + \left(\frac{\delta D}{D} \right)^2 \right]^{0.5} \tag{3.35}$$

$$\frac{\delta f}{f} = \left[\left(\frac{\delta V}{V} \right)^2 + \left(\frac{\delta L}{L} \right)^2 + \left(\frac{\delta \rho_{air}}{\rho_{air}} \right)^2 + \left(\frac{\delta D}{D} \right)^2 + \left(\frac{\delta \Delta P}{\Delta P} \right)^2 \right]^{0.5} \tag{3.36}$$
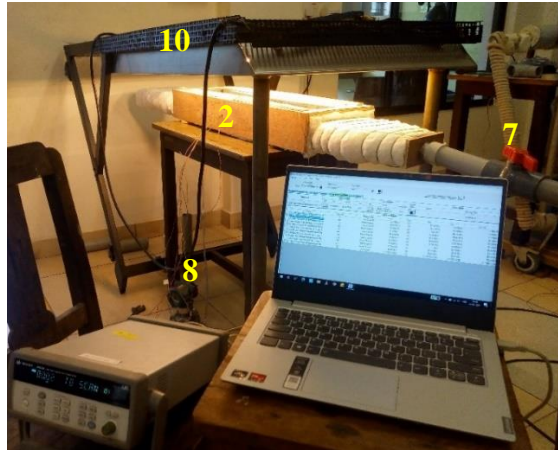
(a)

(b)
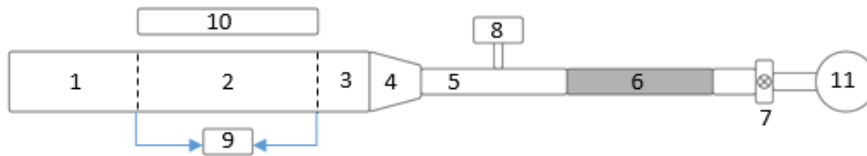
1	Inlet section	2	Test section
3	Exit section	4	Transition section
5	G I Pipe	6	Flexible pipe
7	Valve	8	Flowmeter
9	Differential pressure transducer	10	Solar simulator
11	Centrifugal blower		

(c)
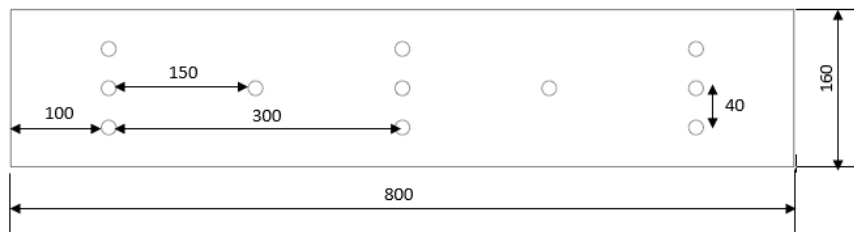
(d)

Fig. 3.12 (a) Experimental setup, (b) Absorber plate with multiple discrete inclined baffles, (c) Schematic diagram of the experimental setup, and (d) Thermocouple positions on the absorber plate (all dimensions are in 'mm').

Table 3.3: Uncertainty values of independent variables.

Parameter	Equipment	Error
Flow rate	Vortex flowmeter	$\pm\, 0.001\ m^3/hr$
Heat flux	Pyranometer	$\pm\, 1\ W/m^2$
Temperature	Thermocouple (K-Type)	$\pm\, 0.5\ ^\circ C$
Pressure drop	Differential pressure transducer	$\pm\, 0.01\ Pa$

3.7 Experimental methodology to study the drying characteristics

The drying characteristics of food samples such as okra (lady's fingers) and two variants of banana (nendran and robusta) are experimentally studied using a laboratory oven, as shown in Fig. 3.13. In this study, the air inlet temperature to the dryer is set equal to the maximum air temperature obtained at the ribbed triangular duct SAH outlet. The drying characteristics of the food samples are compared using smooth and ribbed SAH.

Moisture content (MC) is expressed on a dry basis (db) and is calculated using the following expression,

$$MC_t(db) = \frac{m_t - m_d}{m_d} \tag{3.37}$$

The moisture ratio (MR) at any time t is given by,

$$MR_t = \frac{MC_t - MC_{eq}}{MC_i - MC_{eq}} \tag{3.38}$$

Where MC_i, MC_t and MC_{eq} is the moisture contents at initial time, time t and equilibrium.

As the equilibrium moisture content is relatively small compared to MC_i and MC_t, MR is simplified as follows (Duan et al. 2019),

$$MR_t = \frac{MC_t}{MC_i} \tag{3.39}$$

Several empirical correlations/models are available to predict the MC and MR of a material. Among these models, the modified Page model was suggested to be the best fit for the experimental result (Goud et al. 2019, Rabha et al. 2017, and Shamekhi-Amiri et al. 2018). According to the modified Page model,

$$MR = e^{(-(At)^n)} \qquad (3.40)$$

Where A is a constant

A linear regressions analysis is performed to fit the data points with a straight line such that the coefficient of determination (R^2) value is maximum. The goodness of the fitting model is tested by calculating statistical parameters such as coefficient of determination (R^2) and reduced Chi-square (χ^2) (Goud et al. 2019),

$$R^2 = 1 - \frac{\sum_{i=1}^{N}(MR_{pre,i} - MR_{exp,i})^2}{\sum_{i=1}^{N}(MR_{exp,i})^2} \qquad (3.41)$$

$$\chi^2 = \frac{\sum_{i=1}^{N}(MR_{pre,i} - MR_{exp,i})^2}{N-n} \qquad (3.42)$$

Where $MR_{pre,i}$ and $MR_{exp,i}$ indicates the predicted and experimental moisture ratio, N is the number of observation, and n is the number of constraints in the model.

(a)   (b)
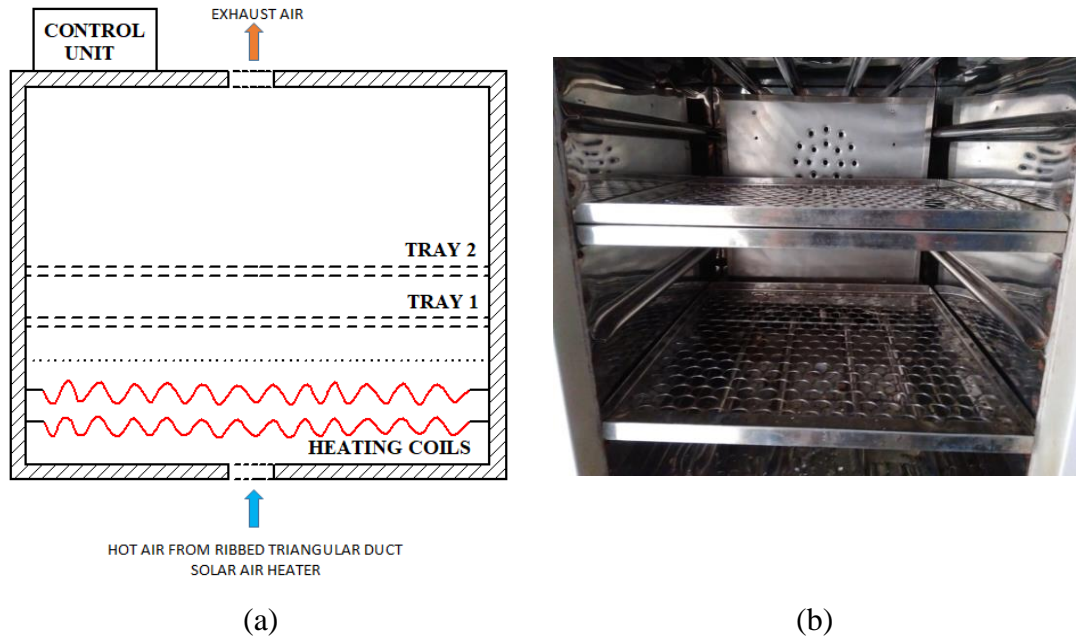
Fig. 3.13 Dryer used for the experimental study (a) Schematic and (b) Pictorial view.

The drying process in solid depends on the diffusion of water in the solid. Diffusion in a drying process is a complex mechanism that involves both the liquid and vapor phase of water and is a function of temperature, pressure, and food sample parameters (Göğüş and Maskan 1999). The moisture ratio of the product at an instant during the drying process can be expressed in terms of equilibrium diffusion coefficient (D_e) (Sallam et al. 2015) and the same is used to calculate D_e.

$$MR = \frac{8}{\pi^2} e^{\left(\frac{-\pi^2 D_e t}{4B^2}\right)}$$

<div align="right">(3.43)</div>

Errors in the experimental measurements are calculated using the methodology suggested by Kline (1953). In this method, the root mean square (RMS) value of errors corresponding to each variable/measurement used to calculate a particular parameter is taken, which gives the error for that parameter. Parameters obtained from the experimental study are moisture ratio (MR) and effective diffusivity parameter (D_e). Maximum uncertainties obtained for moisture ratio (MR) and effective diffusivity parameter (D_e) are 0.019% and 2.90%, respectively.

3.8 Validation

The CFD results are compared to the experimental study and the theoretical correlations (Dittus-Boelter and modified Blasius correlations) to ensure the precision of the numerical methodology. Compared to the experimental study (Luo et al. 2004), the deviation is 2% and 7.1% for Nu and f, respectively, in smooth triangular duct SAH (Fig. 3.14). For triangular duct SAH with inclined ribs, results are validated with the experimental study reported by Bharadwaj et al. (2017), as shown in Fig. 3.15. A similar triangular duct of 92.37 mm hydraulic diameter is created with repeated inclined ribs (e/D = 0.043 and P/e = 4) beneath the absorber plate. The average and maximum deviation in Nu are 4.8% and 6.9%, respectively. In the case of f, the average and maximum deviations are 6.4% and 10.06%, respectively. The obtained deviations may be due to the difference in the rib profile employed. Hence, the current CFD methodology can be applied to study hydraulic and thermal characteristics inside the proposed duct.

The results obtained for smooth plate rectangular SAH are validated with the corresponding experimental results, and a maximum deviation of 8.4% and 7.02% is obtained for Nu and f, respectively (Fig. 3.16(a)). The average variations are 7.8% and 6.5%, respectively, for Nu and f. With the validated methodology, further simulations incorporating artificial roughness are carried out to find the optimum pitch and subsequently to find the impact of the gap position on THPP of the SAH with semi-cylindrical sidewalls.
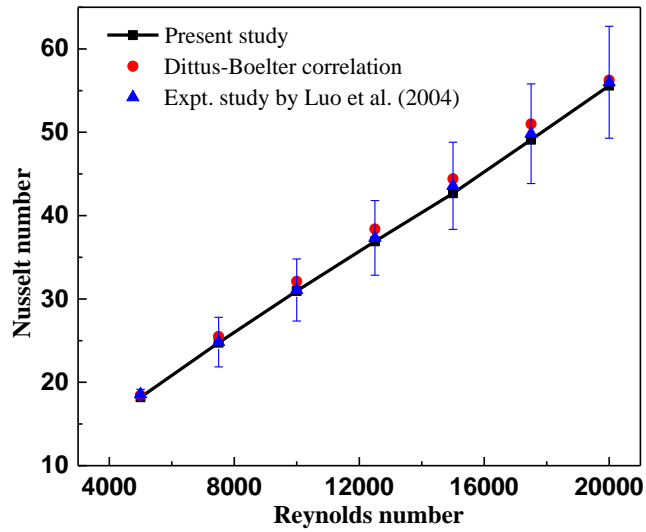
(a)
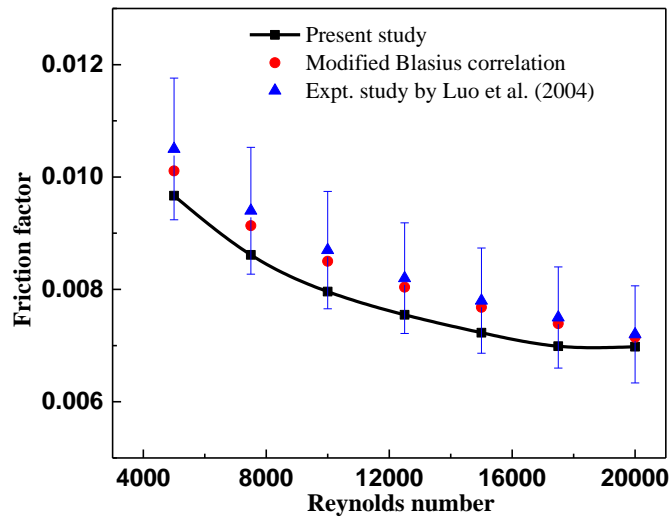
(b)

Fig. 3.14 Smooth triangular SAH CFD model validation (a) Nusselt number variation
with Reynolds number, and (b) Friction factor variation with Reynolds number.

Further, the optimum configuration of SAH with discrete multiple inclined baffles (R_H
= 0.1 and R_P = 0.75) is experimentally studied and compared with the results obtained
from the corresponding CFD model. A maximum deviation of 9.3% and 9.74% is
obtained for Nu and f, respectively (Fig. 3.16(b)). The average deviation of CFD values
with the experimental values are 8.5% and 8.9%, respectively, for Nu and f.
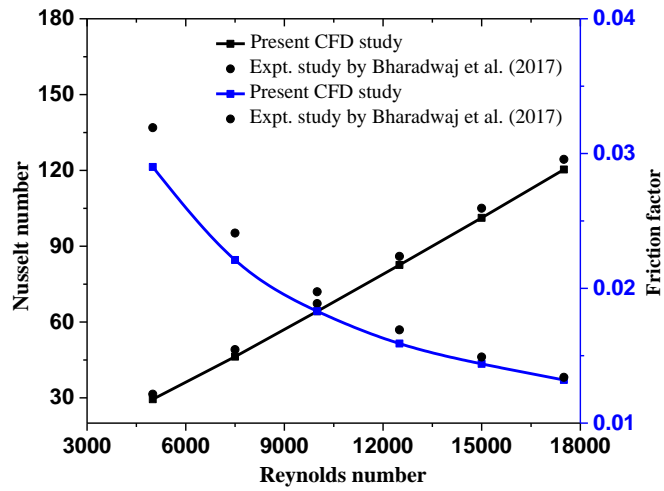
Fig. 3.15 CFD model validation for triangular duct with inclined ribs.

(a)

(b)
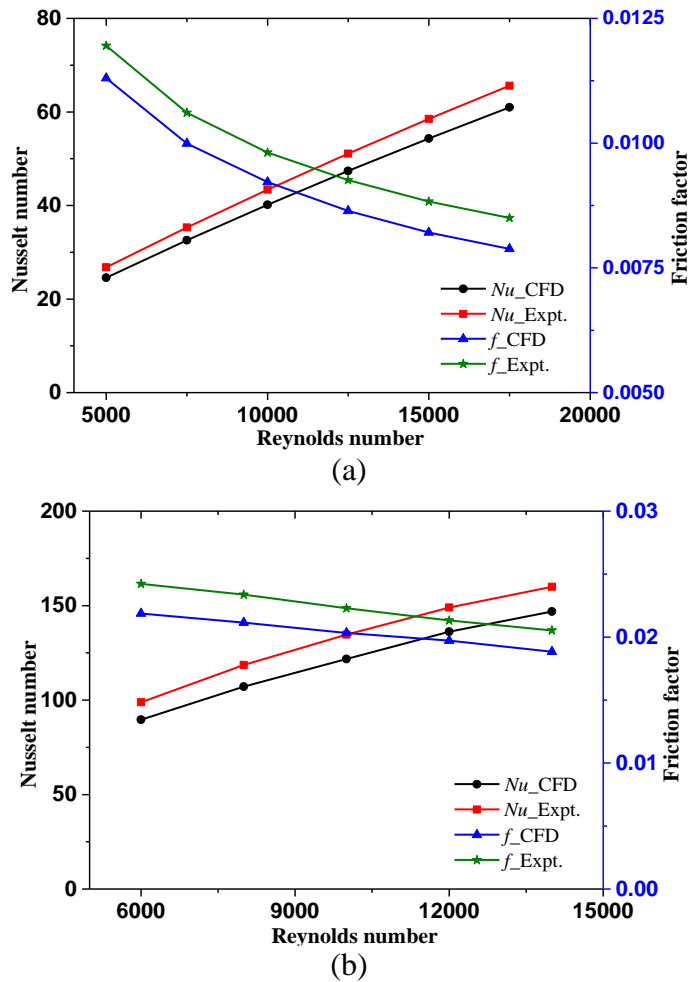
Fig. 3.16 Validation of (a) smooth and (b) baffled solar air heater CFD model with the corresponding experimental model.

The theoretical model and the solution procedure code for exergy analysis are validated using a model (I = 1000 W/m², P/e = 8, β = 60° and e/D = 0.043) similar to that reported by Singh et al. (2012) and Singh (2018). Results are compared in the form of thermal efficiency and exergetic efficiency to ensure the accuracy of the procedure adopted (Figs. 3.17 (a) and (b)). It is observed that the present numerical code is capable of predicting the performance of a triangular duct solar air heater with a reasonable agreement. Upon comparing the thermal efficiency and exergetic efficiency, it is observed that the numerical code generates results with acceptable accuracy.
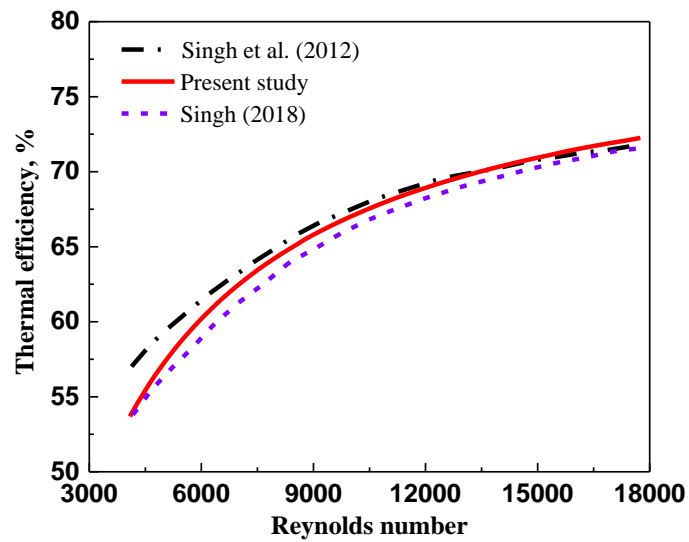
(a)
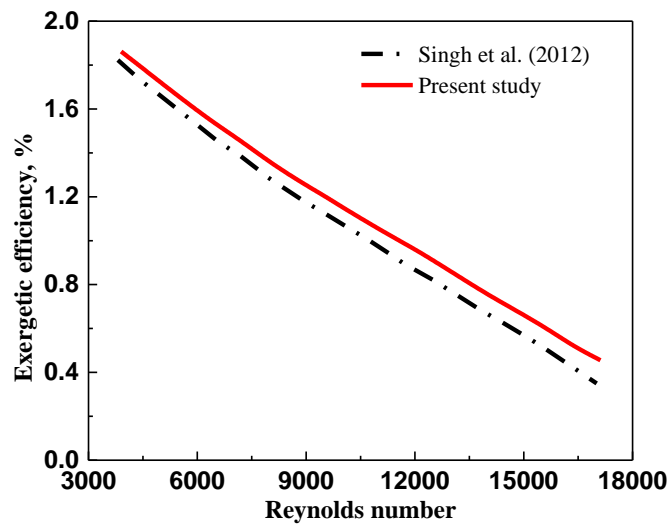
(b)

Fig. 3.17 Comparison of the theoretical model with the literature data (a) Thermal efficiency and (b) Exergetic efficiency.

3.9 Summary

CFD simulation results for artificially roughened SAH with triangular duct and duct with semi-cylindrical sidewalls are analyzed for varying grid elements in terms of Nusselt number (Nu) and friction factor (f). The maximum variation in Nu and f is less than 1.2%, confirming that results are independent of the number of grid elements. RNG $k\text{-}\varepsilon$ turbulence model with enhanced wall treatment delivers the most precise results for Nu and f with an average deviation of 2.5% and 8.4%, respectively. Validation of the CFD results for smooth and artificially roughened SAH (triangular duct and duct with semi-cylindrical sidewalls) with theoretical correlations and experimental data indicates reasonable accuracy.

CHAPTER 4

STUDIES ON TRIANGULAR DUCT SOLAR AIR HEATER WITH V-RIBS AS ARTIFICIAL ROUGHNESS

4.1 Introduction

As the triangular cross-sectional duct has a minimum pressure drop compared to circular, rectangular, and elliptical ducts (Guyer 1999), the same has been applied in solar air heaters. Computational fluid dynamic (CFD) simulations and exergy analysis are conducted to investigate the impact of secondary flow produced by V-ribs on a triangular duct solar air heater (SAH). CFD results are validated with the experimental results from the literature. By varying the rib inclination ($30° \leq \beta \leq 75°$) in the turbulent flow regime ($5000 \leq Re \leq 20000$), the thermal and hydraulic performance of ribbed triangular duct SAH is compared to smooth triangular SAH. The computational domain of triangular duct with V-ribs has been discussed in *section 3.1*. The domain has been discretized into hexahedral cells using non-uniform multi-block meshing (*section 3.2*). The CFD results are validated with theoretical correlations and experimental studies available in the literature (*section 3.8*).

Flow visualization, contours of pressure, velocity, turbulence kinetic energy, temperature, and various characteristic plots (*Nu*, *f,* and THPP) are presented to establish the findings. Based on the CFD results, empirical correlations capable of predicting Nusselt number (*Nu*) and friction factor (*f*) are developed. In addition, exergetic performance analysis is carried out, and the results are presented in terms of various exergetic losses and exergetic efficiency. Further, the superior performance of the rib configuration delivering maximum performance in the present design is studied by comparing with various similar rib configurations in a conventional rectangular duct SAH.

4.2 Thermal performance

The thermal performance of V-rib in a triangular SAH is analyzed at various rib inclinations (30° - 75°) for Reynolds number ranging from 5000 to 20000. For every rib inclination (β), *Nu* monotonically increases with *Re* with enhancement in the range of 1.45 to 2.41 times than the smooth absorber plate. As *Re* increases, the length of the

recirculation zone (low heat transfer zone) reduces. Also, as the flow velocity increases, the turbulent intensity rises, due to which there is a considerable increase in turbulent kinetic energy. Hence, the cumulative effect accounts for the rise of Nu with an increase in Re. For the range of Re, maximum and minimum Nu is obtained for $\beta = 45°$ and $\beta = 90°$, respectively (Fig. 4.1). As β increases from 30° to 90°, Nu increases up to $\beta = 45°$ and further decreases. This may be due to the change in the strength of the secondary flow with rib inclination. The minimum heat transfer rate in $\beta = 90°$ is attributed to the stagnant fluid behind the ribs. In V-ribs, secondary flow develops at both leading edges and subsequently merges near the apex (Fig. 4.2). Secondary flow facilitates hot air mixing near the rib walls with primary air stream, thereby increasing turbulent intensity.
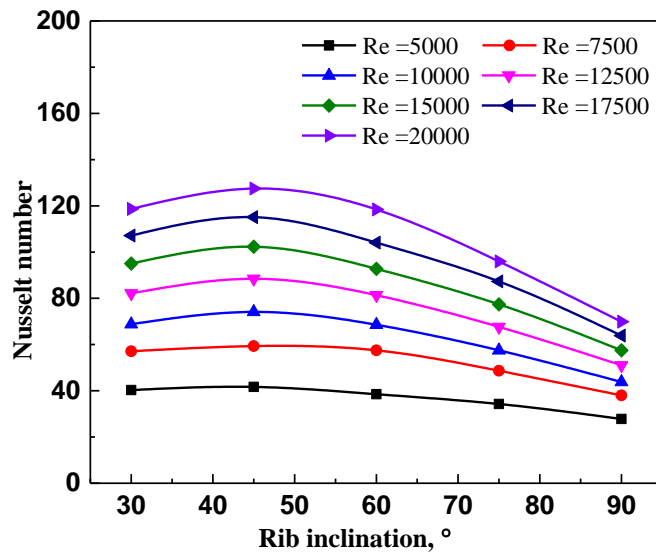
Fig. 4.1 Nusselt number as a function of rib inclination.
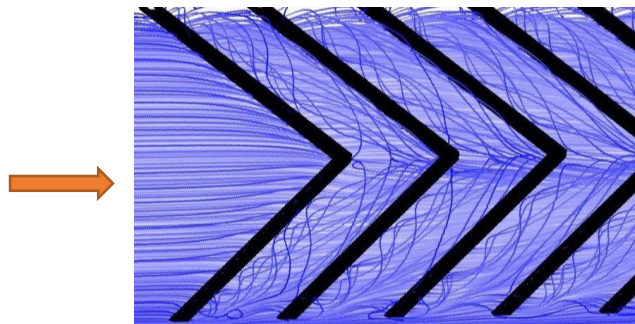
Fig. 4.2 Secondary flow in V-rib (arrow indicates flow direction) at $Re = 7500$.

Velocity contours (Fig. 4.3) indicates that a stagnant recirculation zone is formed in the wake region for $\beta = 90°$, whereas for $\beta = 45°$, there is secondary flow observed along

the rib edges. The stagnant recirculation zones impede the convective heat transfer process. Fig. 4.4 depicts the turbulence kinetic energy (TKE) contours at z = 0.5 m, z = 0.75 m, z = 1 m and z = 1.25 m along the length of the test section. It is observed that TKE is higher along the sides of the duct than the central region for a smooth duct. For the ribbed duct ($\beta = 90°$), TKE is amplified only in the immediate vicinity behind the rib (Fig. 4.4(b)). This occurs due to the stagnant recirculation zone behind the rib. However, secondary flow from the V-rib tips to the apex causes the rise of TKE in the central regions of the duct. Due to this, better mixing of hot and cold air occurs, which causes the augmentation of heat transfer rate. Maximum TKE is reported at the locations of the origin of secondary flow (Fig. 4.4 (c)).

For the smooth and ribbed plate ($\beta = 90°$), the air temperature near the absorber plate is very high (Fig. 4.5 (a)). This is attributed to forming a laminar sublayer within the turbulent boundary layer for a smooth plate. The viscous effects dominate within the laminar sublayer, impeding the convective heat transfer rate. For the ribbed plate ($\beta = 90°$), a stagnant recirculation zone is formed behind the rib, which acts as a low heat transfer zone.

(a) $\beta = 90°$ Stagnant recirculation zone

(b) $\beta = 45°$ Absence of stagnant recirculation zone
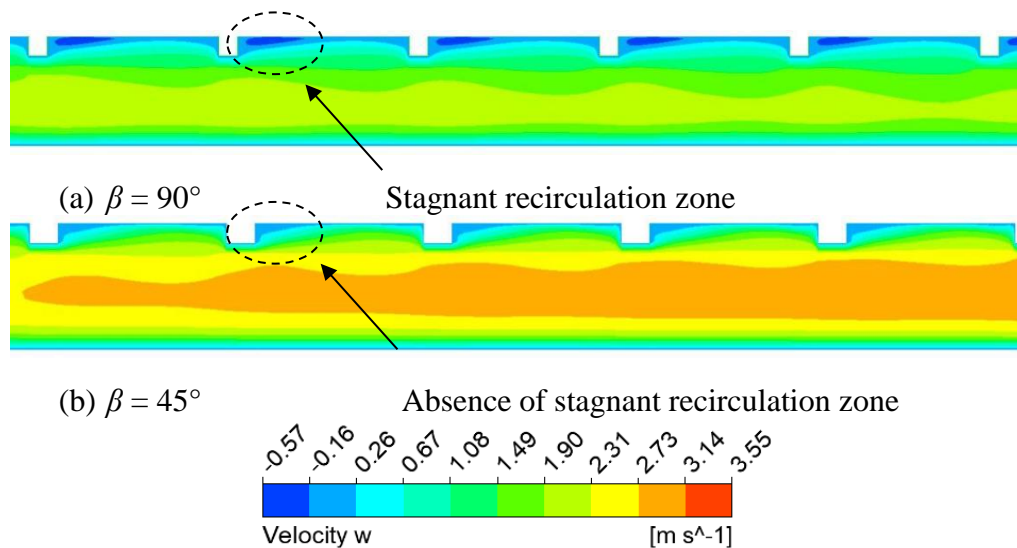
Fig. 4.3 Velocity (z-component) contour along the primary flow direction (on y-z plane) at Re = 7500 for (a) $\beta = 90°$, and (b) $\beta = 45°$.
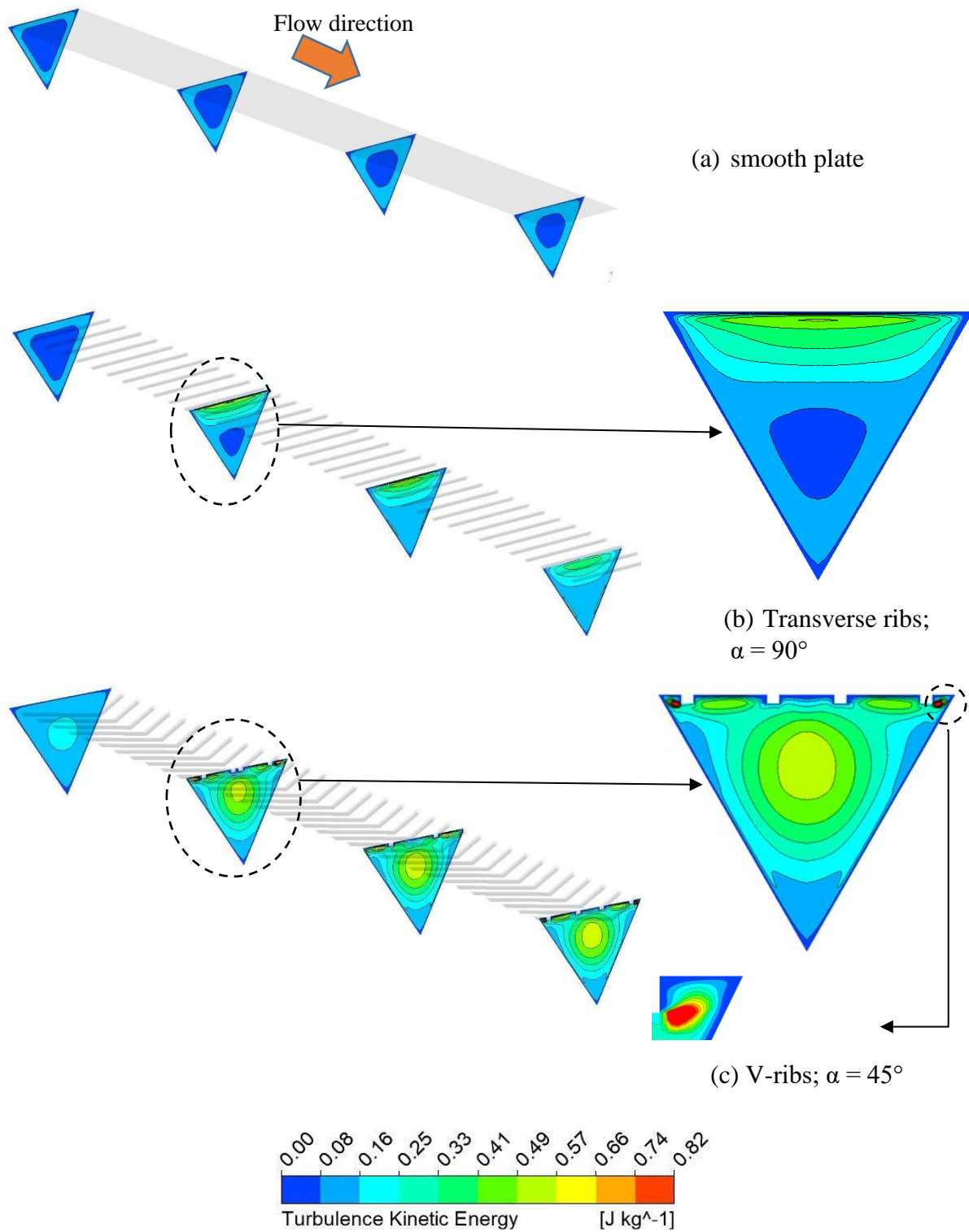
Fig. 4.4 Turbulence kinetic energy contours at various location along the test section at $Re = 7500$ for (a) smooth plate, (b) $\beta = 90°$, and (c) $\beta = 45°$.

(a) Smooth plate
(xy plane at z = 1.25 m)

(b) Transverse rib ; α = 90°

(xy plane at z = 1.25 m)

Merging of secondary flows

(c) V-rib; α = 45°

(x-y plane at z = 1.25 m)
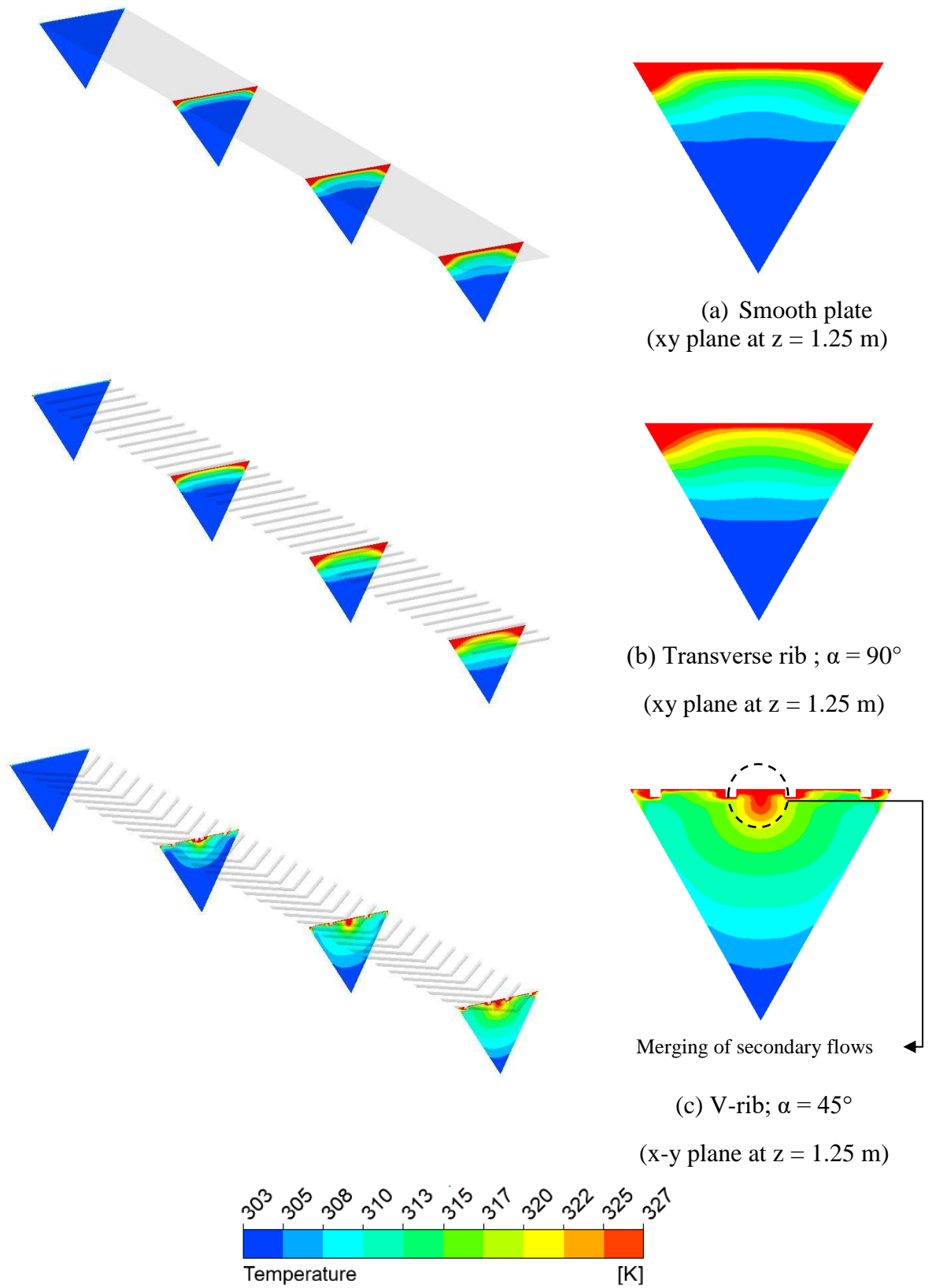
Temperature   [K]

Fig. 4.5 Temperature contours at various location along the test section for (a) smooth plate, (b) $\beta = 90°$, and (c) $\beta = 45°$.

However, the secondary flows generated in each V-rib move and merge at the apex. This results in the better mixing of hot and cold air, increasing the temperature near the apex (Fig. 4.5 (c)). The high-temperature air drifts from the hot plate to the bottom of the duct, further increasing the temperature in the core region.

4.3 Hydraulic performance

Friction factor (f) decreases with Re for both smooth and ribbed SAH. It is observed that there is no significant pressure variation at a particular cross-section of the duct (Fig. 4.6). However, it is noteworthy that the inclusion of the ribs ($\beta = 90°$) altogether changes the pressure distribution. Due to the stagnant recirculation zone behind the ribs ($\beta = 90°$), pressure is lowest in the wake region and highest away from the ribs. This indicates that ribs ($\beta = 90°$) cause a significant pressure drop over a broader flow region. Whereas for V-ribs ($\beta = 45°$), minimum pressure is restricted only to a small area wherein the secondary flow originates. Unlike transverse ribs, the pressure within the duct almost remains uniform with the inclusion of V-ribs. It is observed that f is maximum and minimum corresponding to $\beta = 60°$ and $\beta = 45°$ for the entire range of Re, respectively when compared to the smooth plate (Fig. 4.7). Even though pressure drop increases for an increase in rib inclination, f increases up to 60° and then decreases. This is due to the increase in flow velocity in the inter-rib regions for $\beta \leq 45°$ (Fig. 4.8). This is attributed to the reduction of the length of the low-pressure zone (recirculation zone) and the thickness of the laminar sublayer.
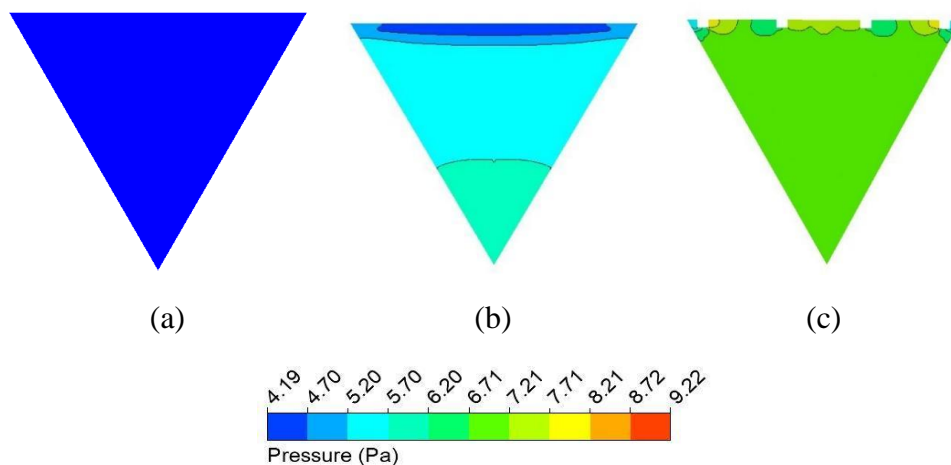
Fig. 4.6 Pressure contour for smooth and ribbed absorber plate; (a) smooth plate, (b) Ribbed plate ($\beta = 90°$), and (c) V-rib ($\beta = 45°$).
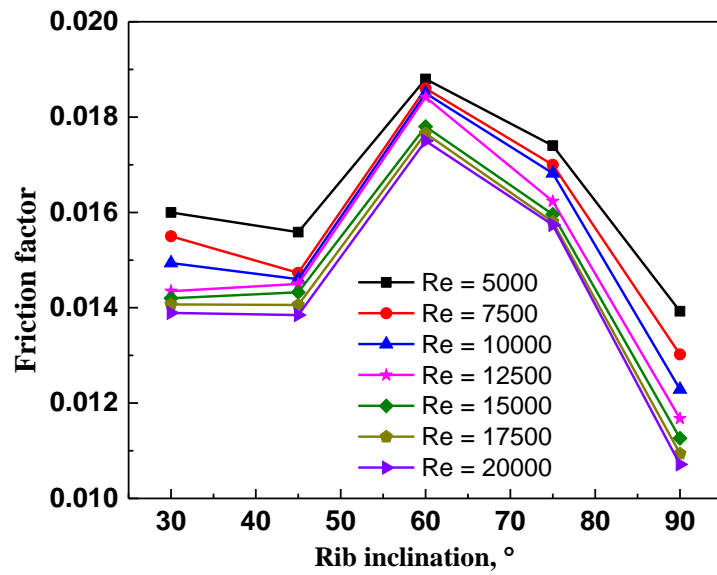
Fig. 4.7 Friction factor characteristics as a function of rib inclination.

(a)   (b)   (c)
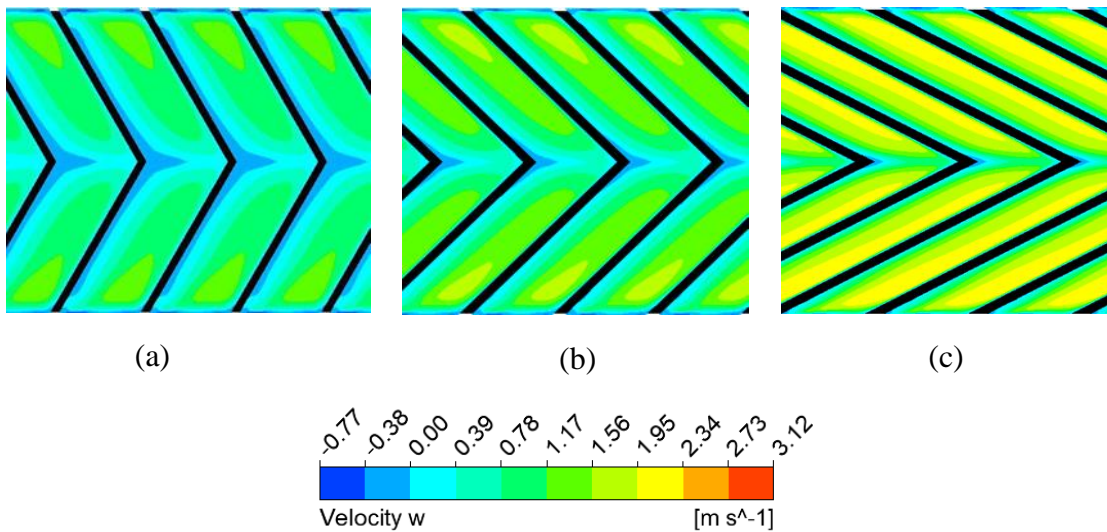
Fig. 4.8 Velocity distribution in the inter-rib regions (a) $\beta = 60°$, (b) $\beta = 45°$, and (c) $\beta = 30°$.

4.4 Thermo-hydraulic performance

The inclusion of ribs in a SAH duct is justified by the value of the thermo-hydraulic performance parameter (THPP). The variation of thermo-hydraulic performance parameter (THPP) for various rib inclinations is plotted as a function of Reynolds number. For a fixed e/D and P/e, the THPP increases with an increase in rib inclination up to 45° and beyond which it decreases (Fig. 4.9). For fixed $e/D = 0.05$ and $P/e = 10$, maximum value of THPP is obtained as 2.01 for $\beta = 45°$ at $Re = 7500$. The *THPP*

obtained with V-rib underneath the absorber plate of a triangular duct SAH is compared with various other artificial roughness in a triangular duct SAH (Table 4.1). The present CFD study proves that the application of V-ribs enhances THPP of triangular duct SAH compared to many previous rib configurations.
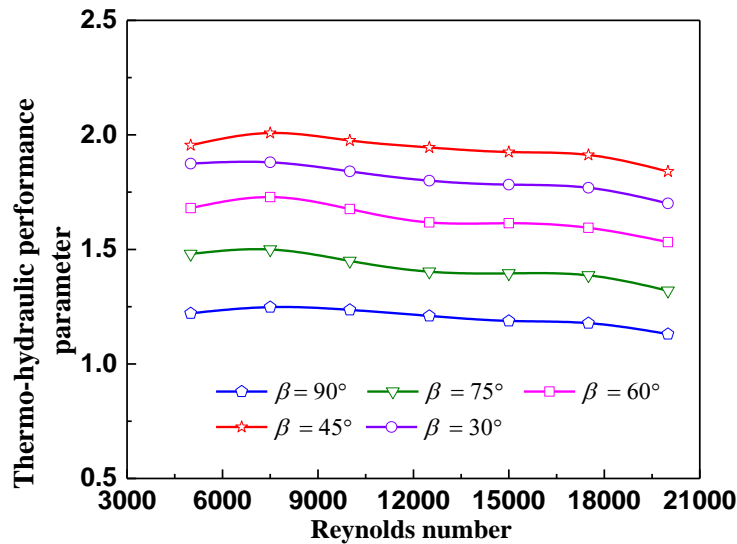
Fig. 4.9 Thermo-hydraulic performance of V-rib at various rib inclinations.

Table 4.1: Comparison of thermo-hydraulic performance parameter of various types of ribs in triangular duct SAH

References	Type of study	Roughness geometry	Thermo-hydraulic performance parameter (THPP)
Kumar et al. (2017)		Transverse square rib	1.89
Kumar et al. (2019)	CFD	Transverse rectangular rib	1.44
Jain et al. (2019)		Discrete square rib	1.98
Present CFD study		*V-rib*	*2.01*

4.5 Development of correlations

Nusselt number and friction factor are required to estimate the thermo-hydraulic performance of a SAH. Empirical correlations are used to measure these parameters. Using CFD results, empirical correlations capable of predicting *Nu* and *f* within an acceptable accuracy range are developed using regression analysis. Characteristic plots

were drawn to know the nature of the dependence of Re and β on Nu and f. The plot obtained is a straight line between ln (Nu) and ln (Re) (Fig. 4.10 (a)). Linear regression analysis is used to compute the slope of this line. The slope of the curve gave the power of Re, as 0.77. The curve of ln ($Nu/Re^{0.77}$) vs. ln (β) is plotted to determine its nature. Quadratic regression analysis is developed as the curve follows a quadratic trend (Fig. 4.10 (b)). Similar steps are followed to generate the correlation for the friction factor.
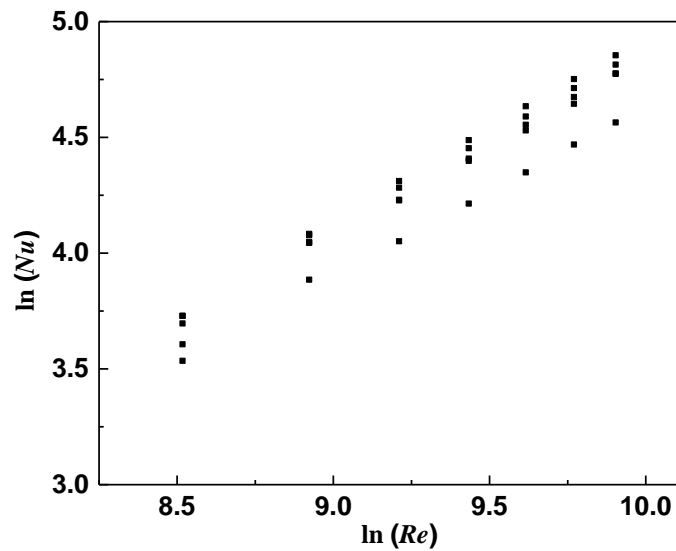
(a)
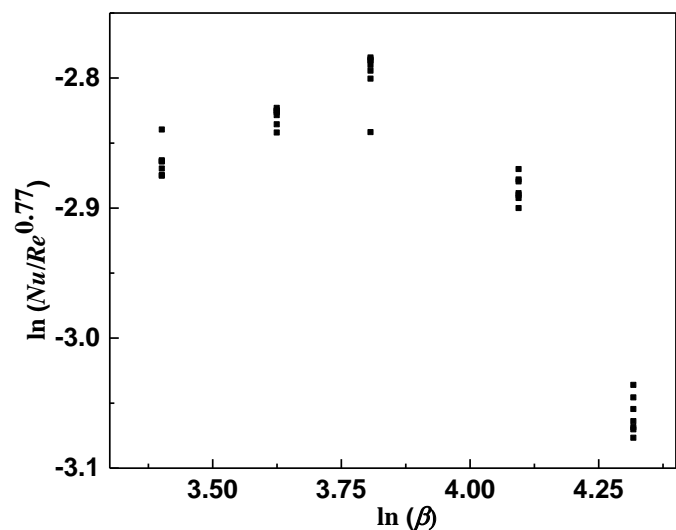
(b)

Fig. 4.10 Correlation development plots (a) ln (Nu) vs ln (Re) and

(b) ln ($Nu/Re^{0.77}$) vs ln (β)
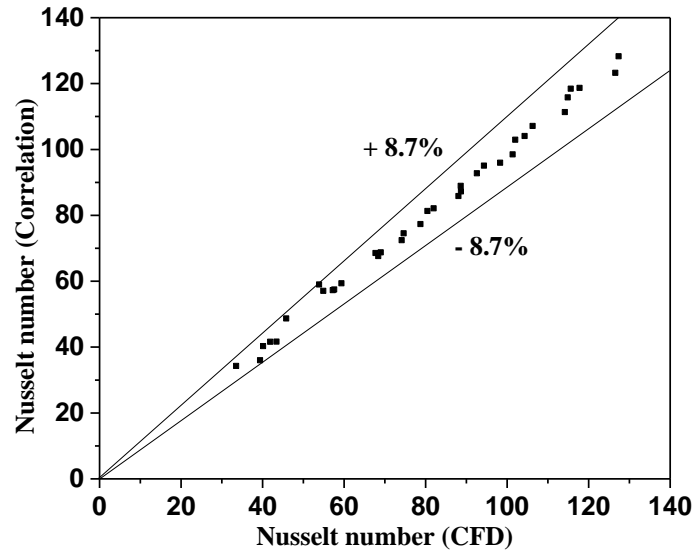
Fig. 4.11 Variance plot for Nusselt number.
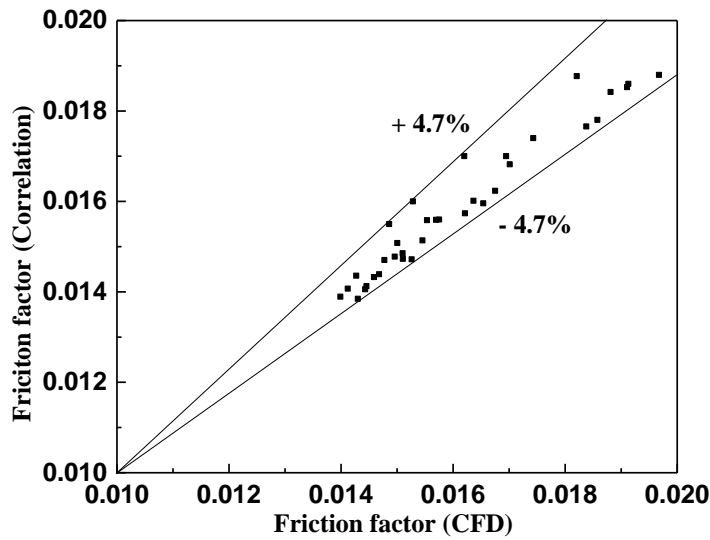
Fig. 4.12 Variance plot for friction factor.

$$Nu = 1.49 \times 10^{-6} \times Re^{0.77} \times \alpha^{5.70} e^{\left(-0.76(ln\,(\beta))^2\right)} \tag{4.1}$$

$$f = Re^{-0.070} e^{c} \tag{4.2}$$

Where

$$c = -13.15 \times (ln\,(\beta))^4 + 201.34 \times (ln\,(\beta))^3 - 1152.54 \times (ln\,(\beta))^2 + 2924.90$$
$$\times (ln\,(\beta)^1) - 2780.33$$

The correlations are valid for the following range of *Re* and *β*:

$5000 \leq Re \leq 20000$

$30° \leq \beta \leq 75°$

The coefficient of determination (R^2) for the correlation curve of *Nu* and *f* is obtained as 0.995 and 0.942, respectively. The accuracy of the developed correlation is calculated by determining the corresponding deviation from the CFD simulation values. Figs. 4.11and 4.12 display the comparison of *Nu* and *f* values obtained from the correlations corresponding to *Nu* and *f* values derived from the CFD simulation, respectively. The maximum deviation of the values predicted by the generated correlation and corresponding CFD values for *Nu* and *f* is 8.7% and 4.7%, respectively.

4.6 Exergetic performance

For evaluating the exergetic performance of a SAH, absorber plate temperature serves as an essential parameter. From Fig. 4.13, it is observed that absorber plate temperature decreases with an increase in *Re*. At higher *Re*, turbulence is higher, and subsequent mixing of fluid particles lowers the absorber plate temperature. As the temperature gradient (between air and plate) narrows, the heat transfer coefficient improves. It is noticed that T_p with V-ribs is much lower than that of a smooth plate.
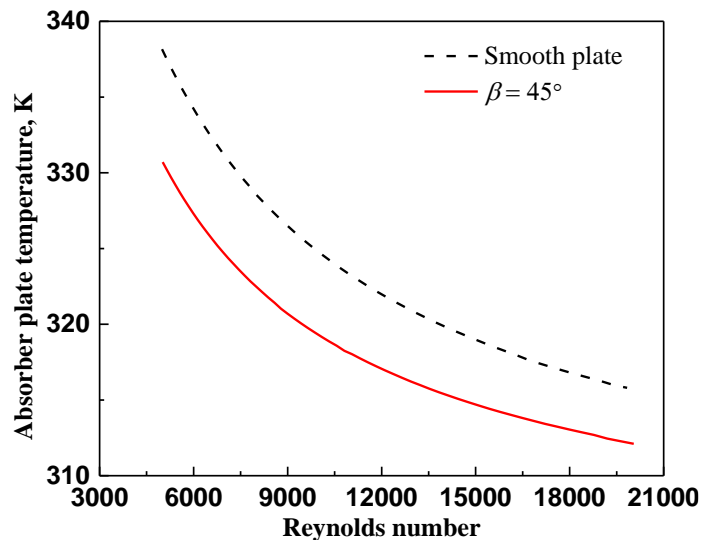
Fig. 4.13 Impact of ribs on absorber plate temperature.

The higher temperature gradient between air and plate temperature may result in higher exergy losses. Minimum T_p is obtained for *β* = 45° for the range of parameters

investigated. The effect of T_p on various exergy losses and efficiency of SAH is discussed in detail below. The optical exergy loss (L_{opt}) considers the radiation reflected from the glass cover, and the variation trend of the same indicates no impact of *Re* (Fig. 4.14).
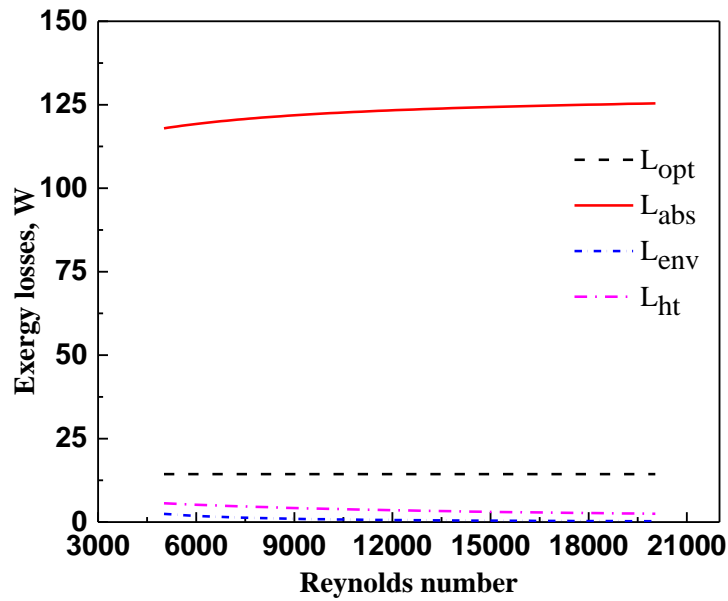
Fig. 4.14 Impact of Reynolds number on various exergy losses.
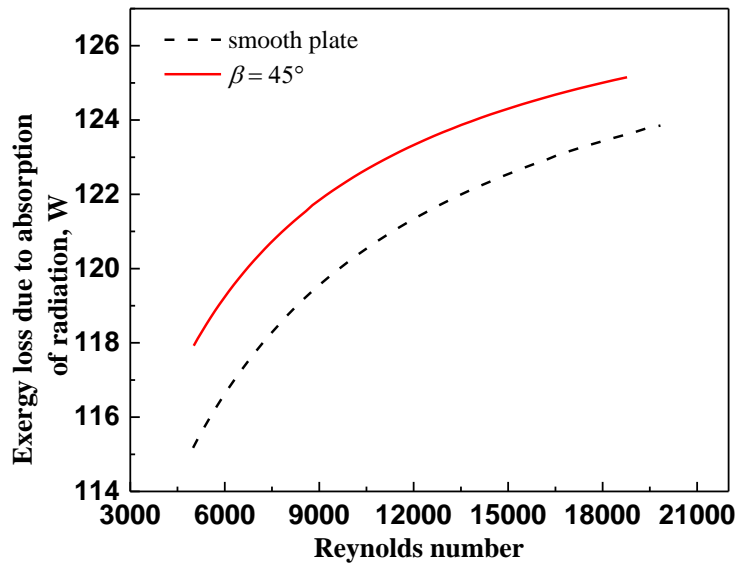
Fig. 4.15 Impact of Reynolds number on exergy loss due to absorption of radiation.

Exergy loss due to absorption of solar radiation (L_{abs}) accounts for the major exergy loss in a SAH (Bliss 1959; Kumar and Layek 2019a). With an increase in *Re*, L_{abs}

increases (Fig. 4.15) owing to decrement in the plate temperature. For a plate with V-ribs, higher L_{abs} are reported in comparison to a smooth absorber plate. At lower *Re,* the exergy loss due to convective and radiation heat transfer to the environment (L_{env}) increases. For the range of parameters studied, minimum L_{env} is obtained for $\alpha = 45°$. The magnitude decreases with an increase in *Re* and becomes invariant at higher *Re* (Fig. 4.16).

The asymptotic behavior of L_{env} at higher *Re* is because of a decrease in absorber plate temperature. The "internal irreversibility" leads to two types of exergy losses: exergy loss due to heat transfer between plate to the air (L_{ht}) and exergy loss due to fluid friction. This exergy loss accounts for the non-uniform temperature distribution of the absorber plate and the finite temperature gradient over which heat transfer occurs (plate and air). L_{ht} follows a similar trend of L_{env} with *Re,* attributed to the lower T_p at higher *Re*. The exergy loss due to the heat transfer process is much more significant than that of pumping power consumption (Xiao et al. 2019). Exergy loss due to flow friction is more pronounced at very high *Re* (Singh et al. 2012).
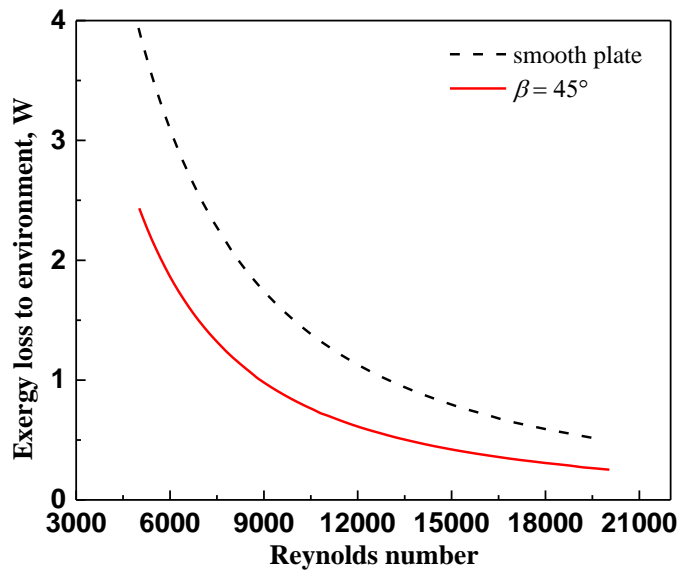
Fig. 4.16 Impact of Reynolds number on exergy loss to the environment.

Besides, the effect of flow friction is explained in detail in the thermo-hydraulic performance analysis; hence, it is not presented here. Finite temperature gradient for heat transfer in the SAH owes to the irreversibility, increasing the entropy generation during the process. For the range of parameters studied, an artificially ribbed plate

reported lower entropy generation than the smooth plate. For various rib inclinations studied, $\beta = 45°$ gave the least entropy generation, and the same variation is depicted in Fig. 4.17.
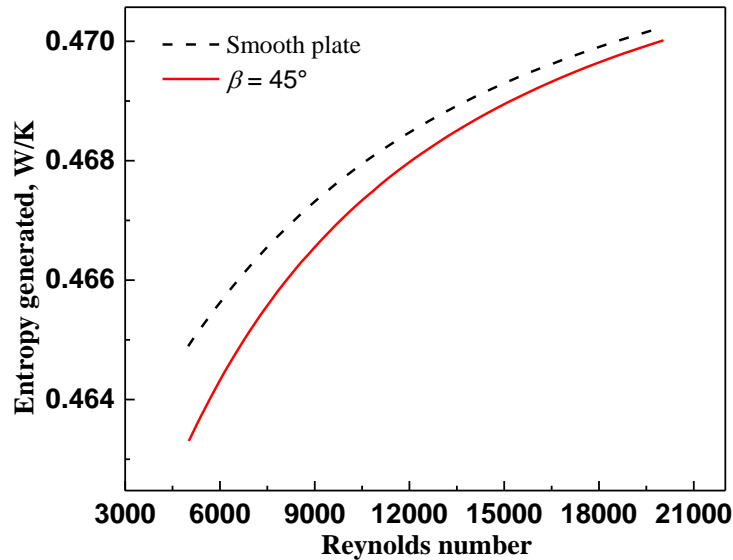
Fig. 4.17 Influence of Reynolds number on entropy generation

Exergetic efficiency (η_{ex}) decreases with an increase in *Re* due to increased exergy losses (Fig. 4.18). For varying V-rib inclinations ($30° \leq \beta \leq 75°$), the η_{ex} reported is in the range 0.8% to 2.34%. A maximum η_{ex} of 2.34% is obtained for $\alpha = 45°$, with an enhancement of 1.24 times compared to the smooth plate. This is because of the minimum entropy generation compared to other rib inclinations. Besides, from Fig. 4.5, it was observed that the fluid temperature is more uniformly distributed across the cross-section, indicating improved heat transfer and consequently lower exergy losses. After performing an in-depth exergetic performance analysis, it is interpreted that V-rib ($\beta = 45°$) has the least entropy generation and highest exergetic efficiency relative to the other rib inclinations studied.

Further, this research points to better results when compared with the exergy studies available in the review article by Gupta and Kaushik (2009), as shown in Fig. 4.19. Ribbed triangular duct SAH delivers a better exergetic performance over a wide range of *Re* than ribbed rectangular duct SAH. Better exergetic efficiency reveals the effective distribution of solar energy in comparison with expanded V-rib (Momin et al. 2002), chamfered rib-groove (Layek et al. 2007), wedge-shaped ribs (Bhagoria et al. 2002),

metal mesh (Saini and Saini 1997), and rib and groove combination (Jaurker et al. 2006) for the entire range of *Re*. However, compared to the rib configuration of chamfered rib with alternate grooves, the present design inherits a lower exergetic performance for a narrow *Re* range of 7500 to 10000.
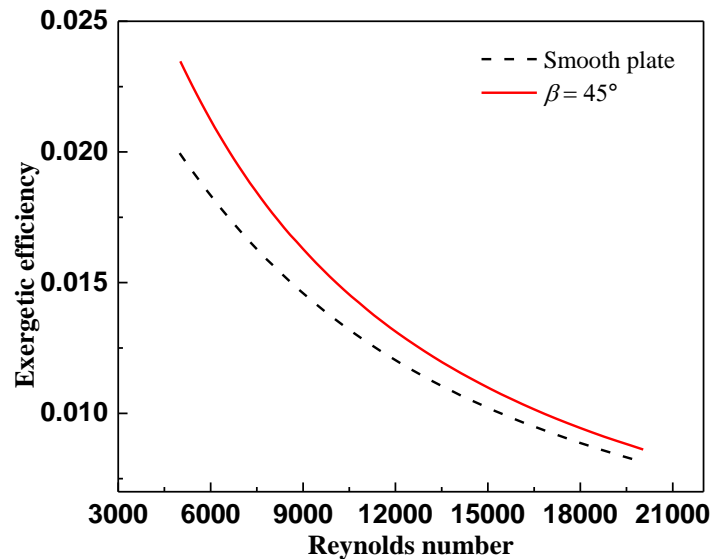
Fig. 4.18 Exergetic efficiency variation with flow Reynolds number.
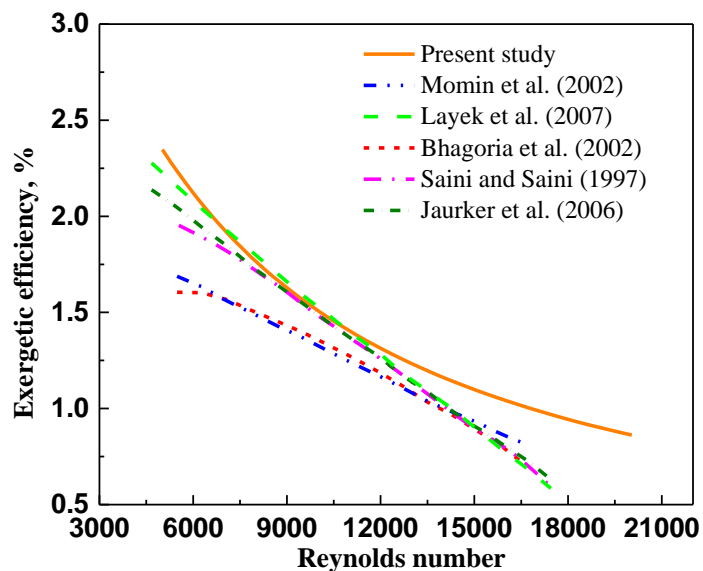
Fig. 4.19 Exergetic efficiency comparison for similar kind of artificial roughness.

The higher exergetic performance of ribbed triangular duct SAH compared to various ribbed rectangular duct SAH may be attributed to lower exergy losses due to fluid friction at higher *Re*. At lower and higher *Re*, triangular duct SAH with V-ribs displayed

better exergetic performance on a comparative basis. It can be inferred that the ribbed triangular duct would be a better choice for an application requiring compact SAH at higher mass flow rates.

4.7 Summary

CFD and exergy analysis of triangular duct SAH with V-rib is conducted for a range of Re (5000 to 20000). The results indicate that the present SAH design exhibits improved overall performance over other artificial roughness employed in the triangular and rectangular duct SAHs, as mentioned in the literature. The following notable conclusions are drawn based on the analysis:

- Peak enhancement in Nu is obtained as 2.41 times that of smooth absorber plate for e/D =0.05, P/e = 10, and β = 45° at Re = 7500. Whereas peak enhancement in f is obtained as 2.53 times that of smooth absorber plate for e/D =0.05, P/e = 10, and β = 60° at Re = 17500.

- Nusselt number and friction factor values are substantially higher than the smooth absorber plate values. This is due to the separation of flow, reattachment, and secondary flow generation caused by the V-ribs.

- The thermo-hydraulic performance parameter (THPP) for the triangular duct SAH with V-ribs is obtained in the range of 1.32 to 2.01. Peak value of 2.01 is obtained for e/D =0.05, P/e = 10, and β = 45° at Re = 7500.

- Minimum entropy generation and maximum exergetic efficiency are obtained for β = 45° compared to the smooth plate SAH. An enhancement in exergetic efficiency (η_{ex}) of 23% is obtained.

- Upon comparing this SAH design with ribbed rectangular duct SAH for similar input conditions, this design exhibits superior performance. Hence, for applications requiring compact heat exchangers, especially at higher flow rates, a V-ribbed (β = 45°) triangular duct SAH is a better choice compared to a ribbed rectangular duct SAH.

CHAPTER 5

DEVELOPMENT OF AN ENERGY-EFFICIENT DRYER USING RIBBED TRIANGULAR DUCT SOLAR AIR HEATER

5.1 Introduction

A triangular duct cross-section is introduced for the solar air heater (SAH) of an indirect type of solar dryer (ITSD). Using computational study, the thermo-hydraulic performance of triangular duct SAH with inclined ribs for varying rib inclination ($30°$ $\leq \beta \leq 75°$) in the turbulent flow regime ($5000 \leq Re \leq 17500$) is studied. The computational domain of triangular duct with inclined ribs has been discussed in *section 3.1*. The domain has been discretized into hexahedral cells using non-uniform multi-block meshing (*section 3.2*). The CFD results are validated with theoretical correlations and experimental studies available in the literature (*section 3.8*). With the rib configuration providing maximum thermo-hydraulic performance, a ribbed triangular duct SAH is designed. The performance of the same is compared to the rectangular duct SAH for similar heat input. For a fixed *e/D* and *P/e*, rib inclination to the main flow stream is varied in the range of $30°$ to $75°$, and various characteristic plots along with flow visualization contours are presented to institute the findings.

Further, the performance of ribbed triangular duct SAH in ITSD is studied for drying characteristics of two variants of banana (nendran and robusta) and okra (lady's fingers) having different initial moisture contents. The details of experimentation and data reduction have been discussed in *section 3.7*. The drying rate of ITSD with ribbed triangular duct is compared to the ITSD having ribbed rectangular duct SAH by studying the maximum temperature obtained at the outlet of the respective SAHs. A suitable drying model is obtained by analyzing various thin layer drying models. Reduction in moisture ratio and average diffusivity coefficient is also studied to confirm the energy efficiency of the present design.

5.2 Thermal performance

The thermal performance of inclined ribs in a triangular duct SAH is analyzed at various rib inclinations ($30°$ - $75°$) for fixed rib height and pitch in the turbulent flow regime ($5000 \leq Re \leq 17500$). As the ribs generate secondary flow in the SAH duct, the accuracy

of the steady-state assumption is verified by conducting a transient analysis for flow through triangular duct SAH for rib inclination of 45°.
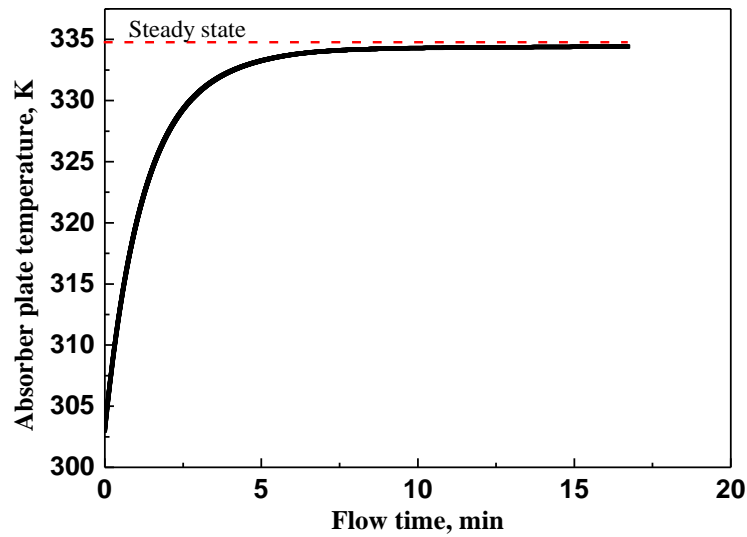
(a)
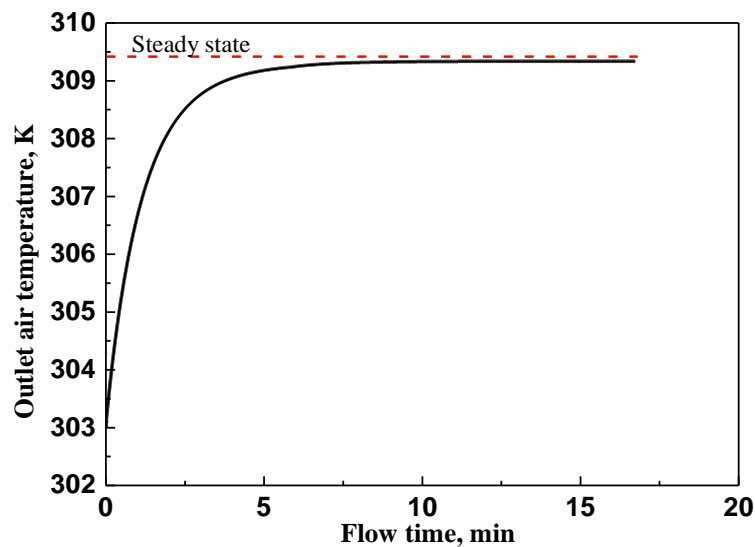
(b)

Fig. 5.1 Transient variation of the (a) absorber plate temperature, and (b) outlet air temperature in the triangular duct SAH for a rib inclination of 45°.

The results are compared in the form of plots of absorber plate temperature and outlet air temperature with flow time, as shown in Fig. 5.1 (a) and (b), respectively. Saha and Acharya (2004) have reported that the most apparent evidence of unsteadiness in the flow is revealed through the time-dependent behavior of secondary flow (cross-flow).

As the inclined ribs create additional secondary flow, verifying whether the secondary flow causes unsteadiness in the primary flow is essential.
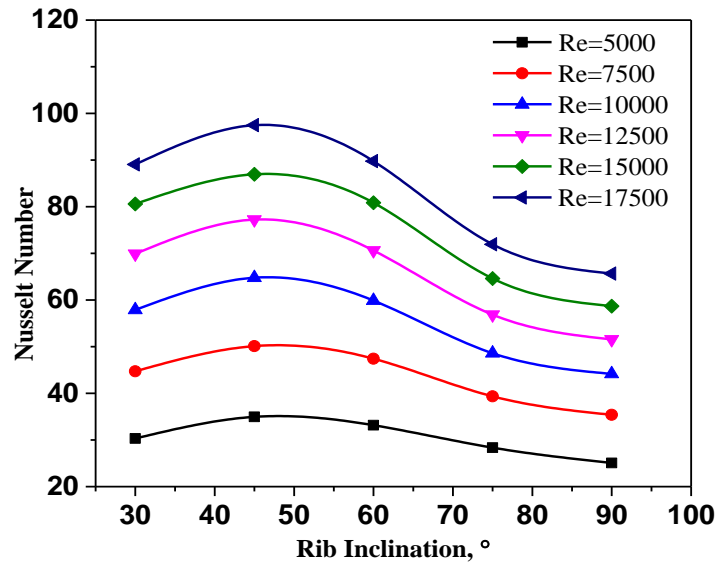
Fig. 5.2 Nusselt number variation with rib inclination for fixed *e/D* and *P/e*.

(a) $\beta = 30°$ (b) $\beta = 45°$

(c) $\beta = 45°$ (d) $\beta = 75°$
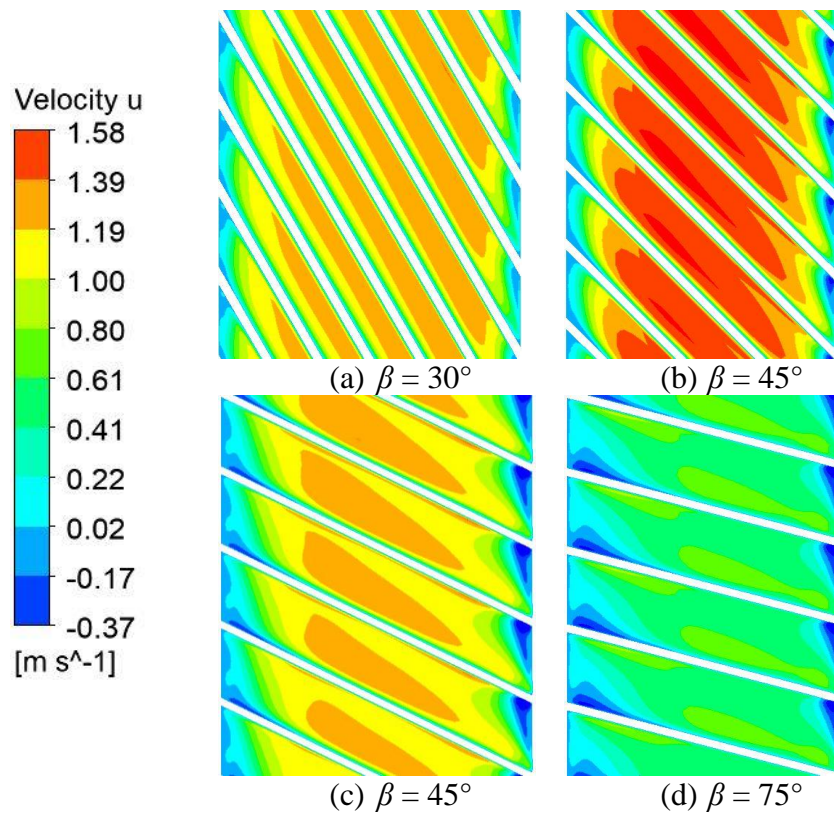
Fig. 5.3 Transverse velocity contour indicating secondary flow strength in the inter-rib regions for *Re* = 10000.
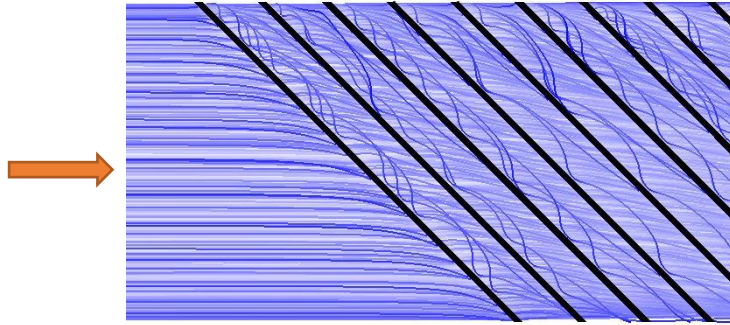
Fig. 5.4 Secondary flow from the leading edge to the trailing edge of the ribs (arrow indicates primary flow direction).
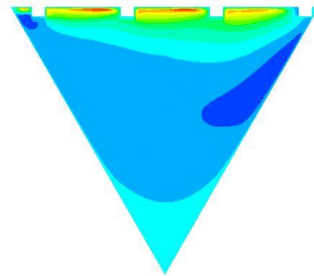
(a) Triangular ribbed duct SAH

(b) Rectangular ribbed duct SAH
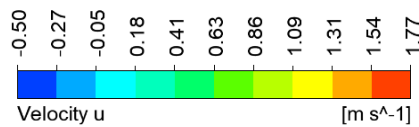
Fig. 5.5 Velocity contour indicating the comparative strength of secondary flow in ribbed triangular and rectangular ducts ($\beta = 45°$) at a cross-section plane ($Z = 0.4$ m) for $Re = 10000$ and similar heat input.

For the range of parameters studied, the range of increase in Nu is obtained as 1.30 to 2.09 compared to smooth SAH, with Nu increasing monotonically with Re. This is because of a reduction in the size of the recirculation zone, usually known as the zone of low heat transfer (Singh and Singh 2018). Besides, as Re increases, turbulent kinetic energy (TKE) rises due to increase in turbulent intensity. The combined effect results in an increase in Nu as the Re increases. Maximum and minimum values of Nu are

recorded for rib inclinations of 45° and 90°, respectively (Fig. 5.2). With the increase in β from 30° to 75°, the heat transfer rate increases up to rib inclination of 45°. It then decreases due to the variation in secondary flow strength, which traverses from the leading edge to the trailing edge of the rib (Fig. 5.3). In addition, the mixing of hot and cold air is facilitated by the secondary flow generated by the inclined rib (Fig. 5.4), thus augmenting the turbulent intensity. For $\beta = 90°$, secondary flow is absent, and instead, fluid particles behind the ribs are stagnant, creating a zone of lower heat transfer.
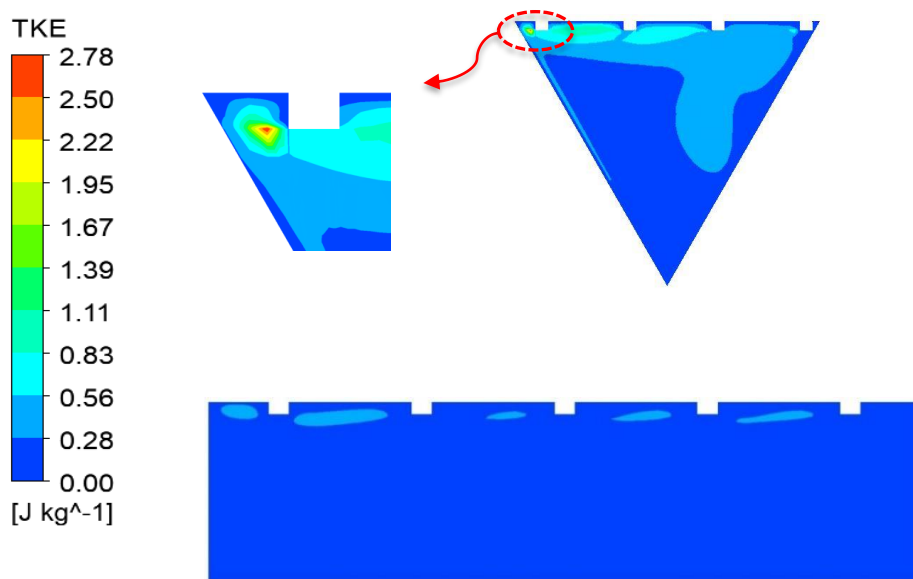
Fig. 5.6 Comparison of Turbulence Kinetic Energy (TKE) contours for triangular and rectangular ribbed duct ($\beta = 45°$) at a cross-section plane ($Z = 0.4$ m) for $Re = 10000$ and similar heat input.

Contours of velocity (Fig. 5.5) specify that the cross-flow strength is relatively higher in the ribbed triangular SAH for similar Re. This facilitates better mixing of hot and cold air carried by the secondary and primary flow streams, respectively in the ribbed triangular duct relative to the ribbed rectangular duct SAH. TKE contours at a cross-section plane ($z = 0.4$) along the length of the absorber plate are displayed in Fig. 5.6. The secondary flow in the triangular duct increases the TKE in the inter-rib regions and the central regions of the duct. For ribbed rectangular duct, TKE generated is of lower magnitude and is only in the vicinity of the ribs. The air temperature adjacent to the absorber plate is higher due to a turbulent boundary layer.

(a)

(b)

Z= 0 m   Z= 0.4 m   Z= 1 m

Air temperature

Z= 0 m

Z= 0.4 m

Z= 1 m
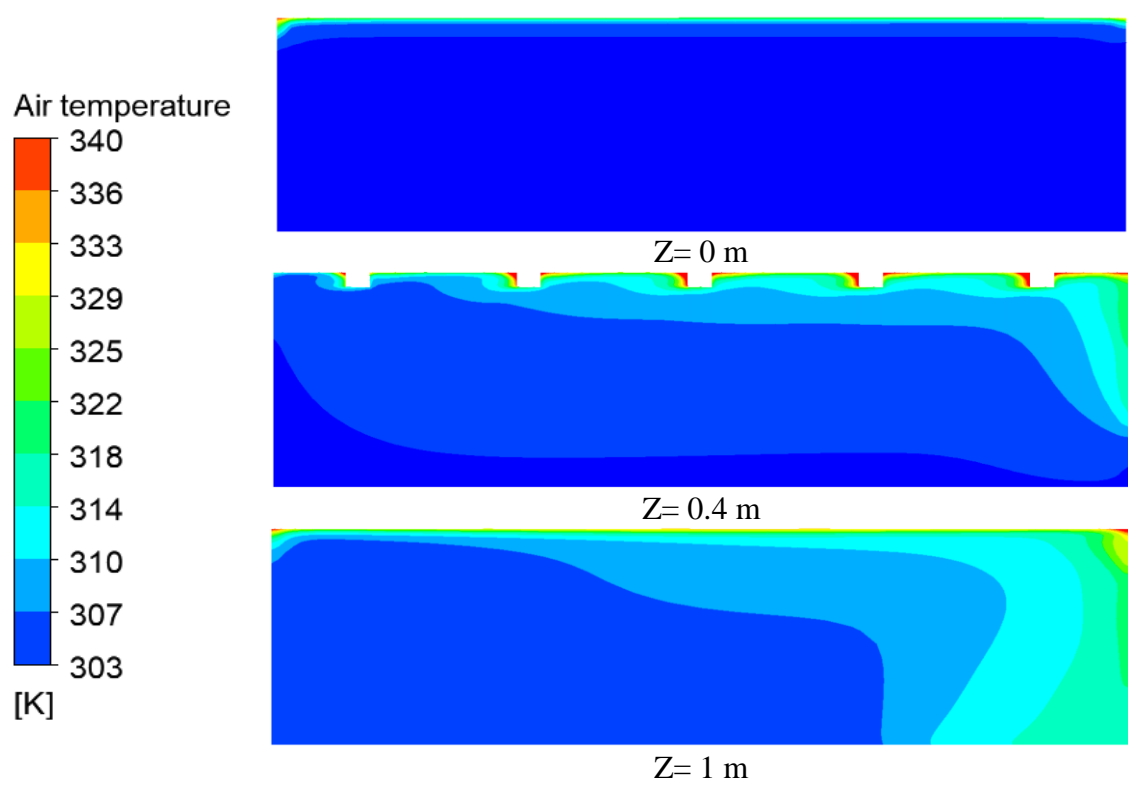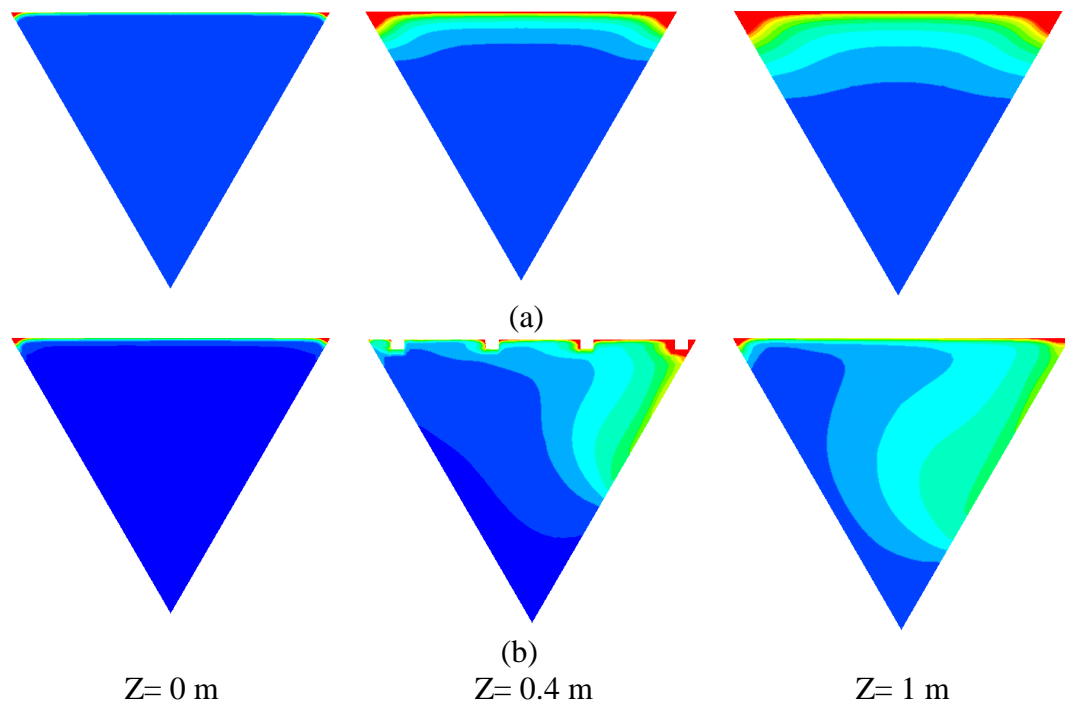
Fig. 5.7 Air temperature variation at different cross-section planes (a) smooth triangular duct, (b) ribbed ($\beta = 45°$) triangular duct, and (c) ribbed ($\beta = 45°$) rectangular duct.

The viscous effects dominate the inertial effects within the stagnant laminar sublayer and impede the heat transfer phenomena (Fig. 5.7 (a)). As the secondary flow moves along the ribs, the air temperature rises, and it merges with the primary stream at the trailing edge of the rib (Fig. 5.7 (b)). In contrast to the ribbed triangular duct ($\beta = 45°$), the cross-flow generated in the ribbed rectangular duct ($\beta = 45°$) is only capable of augmenting the temperature near the trailing edge of the ribs. This limits the rise in temperature near the vertical sidewalls adjacent to the trailing edges of the ribs (Fig. 5.7 (c)).

5.3 Hydraulic performance

For the range of parameters studied, friction factor (*f*) for all rib inclinations decreases as the *Re* increases (Fig. 5.8). It is observed that *f* increases with an increase in α up to 60° and then decreases. Maximum and minimum *f* is obtained for 60° and 30° rib inclinations, respectively. The lower friction factor for $\beta \leq 60°$ is achieved due to higher flow velocity within the rib spaces (Fig. 5.9). For $\beta \geq 60°$, the friction factor is low attributed to the lower strength of secondary flow. There is no significant variation in pressure for a smooth duct at a cross-section. Nevertheless, the integration of ribs significantly changes the pressure distribution. For the triangular duct, the presence of ribs ($\beta = 45°$) alters the pressure distribution only in the proximity of the ribs. In contrast, the presence of ribs ($\beta = 45°$) in a rectangular duct brings about a significant change in pressure variation over a broader flow region (Fig. 5.10).
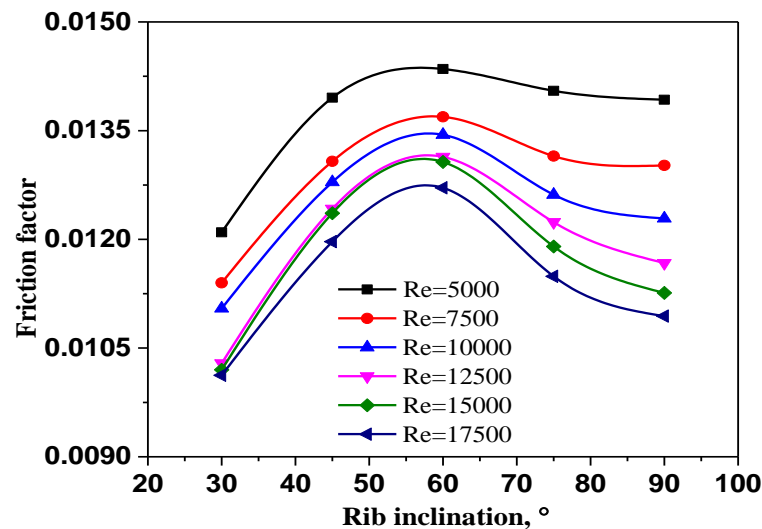
Fig.5.8 Variation of friction factor with different rib inclinations for varying *Re*.
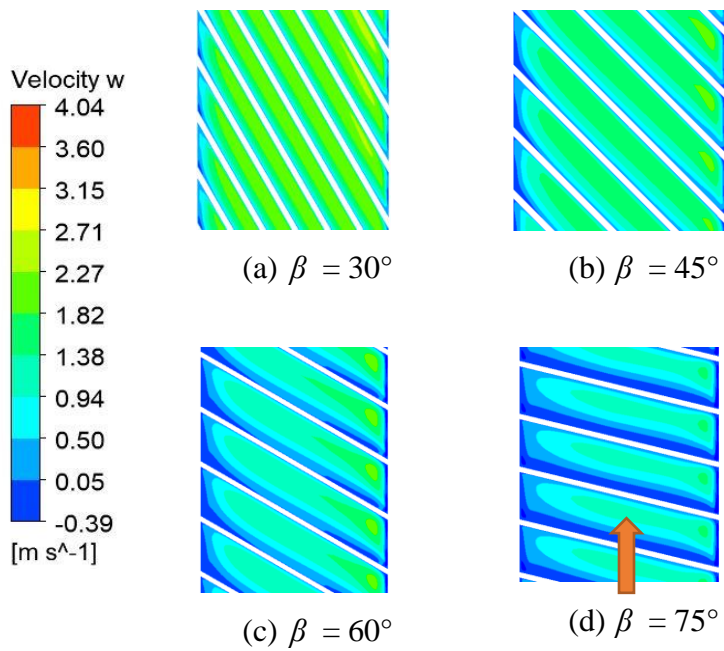
Fig. 5.9 Inter-rib region flow velocity variation in a triangular duct
(arrow indicates the flow direction).
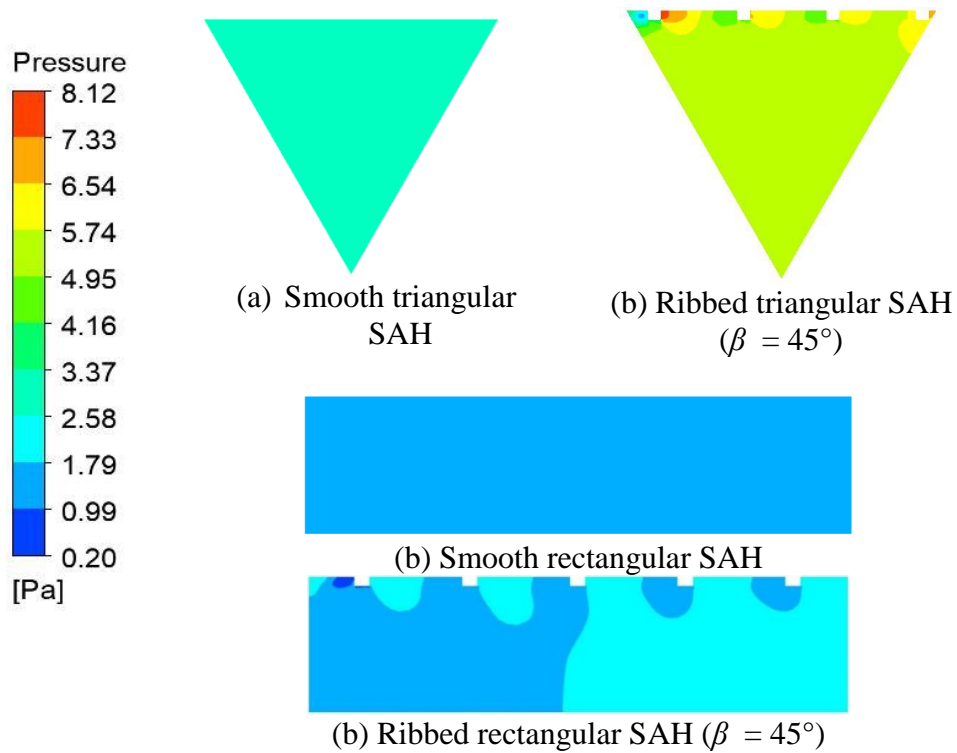
Fig. 5.10 Effect of inclined ribs on the pressure distribution within a triangular and
rectangular duct ($Z = 0.4$ m and $Re = 10000$).

5.4 Thermo-hydraulic performance parameter

Thermo-hydraulic performance parameter (THPP) facilitates the agreement between Nu and f characteristics of the SAH. From Fig. 5.11, it is observed that for a fixed e/D, P/e, and optimum β, a maximum THPP of 1.79 is obtained at $Re = 10000$. The same is compared to the performance of a rectangular duct SAH having a width, depth, and hydraulic diameter of 160 mm, 40 mm, and 64 mm, respectively. The same rib configuration is designed in rectangular duct SAH (conventional SAH), and the performance for similar heat input and Re is compared to the former. Based on the trade-off between heat transfer and pressure drop characteristics, the comparative results indicate that ribbed triangular duct SAH has higher effectiveness at all Re with a maximum enhancement of 17%.
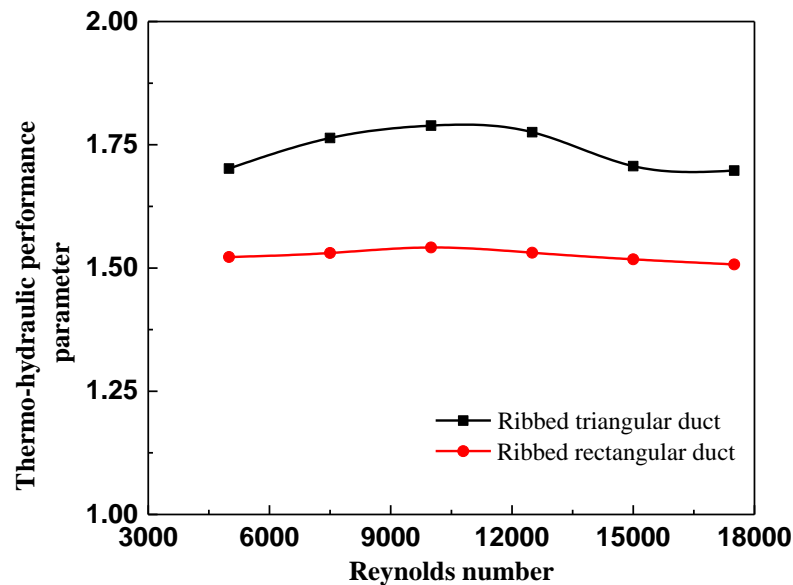
Fig. 5.11. Comparison of thermo-hydraulic performance parameter of the ribbed triangular and rectangular duct ($\beta = 45°$).

The higher performance of the triangular duct SAH when compared to rectangular duct SAH is attributed to the following reasons. In a turbulent flow, air flows from the inside of the duct to the corners (regions of lower shear stress). It contributes to secondary flow near the corner regions. Velocity vector components along x and y-direction describe secondary flow (flow is along the z-direction). Although the secondary flow magnitude is weak compared to the mainstream flow, it causes a significant change in turbulent flow characteristics (Bradshaw 1987). The smaller vortices (encircled) near

the sidewalls of the rectangular duct are eliminated in a triangular duct cross-section, as shown in Fig. 5.12 (a). This helps the cross-flow to move smoothly across the sidewalls in a triangular duct.

(a)

(b)
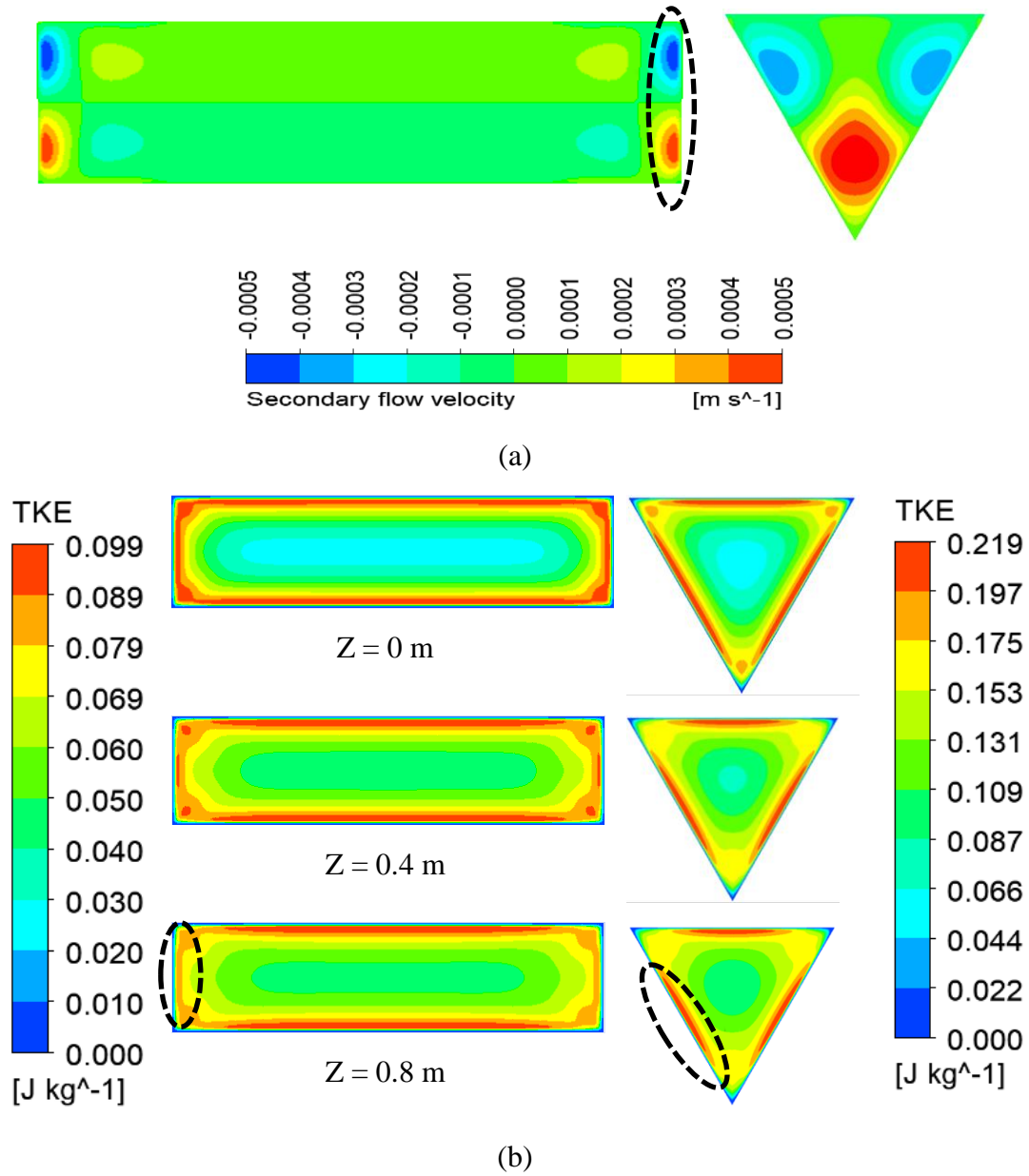
Fig. 5.12 (a) Contours of secondary flow velocity indicating the effect of duct cross-section on the secondary flow development, and b) Turbulent kinetic energy contour indicating for smooth rectangular and triangular duct (*Re* = 10000).

In addition, the secondary flow Vortex formed near the apex of the triangular duct travels inward, and the absence of smaller vortices near the sidewalls increases the turbulent kinetic energy therein, as shown in Fig. 5.12 (b). Hence, the heat transfer rate

in smooth triangular duct SAH is higher than that of smooth rectangular duct SAH. In addition, the turbulent kinetic energy contours indicate that in rectangular duct SAH, the intensity of TKE reduces near the sidewalls along the test section length compared to triangular duct SAH.

Furthermore, a comparison of the temperature difference of the absorber plate temperature and the average fluid temperature is shown in Fig. 5.13. It can be seen that the temperature difference curve in the triangular duct has higher linearity compared to the rectangular duct. The higher the linearity of the temperature distribution curve, the more uniform temperature distribution and higher heat transfer efficiency (Zhang et al. 2020). This indicates a relatively more uniform temperature difference distribution in the triangular duct, which positively affects heat transfer enhancement. The present CFD study results are compared to previous studies with similar rib configurations in triangular and rectangular duct SAH (Table 5.1).
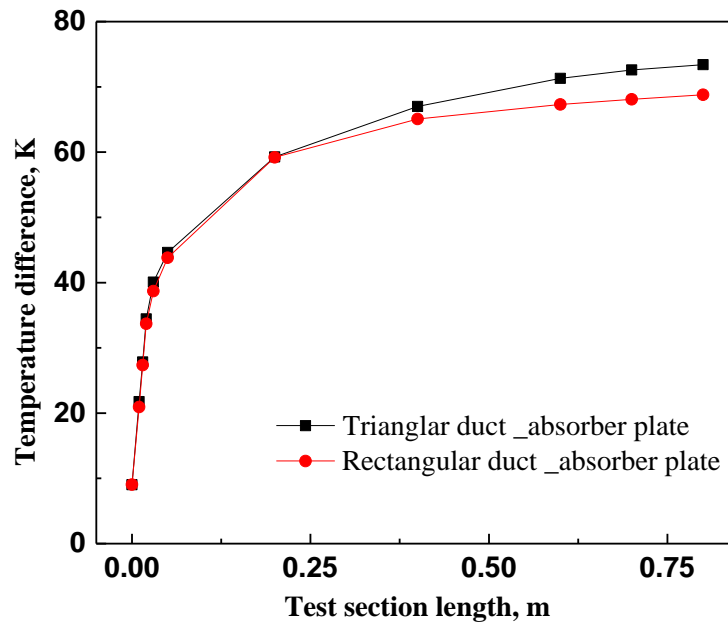
Fig. 5.13. Temperature difference distribution in smooth rectangular and triangular duct at flow $Re = 10000$.

Table 5.1: Comparison of effectiveness parameter for similar artificial roughness in triangular and rectangular duct SAH.

References	Duct cross-section	Rib geometry	Test section length (mm)	THPP
Kumar et al. (2017)		Transverse rectangular rib	300	1.89
Kumar et al. (2018)		Transverse square rib	300	1.44
Jain et al. (2019)	Equilateral Triangular	Inclined discrete square rib	500	1.98
Present study		Inclined square rib	800	**1.77**
Aharwal et al. (2008)	Rectangular	Inclined rib	1200	1.55
Kaewchoothong et al. (2017)		Inclined rib	800	1.34

5.5 Performance of solar dryer

The performance of an indirect type solar dryer (ITSD) is analyzed by integrating triangular duct SAH with the inclined rib configuration providing maximum THPP to study the drying characteristics. With the outlet air temperature delivered by the optimal SAH configuration of both ribbed triangular and rectangular duct SAH, the drying characteristics of food samples are studied. Moisture ratio (*MR*) curves of all the food samples show an exponentially decreasing trend with an increase in drying time (Fig. 5.14)
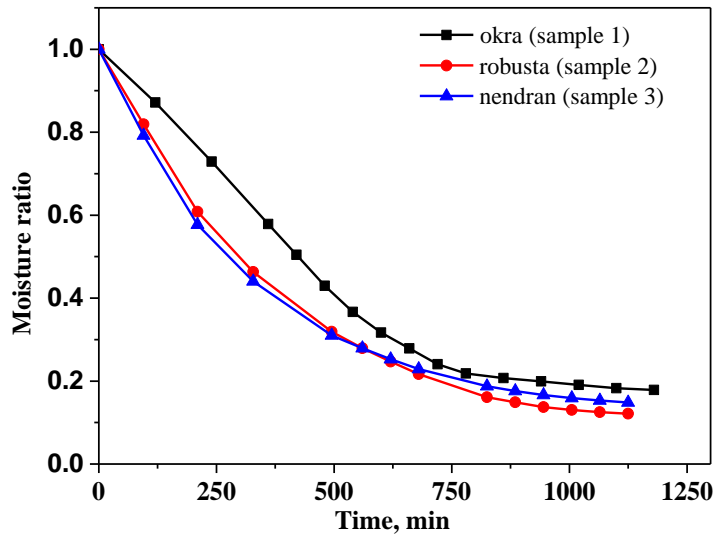
Fig 5.14 Drying rate comparison of ITSD with ribbed rectangular and triangular duct SAH for banana samples.

In the initial drying period (3 to 4 hrs), the slope of the *MR* curve is steep, owing to moisture removal from the surface of the food sample. It is also observed that the slope of *MR* for both banana samples is higher than okra. This is because of the case hardening or formation of a thin layer of gel on the surface of okra samples during the initial 3 to 4 hrs drying time. This layer gets solidified and slows down the rate of moisture removal.

During drying, diffusion occurs due to the passive transport of water particles across a concentration gradient. With a rise in temperature, the mass transfer rate increases owing to the rise in the average kinetic energy of the water. At higher temperatures, less energy is required to remove water molecules as they are loosely bound to the food matrix (Xiong et al. 1992). As moisture removal rate inside the materials is controlled by diffusion of water particles to the outer surface and its subsequent reduction closer to the equilibrium value, moisture diffusivity is also affected by the shrinkage effect during drying. (Senadeera et al. 2000; Mayor and Sereno 2004; Katekawa and Silva 2006).
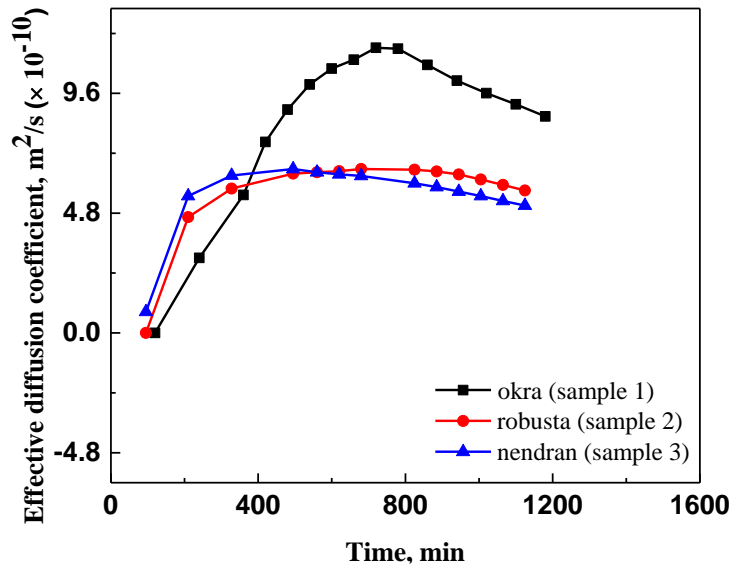
Fig 5.15. Effective diffusion coefficient as a function of drying time

In isothermal drying, the effective diffusivity increases initially and becomes almost invariant with time for the constant drying rate period. This is because diffusion of liquid water might be the predominant mass transfer mechanism during the falling rate period. Drying occurs due to water vapor diffusion from the surface. The average values of the effective diffusion coefficient obtained are 8.316×10^{-10}, 5.65×10^{-10}, and 5.513×10^{-10} for okra, robusta, and nendran. Due to its porous structure, a higher diffusion coefficient value in okra samples is observed (Fig. 5.15).

5.6 Evaluation of the drying model

Regression analysis is carried out to calculate the coefficients involved in the modified page model; plots of ln (t) and ln (-ln (MR)) are drawn for all three samples (Figs. 5.16 (a), (b), and (c). Linear regression analysis yields the slope and y-axis intercept of the best-fit linear curve. Coefficients in the modified page model are obtained using the slope and y-axis intercept. The goodness of fit of the modified page model is verified by calculating R^2 and reduced χ^2. R^2 is obtained as 0.990, 0.998, and 0.997 for okra (sample 1), robusta (sample 2), and nendran (sample 3), respectively. Reduced χ^2 value is obtained as 0.00205, 0.00035, and 0.00050 for samples 1, 2, and 3, respectively.
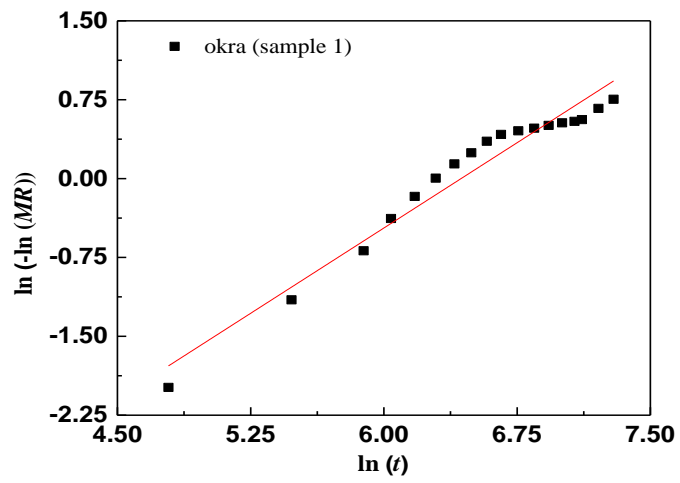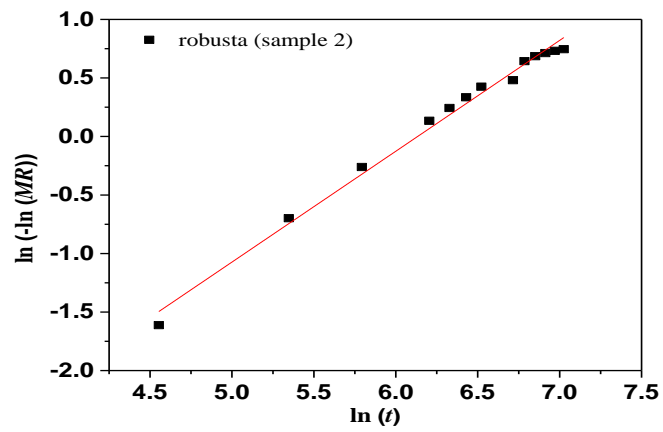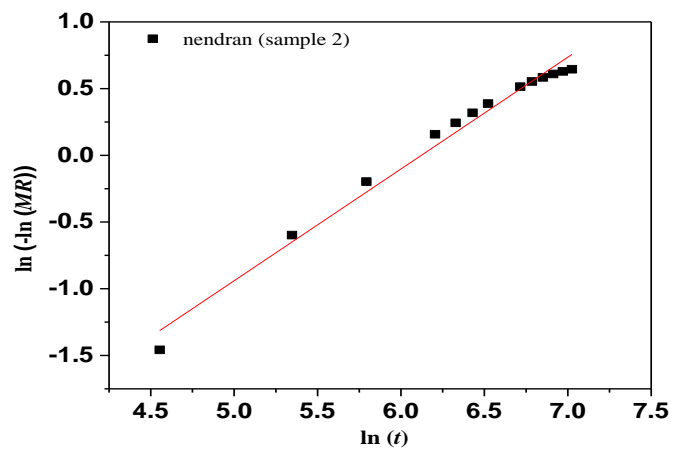
Fig 5.16 Regression analysis plots for (a) okra (sample 1) (b) robusta (sample 2), and

(c) nendran (sample 3)

5.7 Impact of duct cross-section on drying kinetics

To study and quantify the impact of solar air heater duct cross-section on the drying kinetics of the food samples, moisture ratio and effective diffusion coefficient of the two food samples are evaluated for ribbed triangular and ribbed rectangular duct SAH.
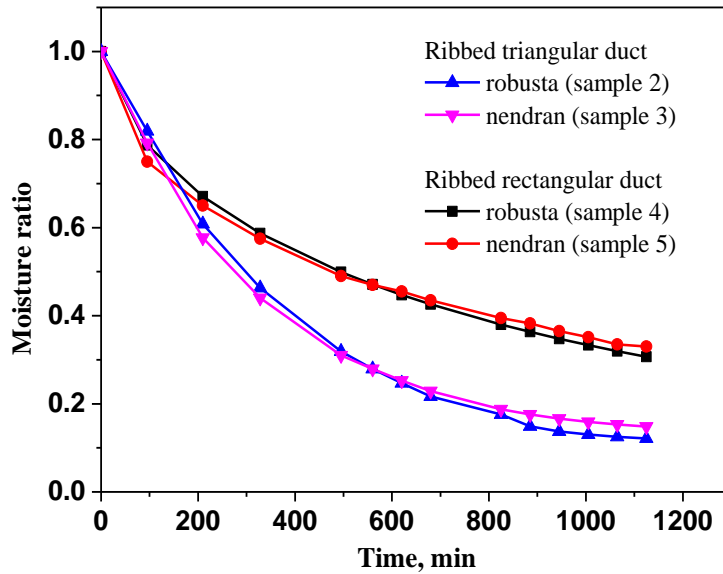
Fig. 5.17 Moisture ratio comparison of ITSD with ribbed rectangular and triangular duct SAH.
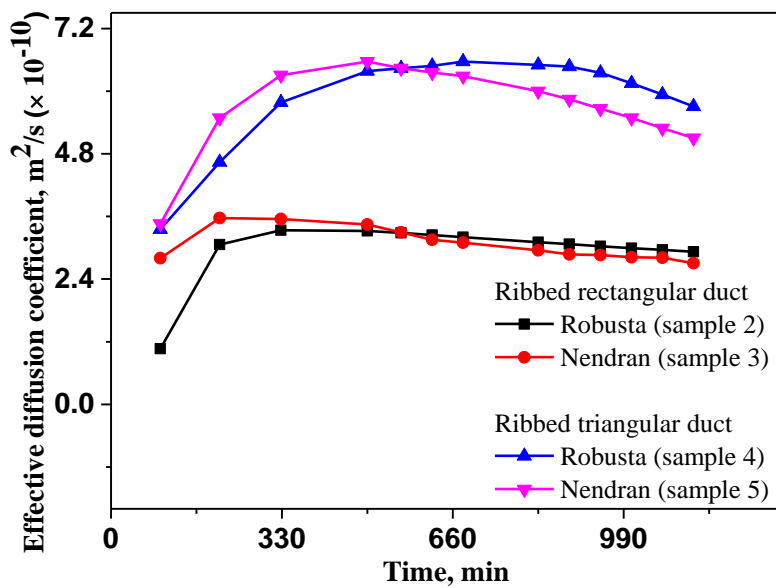
Fig. 5.18 Effective diffusion coefficient comparison of ITSD with ribbed rectangular and triangular duct SAH.

Compared to the ribbed rectangular duct, ribbed triangular duct SAH exhibits 60.4% and 55% reduction in moisture ratio for food samples robusta and nendran, respectively, for the same drying time (Fig. 5.17). With ribbed triangular duct SAH, an increase of 97.9% and 93.3% in average effective diffusion coefficient is observed for food samples robusta and nendran, respectively, relative to that of ribbed rectangular duct SAH operated ITSD (Fig. 5.18).

5.8 Summary

A triangular duct solar air heater (SAH) with inclined ribs is designed and computationally studied for an indirect type solar dryer (ITSD). With the hot air supplied by the ribbed triangular duct solar air heater (SAH), drying characteristics of okra and two variants of banana are studied experimentally and the salient conclusions obtained are:

- For similar heat input and flow Re, inclined ribs enhance the overall performance of a triangular duct SAH by 17% relative to rectangular duct SAH with a maximum value of 1.79 obtained for $\beta = 45°$ at flow $Re = 10000$. This is attributed to the secondary flow generated by the inclined ribs.

- Compared to the dryer with ribbed rectangular duct, ribbed triangular duct SAH exhibits 60.4% and 55% reduction in moisture ratio for food samples robusta and nendran, respectively, for the same drying time.

- Compared to the dryer with ribbed rectangular duct, ribbed triangular duct SAH exhibits a 97.9% and 93.3% increase in average values of the diffusivity coefficient of robusta and nendran, respectively.

- For the results obtained from the drying of food samples, the modified Page model adequately describes the thin layer drying behavior of all the food samples with an R^2 value in the range of 0.990 to 0.998.

- For similar heat input and flow Re, triangular duct SAH with inclined ribs displays a higher performance relative to similar rib configuration in rectangular SAH, evidently making it a better choice for ITSD applications. This design can be incorporated into the existing ITSD with minimal modifications and without additional energy requirements.

CHAPTER 6

STUDY OF A SOLAR AIR HEATER WITH SEMI-CYLINDRICAL SIDEWALLS AND W-BAFFLES

6.1 Introduction

As the ducts with semi-cylinder sidewalls enhance the secondary flow (Vidal et al. 2017; Vidal et al. 2018), a solar air heater (SAH) with semi-cylindrical sidewalls and W-baffles is analyzed for energy and exergy efficiency in the turbulent flow regime. Computational fluid dynamics (CFD) analysis is carried out for a fixed baffle inclination ($\beta = 45°$). Relative baffle height ($R_H = e/D$) and relative baffle pitch ($R_P = P/D$) are varied in the range of 0.046 to 0.115 and 0.46 to 1.15, respectively. The numerical methodology is substantiated for Reynolds number ($5000 \leq Re \leq 17500$) using experimental results and theoretical correlations obtained from the literature. The computational domain SAH with semi-cylindrical sidewalls and W-baffles has been discussed in *section 3.1*. The multi-block meshing technique discretizes the SAH domain into non-uniform hexahedral cells (*section 3.2*). The CFD results are validated with theoretical correlations and experimental studies available in the literature (*section 3.8*).

The findings from the computational simulations are detailed using flow pattern visualization and contours of velocity, pressure, etc., to demonstrate the improved thermal and hydraulic performance of a SAH with semi-cylindrical sidewalls and W-baffles. Suitable correlations are developed for Nusselt number (*Nu*) and friction factor (*f*) with the data obtained. To identify the exergy losses, exergetic performance analysis is carried out, and exergetic efficiency is evaluated. Finally, the present design is compared with ribbed rectangular duct SAH to confirm the superior performance of the former.

6.2 Advantage of semi-cylindrical sidewalls in a SAH duct

Superior performance in heat transfer and friction factor characteristics is obtained for a SAH with semi-cylindrical sidewalls compared to a duct with vertical sidewalls. As shown in Fig. 6.1, Nu is marginally high for the entire Re range in duct with semi-

cylindrical sidewalls. However, a 15% reduction in *f* significantly improves thermo-hydraulic performance.
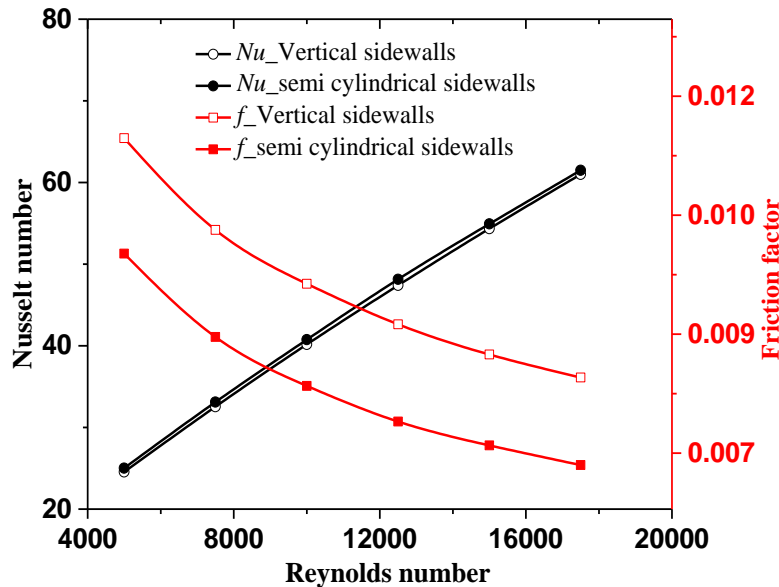
Fig. 6.1 Impact of sidewall geometry on the thermo-hydraulic performance of SAH.

6.3 Thermal performance

In a turbulent flow, air flows from the inside of the duct to the corners (regions of lower shear stress). It contributes to secondary flow near the corner regions. Velocity vector components along y and z-direction describe secondary flow (primary flow is along x-direction). Although the secondary flow magnitude is weak compared to the mainstream flow, it causes a significant change in turbulent flow characteristics (Bradshaw et al. 1987). The rounding off the duct corners removes the smaller vortices near the corners, as shown in Fig. 6.2. This helps the cross-flow to move smoothly across the sharp corners. The secondary flow vortices travel inward, increasing the turbulent kinetic energy near the semi-cylindrical sidewalls, as shown in Fig. 6.3. Hence, the heat transfer rate in SAH with semi-cylindrical sidewalls is higher than that of SAH with vertical sidewalls. As the SAH with semi-cylindrical sidewalls exhibits superior thermal characteristics, W-baffle is placed beneath the absorber plate to augment the heat transfer further. The heat transfer characteristics of a SAH with semi-cylindrical sidewalls and W-baffles is explored for varying relative baffle height (R_H) and relative baffle pitch (R_P).
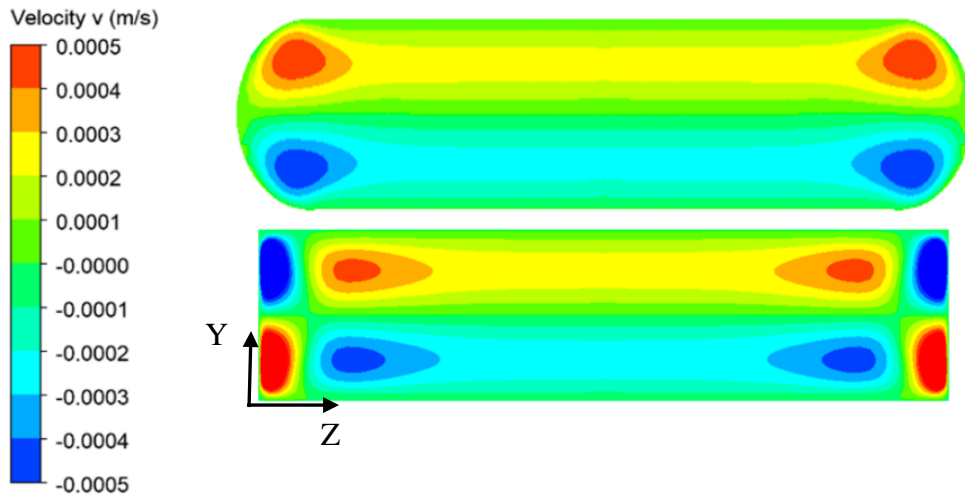
Fig. 6.2 Contours of transverse velocity (*v*) indicating the effect of sidewall shape on the secondary flow development at *Re* = 5000 (primary flow is along x-direction).
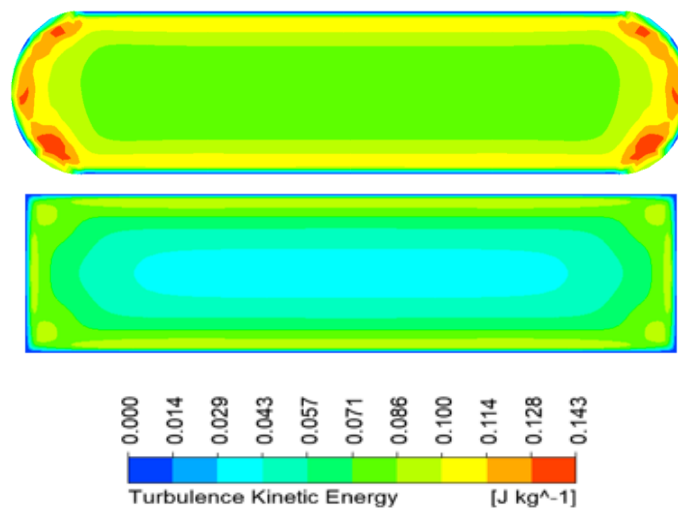
Fig. 6.3 Contours of turbulence kinetic energy for a duct with vertical and semi-cylindrical sidewalls at *Re* = 5000.

The length of the recirculation zone behind the baffle decreases as *Re* increases, as shown in Fig. 6.4. The recirculation area behind the baffle represents a zone of lower heat transfer. Further, the heat transfer rate increases due to reduced recirculation zone length. In addition, the heat transfer rate increases with an increase in the number of reattachment points, as reattachment points represent localized points of maximum heat transfer, in accordant with the observations reported by Singh et al. (2018).
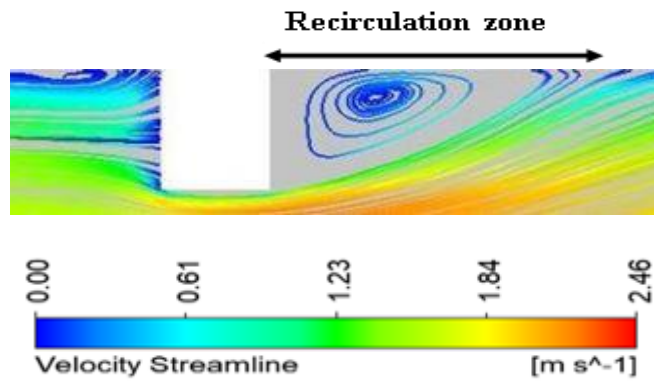
(a) *Re* = 5000
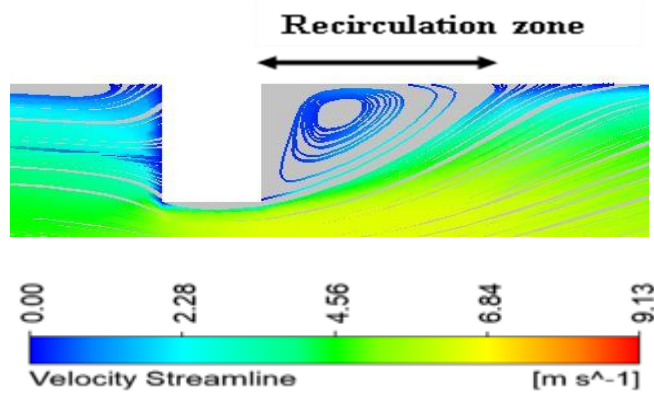
(b) *Re* = 17500

Fig. 6.4 Surface streamlines on a plane perpendicular to the absorber at the baffle tip (a) *Re* = 5000 and (b) *Re* = 17500.

Leading edges at which secondary flow originates
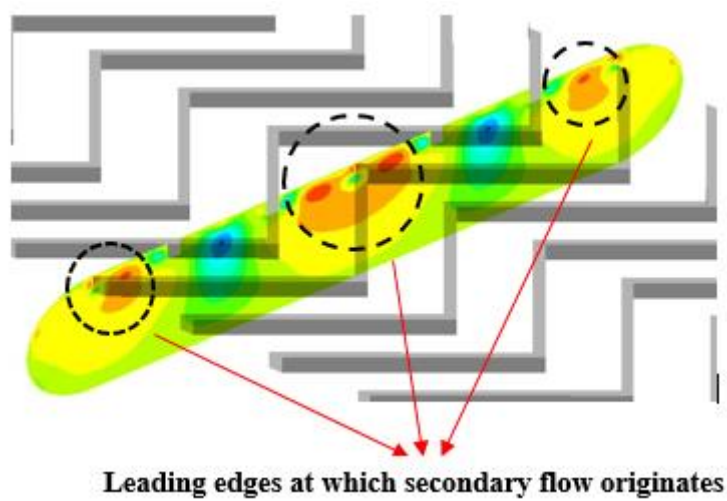
Fig. 6.5 Transverse velocity contour indicating the points at which secondary flow originates.

Turbulent kinetic energy increases with velocity due to the rise in turbulent intensity. Hence, due to the combined effect of reduction in recirculation zone length and increased turbulent kinetic energy, Nu increases with Re. There are three leading points where the secondary flow originates for a W-baffle, as shown in Fig. 6.5.

(a)

(b)   (c)
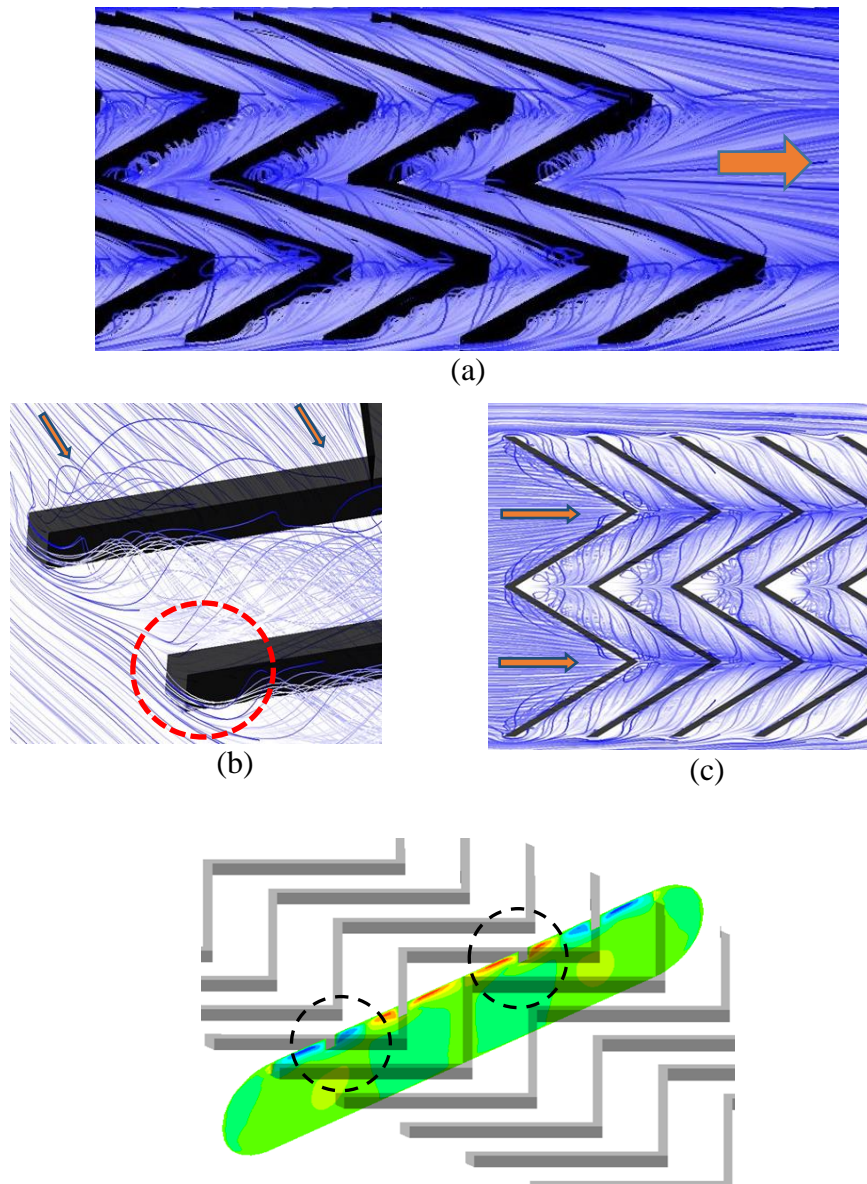
Fig. 6.6 (a) Streamlines indicating the secondary flow (arrow indicates the flow direction). (b) Magnified view of the leading edge near the semi-cylindrical sidewalls. (c) Merging of the secondary flow within the inter-baffle regions (Top-view). (d) Four pairs of counter-rotating secondary flow.

When the vertical sidewalls are replaced with semi-cylindrical sidewalls, the air rushes along the sides into the inter-baffle region, further strengthening the secondary flow (Figs. 6.6 (a) and (b)). The secondary flows merge at the trailing edges of the baffle, as shown in Fig. 6.6 (c), creating a zone of high turbulence. This promotes the mixing of hot and cold air carried by the secondary and primary flow.
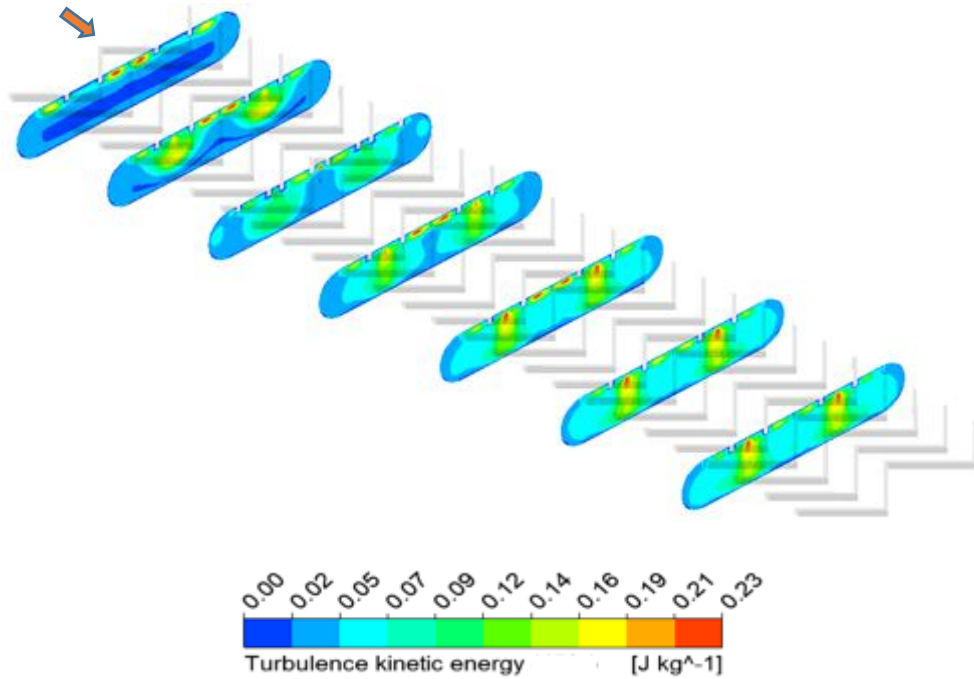
Fig. 6.7 Contours of turbulence kinetic energy at multiple cross-sections along the length of the duct at $Re = 5000$ (arrow indicates the flow direction).
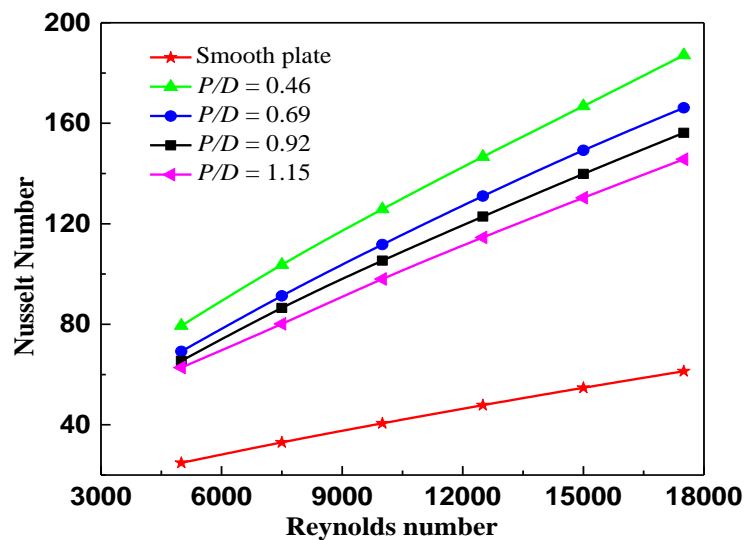
Fig. 6.8 Nusselt number variation with relative baffle pitch (R_P) for fixed R_H.

Four pairs of counter-rotating secondary flows (a pair along each limb of the baffle) are developed due to W-baffle, as shown in Fig. 6.6 (d). Fig. 6.7 shows the variation of turbulence kinetic energy along the flow direction. The turbulence initiated through the W-baffles increases and spreads to the entire channel as the flow proceeds to the outlet. For the parametric range of study, maximum heat transfer is achieved for $R_p = 0.463$, as shown in Fig. 6.8. With an increase in R_p, the length of the inter-baffle region increases, leading to an increase in the length of the boundary layer flow after reattachment. Besides, as R_p increases, the number of reattachment points for the same length of the absorber plate decreases. As R_h increases, the blockage effect created by the baffle increases. Hence with incremental values of R_h, Nu also increases, as depicted in Fig. 6.9.
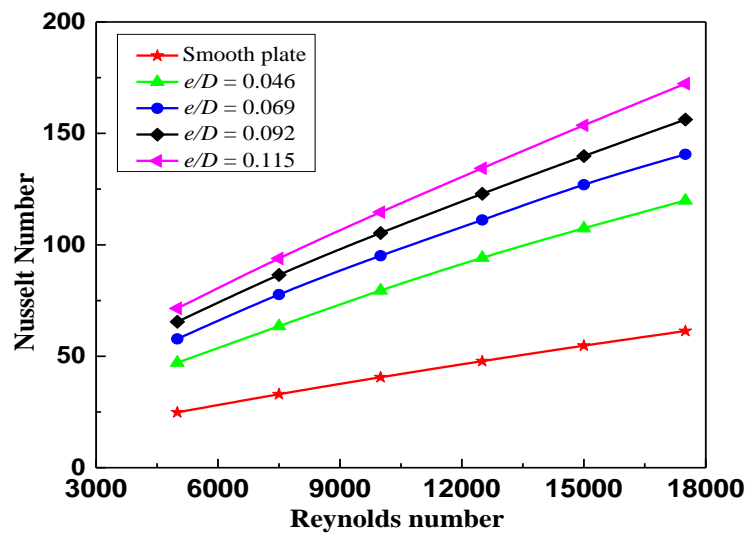
Fig. 6.9 Nusselt number variation with relative baffle height for fixed R_P.

6.4 Hydraulic performance

Baffles in a SAH duct impede the flow and cause an additional pressure drop than smooth SAH. This pressure drop represents an enhancement in the friction factor. Fig. 6.10 shows the influence of Re on f for varying R_H. It is observed that as R_h increases, f increases. This is obvious because a higher relative baffle height increases the blockage and thus the flow resistance. The vertical sidewalls create stagnant regions near the corners, absent in duct with semi-cylindrical sidewalls. Increasing the relative baffle height (e) makes the flow decelerate more near the absorber plate, which results in higher static pressure, as shown in Fig. 6.11. This may also be due to fluid diffusing in

a broader region near the baffle. The effect of baffle pitch on *f* is depicted in Fig. 6.12. As R_P increases, the number of baffles reduces, causing a reduction in the pressure drop.
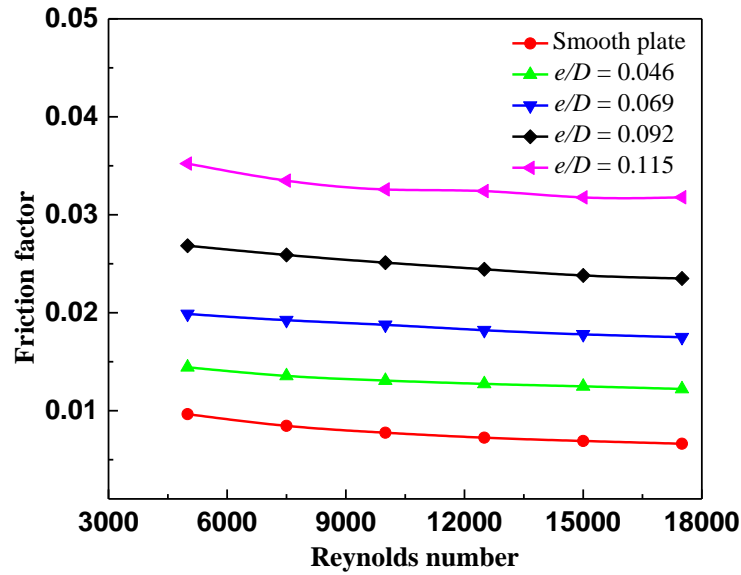
Fig. 6.10 Friction factor variation with relative baffle height for fixed R_P.

(a) *e/D* = 0.046

(b) *e/D* = 0.069

(c) *e/D* = 0.092

(d) *e/D* = 0.115
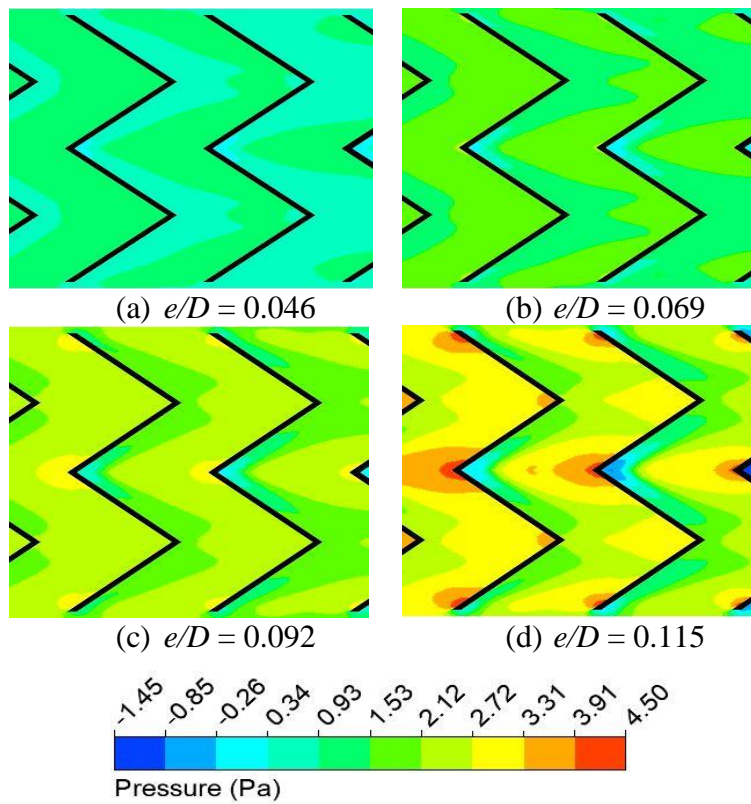
Pressure (Pa)

Fig. 6.11 Static pressure contours in the inter-baffle region at various planes.
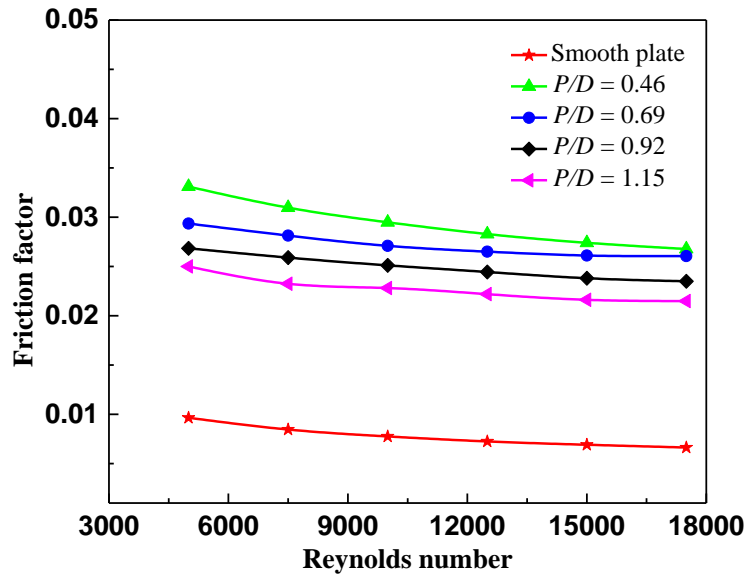
Fig. 6.12 Friction factor variation with relative baffle pitch for fixed R_H.

6.5 Thermo-hydraulic performance parameter

Thermo-hydraulic performance parameter (THPP) facilitates the agreement between *Nu* and *f* characteristics of the SAH. From Fig. 6.13, it is observed that THPP increases with an increase in RH up to 0.092 and further decreases for a fixed RP. Upon varying R_P, for R_H = 0.092, higher THPP is obtained at R_P = 0.092.
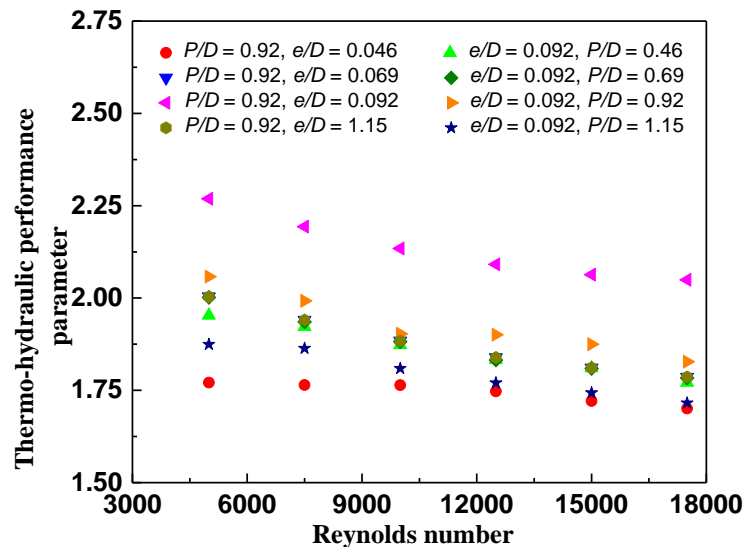
Fig. 6.13 Thermo-hydraulic performance parameter variation with Reynolds number.

For the entire parametric range of study, maximum THPP is attained as 2.27 for $R_H = 0.092$ and $R_P = 0.92$ at $Re = 5000$. Table 6.1 lists out various similar roughness shapes and their corresponding THPP.

Table 6.1: Comparison of effectiveness parameter of similar artificial roughness

Sl. No.	References	Duct shape	Roughness Geometry	THPP
1	Kumar et al. (2009)	Rectangle	Discrete W-up rib	1.54
2	Lanjewar et al. (2011a)	Rectangle	W-down rib	1.98
3	Lanjewar et al. (2011b)	Rectangle	W-up rib	1.81
4	Tamna et al. (2014)	Rectangle	V-baffle	1.83
5	*Present CFD study*	*semi-cylindrical sidewalls*	*W- baffle*	*2.27*

6.6 Correlation for Nusselt number and friction factor

Estimation of the thermo-hydraulic performance of a SAH requires the magnitude of *Nu* and *f*. The magnitude is obtained from the empirical correlations developed for the specific SAH based on in-depth analysis. For the CFD data obtained, suitable expressions correlating *Nu* and *f* with other parameters used in the study, namely R_h, R_p, and *Re* are developed employing the regression analysis. Initially, the characteristics curves are drawn to figure out the nature of variation of *Nu* and *f* with *Re*, *e/D*, and *P/D* (Fig. 6.14). The nature of the characteristic curve obtained for ln (*Nu*) and ln (*Re*) is a straight line. The slope of the line is computed employing linear regression. The Y-intercept of the curve is found to vary with *e/D* and *P/D*. The slope of the curve is found out to be 0.7, which gives the degree of *Re* in the correlations. The relationship between ln ($Nu / Re^{0.7}$) and ln (*P/D*) is drawn to determine the power of *P/D* in the correlation. Similarly, the graph between ln ($Nu / (Re^{0.7} \times (P/D)^{-0.26})$) and ln (*e/D*) is drawn to determine the power of *e/D* in the correlation.
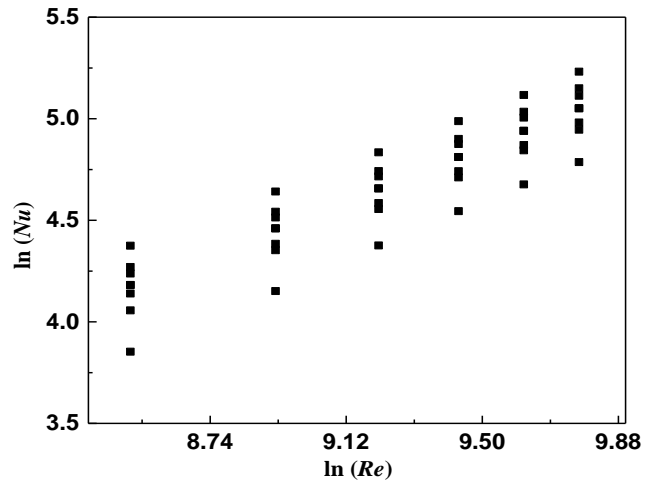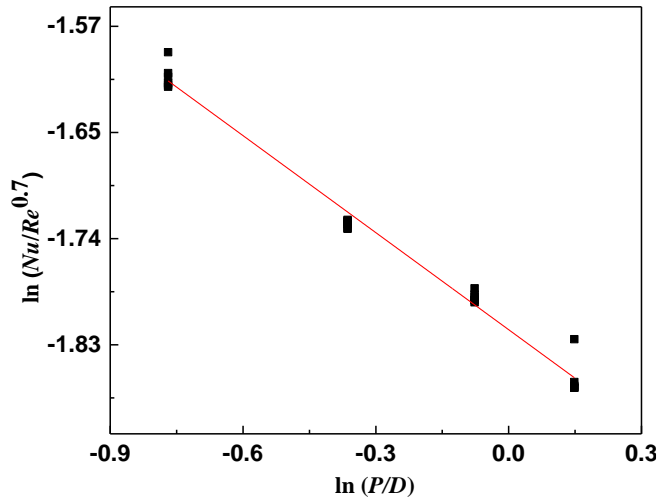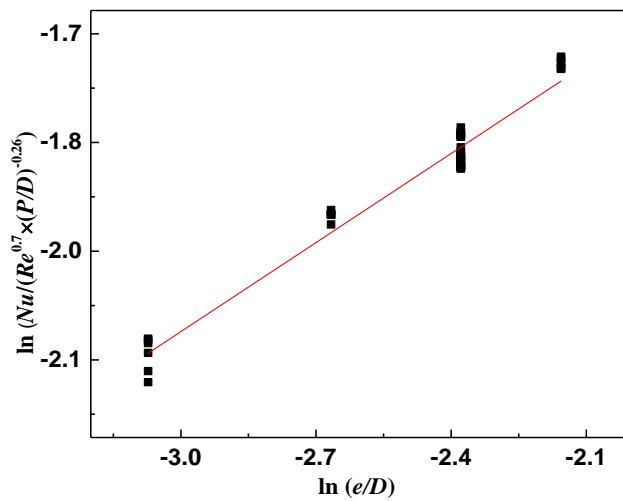
Fig. 6.14 Development of correlation (a) ln (*Nu*) vs ln (*Re*), (b) ln(*Nu*/*Re*$^{0.7}$) vs relative baffle pitch, and (c) ln *Nu*/(*Re*$^{0.7}$×(*P/D*)$^{-0.26}$) vs relative baffle height
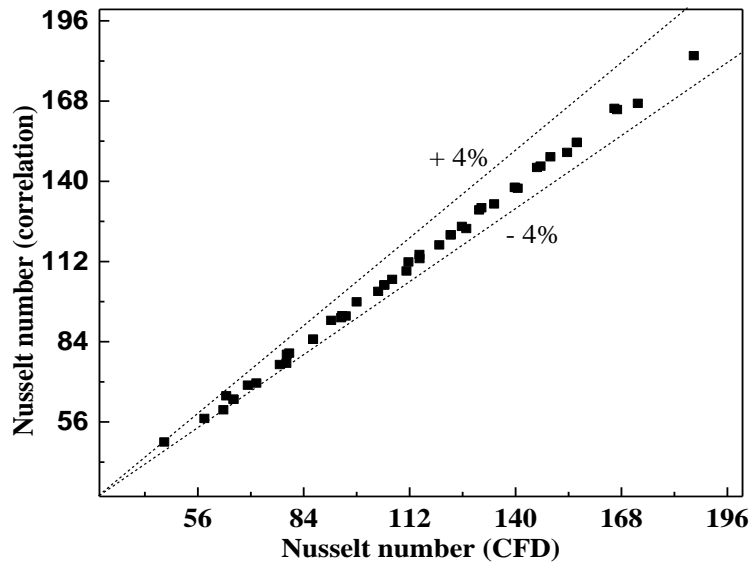
Fig. 6.15 Parity plot for Nusselt number.
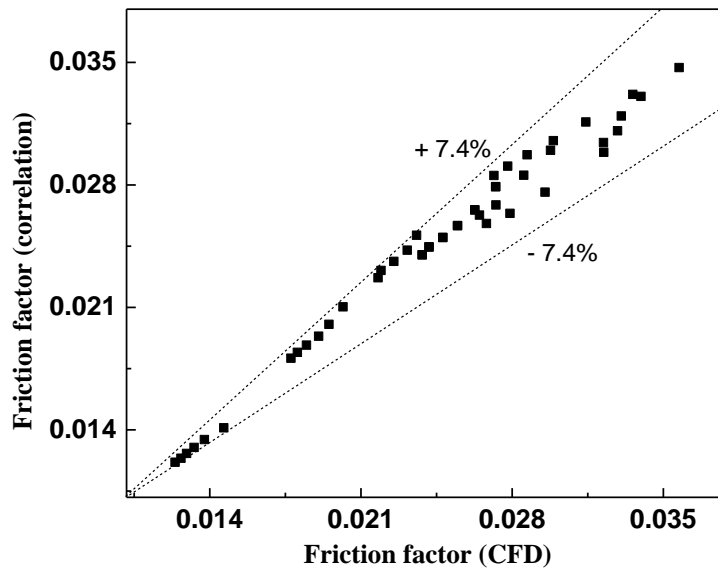
Fig. 6.16 Parity plot for friction factor.

As shown in Fig. 6.14 (a), the graph follows a linear trend. The correlation is thus formed using linear regression analysis. A similar procedure is employed to generate the friction factor correlation. The following comparisons indicate *Nu* and *f* dependence on *Re*, *P/D*, and *e/D* for the range of parameters investigated.

$$Nu = 0.4(Re)^{0.7} \left(\frac{P}{D}\right)^{-0.26} \left(\frac{e}{D}\right)^{0.382} \tag{6.1}$$

118

$$f = 0.773(Re)^{-0.12} \left(\frac{P}{D}\right)^{-0.25} \left(\frac{e}{D}\right)^{0.981} \tag{6.2}$$

Valid for

$5000 \leq Re \leq 17500$

$0.046 \leq e/D \leq 0.115$

$0.46 \leq P/D \leq 1.15$

The determination coefficient (R^2) for Nu and f correlation curves are obtained as 0.99 and 0.97, respectively. The deviation in Nu and f obtained from the correlation with that of the corresponding CFD values are 4% (Fig. 6.15) and 7.4% (Fig. 6.16), respectively.

6.7 Exergetic performance

In this section, exergetic performance of W-baffle ($R_H = 0.092$ and $R_P = 0.92$) SAH with semi-cylindrical sidewalls is analyzed and compared to smooth SAH. The temperature of the absorber plate plays a crucial role in the exergy analysis of SAH. With an increase in Re, the temperature of the absorber plate (T_p) decreases (Fig. 6.17). This is attributed to higher turbulence at higher flow velocities, leading to the mixing of hot and cold air lowering the T_p. It is noteworthy that T_p of SAH with W-baffles and semi-cylindrical sidewalls is significantly lower than the conventional SAH owing to the mixing created by additional turbulence and increased secondary flow due to the semi-cylindrical sidewalls. The impact of T_p on various exergy losses, thermal efficiency, and exergetic efficiency of the SAH is studied in detail. Exergy loss due to optical losses (L_{opt}) accounts for the radiation reflected and does not vary with the Re (Fig. 6.18), roughly 20% of the exergy input. Major exergy destruction (L_{abs}) in a SAH is due to the losses occurring during the absorption of solar insolation (Bliss and Raymond 1959; Ge et al. 2014). This is attributed to the significant temperature difference between the absorber plate and the sun. With an increase in Re, the heat transfer rate increases, causing a drop in the plate temperature, subsequently increasing the L_{abs} (Fig. 6.19). At lower Re, absorber plate temperature is higher, reducing the L_{abs}. With the addition of baffles, T_P reduces, and L_{abs} increases upon comparison to smooth SAH. However, this increment (12.9%) is considerably lower than the reduction in L_{env} and L_{ht} of 240% and 24%, respectively, as discussed below.
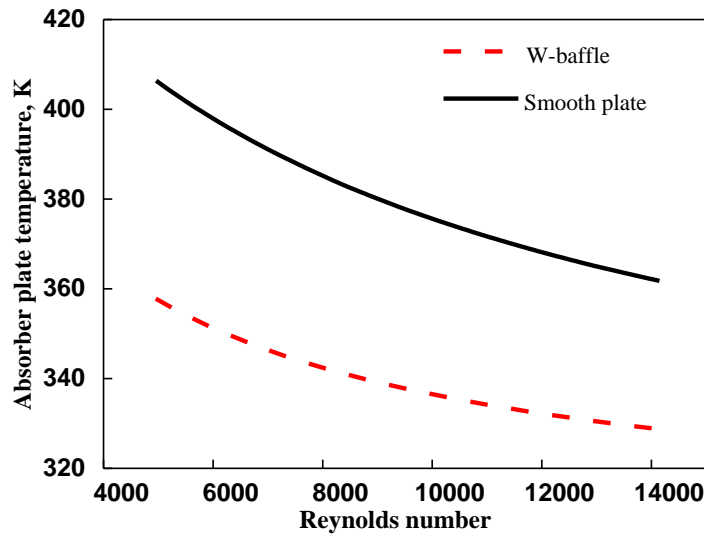
Fig. 6.17 Impact of W-baffle and semi-cylindrical sidewalls ($R_H = 0.092$ and $R_P = 0.92$) on absorber plate temperature.
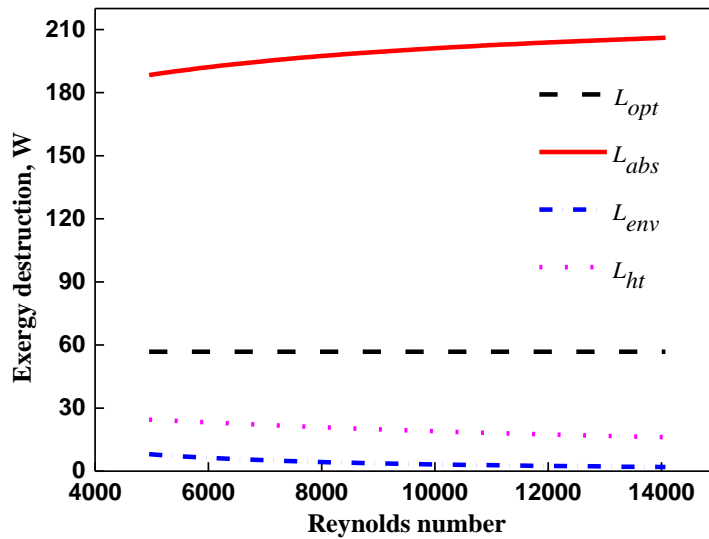
Fig. 6.18 Various exergy losses for SAH with W-baffle and semi-cylindrical sidewalls ($R_H = 0.092$ and $R_P = 0.92$).

Exergy destruction due to heat leakage (L_{env}) from the SAH to the ambient air is higher at lower Re (Fig. 6.20). This is attributed to a lower heat loss coefficient for SAH with W-baffles and semi-cylindrical sidewalls. As the baffle increases the heat transfer area and creates additional turbulence, aided by the additional secondary flow generated by the semi-cylindrical sidewalls, the heat transfer rate is augmented considerably, leading to a drop in plate temperature. Thus lower temperature difference between the plate and

ambient air reduces the heat loss to the environment. L_{env} drops with Re and at higher Re follows an asymptotic trend. Owing to lower $T_{P,}$ a reduction of 240% is obtained in L_{env} compared to smooth SAH.
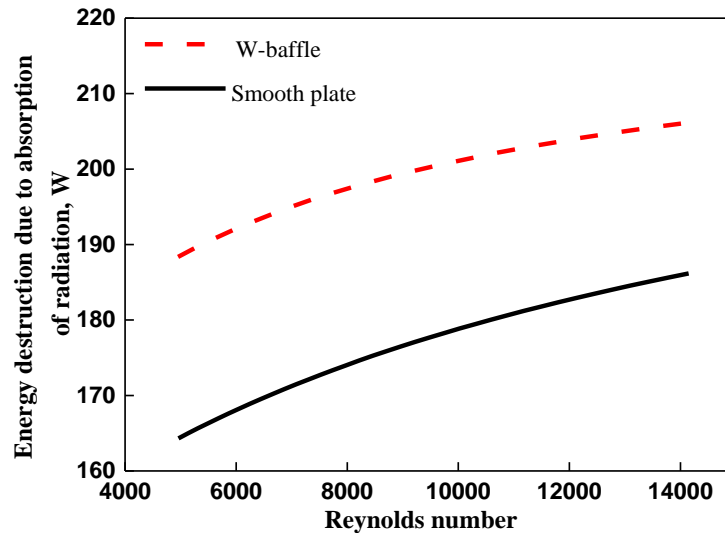
Fig. 6.19 variation of exergy destruction due to absorption for SAH with W-baffle and semi-cylindrical sidewalls ($R_H = 0.092$ and $R_P = 0.92$).

Exergy loss due to heat transfer (L_{ht}), and flow friction arises due to the internal irreversibility within the SAH. The temperature distribution over the heated absorber plate is non-uniform, and the heat transfer between plate and air occurring under the finite temperature difference creates exergy loss (L_{ht}). With an increase in Re, L_{ht} decreases on account of a higher heat transfer rate, and a similar trend is also displayed by $L_{env.}$ With W-baffles, a reduction of 24% is obtained in L_{ht} at lower $Re = 5000$ (Fig. 6.21). L_{ht} is more pronounced than exergy loss due to flow friction (Xiao et al. 2019). Exergy destruction due to pressure drop is noticeable only at higher Re (Singh et al. 2012). Besides, the impact of pressure drop on the SAH's overall performance is discussed in detail in the energy analysis, hence not presented here. Due to heat transfer at finite temperature differences, these irreversibilities increase the entropy generation within the SAH. With W-baffles and semi-cylindrical sidewalls, SAH has lower entropy generation than conventional SAH (Fig. 6.22). Exergetic efficiency (η_{ex}), a measure of exergetic gain, reduces with Re due to an increase in L_{abs} and entropy generation (Fig. 6.23). However, the increase in heat transfer coefficient reduces T_p, which in turn reduces the thermal losses while augmenting the thermal efficiency (η_{th}).

W-baffle and semi-cylindrical sidewalls enhance the η_{ex} and η_{th} of the SAH by 95.4% and 40.7%, respectively, compared to conventional SAH. Due to lower exergy losses, 1.95 times higher exergy gain results in higher η_{ex} at $Re = 5000$ than conventional SAH for similar exergy input.
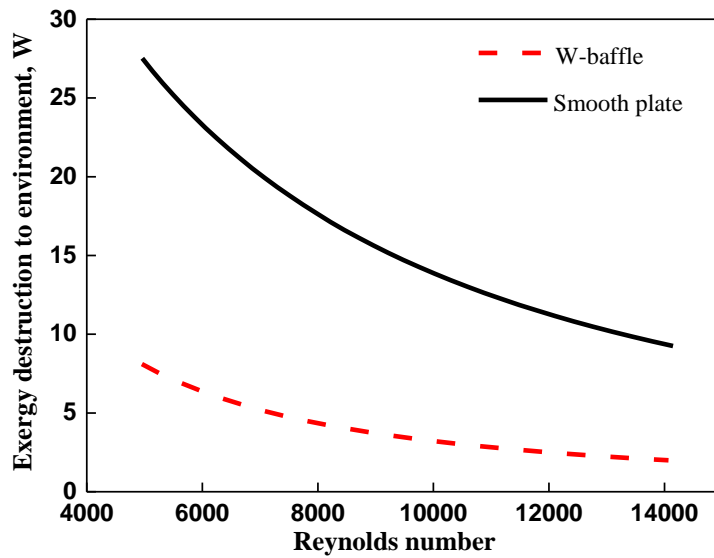
Fig. 6.20 variation of exergy destruction due to heat leakage to the environment for SAH with W-baffle and semi-cylindrical sidewalls ($R_H = 0.092$ and $R_P = 0.92$).
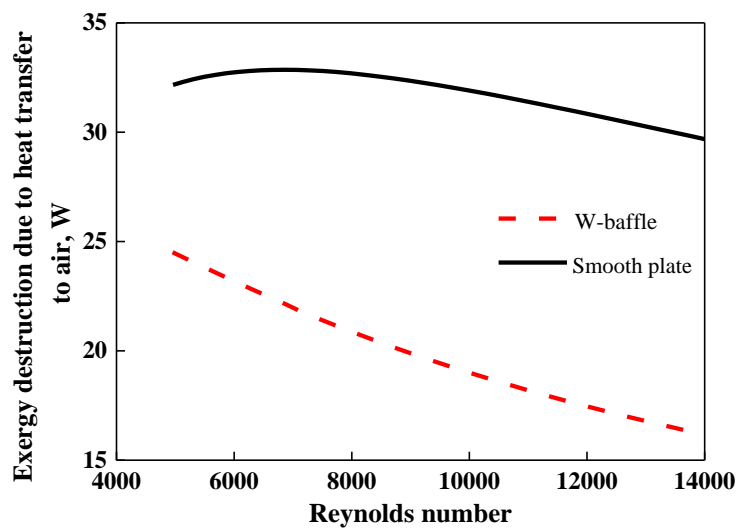
Fig. 6.21 Variation of exergy destruction due to heat transfer between plate and air for SAH with W-baffle and semi-cylindrical sidewalls ($R_H = 0.092$ and $R_P = 0.92$).
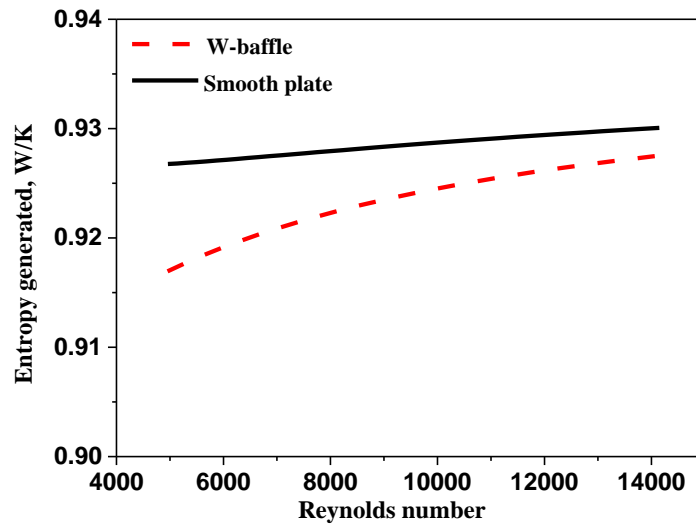
Fig. 6.22 Influence of Reynolds number on entropy generation for SAH with W-baffle and semi-cylindrical sidewalls ($R_H = 0.092$ and $R_P = 0.92$).
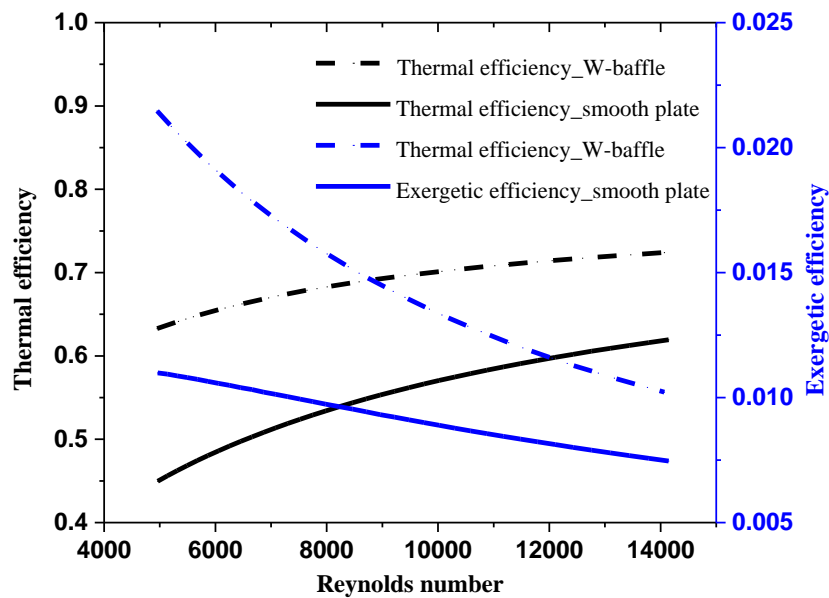
Fig. 6.23 Exergetic efficiency variation with flow Reynolds number for SAH W-baffle and semi-cylindrical sidewalls ($R_H = 0.092$ and $R_P = 0.92$).

Further, SAH with W-baffles and semi-cylindrical sidewalls is compared to ribbed SAH with vertical sidewalls (Kumar et al. 2009, Lanjewar et al. 2011a) w.r.t. exergetic performance. W-baffle SAH with semi-cylindrical sidewalls has higher thermal efficiency than discrete W-rib SAH (Kumar et al. 2009) and continuous W-rib SAH with vertical sidewalls for a wide range of Re (5000 - 14000). Additional secondary

flow generated by the semi-cylindrical sidewalls increases the turbulence and enhances the heat transfer rate between plate and air.
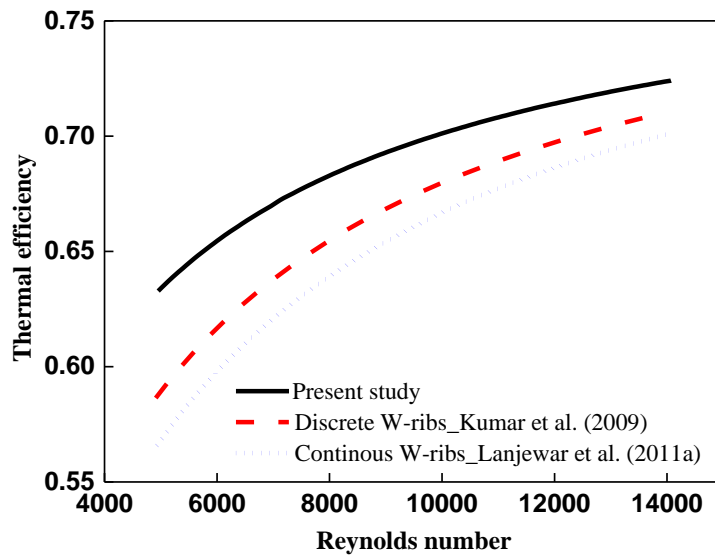
(a)
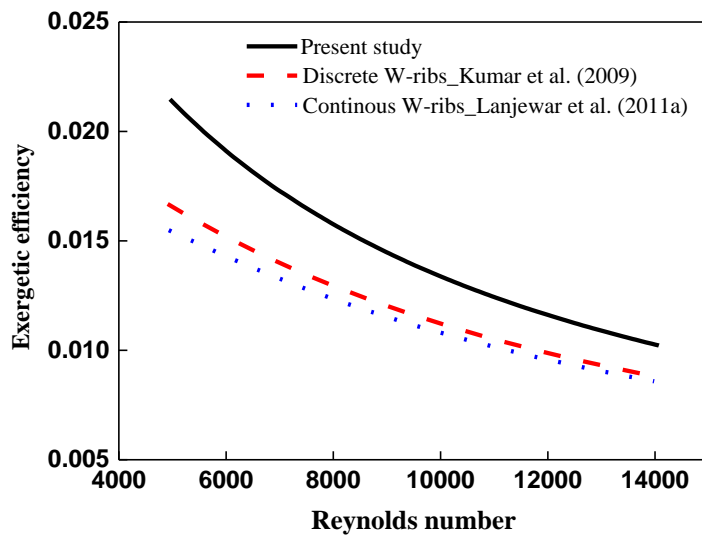
(b)

Fig. 6.24 Comparison of SAH with W-baffle and semi-cylindrical sidewalls with the literature data (a) Thermal efficiency and (b) Exergetic efficiency.

As a result, an increase of 8% and 11.8% is obtained in η_{th} compared to discrete W-rib and continuous W-rib SAH with vertical sidewalls, respectively (Fig. 6.24 (a)). With a higher exergy gain of 1.28 and 1.38 times compared to the discrete W-rib SAH (Kumar et al. 2009) and the continuous W-rib SAH (Lanjewar et al. 2011a) with vertical sidewalls, respectively, the W-baffle SAH with semi-cylindrical sidewalls has higher

exergetic performance for a wide range of *Re* (Fig. 6.24 (b)). Hence, it is evident that a SAH duct having semi-cylindrical sidewalls and baffles performs better for a wide range of *Re*, with maximum enhancement in performance occurring at lower *Re*.

6.8 Summary

Performance analysis of W-baffle SAH with semi-cylindrical sidewalls is studied based on energy and exergy perspectives. The results indicate the superiority of the present SAH design upon comparison to other similar ribbed SAH. Based on the analysis, notable conclusions drawn are as follows:

1. With an increase in *Re*, *Nu* increases monotonically due to the reduced size of the recirculation zone. Peak augmentation in *Nu* and *f* is obtained as 3.24 and 4.03 times, respectively, compared to smooth SAH. This is due to the secondary flow and turbulence caused by the W-baffles and the higher secondary flow generated by the semi-cylindrical sidewalls.

2. The rounding off the duct corners removes the smaller vortices near the corners and facilitates the smooth movement of cross-flow across the sharp corners, which increases the turbulent kinetic energy near the semi-cylindrical sidewalls.

3. Thermo-hydraulic performance parameter (THPP) for the SAH duct with semi-cylindrical sidewalls and W-baffles is obtained in the range of 1.70 to 2.27. Peak THPP of 2.27 is obtained for $R_H = 0.092$ and $R_P = 0.92$ at $Re = 5000$.

4. THPP of the proposed SAH model has been compared and found to be better than similar geometries, such as W-down rib (THPP = 1.98), W-up rib (THPP = 1.81), discrete W-up rib (THPP = 1.54), and V-baffle (THPP = 1.83).

5. The contrast of CFD values for Nusselt number, and friction factor with those determined by the correlation is within an absolute deviation of 4% and 7.4%, respectively. Therefore, the statistical correlations formed can be used to predict *Nu* and *f* with reasonable accuracy.

6. Maximum enhancement in thermal and exergetic efficiency is obtained as 40.7 % and 95.4%, respectively, for the proposed SAH relative to conventional SAH at $Re = 5000$.

7. For the same exergy input, the SAH design with semi-cylindrical sidewalls performs better with an enhancement of 28.7% and 38.7% in exergetic

efficiency at Re = 5000 compared to continuous and discrete W-rib, respectively. Additionally, the present SAH design is superior to the conventional ribbed SAH for a wide range of Re.

CHAPTER 7

STUDY OF MULTIPLE DISCRETE INCLINED BAFFLES IN SOLAR AIR HEATER WITH SEMICYLINDRICAL SIDEWALLS

7.1 Introduction

An experimental and computational fluid dynamics (CFD) study is carried out to investigate the impact of secondary flow strength on the thermo-hydraulic performance of discrete multiple inclined baffles in a flat plate solar air heater (SAH) with semicylindrical sidewalls. Initially, for a fixed relative baffle height (R_H = 0.1), the relative baffle pitch (R_P) for continuous baffles is varied in the range of 0.6 to 1 to obtain the optimum baffle pitch for $6000 \leq Re \leq 14000$.

The computational domain for SAH with semicylindrical sidewalls and discrete multiple inclined baffles has been discussed in *section 3.1*. The multi-block meshing technique discretizes the SAH domain into non-uniform hexahedral cells (*section 3.2*). The SAH duct with semicylindrical sidewalls and optimum baffle configuration is fabricated and experimentally validated. In addition, the impact of gaps at leading, at trailing, and at both leading and trailing apices are studied as three different configurations. The findings are detailed using characteristic plots, flow pattern visualization, and contours of velocity, pressure, etc., to demonstrate the impact of secondary flow on the thermo-hydraulic performance of a SAH with semicylindrical sidewalls and discrete inclined baffles. Exergetic performance analysis is carried out, and exergetic efficiency is evaluated. Finally, the coefficient of performance (COP) of the present design is compared with similar ribbed rectangular duct SAH to confirm the superior performance of the former.

7.2 Thermohydraulic performance

Thermo-hydraulic performance of SAH with semicylindrical sidewalls and discrete multiple inclined baffles is studied by varying flow Reynolds number (6000 - 14000), relative baffle pitch (0.6 - 1), and location of the gap in the baffle (leading apex, trailing apex, and both leading and trailing apices). From Fig. 7.1, it is observed that Nu increases for all configurations ($0.6 < R_P < 1$) monotonically with an increase in *Re*.

This is attributed to the reduction in recirculation zone, an area of low heat transfer behind the baffle (Fig. 7.2).
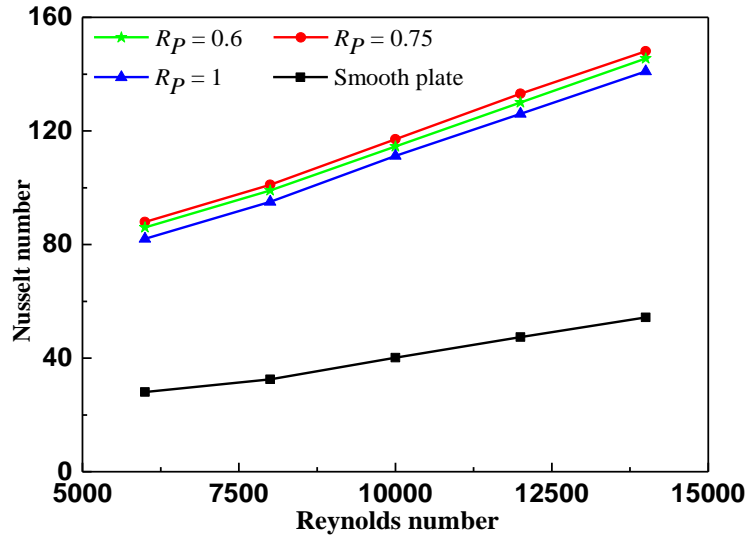
Fig. 7.1 Nusselt number variation with Reynolds number for a fixed baffle height at varying pitch.
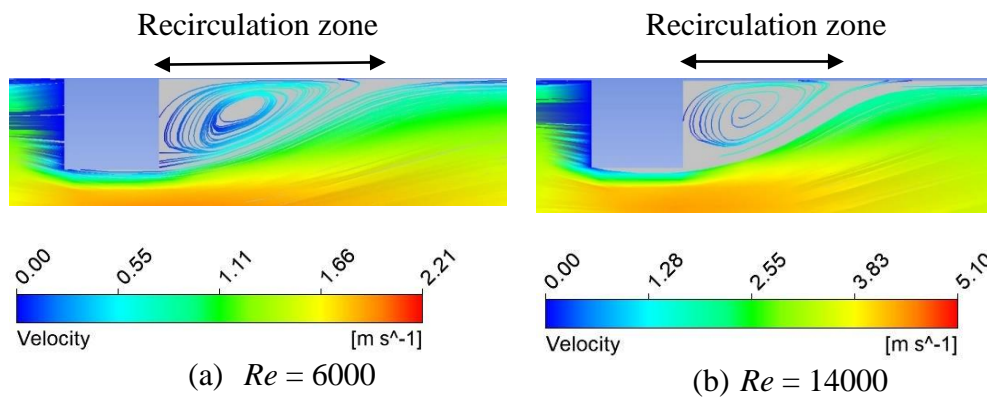
(a) $Re = 6000$ (b) $Re = 14000$

Fig. 7.2 Streamlines depicting the recirculation zone on a plane perpendicular to the absorber plate for (a) $Re = 6000$ and (b) $Re = 14000$.

Besides, the contours of temperature distribution on the absorber plate indicate that for low Re (= 6000), the temperature near the trailing apices of the multiple inclined baffles are higher than the temperature at the corresponding location at higher Re (= 14000), as shown in Fig. 7.3. These high-temperature regions cause a rise in the average temperature of the plate and thus lower the convective heat transfer rate. The friction factor decreases with an increase in Re. With the inclusion of baffles, an additional

pressure drop occurs compared to the smooth duct, thereby increasing the friction factor (Fig. 7.4).
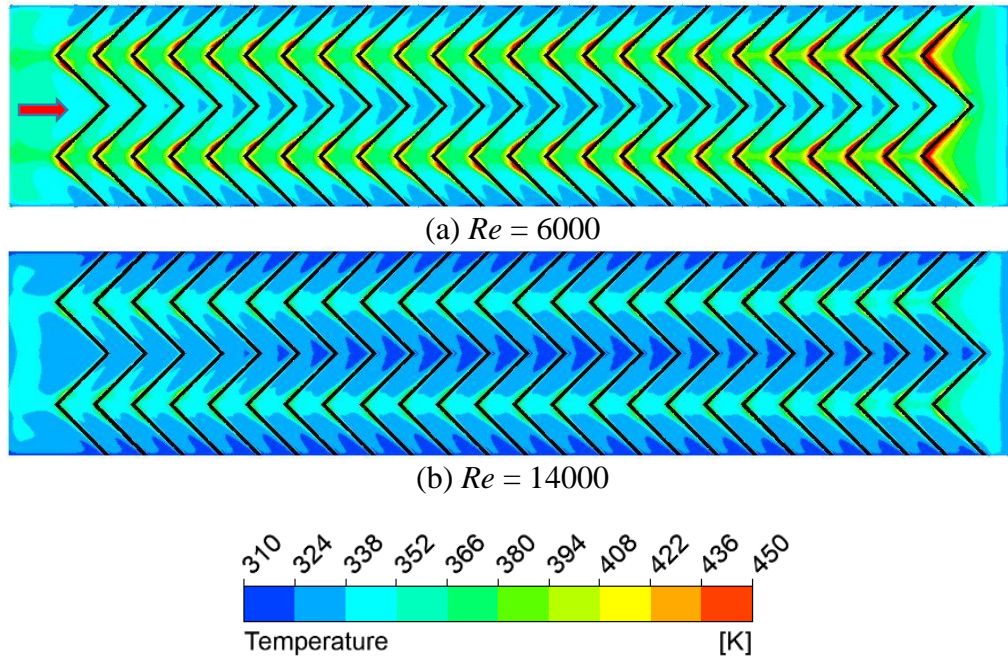
(a) $Re = 6000$

(b) $Re = 14000$

Fig. 7.3 Temperature distribution on the absorber plate for (a) $Re = 6000$ and (b) $Re = 14000$.
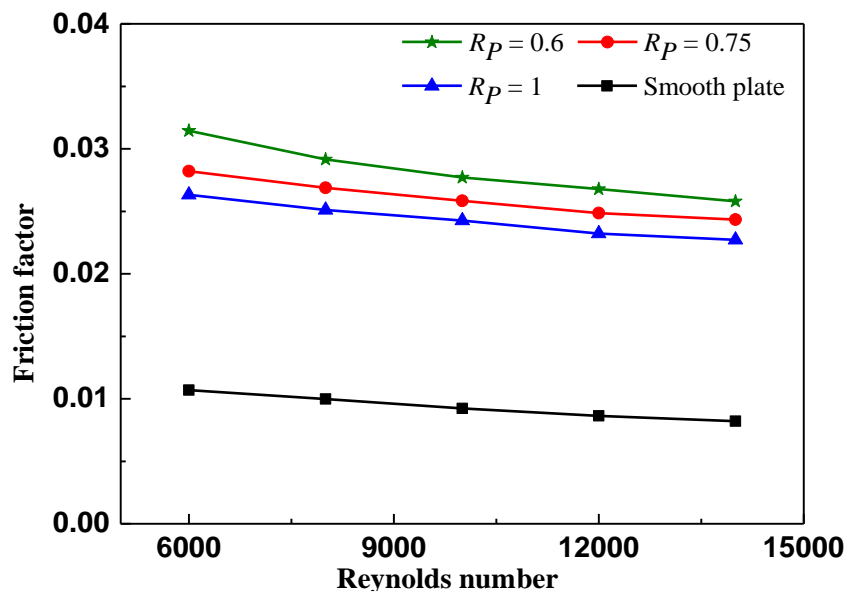
Fig. 7.4 Friction factor variation with Reynolds number for a fixed baffle height at a different pitch.

For a fixed $R_H = 0.1$, upon increasing R_P, it is noticed that the Nu decreases up to 0.75, and a further increase in R_P causes a drop in Nu. For $R_P < 0.75$, flow reattachment may

not have occurred, and for $R_P > 0.75$, the boundary layer reattachment length increases due to an increase in the inter-baffle region. In addition, as R_P increases, the number of reattachment points decreases for a fixed plate length. For the range of parameters studied, maximum heat transfer is obtained for $R_P = 0.75$ (Fig. 7.1). For an artificially roughened SAH to be efficient, the baffle accompanied pressure drop should not offset the heat transfer gains. Hence, the friction factor variation with Re is studied for a similar parametric range. It is observed that with an increase in R_P, the friction factor decreases due to a reduction in the number of baffles resulting in a lower blockage effect. The trade-off between an increase in heat transfer and accompanying additional pressure drop is obtained by considering the thermo-hydraulic performance parameter (THPP) variation with Re for a fixed R_H to arrive at an optimum value of R_P (Fig. 7.5). It is observed that maximum THPP is obtained for $R_P = 0.75$ at lower Re (= 6000).
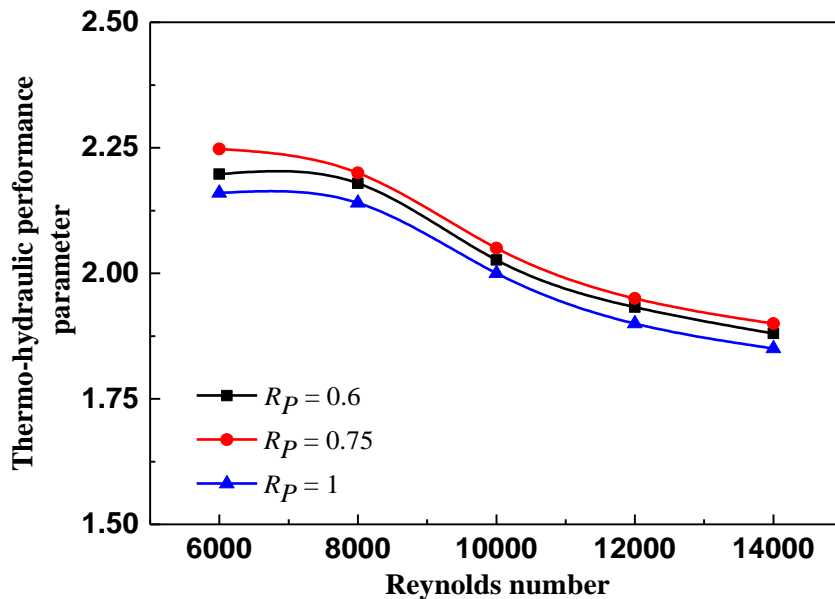
Fig. 7.5 Variation of thermo-hydraulic performance parameter with Re for continuous baffles

Furthermore, the impact of the gap width ($g/e = 1$) and position ($d/W = 0.25$) on the thermo-hydraulic performance is studied by considering three cases, namely, the gap at the leading apex, a gap at the trailing apex, and the gap at both leading and trailing apices of the inclined baffle. The value of gap width and gap position chosen is the optimum as described in the studies conducted by Aharwal et al. (2009) and Singh et al. (2011). Nusselt number and friction factor variation in 3 cases of discrete inclined

baffles are as shown in Figs. 7.6 (a) and (b), respectively. Maximum heat transfer enhancement of 2.47 times is obtained for multiple inclined baffles with the gap at trailing apex for $Re = 14000$ with 3.07 times increment in friction factor compared to smooth SAH. A maximum THPP of 2.69 is obtained for lower Re (= 6000) when the gap is positioned at the trailing apex (Fig. 7.7).

(a)

(b)
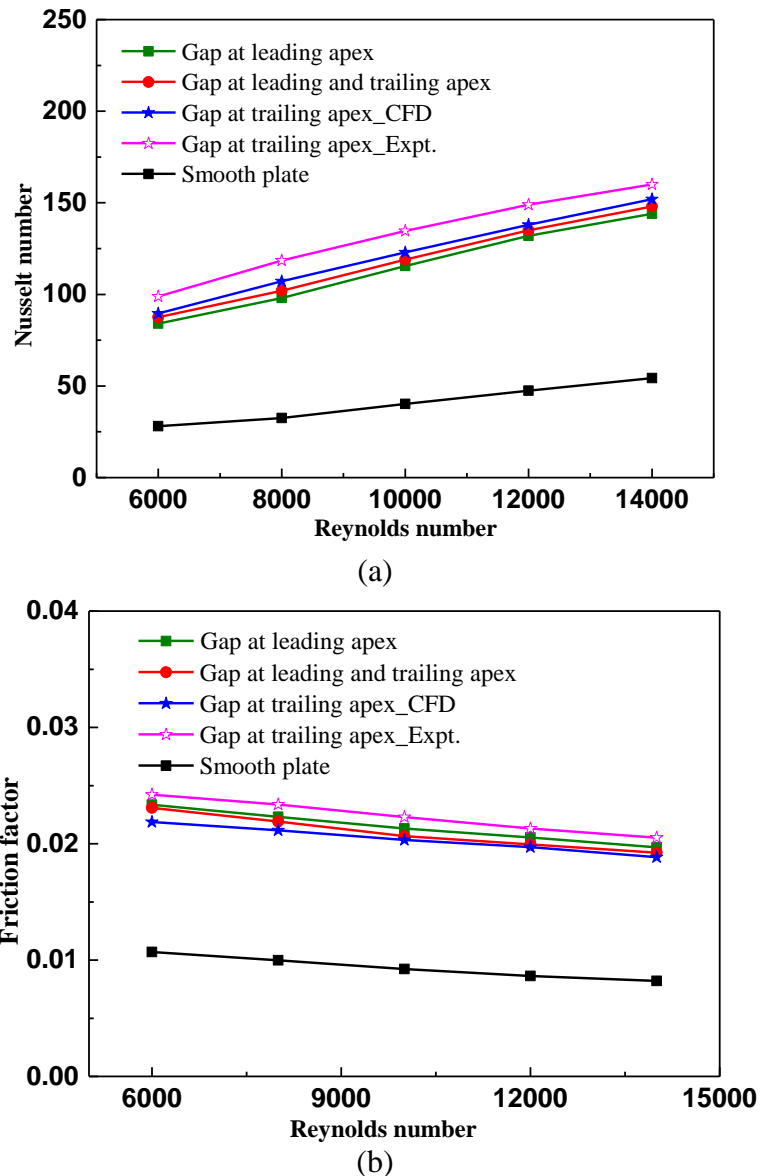
Fig. 7.6 Nusselt number and friction factor variation with Re for discrete baffle.

When the gap is positioned at the leading apex, minimum heat transfer enhancement and maximum pressure drop are obtained, giving the lowest thermo-hydraulic performance (THPP = 2.32). The physical aspects of the above observation are discussed in the following paragraphs.
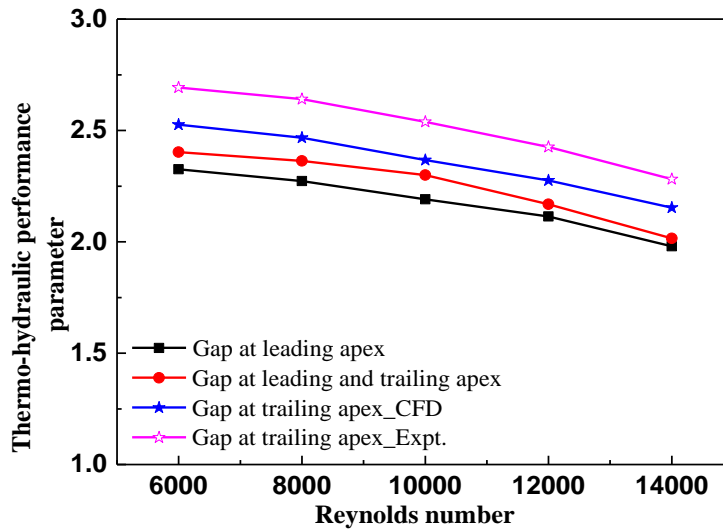
Fig. 7.7 Variation of thermo-hydraulic performance parameter for discrete baffles with Reynolds number.

The streamline pattern for the three cases of discrete inclined baffles is shown in Fig. 7.8. For the gap at the leading apex, owing to the main flow stream striking the leading apex at a comparatively higher velocity, a re-circulatory flow is created behind the leading apex (Fig 7.8 (a)). This causes a localized temperature rise in that region, increasing the absorber plate's average temperature (Fig. 7.9 (a)).
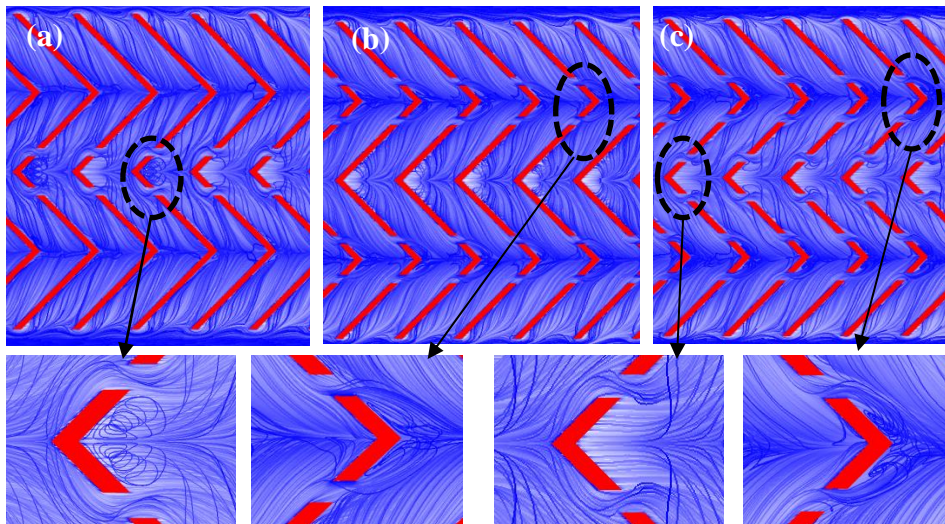
Fig. 7.8 Streamline pattern for various discrete baffle configuration (a) Gap at the leading apex, (b) Gap at the trailing apex and (c) Gap at the leading and trailing apices.
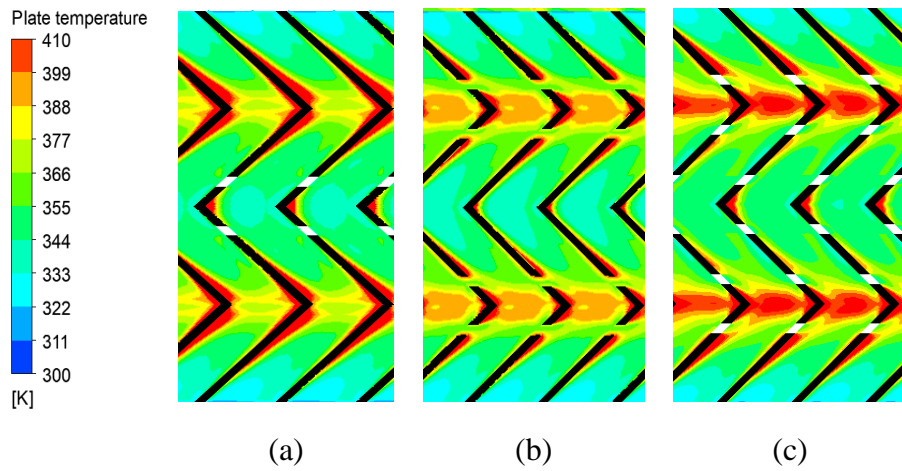
Fig. 7.9 Contours of temperature distribution on the absorber plate for
(a) Gap at the leading apex, (b) Gap at the trailing apex and (c) Gap
at the leading and trailing apices.
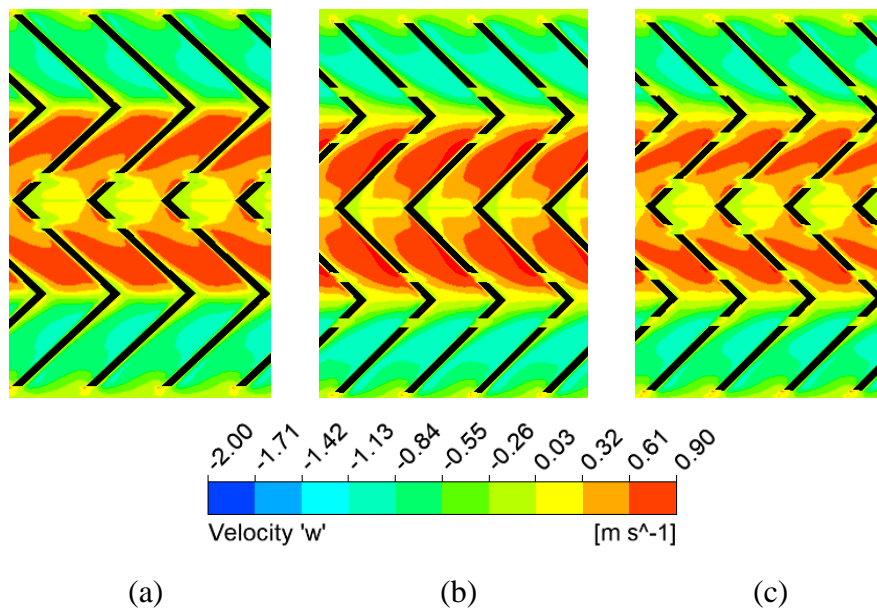
Fig. 7.10 Contours of transverse velocity in the inter baffle regions
indicating the strength of the secondary flow for various discrete
baffle configuration (a) Gap at the leading apex, (b) Gap at the
trailing apex, and (c) Gap at the leading and trailing apices.

Whereas the gap positioned at the trailing apex does not cause any re-circulatory flow
(Fig. 7.8 (b)), the higher temperature regions on the absorber plate are thus relatively
smaller (Fig. 7.9 (b)). When the gap is placed at both the leading and trailing apices,

the secondary flow strength is reduced considerably; (Fig. 7.10 (c)) relative to the strength of the secondary flow in the other two cases (Figs. 7.10 (a) and (b)).
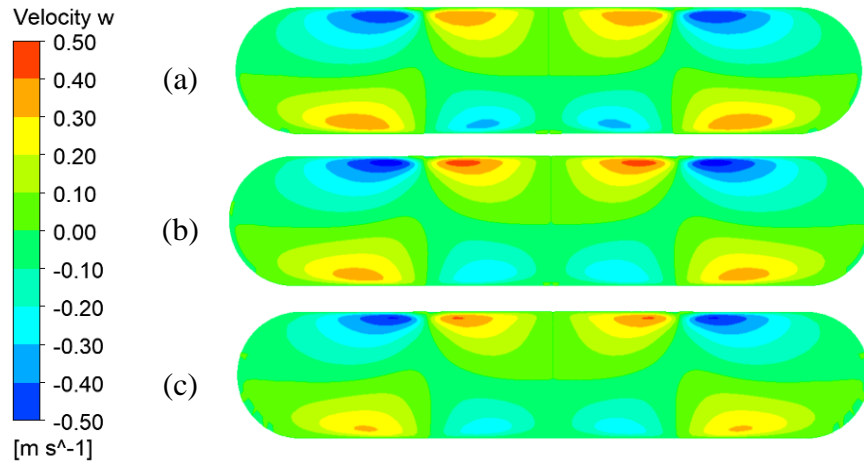
Fig. 7.11 Contours of transverse velocity at test section exit for discrete baffle configuration (a) Gap at the leading apex, (b) Gap at the trailing apex, (c) Gap at the leading and trailing apices
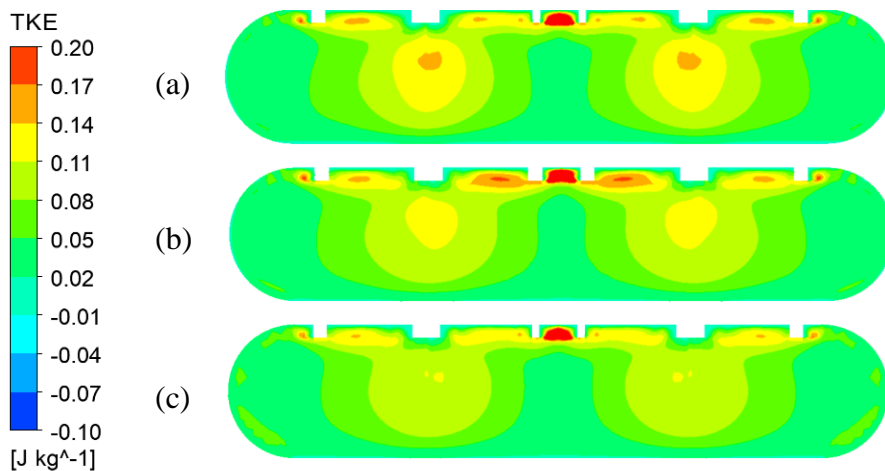
Fig. 7.12 Contours of turbulent kinetic energy at test section exit for discrete baffle configuration (a) Gap at the leading apex, (b) Gap at the trailing apex, (c) Gap at the leading and trailing apices

The gap at the leading apex allows the flow stream to pass through it instead of being carried to the trailing tip, reducing the possible heat that secondary flow would have gained while moving along the baffles. The same aspect is displayed through Fig. 7.11, in which the secondary flow vortices are shown in a cross-section plane at the test

134

section exit. Furthermore, the contours of turbulent kinetic energy (TKE), established in Fig. 7.12, indicating that the gap positioned at the trailing apex raises the turbulent kinetic energy over a larger region within the duct.

Table 7.1: Comparison of THPP of various SAH configurations

References	Duct shape	Type of study	Artificial roughness	THPP
Kumar et al. (2009)	Rectangle	Experimental	Discrete W-up rib	1.54
Lanjewar et al. (2011a)	Rectangle	Experimental	W-down rib	1.98
Tamna et al. (2014)	Rectangle	Experimental and CFD	V-baffle	1.83
Present study (*Chapter 6*)	Rectangular with semi-cylindrical sidewalls	CFD	W- baffle	2.27
Present study	Rectangular with semi-cylindrical sidewalls	Experimental and CFD	Discrete multiple inclined baffles	**2.69**

In addition, the THPP of SAH with semicylindrical sidewalls and discrete inclined baffles is compared with SAH having artificial roughness as detailed in Table 7.1. Discrete multiple inclined baffles underneath the absorber plate of SAH with semicylindrical sidewalls is efficient compared to artificial roughness of similar configuration in the turbulent flow regime.

7.3 Exergetic performance

Apart from the energy analysis, which evaluates the process effectiveness, exergetic analysis is another essential tool to study the realistic behavior of the process involving various energy losses and internal irreversibility. In a SAH, heat transfer between heated absorber plate and air (working fluid) occurs at a finite temperature difference leading to heat losses.

The exergetic performance of the present SAH design is studied for parameters such as collector efficiency, exergetic efficiency, exergy loss due to heat transfer between heated surface and air, and exergy loss due to heat loss to the environment. Collector efficiency computes the net energy gain while deducting the flow pumping power and is a practical parameter to analyze the efficiency of the SAH compared to useful heat gain-based thermal efficiency.
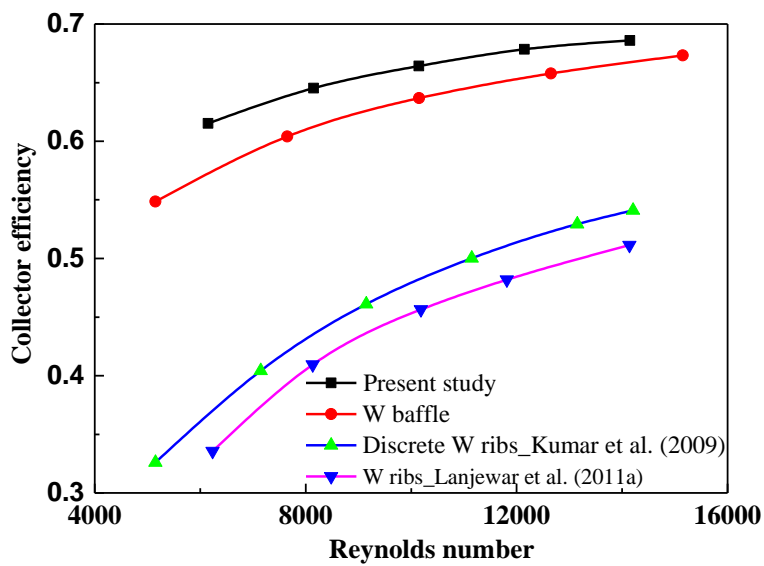
Fig. 7.13 Collector efficiency variation with Reynolds number for different SAH designs.
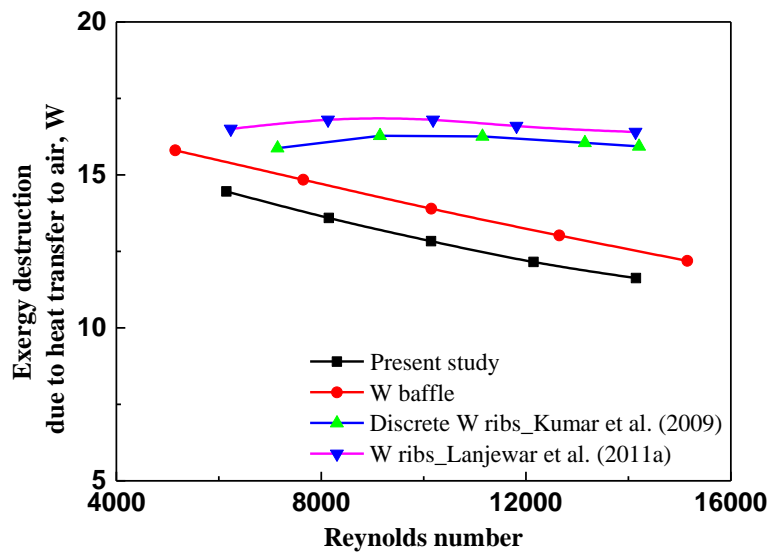
Fig. 7.14 Variation of exergy loss due to heat transfer from absorber plate to air.

As a function of *Re*, collector efficiency increases for all the SAH designs, and SAH with semicylindrical sidewalls depicts a higher efficiency relative to rectangular duct SAH (Fig. 7.13). This may be due to lower pressure drop and, in turn, lower pumping power requirement upon replacing the vertical sidewalls with semicylindrical ones. Collector efficiency is obtained in the range of 55 to 70% and 30 to 55%, respectively, for artificially roughened SAH design with semicylindrical sidewalls and vertical sidewalls. Discrete inclined baffles provided a 10% higher collector efficiency than continuous inclined baffles in SAH with the semicylindrical duct.

Due to turbulence created by the baffles, better air mixing occurs, leading to a lower average plate temperature, thereby reducing the temperature gradient and associated irreversibility. In the present design, the gaps in the inclined baffles increase the strength of the secondary flow (Fig. 7.10) and significantly increase the turbulence in the inter-rib regions. With the increase in *Re*, the velocity of secondary flow increases, accelerating the retarded boundary layer flow and considerably enhancing the convective heat transfer rate in artificially roughened SAH with semicylindrical sidewalls. Hence, the average plate temperature decreases, and the exergy loss due to heat transfer between the plate and air decreases (Fig. 7.14). Upon comparison, the losses in the present SAH design are lower than the conventional SAH designs. In addition, in a SAH duct with semicylindrical sidewalls, the exergy losses at higher *Re* decrease due to higher secondary flow strength relative to rectangular duct SAH.
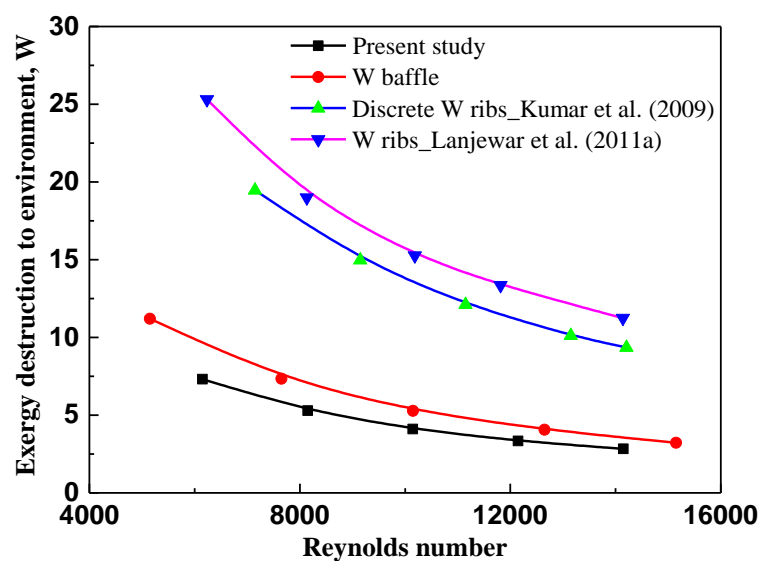
Fig. 7.15 Variation of exergy loss due to heat loss to the environment.

Similarly, lower plate temperature due to a higher heat transfer rate in SAH with semicylindrical sidewalls reduces the heat loss from the bottom and sidewalls to the ambient air (Fig. 7.15). In addition, smooth air movement along the curved sidewalls eliminates the smaller vortices near the sidewalls facilitating better mixing and reducing the heat loss to the ambient air relative to rectangular duct SAH. Hence, due to lower heat losses and higher collector efficiency, the present design exhibits higher exergetic efficiency for the entire range of Re (Fig. 7.16).
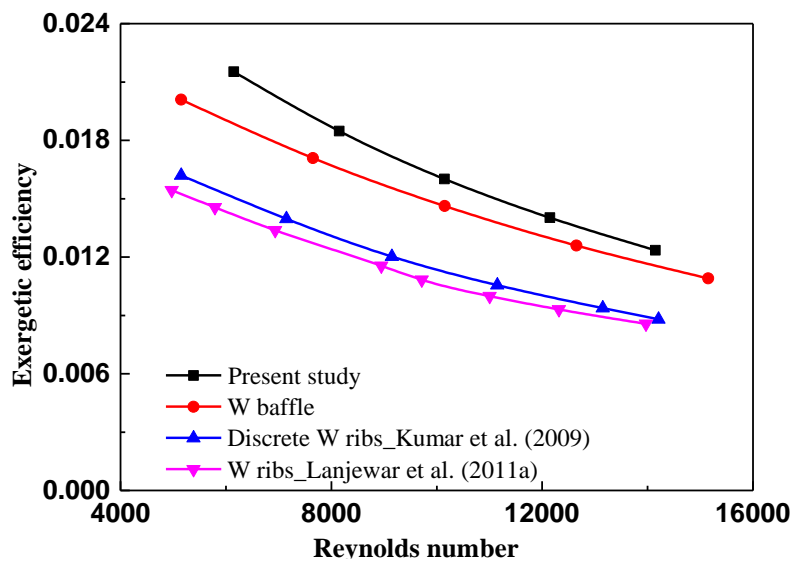
Fig. 7.16 Exergetic efficiency variation with Reynolds number for different SAH designs.
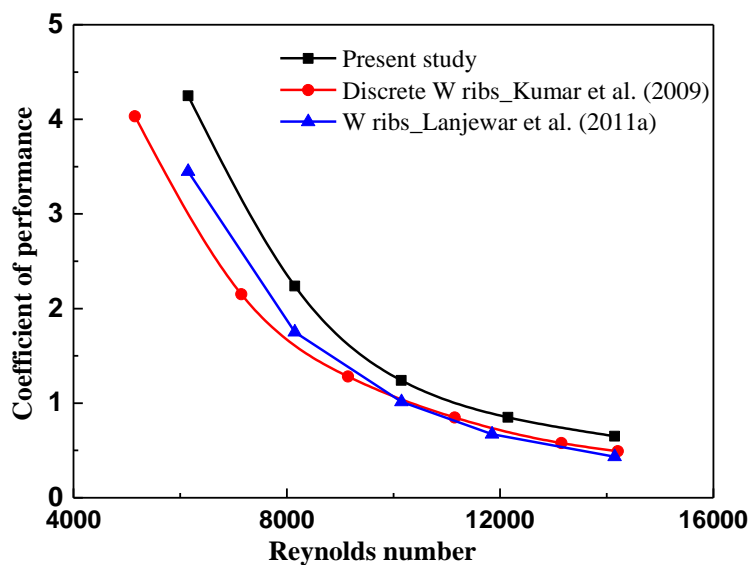
Fig. 7.17 Variation of average COP values with Reynolds number.

138

Further, to evaluate the cost-effectiveness of the present SAH design, the coefficient of performance (COP) is computed (Khanlari et al. 2020), and the same is compared to rectangular duct SAH with a similar kind of artificial roughness. COP of a SAH design depends upon the magnitude of the air temperature rise and the power required to pump air through the SAH duct. It is observed that higher COP is obtained at lower Re for all the SAH designs studied. This may be attributed to the higher air residence time and smaller pressure drop. At higher Re, the heat gain by air is considerably lower and is offset by the accompanying pressure drop, leading to lower COP. Further, at low Re, the present SAH design has higher COP than conventional SAH designs (Fig. 7.17).

7.4 Summary

Energy and exergy analysis of SAH with semicylindrical sidewalls and discrete multiple inclined baffles is carried out to improve the thermo-hydraulic performance and cost-effectiveness. Using CFD simulation, heat transfer and friction factor characteristics are studied and compared for both smooth and baffled SAH. Optimum baffle configuration is fabricated and experimentally studied to validate the result obtained from the CFD study. The results indicate that the SAH designs exhibit higher overall performance than similar kinds of SAH configurations. Significant findings based on the study are as follows.

1. For baffled SAH, Nusselt number increases monotonically with Re due to the reduction in recirculation zone (an area of low heat transfer). However, the friction factor decreases with an increase in Re for the baffle configurations investigated.

2. As R_P increases, the number of reattachment points for the same length of the absorber plate decreases. For a fixed relative baffle height ($R_H = 0.01$), the optimum value of relative baffle pitch (R_P) is obtained as 0.75 based on the trade-off between heat transfer enhancement rate and accompanying pressure drop.

3. For the optimum continuous baffle configuration, the impact of gap location on the performance enhancement is studied by placing the gap at the leading apex, at the trailing apex, and at both leading and trailing apices. The position of gap has a strong influence on the secondary flow movement.

4. Peak enhancement in *Nu* and *f* are obtained as 2.47 and 3.07 times that of the smooth absorber plate, respectively, for $R_P = 0.75$ and gap position at trailing apex for $Re = 14000$.

5. Thermo-hydraulic performance parameter (THPP) is obtained in the range of 1.94 to 2.69. Peak THPP of 2.69 is obtained for $R_P = 0.75$ and gap position at the trailing apex for $Re = 6000$.

6. The present design has higher collector efficiency, in the range of 55 to 70%, compared to ribbed rectangular SAH design exhibiting 30 to 55%.

7. The exergy losses due to heat transfer between the heated plate and air; and heat loss to the ambient air are lower for the present design. Owing to lower exergy losses and higher collector efficiency, SAH with semicylindrical sidewalls and discrete inclined baffles has higher exergetic efficiency.

8. The higher COP indicates the cost-effectiveness of the present design compared to rectangular duct SAH with similar artificial roughness.

CHAPTER 8

CONCLUSIONS AND SCOPE OF FUTURE WORK

8.1 Conclusions

This dissertation presents computational simulations validated with experimental studies on the impact of duct cross-section on the thermo-hydraulic performance of flat plate solar air heater (SAH) in conjunction with various kinds of artificial roughness capable of inducing secondary flow. Rib geometry and operating parameters are varied in the turbulent flow regime to obtain a configuration that maximizes the thermo-hydraulic performance parameter (THPP). Triangular and modified rectangular duct with semi-cylindrical sidewalls has been investigated for varying rib configurations such as inclined ribs, V-ribs, W-ribs, and multiple discrete inclined ribs with the gap at leading and trailing apices. Geometrical aspects of artificial roughness such as relative roughness height, relative roughness pitch, and inclination of the roughness to the primary flow stream are varied w.r.t. Reynolds number in the range of 5000 to 20000. Correlations are developed for predicting Nusselt number (Nu) and friction factor (f) for the range of the studied parameter. Apart from energy analysis, second law analysis is also carried out to account for the various exergy losses and to compare the exergetic efficiency of the proposed SAH design with that of the conventional ribbed SAH. To give a concise overview of the dissertation, all the studies are compiled briefly, and the notable observations are restated in the subsequent sections.

8.1.1 Major outcome of the studies on V-ribs in triangular duct SAH

Steady-state CFD analyses have been carried out on V-ribbed triangular duct SAH in the turbulent flow regime ($5000 \leq \mathrm{Re} \leq 20000$). The results indicate that the proposed SAH design exhibits improved thermo-hydraulic performance compared to various similar kinds of artificial roughness employed in triangular and rectangular duct SAHs. Major outcomes of the study are the following:

- The thermo-hydraulic performance parameter (THPP) for the triangular duct SAH with V-ribs is obtained in the range of 1.32 to 2.01. Peak value of 2.01 is obtained for e/D=0.05, $P/e = 10$, and $\beta = 45°$ at $Re = 7500$.

- The developed empirical correlations can predict Nu and f with an absolute variance of 8.7% and 4.7%, respectively.

- Minimum entropy generation and maximum exergetic efficiency are obtained for $\beta = 45°$ compared to the smooth plate SAH. An enhancement in exergetic efficiency (η_{ex}) of 23 % is obtained.

- The present design exhibits superior performance when comparing this SAH design with ribbed rectangular duct SAH for similar input conditions. Hence, for applications requiring compact heat exchangers, especially at higher flow rates, a V-ribbed ($\beta = 45°$) triangular duct SAH is a better choice compared to a ribbed rectangular duct SAH.

8.1.2 Major outcome on the development of an energy-efficient dryer using ribbed triangular duct solar air heater

A triangular duct solar air heater (SAH) with inclined ribs is designed and computationally studied for an indirect type solar dryer (ITSD). With the hot air supplied by the ribbed triangular duct solar air heater (SAH), drying characteristics of okra and two variants of banana are studied experimentally and the salient conclusions obtained are:

- For similar heat input and flow Re, inclined ribs enhance the overall performance of a triangular duct SAH by 17% relative to rectangular duct SAH with a maximum value of 1.79 obtained for $\beta = 45°$ at flow $Re = 10000$. This is attributed to the secondary flow generated by the inclined ribs.

- Compared to the ribbed rectangular duct, ribbed triangular duct SAH exhibits 60.4% and 54.5% reduction in moisture ratio for food samples robusta and nendran, respectively, for the same drying time.

- Compared to the ribbed rectangular duct, ribbed triangular duct SAH exhibits a 97.9% and 93.3% increase in average values of the diffusivity coefficient of robusta and nendran, respectively.

- For similar heat input and flow Re, triangular duct SAH with inclined ribs displays a higher performance relative to similar rib configuration in rectangular SAH, evidently making it a better choice for ITSD applications. This design can

be incorporated into the existing ITSD with minimal modifications and without additional energy requirements.

8.1.3 Major outcome of the studies on solar air heater with semicylindrical sidewalls and W-baffles

Performance analysis of W-baffle SAH with semi-cylindrical sidewalls is studied based on energy and exergy perspectives. The results indicate the superiority of the present SAH design upon comparison to other similar ribbed SAH configurations. Based on the analysis, notable conclusions drawn are as follows:

- The rounding off the duct corners removes the smaller vortices near the corners and facilitates the smooth movement of cross-flow across the sharp corners, which increases the turbulent kinetic energy near the semi-cylindrical sidewalls.

- Thermo-hydraulic performance parameter (THPP) for the SAH duct with semi-cylindrical sidewalls with W-baffles is obtained in the range of 1.70 to 2.27. Peak THPP of 2.27 is obtained for $R_H = 0.092$ and $R_P = 0.92$ at $Re = 5000$.

- THPP of the proposed SAH model has been compared and found to be better than similar geometries, such as W-down rib (THPP = 1.98), W-up rib (THPP = 1.81), discrete W-up rib (THPP = 1.54) and V-baffle (THPP = 1.83).

- The contrast of CFD values for Nusselt number and friction factor with those determined by the correlation is within an absolute deviation of 4% and 7.4%, respectively. Therefore, the statistical correlations formed can be used to predict Nu and f with reasonable accuracy.

- Maximum enhancement in thermal and exergetic efficiency is obtained as 40.7 % and 95.4 %, respectively, for the proposed SAH relative to conventional SAH at $Re = 5000$.

- For the same exergy input, the SAH design with semi-cylindrical sidewalls stands out with an enhancement of 28.7% and 38.7% in exergetic efficiency at $Re = 5000$ compared to continuous and discrete W-rib, respectively. Additionally, the present SAH design is superior to the conventional ribbed SAH for a wide range of Re.

8.1.4 Major outcome of the studies on solar air heater with semicylindrical sidewalls and discrete multiple inclined baffles

Energy and exergy analysis of SAH with semi-cylindrical sidewalls and discrete inclined baffles with gaps at leading and trailing apices are carried out to improve the overall performance and cost-effectiveness. Baffle configuration providing the maximum thermo-hydraulic performance is fabricated and experimentally studied to validate the result obtained from the CFD study. The proposed SAH designs exhibit higher overall performance compared to ribbed rectangular duct SAH configurations, justified by the following significant observations:

- For the optimum continuous baffle configuration, the impact of gap location on the performance enhancement is studied by placing the gap at the leading apex, at the trailing apex, and at both leading and trailing apices. The position of the gap has a strong influence on the secondary flow movement.

- Thermo-hydraulic performance parameter (THPP) is obtained in the range of 1.94 to 2.69. Peak THPP of 2.69 is obtained for $R_P = 0.75$ and gap position at the trailing apex for $Re = 6000$.

- The present design has higher collector efficiency, in the range of 55 to 70%, compared to ribbed rectangular SAH design exhibiting 30 to 55%.

- The exergy losses due to heat transfer between the heated plate and air; and heat loss to the ambient air are lower for the present design. Owing to lower exergy losses and higher collector efficiency, SAH with semi-cylindrical sidewalls and discrete inclined baffles has higher exergetic efficiency.

- The higher COP indicates the cost-effectiveness of the present design compared to rectangular duct SAH with similar artificial roughness.

8.2 Scope for future work

The present dissertation has analyzed the impact of duct cross-section in conjunction with artificial roughness in enhancing the thermo-hydraulic performance of a SAH. In the course of the present study, a few areas have been identified for further research and are as follows:

i. Further studies can be carried out to study the impact of duct cross-section on the secondary flow enhancement within the duct. It has been noted that flow laminarisation occurs in the sharp corners of the duct, creating zones of high temperature and reducing the heat transfer to air.

ii. Owing to lower pressure drop, further studies on the triangular duct in flat plate SAH with artificial roughness to enhance the heat transfer rate can be conducted. The same can be studied for application in indirect type solar dryer for better drying characteristics.

iii. Flexible ribs/turbulators can be employed To reduce the additional pressure drop that mitigates the potential gain in heat transfer rate owing to the application of rigid artificial roughness.

iv. Phase change materials can be integrated into the triangular duct SAH to ensure continuous operation throughout a day.

REFERENCES

Abhay,L., Chandramohan,V.P., and Raju,V.R.K. (2018). "Numerical analysis on solar air collector provided with artificial square shaped roughness for indirect type solar dryer". *J. Clean. Prod.*, 190, 353–367.

Abuşka,M. (2018). "Energy and exergy analysis of solar air heater having new design absorber plate with conical surface". *Appl. Therm. Eng.*, 131.

Aharwal,K.R., Gandhi,B.K., and Saini,J.S. (2008). "Experimental investigation on heat-transfer enhancement due to a gap in an inclined continuous rib arrangement in a rectangular duct of solar air heater". *Renew. Energy*, 33.

Aharwal,K.R., Gandhi,B.K., and Saini,J.S. (2009). "Heat transfer and friction characteristics of solar air heater ducts having integral inclined discrete ribs on absorber plate". *Int. J. Heat Mass Transf.*, 52.

Ahn,S.W. (2001). "The effects of roughness types on friction factors and heat transfer in roughened rectangular duct". *Int. Commun. Heat Mass Transf.*, 28.

Akhtar,N. and Mullick,S.C. (1999). "Approximate method for computation of glass cover temperature and top heat-loss coefficient of solar collectors with single glazing". *Sol. Energy*, 66.

Akpinar,E.K. and Koçyiĝit,F. (2010). "Energy and exergy analysis of a new flat-plate solar air heater having different obstacles on absorber plates". *Appl. Energy*, 87.

Al-Juamily,K.E.J., Khalifa,A.J.N., and Yassen,T.A. (2007). "Testing of the performance of a fruit and vegetable solar drying system in Iraq". *Desalination*, 209.

Al-Shetwi,A.Q., Hannan,M.A., Jern,K.P., Mansur,M., and Mahlia,T.M.I. (2020). "Grid-connected renewable energy sources: Review of the recent integration requirements and control methods". *J. Clean. Prod.*, 253.

Alam,T. and Kim,M.H. (2017a). "A critical review on artificial roughness provided in rectangular solar air heater duct". *Renew. Sustain. Energy Rev.*, 69.

Alam,T. and Kim,M.H. (2017b). "Heat transfer enhancement in solar air heater duct

with conical protrusion roughness ribs". *Appl. Therm. Eng.*, 126.

Alam,T. and Kim,M.H. (2016). "Numerical study on thermal hydraulic performance improvement in solar air heater duct with semi ellipse shaped obstacles". *Energy*, 112.

Bastida,L., Cohen,J.J., Kollmann,A., Moya,A., and Reichl,J. (2019). "Exploring the role of ICT on household behavioural energy efficiency to mitigate global warming". *Renew. Sustain. Energy Rev.*, 103.

Benli,H. (2013). "Experimentally derived efficiency and exergy analysis of a new solar air heater having different surface shapes". *Renew. Energy*, 50.

Van Berkel,R. (2018). "Evolution of Solar Thermal Process Heating in India".

Bhagoria,J.L., Saini,J.S., and Solanki,S.C. (2002). "Heat transfer coefficient and friction factor correlations for rectangular solar air heater duct having transverse wedge shaped rib roughness on the absorber plate". *Renew. Energy*, 25.

Bharadwaj,G., Varun, Kumar,R., and Sharma,A. (2017). "Heat transfer augmentation and flow characteristics in ribbed triangular duct solar air heater: An experimental analysis". *Int. J. Green Energy*, 14.

Bhargava,A.K. and Rizzi,G. (1990). "A solar air heater with variable flow passage width". *Energy Convers. Manag.*, 30.

Bhushan,B. and Singh,R. (2010). "A review on methodology of artificial roughness used in duct of solar air heaters". *Energy*, 35.

Bliss,R.W. (1959). "The derivations of several 'Plate-efficiency factors' useful in the design of flat-plate solar heat collectors". *Sol. Energy*, 3.

Boache,P.J. (1994). "Perspective: A method for uniform reporting of grid refinement studies". *J. Fluids Eng. Trans. ASME*, 116.

Bopche,S.B. and Tandale,M.S. (2009). "Experimental investigations on heat transfer and frictional characteristics of a turbulator roughened solar air heater duct". *Int. J. Heat Mass Transf.*, 52.

Boughali,S., Benmoussa,H., Bouchekima,B., Mennouche,D., Bouguettaia,H., and

Bechki,D. (2009). "Crop drying by indirect active hybrid solar - Electrical dryer in the eastern Algerian Septentrional Sahara". *Sol. Energy*, 83.

Bradshaw,P. (1987). "Turbulent Secondary Flows.". *Annu. Rev. Fluid Mech.*, 19, 53–74.

Braga,S.L. and Saboya,F.E.M. (1996). "Turbulent heat transfer and pressure drop in an internally finned equilateral triangular duct". *Exp. Therm. Fluid Sci.*, 12.

Close,D.J. (1963). "Solar air heaters for low and moderate temperature applications". *Sol. Energy*, 7.

Cozzi, L., Gould, T., Bouckart, S., Crow, D., Kim, T. Y., Mcglade, C., ... & Wetzel, D. (2020). "World Energy Outlook 2020". *Paris: IEA*

Deo,N.S., Chander,S., and Saini,J.S. (2016). "Performance analysis of solar air heater duct roughened with multigap V-down ribs combined with staggered ribs". *Renew. Energy*, 91.

Duan,Q., Wang,D., Li,X., Li,Y., and Zhang,S. (2019). "Thermal characteristics of a novel enclosed cascade-like heat pump dryer used in a tunnel type drying system". *Appl. Therm. Eng.*, 155.

Duffie,J.A., Beckman,W.A., and Worek,W.M. (1994). "Solar Engineering of Thermal Processes, 2nd ed.". *J. Sol. Energy Eng.*, 116.

Ebrahim Momin,A.M., Saini,J.S., and Solanki,S.C. (2002). "Heat transfer and friction in solar air heater duct with V-shaped rib roughness on absorber plate". *Int. J. Heat Mass Transf.*, 45.

Einstein,D., Worrell,E., and Khrushch,M. (2001). "Steam systems in industry: Energy use and energy efficiency improvement potentials". In, *Proceedings ACEEE Summer Study on Energy Efficiency in Industry*.

Ekechukwu,O. V. (1999). "Review of solar-energy drying systems I: An overview of drying principles and theory". *Energy Convers. Manag.*, 40.

Fudholi,A., Sopian,K., Yazdi,M.H., Ruslan,M.H., Gabbasa,M., and Kazem,H.A. (2014). "Performance analysis of solar drying system for red chili". *Sol. Energy*, 99.

Garg & Prakash,H.P.G. (2000). "Solar energy: Fundamentals and Applications".

Gawande,V.B., Dhoble,A.S., Zodpe,D.B., and Chamoli,S. (2016). "Experimental and CFD investigation of convection heat transfer in solar air heater with reverse L-shaped ribs". *Sol. Energy*, 131.

Ge,Z., Wang,Huitao, Wang,Hua, Zhang,S., and Guan,X. (2014). "Exergy analysis of flat plate solar collectors". *Entropy*, 16.

Göğüş,F. and Maskan,M. (1999). "Water adsorption and drying characteristics of Okra (Hibiscus Esculentus L.)". *Dry. Technol.*, 17.

Goud,M., Reddy,M.V.V., V.P.,C., and S.,S. (2019). "A novel indirect solar dryer with inlet fans powered by solar PV panels: Drying kinetics of Capsicum Annum and Abelmoschus esculentus with dryer performance". *Sol. Energy*, 194.

Gupta,D., Solanki,S.C., and Saini,J.S. (1993). "Heat and fluid flow in rectangular solar air heater ducts having transverse rib roughness on absorber plates". *Sol. Energy*, 51.

Gupta,D., Solanki,S.C., and Saini,J.S. (1997). "Thermohydraueic performance of solar air heaters with roughened absorber plates". *Sol. Energy*, 61, 33–42.

Gupta,M.K. and Kaushik,S.C. (2009). "Performance evaluation of solar air heater for various artificial roughness geometries based on energy, effective and exergy efficiencies". *Renew. Energy*, 34.

Guyer, E. C. (1999). "Handbook of applied thermal design". CRC press.

Hans,V.S., Saini,R.P., and Saini,J.S. (2010). "Heat transfer and friction factor correlations for a solar air heater duct roughened artificially with multiple v-ribs". *Sol. Energy*, 84.

Hans,V.S., Saini,R.P., and Saini,J.S. (2009). "Performance of artificially roughened solar air heaters-A review". *Renew. Sustain. Energy Rev.*, 13.

Hans,V.S., Gill,R.S., and Singh,S. (2017). "Heat transfer and friction factor correlations for a solar air heater duct roughened artificially with broken arc ribs". *Exp. Therm. Fluid Sci.*, 80.

Hegazy,A.A. (1996). "Optimization of flow-channel depth for conventional flat-plate solar air heaters". *Renew. Energy*, 7.

Imoudu,P.B. and Olufayo,A.A. (2000). "The effect of sun-drying on milling yield and quality of rice". *Bioresour. Technol.*, 74.

Istanto,T., Danardono,D., Yaningsih,I., and Wijayanta,A.T. (2016). "Experimental study of heat transfer enhancement in solar air heater with different angle of attack of V-down continuous ribs". In, *AIP Conference Proceedings*.

Jain,S.K., Agrawal,G. Das, Misra,R., Verma,P., Rathore,S., and Jamuwa,D.K. (2019). "Performance Investigation of a Triangular Solar Air Heater Duct Having Broken Inclined Roughness Using Computational Fluid Dynamics". *J. Sol. Energy Eng. Trans. ASME*, 141.

Jaurker,A.R., Saini,J.S., and Gandhi,B.K. (2006). "Heat transfer and friction characteristics of rectangular solar air heater duct using rib-grooved artificial roughness". *Sol. Energy*, 80.

Jin,D., Zhang,M., Wang,P., and Xu,S. (2015). "Numerical investigation of heat transfer and fluid flow in a solar air heater duct with multi V-shaped ribs on the absorber plate". *Energy*, 89.

Kalogirou,S. (2003). "The potential of solar industrial process heat applications". *Appl. Energy*, 76.

Karmare,S. V. and Tikekar,A.N. (2007). "Heat transfer and friction factor correlation for artificially roughened duct with metal grit ribs". *Int. J. Heat Mass Transf.*, 50.

Karsli,S. (2007). "Performance analysis of new-design solar air collectors for drying applications". *Renew. Energy*, 32.

Karwa,R., Bairwa,R.D., Jain,B.P., and Karwa,N. (2005). "Experimental study of the effects of rib angle and discretization on heat transfer and friction in an asymmetrically heated rectangular duct". *J. Enhanc. Heat Transf.*, 12.

Karwa,R., Solanki,S.C., and Saini,J.S. (1999). "Heat transfer coefficient and friction factor correlations for the transitional flow regime in rib-roughened

rectangular ducts". *Int. J. Heat Mass Transf.*, 42.

Katekawa,M.E. and Silva,M.A. (2006). "A review of drying models including shrinkage effects". *Dry. Technol.*, 24.

Khanlari,A., Sözen,A., Şirin,C., Tuncer,A.D., and Gungor,A. (2020). "Performance enhancement of a greenhouse dryer: Analysis of a cost-effective alternative solar air heater". *J. Clean. Prod.*, 251.

Kline,S. and McClintock,F. (1953). "Describing uncertainties in single-sample experiments". *Mech. Eng.*, 75.

Kreith, F., & Kreider, J. F. (1978). "Principles of solar engineering". Washington.

Kumar,A., Bhagoria,J.L., and Sarviya,R.M. (2009). "Heat transfer and friction correlations for artificially roughened solar air heater duct with discrete W-shaped ribs". *Energy Convers. Manag.*, 50.

Kumar,A., Saini,R.P., and Saini,J.S. (2012). "Experimental investigation on heat transfer and fluid flow characteristics of air flow in a rectangular duct with Multi v-shaped rib with gap roughness on the heated plate". *Sol. Energy*, 86.

Kumar,K., Prajapati,D.R., and Samir,S. (2017). "Heat transfer and friction factor correlations development for solar air heater duct artificially roughened with 'S' shape ribs". *Exp. Therm. Fluid Sci.*, 82.

Kumar,R., Kumar,A., and Goel,V. (2017). "A parametric analysis of rectangular rib roughened triangular duct solar air heater using computational fluid dynamics". *Sol. Energy*, 157.

Kumar,A. and Layek,A. (2019a). "Energetic and exergetic performance evaluation of solar air heater with twisted rib roughness on absorber plate". *J. Clean. Prod.*, 232.

Kumar,A. and Layek,A. (2019b). "Nusselt number and friction factor correlation of solar air heater having twisted-rib roughness on absorber plate". *Renew. Energy*, 130.

Kumar,R., Kumar,A., and Goel,V. (2019). "Performance improvement and development of correlation for friction factor and heat transfer using computational

fluid dynamics for ribbed triangular duct solar air heater". *Renew. Energy*, 131.

Kumar,R., Varun, and Kumar,A. (2016). "Thermal and fluid dynamic characteristics of flow through triangular cross-sectional duct: A review". *Renew. Sustain. Energy Rev.*, 61.

Labed,A., Moummi,N., Aoues,K., and Benchabane,A. (2016). "Solar drying of henna (Lawsonia inermis) using different models of solar flat plate collectors: An experimental investigation in the region of Biskra (Algeria)". *J. Clean. Prod.*, 112.

Lalude,O. and Buchberg,H. (1971). "Design and application of honeycomb porous-bed solar-air heaters". *Sol. Energy*, 13.

Lanjewar,A., Bhagoria,J.L., and Sarviya,R.M. (2011a). "Heat transfer and friction in solar air heater duct with W-shaped rib roughness on absorber plate". *Energy*, 36.

Lanjewar,A.M., Bhagoria,J.L., and Sarviya,R.M. (2011b). "Performance analysis of W-shaped rib roughened solar air heater". *J. Renew. Sustain. Energy*, 3.

Lanjewar,A.M., Bhagoria,J.L., and Agrawal,M.K. (2015). "Review of development of artificial roughness in solar air heater and performance evaluation of different orientations for double arc rib roughness". *Renew. Sustain. Energy Rev.*, 43.

Lansing,F.L., Clarke,V., and Reynolds,R. (1979). "A high performance porous flat-plate solar collector". *Energy*, 4.

Layek,A., Saini,J.S., and Solanki,S.C. (2007a). "Heat transfer and friction characteristics for artificially roughened ducts with compound turbulators". *Int. J. Heat Mass Transf.*, 50.

Layek,A., Saini,J.S., and Solanki,S.C. (2007b). "Second law optimization of a solar air heater having chamfered rib-groove roughness on absorber plate". *Renew. Energy*, 32.

Lewis,N.S. (2007). "Toward cost-effective solar energy use". *Science (80-.).*, 315.

Luo,D.D., Leung,C.W., and Chan,T.L. (2004). "Forced convection and flow friction characteristics of air-cooled horizontal equilateral triangular ducts with ribbed internal surfaces". *Int. J. Heat Mass Transf.*, 47.

Manjunath,M.S., Vasudeva Karanth,K., and Yagnesh Sharma,N. (2019). "Numerical analysis of flat plate solar air heater integrated with an array of pin fins on absorber plate for enhancement in thermal performance". *J. Sol. Energy Eng. Trans. ASME*, 141.

Mayor,L. and Sereno,A.M. (2004). "Modelling shrinkage during convective drying of food materials: A review". *J. Food Eng.*, 61.

Methods of testing to determine the thermal performance of solar collectors (2003). *ASHRAE Stand.*

Nozik,A.J. (1978). "Photoelectrochemistry: Applications to Solar Energy Conversion". *Annu. Rev. Phys. Chem.*, 29.

Nwosu,N.P. (2010). "Employing exergy-optimized pin fins in the design of an absorber in a solar air heater". *Energy*, 35.

Pandey,N.K., Bajpai,V.K., and Varun (2016). "Experimental investigation of heat transfer augmentation using multiple arcs with gap on absorber plate of solar air heater". *Sol. Energy*, 134.

Patel,Y.M., Jain,S. V., and Lakhera,V.J. (2020). "Thermo-hydraulic performance analysis of a solar air heater roughened with reverse NACA profile ribs". *Appl. Therm. Eng.*, 170.

Patil,A.K., Saini,J.S., and Kumar,K. (2011). "Effect of gap position in broken V-rib roughness combined with staggered rib on thermohydraulic performance of solar air heater". *Green*, 1.

Patil,A.K. (2015). "Heat transfer mechanism and energy efficiency of artificially roughened solar air heaters - A review". *Renew. Sustain. Energy Rev.*, 42.

Prasad,B.N. and Saini,J.S. (1988). "Effect of artificial roughness on heat transfer and friction factor in a solar air heater". *Sol. Energy*, 41.

Prasad,B.N. and Saini,J.S. (1991). "Optimal thermohydraulic performance of artificially roughened solar air heaters". *Sol. Energy*, 47.

Prasad,K. and Mullick,S.C. (1983). "Heat transfer characteristics of a solar air heater used for drying purposes". *Appl. Energy*, 13.

Promthaisong,P. and Eiamsa-ard,S. (2019). "Fully developed periodic and thermal performance evaluation of a solar air heater channel with wavy-triangular ribs placed on an absorber plate". *Int. J. Therm. Sci.*, 140.

Purohit,S., Madhwesh,N., Vasudeva Karanth,K., and Yagnesh Sharma,N. (2019). "Heat Transfer Augmentation Using an Innovative Helicoidal Finned Absorber Plate in a Solar Air Heater-A Numerical Study". *J. Sol. Energy Eng. Trans. ASME*, 141.

Putra,R.N. and Ajiwiguna,T.A. (2017). "Influence of Air Temperature and Velocity for Drying Process". In, *Procedia Engineering*.

Rabha,D.K., Muthukumar,P., and Somayaji,C. (2017). "Experimental investigation of thin layer drying kinetics of ghost chilli pepper (Capsicum Chinense Jacq.) dried in a forced convection solar tunnel dryer". *Renew. Energy*, 105.

Roache,P.J., Ghia,K.N., and White,F.M. (1986). "Editorial policy statement on the control of numerical accuracy". *J. Fluids Eng. Trans. ASME*, 108.

Saha,A.K. and Acharya,S. (2004). "Unsteady simulation of turbulent flow and heat transfer in a channel with periodic array of cubic pin-fins". *Numer. Heat Transf. Part A Appl.*, 46.

Sahu,M.K. and Prasad,R.K. (2016). "Exergy based performance evaluation of solar air heater with arc-shaped wire roughened absorber plate". *Renew. Energy*, 96.

Sahu,M.M. and Bhagoria,J.L. (2005). "Augmentation of heat transfer coefficient by using 90° broken transverse ribs on absorber plate of solar air heater". *Renew. Energy*, 30.

Saini,R.P. and Saini,J.S. (1997). "Heat transfer and friction factor correlations for artificially roughened ducts with expanded metal mesh as roughness element". *Int. J. Heat Mass Transf.*, 40.

Saini,S.K. and Saini,R.P. (2008). "Development of correlations for Nusselt number and friction factor for solar air heater with roughened duct having arc-shaped wire as artificial roughness". *Sol. Energy*, 82.

Saini,V., Tiwari,S., and Tiwari,G.N. (2017). "Environ economic analysis of various

types of photovoltaic technologies integrated with greenhouse solar drying system". *J. Clean. Prod.*, 156.

Sallam,Y.I., Aly,M.H., Nassar,A.F., and Mohamed,E.A. (2015). "Solar drying of whole mint plant under natural and forced convection". *J. Adv. Res.*, 6.

Satcunanathan,S. and Deonarine,S. (1973). "A two-pass solar air heater". *Sol. Energy*, 15.

Selçuk,K. (1971). "Thermal and economic analysis of the overlapped-glass plate solar-air heater". *Sol. Energy*, 13.

Senadeera,W., Bhandari,B., Young,G., and Wijesinghe,B. (2000). "Physical Properties and Fluidization Behaviour of Fresh Green Bean Particulates During Fluidized Bed Drying". *Food Bioprod. Process.*, 78.

Shamekhi-Amiri,S., Gorji,T.B., Gorji-Bandpy,M., and Jahanshahi,M. (2018). "Drying behaviour of lemon balm leaves in an indirect double-pass packed bed forced convection solar dryer system". *Case Stud. Therm. Eng.*, 12.

Sharma,S.K. and Kalamkar,V.R. (2015). "Thermo-hydraulic performance analysis of solar air heaters having artificial roughness-A review". *Renew. Sustain. Energy Rev.*, 41.

Singh,A. and Singh,S. (2017). "CFD investigation on roughness pitch variation in non-uniform cross-section transverse rib roughness on Nusselt number and friction factor characteristics of solar air heater duct". *Energy*, 128.

Singh,A.P., Varun, and Siddhartha (2014). "Heat transfer and friction factor correlations for multiple arc shape roughness elements on the absorber plate used in solar air heaters". *Exp. Therm. Fluid Sci.*, 54.

Singh Bisht,V., Kumar Patil,A., and Gupta,A. (2018). "Review and performance evaluation of roughened solar air heaters". *Renew. Sustain. Energy Rev.*, 81.

Singh,I. and Singh,S. (2018a). "A review of artificial roughness geometries employed in solar air heaters". *Renew. Sustain. Energy Rev.*, 92.

Singh,I. and Singh,S. (2018b). "CFD analysis of solar air heater duct having square wave profiled transverse ribs as roughness elements". *Sol. Energy*, 162.

156

Singh,S. (2018). "Thermal performance analysis of semicircular and triangular cross-sectioned duct solar air heaters under external recycle". *J. Energy Storage*, 20.

Singh,S., Chander,S., and Saini,J.S. (2012). "Exergy based analysis of solar air heater having discrete V-down rib roughness on absorber plate". *Energy*, 37.

Singh,S., Chander,S., and Saini,J.S. (2011). "Heat transfer and friction factor correlations of solar air heater ducts artificially roughened with discrete V-down ribs". *Energy*, 36.

Singh,S., Singh,B., Hans,V.S., and Gill,R.S. (2015). "CFD (computational fluid dynamics) investigation on Nusselt number and friction factor of solar air heater duct roughened with non-uniform cross-section transverse rib". *Energy*, 84.

Singh,I., Vardhan,S., Singh,S., and Singh,A. (2019). "Experimental and CFD analysis of solar air heater duct roughened with multiple broken transverse ribs: A comparative study". *Sol. Energy*, 188.

Tamna,S., Skullong,S., Thianpong,C., and Promvonge,P. (2014). "Heat transfer behaviors in a solar air heater channel with multiple V-baffle vortex generators". *Sol. Energy*, 110.

Tanda,G. (2011). "Performance of solar air heater ducts with different types of ribs on the absorber plate". *Energy*, 36.

Thakur,D.S., Khan,M.K., and Pathak,M. (2017). "Performance evaluation of solar air heater with novel hyperbolic rib geometry". *Renew. Energy*, 105.

Varun, Saini,R.P., and Singal,S.K. (2008). "Investigation of thermal performance of solar air heater having roughness elements as a combination of inclined and transverse ribs on the absorber plate". *Renew. Energy*, 33.

Verma,S.K. and Prasad,B.N. (2000). "Investigation for the optimal thermohydraulic performance of artificially roughened solar air heaters". *Renew. Energy*, 20.

Vidal,A., Vinuesa,R., Schlatter,P., and Nagib,H.M. (2017). "Influence of corner geometry on the secondary flow in turbulent square ducts". *Int. J. Heat Fluid Flow*, 67, 69–78.

Vidal,A., Vinuesa,R., Schlatter,P., and Nagib,H.M. (2018). "Turbulent rectangular ducts with minimum secondary flow". *Int. J. Heat Fluid Flow*, 72, 317–328.

Wang, L., & Sundén, B. (2007). "Experimental investigation of local heat transfer in a square duct with various-shaped ribs". *Heat and Mass Transfer*, *43*(8), 759-766.

Wang,D., Liu,Jin, Liu,Y., Wang,Y., Li,B., and Liu,Jiaping (2020). "Evaluation of the performance of an improved solar air heater with "S" shaped ribs with gap". *Sol. Energy*, 195.

Webb,R.L. and Eckert,E.R.G. (1972). "Application of rough surfaces to heat exchanger design". *Int. J. Heat Mass Transf.*, 15.

Xiong,X., Narsimhan,G., and Okos,M.R. (1992). "Effect of composition and pore structure on binding energy and effective diffusivity of moisture in porous food". *J. Food Eng.*, 15.

Xiao,H., Wang,J., Liu,Z., and Liu,W. (2019). "Turbulent heat transfer optimization for solar air heater with variation method based on exergy destruction minimization principle". *Int. J. Heat Mass Transf.*, 136.

Yadav,A.S. and Bhagoria,J.L. (2013a). "A CFD (computational fluid dynamics) based heat transfer and fluid flow analysis of a solar air heater provided with circular transverse wire rib roughness on the absorber plate". *Energy*, 55.

Yadav,A.S. and Bhagoria,J.L. (2013b). "Heat transfer and fluid flow analysis of solar air heater: A review of CFD approach". *Renew. Sustain. Energy Rev.*, 23.

Yadav,A.S. and Bhagoria,J.L. (2014). "A CFD based thermo-hydraulic performance analysis of an artificially roughened solar air heater having equilateral triangular sectioned rib roughness on the absorber plate". *Int. J. Heat Mass Transf.*, 70.

Zhang,X., Liu,B., Liu,J., Wang,X., and Zhang,H. (2020). "Experimental and numerical analysis of heat transfer and flow characteristics in parabolic ducts". *Int. J. Heat Mass Transf.*, 147.

APPENDIX

EXPERIMENTAL UNCERTAINTY ANALYSIS

The method to estimate the uncertainty in the determination of experimental parameters are discussed in this section.

Let the error in measurement of the following experimental parameters be represented as follows,

Error in the measurement of hydraulic diameter	$= \Delta D$
Error in the measurement of cross-sectional area of SAH	$= \Delta A_c$
Error in the measurement of surface area of absorber plate	$= \Delta A_p$
Error in the measurement of air velocity	$= \Delta V$
Error in the measurement of air mass flow rate	$= \Delta \dot{m}$
Error in the measurement of Reynolds number	$= \Delta Re$
Error in the measurement of air outlet temperature	$= \Delta T_o$
Error in the measurement of air inlet temperature	$= \Delta T_i$
Error in the measurement of heat gained	$= \Delta \dot{Q}$
Error in the measurement of convective heat transfer coefficient	$= \Delta h$
Error in the measurement of Nusselt number	$= \Delta Nu$
Error in the measurement of friction factor	$= \Delta f$

Reynolds number (Re)

$$Re = \frac{\rho V D}{\mu}$$

$$\frac{\partial Re}{\partial V} = \frac{\rho D}{\mu}$$

$$\frac{\partial Re}{\partial D} = \frac{\rho V}{\mu}$$

Uncertainty in the measurement of Reynolds number is given by,

$$\Delta Re = \pm \sqrt{\left(\frac{\partial Re}{\partial V}\right)^2 \times (\Delta V)^2 + \left(\frac{\partial Re}{\partial D}\right)^2 \times (\Delta D)^2}$$

The percentage uncertainty in determining Reynolds number is,

$$U_{Re} = \frac{\Delta Re}{Re} \times 100$$

Convective heat transfer coefficient *(h)*

$$h = \frac{q}{(T_p - T_b)}$$

$$\frac{\partial h}{\partial q} = \frac{1}{(T_p - T_b)}$$

$$\frac{\partial h}{\partial (T_p - T_b)} = \frac{-q}{(T_p - T_b)^2}$$

Uncertainty in evaluating convective heat transfer coefficient is,

$$\Delta h = \pm \sqrt{\left(\frac{\partial h}{\partial q}\right)^2 \times (\Delta q)^2 + \left(\frac{\partial h}{\partial (T_p - T_b)}\right)^2 \times \left(\Delta(T_p - T_b)\right)^2}$$

The percentage uncertainty in determining convective heat transfer coefficient is,

$$U_h = \frac{\Delta h}{h} \times 100$$

Nusselt number *(Nu)*

$$Nu = \frac{hD}{\lambda}$$

$$\frac{\partial Nu}{\partial D} = \frac{h}{\lambda}$$

$$\frac{\partial Nu}{\partial h} = \frac{D}{\lambda}$$

Uncertainty in evaluating Nusselt number is,

$$\Delta Nu = \pm \sqrt{\left(\frac{\partial Nu}{\partial D}\right)^2 \times (\Delta D)^2 + \left(\frac{\partial Nu}{\partial h}\right)^2 \times (\Delta h)^2}$$

The percentage uncertainty in determining Nusselt number is,

$$U_{Nu} = \frac{\Delta Nu}{Nu} \times 100$$

Friction factor (*f*)

$$f = \frac{P_d D}{2\rho L V^2}$$

$$\frac{\partial f}{\partial P_d} = \frac{D}{2\rho L V^2}$$

$$\frac{\partial f}{\partial D} = \frac{P_d}{2\rho L V^2}$$

$$\frac{\partial f}{\partial V} = \frac{P_d D}{2\rho L} \times \left(\frac{-2}{V^3}\right)$$

Uncertainty in evaluating friction factor is,

$$\Delta f = \pm \sqrt{\left(\frac{\partial f}{\partial P_d}\right)^2 \times (\Delta P_d)^2 + \left(\frac{\partial f}{\partial D}\right)^2 \times (\Delta D)^2 + \left(\frac{\partial f}{\partial V}\right)^2 \times (\Delta V)^2}$$

The percentage uncertainty in determining friction factor (*f*) is,

$$U_f = \frac{\Delta f}{f} \times 100$$

SAMPLE CALCULATION OF EXPERIMENTAL UNCERAINTY ANALYSIS

For the experimental data of thermo-hydraulic performance analysis of solar air heater with artificial roughness, the uncertainty analysis is carried out as follows:

Length of the test section (L) = 0.8 m; Width of the test section (W) = 0.16 m; Height of the test section (H) = 0.04 m; Hydraulic diameter of the test section (D) = 0.064 m; Reynolds number (Re) = 10000; Air velocity (V) = 2.38 m/s; Inlet air temperature (T_i) = 303 K; Heat flux (q) = 1000 W/m²; Outlet air temperature (T_o) = 313 K; Bulk mean temperature (T_b) = 308 K; Absorber plate temperature (T_p) = 336 K; Convective heat transfer coefficient (h) = 49.68 W/m²K and Nusselt number (Nu) = 134.

Let the error in measurement of the experimental parameters be represented as follows,

Error in the measurement of mass flow rate of air = $\Delta \dot{m} = \pm 3.4 \times 10^{-7}$ kg/sec

Error in the measurement of air temperature = $\Delta T_a = \pm\ 0.5°C$

Error in the measurement of absorber plate temperature = $\Delta T_p = \pm\ 0.5°C$

Error in the measurement of heat flux = $\Delta q = \pm\ 1\ W/m^2$

Error in the measurement of pressure drop = $\Delta P_d = \pm\ 0.01\ Pa$

Reynolds number (*Re*)

$$Re = \frac{\rho V D}{\mu} = \left(\frac{1.225 \times 2.38 \times 0.064}{1.785 \times 10^{-5}}\right) = 10000$$

$$\frac{\partial Re}{\partial V} = \frac{\rho D}{\mu} = \left(\frac{1.225 \times 0.064}{1.785 \times 10^{-5}}\right) = 4392.15$$

$$\frac{\partial Re}{\partial D} = \frac{\rho V}{\mu} = \left(\frac{1.225 \times 2.38}{1.785 \times 10^{-5}}\right) = 163333.33$$

Uncertainty in the measurement of Reynolds number (*Re*) is given by,

$$\Delta Re = \pm\sqrt{\left(\frac{\partial Re}{\partial V}\right)^2 \times (\Delta V)^2 + \left(\frac{\partial Re}{\partial D}\right)^2 \times (\Delta D)^2}$$

$$= \pm\sqrt{(4392.15)^2 \times (0.0585)^2 + (163333.33)^2 \times (0.001)^2}$$

$$= \pm 304.46$$

The percentage uncertainty in determining Reynolds number (*Re*) is,

$$U_{Re} = \frac{\Delta Re}{Re} \times 100 = \frac{304.46}{10000} \times 100 = \pm 3\%$$

Convective heat transfer coefficient *(h)*

$$h = \frac{q}{(T_p - T_b)} = \frac{1000}{18.5} = 54\ W/m^2K$$

$$\frac{\partial h}{\partial q} = \frac{1}{(T_p - T_b)} = \frac{1}{18.5} = 0.054\ 1/K$$

$$\frac{\partial h}{\partial (T_p - T_b)} = \frac{-q}{(T_p - T_b)^2} = -2.92\ W/m^2$$

Uncertainty in evaluating convective heat transfer coefficient is,

$$\Delta h = \pm \sqrt{\left(\frac{\partial h}{\partial q}\right)^2 \times (\Delta q)^2 + \left(\frac{\partial h}{\partial (T_p - T_b)}\right)^2 \times \left(\Delta(T_p - T_b)\right)^2}$$

$$= \pm\sqrt{(0.054)^2 \times (1)^2 + (-2.92)^2 \times (0.5)^2}$$

$$= \pm 2.24 \text{ W/m}^2\text{K}$$

The percentage uncertainty in determining convective heat transfer coefficient *(h)* **is,**

$$U_h = \frac{\Delta h}{h} \times 100 = \frac{2.24}{54} = \pm 4.1\%$$

Nusselt number *(Nu)*

$$Nu = \frac{hD}{\lambda} = \frac{54 \times 0.064}{0.0258}$$

$$\frac{\partial Nu}{\partial D} = \frac{h}{\lambda} = \frac{54}{0.0258} = 2093.02$$

$$\frac{\partial Nu}{\partial h} = \frac{D}{\lambda} = \frac{0.064}{0.0258} = 2.48$$

Uncertainty in evaluating Nusselt number is,

$$\Delta Nu = \pm \sqrt{\left(\frac{\partial Nu}{\partial D}\right)^2 \times (\Delta D)^2 + \left(\frac{\partial Nu}{\partial h}\right)^2 \times (\Delta h)^2}$$

$$= \pm\sqrt{(2093.02)^2 \times (1.65 \times 10^{-3})^2 + (2.48)^2 \times (2.24)^2}$$

$$= \pm 4.84$$

The percentage uncertainty in determining Nusselt number *(Nu)* **is,**

$$U_{Nu} = \frac{\Delta Nu}{Nu} \times 100 = \frac{4.84}{134} = \pm 3.6\%$$

Friction factor *(f)*

$$f = \frac{P_d D}{2\rho L V^2} = \frac{3.50 \times 0.064}{2 \times 1.225 \times 0.8 \times 2.38^2} = 0.024$$

$$\frac{\partial f}{\partial P_d} = \frac{D}{2\rho LV^2} = \frac{0.064}{2 \times 1.225 \times 0.8 \times 2.38^2} = 6.33 \times 10^{-3}$$

$$\frac{\partial f}{\partial D} = \frac{P_d}{2\rho LV^2} = \frac{3.50}{2 \times 1.225 \times 0.8 \times 2.38^2} = 0.346$$

$$\frac{\partial f}{\partial V} = \frac{P_d D}{2\rho L} \times \left(\frac{-2}{V^3}\right) = \frac{3.50 \times 0.064 \times (-2)}{2 \times 1.225 \times 0.8 \times 2.38^3} = -0.019$$

Uncertainty in evaluating friction factor is,

$$\Delta Nu =$$

$$\pm\sqrt{(6.33 \times 10^{-3})^2 \times (0.01)^2 + (0.346)^2 \times (1.65 \times 10^{-3})^2 + (-0.019)^2 \times (0.0585)^2}$$

$$= \pm 1.276 \times 10^{-3}$$

The percentage uncertainty in determining friction factor (*f*) is,

$$U_f = \frac{1.276 \times 10^{-3}}{0.024} \times 100 = \pm 5.3\%$$

LIST OF PUBLICATIONS BASED ON RESEARCH WORK

Sl. No.	Title of the paper	Authors	Name of the Journal/ Conference, Vol., No., Pages	Month & Year of Publication	Category *
1	Thermo-hydraulic and exergetic performance of a cost-effective solar air heater: CFD and experimental study	**Nidhul, K.**, Yadav, A. K., Anish, S., & Arunachala, U. C.	Renewable Energy, Volume 184, Pages 627-641. https://doi.org/10.1016/j.renene.2021.11.111 **(SCI, IF: 8.00)**	December 2021	1
2	Critical review of ribbed solar air heater and performance evaluation of various V-rib configuration	**Nidhul, K.**, Yadav, A. K., Anish, S., & Kumar, S.	Renewable and Sustainable Energy Reviews, Volume 142, Pages 110871. https://doi.org/10.1016/j.rser.2021.110871 **(SCI, IF: 14.98)**	March 2021	1
3	Computational and experimental studies on the development of an energy-efficient drier using ribbed triangular duct solar air heater	**Nidhul, K.**, Kumar, S. Yadav, A. K. & Anish, S.	Solar Energy, Volume 209, Pages 454-469. https://doi.org/10.1016/j.solener.2020.09.012 **(SCI, IF: 5.74)**	September 2020	1
4	Efficient design of an artificially roughened solar air heater with semi-cylindrical side walls: CFD and exergy analysis	**Nidhul, K.**, Yadav, A. K., Anish, S., & Arunachala, U. C.	Solar Energy, Volume 207, Pages 289-304. https://doi.org/10.1016/j.solener.2020.06.054 **(SCI, IF: 5.74)**	July 2020	1
5	Enhanced thermo-hydraulic performance in a V-ribbed triangular duct solar air heater: CFD and exergy analysis	**Nidhul, K.**, Kumar, S. Yadav, A. K. & Anish, S.	Energy, Volume 200, Pages 117448. https://doi.org/10.1016/j.energy.2020.117448 **(SCI, IF: 7.14)**	March 2020	1

6	Influence of Rectangular Ribs on Exergetic Performance in a Triangular Duct Solar Air Heater	**Nidhul, K.**, Kumar, S. Yadav, A. K. & Anish, S.	J. Thermal Sci. Eng. Appl., 12 (5), 051010 https://doi.org/10.1115/1.4046057 **(SCI, IF: 1.47)**	January 2020	1
7	Enhancing thermo-hydraulic performance of a solar air heater using square rib roughness: CFD analysis	**Nidhul K.**, Ajay Kumar Yadav & Anish S.	25th National and 3rd International ISHMT-ASTFE Heat and Mass Transfer Conference (IHMTC 2019), IIT Roorkee, Uttarakhand, India	December 2019	3
8	Numerical analysis on the impact of rib profile on thermo-hydraulic performance of a solar air heater	**Nidhul K.**, Ajay Kumar Yadav & Anish S.	11th International Exergy, Energy and Environment Symposium (IEEES-11), SRM University, Chennai	July 2019	3
9	Exergy analysis of a square rib roughened triangular duct solar air heater	**Nidhul, K.**, Kumar, S. Yadav, A. K. & Anish, S.	11th International Exergy, Energy and Environment Symposium (IEEES-11), SRM University, Chennai	July 2019	3

* Category: 1: Journal paper, full paper reviewed

2: Journal paper, Abstract reviewed

3: Conference/Symposium paper, full paper reviewed

4: Conference/Symposium paper, abstract reviewed

5: others (Book chapter, NITK Research Bulletins, Short notes etc.)

Nidhul K.
Research Scholar
Name & Signature, with Date

Dr. Ajay Kumar Yadav
Research Guide
Name & Signature, with Date

Dr. Anish S.
Research Guide
Name & Signature, with Date

BIODATA

Name: NIDHUL K.

Date of Birth: 13/03/1989

Mobile Number: +91-9061402950

E-mail ID: nidhul07@gmail.com

Residential Address: Nidhul K.

S/o: Narayanan V. K.

Udayam House

(P.O.) Chala, Chala East

Kannur, Kerala. (670621)

Qualification:

Examination	Institute	University	Year	Percentage /CGPA
B.Tech (Mechanical Engineering)	Government College of Engineering Kannur	Kannur University	2011	68.7%
M.Tech (Internal Combustion Engines and Turbomachinery)	Government Engineering College Thrissur	University of Calicut	2014	8.21

Research Interests: Solar Air Heater, Computational Fluid Dynamics, Heat Transfer, Fluid Mechanics.